Residual Stress Effects on

Fatigue and Fracture Testing

and Incorporation of Results into Design

J. O. Bunch
M. R. Mitchell

Editors

ASTM INTERNATIONAL
Standards Worldwide

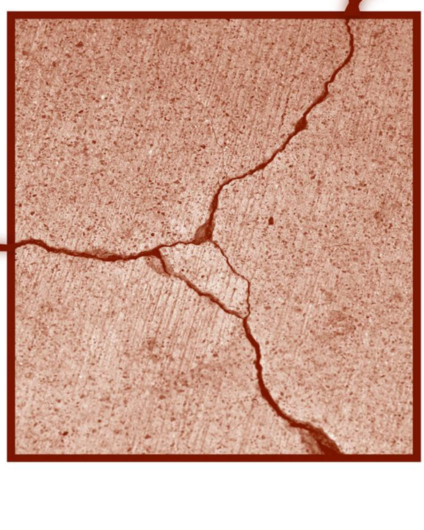

STP 1497

STP 1497

Residual Stress Effects on Fatigue and Fracture Testing and Incorporation of Results into Design

Jeffrey O. Bunch and M. R. Mitchell, editors

ASTM Stock Number: STP1497

ASTM
100 Barr Harbor Drive
PO Box C700
West Conshohocken, PA 19428-2959

Printed in the U.S.A.

INTERNATIONAL

ISBN: 0-8031-4472-5
ISBN: 978-0-8031-4472-9

Library of Congress Cataloging-in-Publication Data

Residual Stress Effects on Fatigue and Fracture Testing and Incorporation of Results into Design / Jeffrey O. Bunch, editor. I, Michael R. Mitchell, II
p. cm. -- (STP 1497)
ISBN 0-8031-4472-5 ISBN 978-0-8031-4472-9
1. Impact--Testing--Equipment and supplies. 2. Pendulum. 3. Notched bar testing--Equipment and supplies. J. O. Bunch, I. Michael R. Mitchell, II., :ASTM special technical publication ; 1497.

TA418.34.P46
620.1'125--dc22 2007
2006016951

Peer Review Policy

Each paper published in this volume was evaluated by two peer reviewers and at least one editor. The authors addressed all of the reviewers' comments to the satisfaction of both the technical editor(s) and the ASTM International Committee on Publications.

The quality of the papers in this publication reflects not only the obvious efforts of the authors and the technical editor(s), but also the work of the peer reviewers. In keeping with long-standing publication practices, ASTM International maintains the anonymity of the peer reviewers. The ASTM International Committee on Publications acknowledges with appreciation their dedication and contribution of time and effort on behalf of ASTM International.

Printed in Lancaster, PA
January 2007

Foreword

This publication, *Residual Stress Effects on Fatigue and Fracture Testing and Incorporation of Results into Design*, contains papers presented at the Symposium on Residual Stress, which was held in Salt Lake City, UT on 19-20 May, 2004. The symposium was sponsored by ASTM International Committee E08 on Fatigue and Fracture. Dr. Jeffrey O. Bunch, Boeing Integrated Defense Systems, presided as symposium chairman and served as editor of this compilation. Co-chair of the symposium, was Dr. Michael R. Mitchell, Northern Arizona University.

Dr. Jeffrey O. Bunch
Boeing Integrated Defense Systems
Seattle, WA
Symposium Chairman and Editor

Dr. Michael R. Mitchell
Northern Arizona University
Flagstaff, AZ
Symposium Co-chair and Editor

Contents

Overview

This book represents the research of several authors presented at the *Symposium on Residual Stress Effects on Fatigue and Fracture Testing and Incorporation of Results into Design* held in Salt Lake City, Utah, May 19-20, 2004. This symposium brought together researchers, practitioners of residual stress measurement techniques, structural analysts, and designers specializing in the influence of residual stress on fatigue and fracture. The intent of the symposium was to foster continued dialogue between these groups and thereby provide each with an understanding of the state of knowledge concerning residual stresses and their effect on structural integrity. Residual stresses can be present due to processing and manufacturing of materials and structures, so it is imperative to understand how and why they can influence the test data that we used in structural design methodologies. Residual stresses may also be intentionally engineered into structures in attempts to improve fatigue life, and it is equally important that designers understand how to account for these potential effects on fatigue life.

ASTM Committee E08 on Fatigue and Fracture is committed to providing timely information on the state-of-the-art of fatigue and fracture testing and lifetime prediction methods. Contained in this STP is a continuation of that commitment. Manuscripts covering the influence of processing and methods to account for residual stresses in predicting fatigue life are provided in this volume. Also included are manuscripts in which are discussed several applications of residual stress measurement methods. Engineered residual stresses further address fatigue crack growth and fatigue lifetime predictions of cold-worked holes and the influence of shot peening.

Future workshops and symposia sponsored by ASTM Committee E08 on Fatigue and Fracture are planned and will continue to foster dialogue on this highly important subject in fatigue and fracture.

Dr. Jeffrey O. Bunch
Boeing Integrated Defense Systems
Seattle, WA
Symposium Chairman and Editor

Dr. Michael R. Mitchell
Northern Arizona University
Flagstaff, AZ
Symposium Co-chair and Editor

Journal of ASTM International, May 2005, Vol. 2, No. 5
Paper ID JAI12556
Available online at www.astm.org

Matthew T. Kokaly,[1] *Ph.D., Joy S. Ransom,*[1] *B.S., Jude H. Restis,*[1] *M.Sc., and Len Reid,*[1] *M.Sc.*

Predicting Fatigue Crack Growth in the Residual Stress Field of a Cold Worked Hole

ABSTRACT: Cold working of holes generates compressive residual stresses resulting in a significant fatigue life improvement over a non-cold worked hole. Current fatigue life prediction methods for cold worked holes are based on two-dimensional (2-D) linear superposition of stress intensity factor, K, solutions of the non-cold worked hole and the residual stresses. Such predictions have shown various levels of agreement with the overall fatigue life and have generally underpredicted the crack growth over the majority of life. An inverse process was used to generate K solutions for the residual stresses of two experimental data sets using AFGROW and the crack growth data from the experiments. The inverse K solutions were inconsistent with the residual stress distribution indicating that it contained mechanisms or features not inherent to the 2-D weight function method. The predicted fatigue life was found to be very sensitive to a ± 1 % variance in the inversely generated K solution. This sensitivity of the K method is a very important issue that must be addressed in the future. A 2-D FEA model indicated that the crack remained completely closed over a range of crack lengths despite experimental crack growth indicating that the model was not an accurate physical representation of the real crack. The results of this study combined with the significantly faster crack growth observed on the side of the hole corresponding to the entry side of the mandrel and the through thickness residual hoop stress variation show that the current methodology based on a 2-D assumptions is inadequate in predicting the fatigue crack growth from cold worked holes for the range of specimen thicknesses in this study. It is suggested that further research focus on incorporating the through thickness stress variance in a solution that predicts crack growth both in the radial and through thickness directions to capture the peculiar crack growth associated with cold working.

KEYWORDS: cold working, residual stress, fatigue, crack growth, stress intensity factor

Introduction

Cold working of a hole generates large compressive stresses that result in a significant fatigue life improvement over a non-cold worked hole. This fatigue life improvement, while extensively documented, has not been easy to predict using conventional analytical methods. The success of the stress intensity factor, K, in predicting fatigue crack growth in other fatigue situations has resulted in numerous attempts to modify known solutions to fit that of a cold worked hole. Most of these are composed of a linear superposition of the known non-cold worked hole K solution and a K solution based on the residual stresses (often derived via a weight function) to generate an effective K.

$$K_{eff} = K_{\text{non-cold worked}} + K_{\text{residual stresses}} \tag{1}$$

These attempts have resulted in varying degrees of success in predicting the overall fatigue life of holes [1–4] but at the same time have significantly underestimated the crack length over the majority of life.

Manuscript received 6 April 2004; accepted for publication 2 November 2004; published May 2005. Presented at ASTM Symposium on Residual Stress Effects on Fatigue and Fracture Testing and Incorporation of Results into Design on 19-21 May 2004 in Salt Lake City, UT.
[1] Fatigue Technology, Inc., Seattle, WA.

The underprediction of the crack length over time can result in erroneous damage tolerance and inspection intervals if such an analysis is used. To correctly establish inspection limits and to accurately assess the replacement of a part in a damage tolerance program, the entire crack growth from small cracks to failure must be more accurately determined over a significant portion of the life.

Cold Working a Hole

Cold working of a hole is typically achieved by pulling an oversized mandrel through a split sleeve inserted into the hole. The radial expansion of the hole is large enough to cause plastic deformation in the parent material. Once the mandrel exits the material, a stress equilibrium is reached between the plastically deformed material (in compression) and the material surrounding the plastic zone (in tension). The plastic zone and compressive stresses extend approximately one radius from the edge of the hole. It is important to note that the residual stress field is not uniform through the thickness of the part due to axial material flow during the mandrel pull through process and free edge effects during relaxation as seen in Fig. 1 for a 7xxx series aluminum. Two-dimensional (2-D) plane stress models of the process are typically representative of the material at the free edges, while plane strain models are typically representative of the stresses near the center of the parent material.

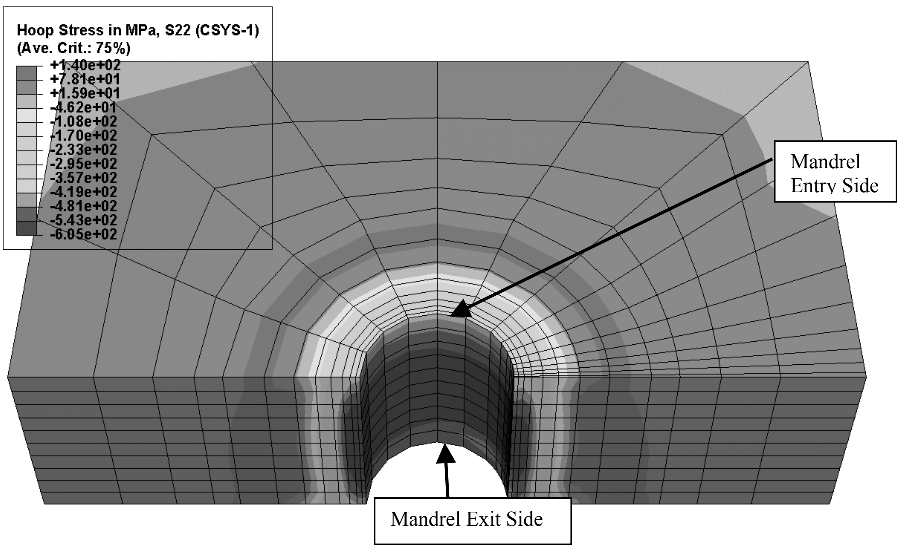

FIG. 1—*Cold worked hole through thickness residual hoop stress gradient in a typical 7xxx series aluminum.*

Objective

The objective of this study was to investigate the usefulness of combining experimental, analytical, and numerical methods to further understanding of the crack growth mechanisms and current prediction methodologies of fatigue cracks growing from cold worked holes.

Method of Approach

This introductory study was divided into two parts:

- K solution investigation: The K solution was calculated inversely using data from the literature and from a new round of testing to further understand the K method as applied to cold worked holes. Crack length (a) versus the number of cycles (N) data was used in an inverse approach with AFGROW to determine the K solution due to the residual stresses ($K_{residual\ stress}$ in Eq 1) required to match the crack growth curves. The robustness of K based methods was explored by examining the effect of varying the inversely calculated K solution on the crack growth prediction. General features about the K solution were also noted.
- Finite Element Analysis: A ½ symmetry two-dimensional (2-D) FEA model of the test specimens was created to observe the crack mechanics at various crack lengths.

$K_{residual\ stress}$ Investigation

$K_{residual\ stress}$ can be determined indirectly from a fatigue test when the crack length versus the number of cycles has been recorded. The AFGROW crack prediction software contains an option to enter modifications to the stress intensity factor of a given crack model at various crack lengths. This option can be used in an inverse process to match the crack growth curve of an experiment. The resulting $K_{residual\ stress}$ distribution should be representative of the contribution of the residual stresses to K_{eff}.

Two different sets of experimental data were used in the inverse process: the results of an earlier study by Saunder and Grandt [5] and results of testing performed at Fatigue Technology, Incorporated (FTI). The tests were very similar with a few exceptions. Details of the two specimens are given in Table 1, and details of the two tests are shown in Table 2. The level of expansion was determined by the FTI standard system based on the size of the hole.

TABLE 1—*Specimen parameters.*

	Saunder and Grandt [5]	FTI
Type of Specimen	Dogbone	Dogbone
Material	7075-T651	7075-T651
Specimen Width	63.5 mm	59.7 mm
Specimen Thickness	6.35 mm	5.08 mm
Final Hole Size	6.35 mm	9.91 mm
Initial Crack Size	1.24 mm	0.51 mm
Special Notes	Pre-cracked before coldworking, hole was offset with e/D = 4.0	Pre-cracked after coldworking, hole was centered

TABLE 2—*Fatigue test parameters.*

	Saunder and Grandt [5]	FTI
Type of Fatigue Loading	Constant Amplitude	Constant Amplitude
R Ratio	0.05	0.05
Peak Stress	206 MPa	172 MPa
Number of Specimens	1 Cold Worked	1 Cold Worked, 1 Non-Cold Worked

The results of Saunder and Grandt [5] were subjected first to the inverse process. Saunder and Grandt fitted a segmented Walker Equation to their experimental da/dN versus ΔK data and to additional data given in [6] for the 7075-T651 aluminum used in their study. The same relation was used here. Test specimens consisted of dogbones with different offset 6.35 mm-in. cold worked holes. Since edge margins (e/D) can significantly affect the residual stress field and resulting crack growth, only the data from the specimen with e/D = 4.0 were used in this study. The data with e/D = 4.5 were not used, as they did not appear consistent with the rest of the data.

Figure 2 shows the average crack length (a) versus number of cycles (N) for the e/D = 4.0 specimen. It should be noted that a large difference between the size of the crack on the entry and exit sides was observed, though it is not shown here. The majority of the fatigue life occurred when the crack length was less than approximately 2.54-mm long. A simple 2-D plane stress FEA model confirmed that the edge of the compressive zone for a hole this size in 7075-T651 extended approximately 2.54-mm from the edge of the hole as seen in Fig. 3.

Figure 2 also shows the a versus N curve obtained from the AFGROW inverse process. The experimental and inverse curves were nearly identical as expected. The values of $K_{residual\ stress}$ versus crack length used to generate the AFGROW a versus N curve are provided in Fig. 4. $K_{residual\ stress}$ was nearly constant over a range of crack lengths from ~1.52-mm to 2.54-mm. This same crack length range was associated with nearly 100 000 of the total 120 000 cycles of the fatigue life. Over that same range, the residual stress decreased significantly as seen in Fig. 3.

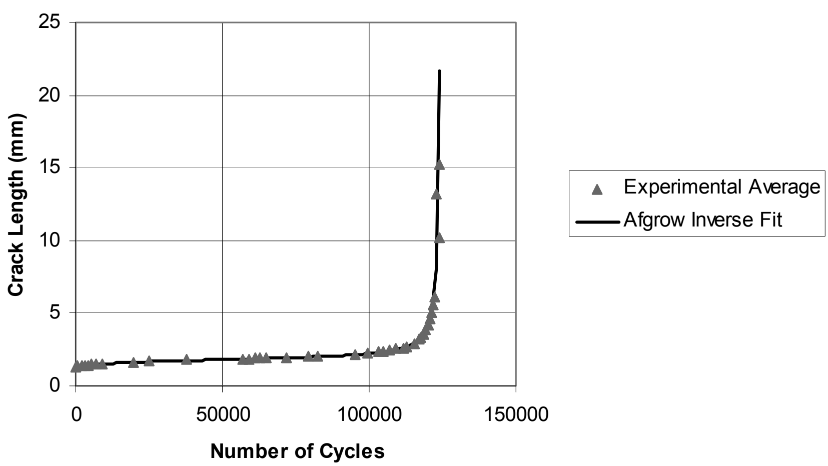

FIG. 2—*Crack growth data of Saunder and Grandt [5].*

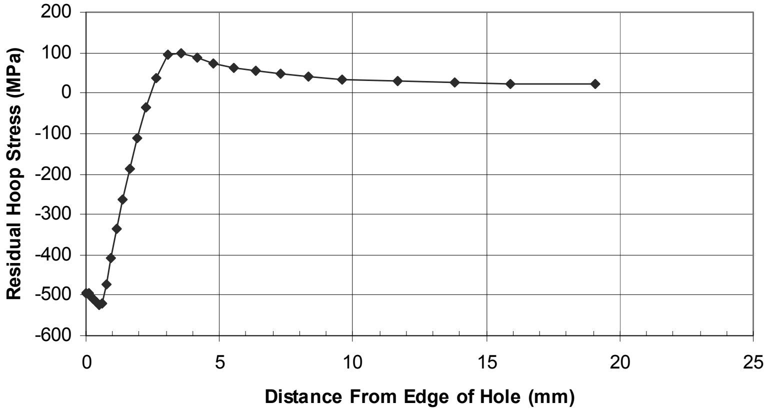

FIG. 3—*2-D FEA residual hoop stress distribution around a 6.35 mm cold worked hole in 7075-T651.*

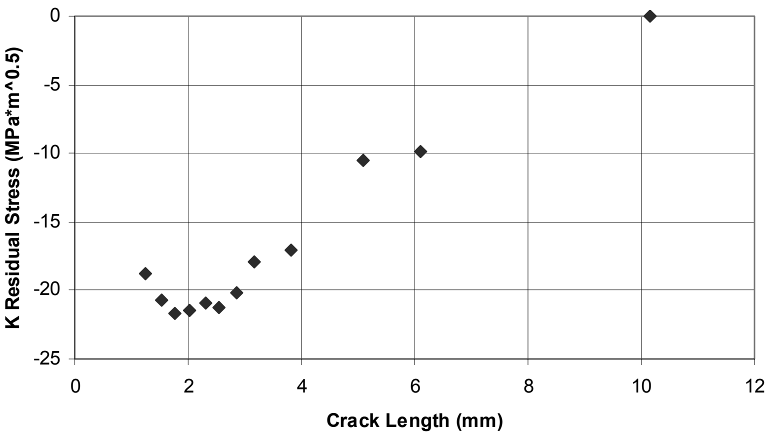

FIG. 4—$K_{residual\ stress}$ *from the AFGROW inverse analysis on data of Saunder and Grandt [5].*

The effect of increasing and decreasing $K_{residual\ stress}$ on the fatigue life was examined to determine the sensitivity of the K based method. Unfortunately, estimates of the level of error inherent in the prediction of K via the current linear superposition method (errors in the residual stress profile and material properties) were lacking. A value of ± 1 % was chosen with high confidence that the level of actual error was higher.

The results are shown in Fig. 5. The 1 % variance of $K_{residual\ stress}$ translated into a range of fatigue life from 96 000–160 000 cycles, severely underpredicting and overpredicting the actual fatigue life of 120 000 cycles. The majority of the difference in life again occurred over a small range of crack lengths bound by the compressive zone. This level of sensitivity is troubling since errors in material data and estimates of the residual stress field are expected to be larger than 1 %. This sensitivity issue must be addressed before methods employing K will yield reliable and consistent predictions of crack growth from cold worked holes.

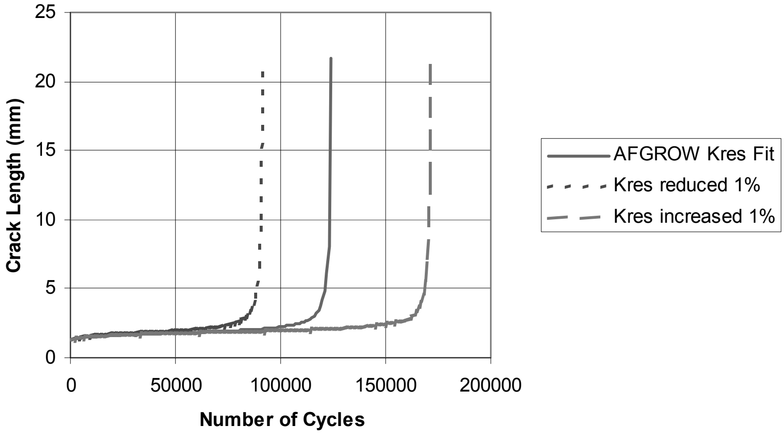

FIG. 5—*Effect of ± 1 % Change in $K_{residual\ stress}$ on the predicted fatigue life.*

FTI conducted similar tests to Saunder and Grandt as seen in Tables 1 and 2. Tests were performed on both a cold worked (Cx) and non-cold worked (NCx) specimen. The Cx specimen was first cold worked at a diameter of 9.22 mm. A 0.38-mm long notch was introduced, and the tip was sharpened with a razor blade. The specimen was then fatigue cracked at 172 MPa until the crack extended a distance of 5.46 mm from the centerline of the hole. The hole was then reamed to a diameter of 9.91 mm to clean up the notch. The same procedure was performed on the NCx specimen without the cold working step.

To determine the validity of the AFGROW model and the use of material data from Saunder and Grandt in the current investigation, the a versus N curve of the FTI NCx test was compared with the AFGROW prediction using the material data from [5]. The AFGROW prediction closely matched the experimental data for the NCx specimen indicating the validity of the non-cold worked K solution used in AFGROW and the material data [5] as seen in Fig. 6.

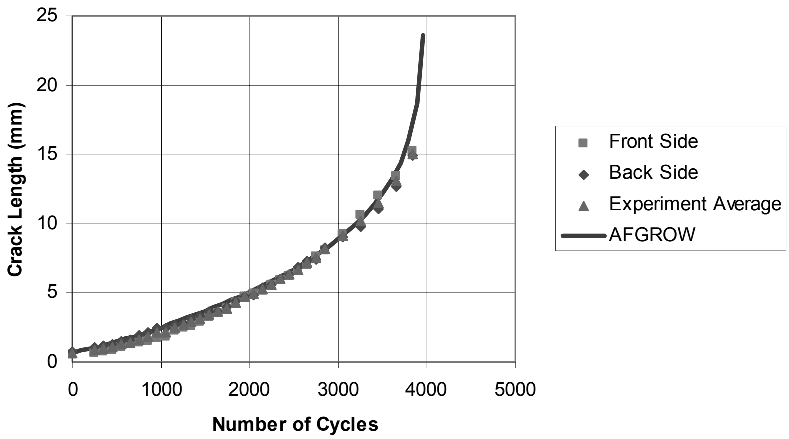

FIG. 6—*Comparison of NCx AFGROW prediction and FTI NCx data.*

The crack growth data for the Cx specimen is shown in Fig. 7. Similar to the Saunder and Grandt data, the crack length was significantly higher on the mandrel entry side than the mandrel exit side. The average of the cracks on these two surfaces was used in the AFGROW inverse process. As with the analysis of the Saunder and Grandt data, the majority of life occurred over a very small range of crack lengths. A simple 2-D plane stress model of the residual compressive stress shows that this region also correlated with the approximate size of the compressive zone as shown in Fig. 8.

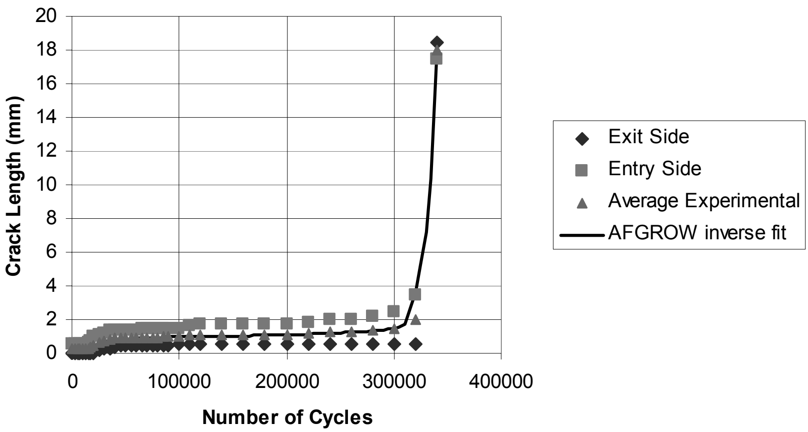

FIG. 7—*FTI crack growth data.*

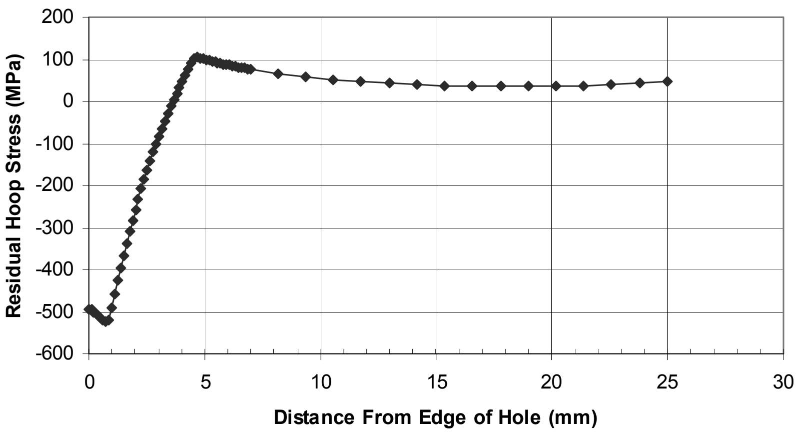

FIG. 8—*2-D FEA residual hoop stress distribution around a 9.91 mm cold worked hole in 7075-T651.*

The $K_{residual\ stress}$ from the inverse process on the FTI data is given in Fig. 9. The curve is of a similar shape to the results shown in Fig. 4 with a pronounced flat region. The flattened region of the $K_{residual\ stress}$ solution again occurred over a region of decreasing residual compressive stress. A $K_{residual\ stress}$ solution generated via weight function methods and the residual stress profile result in a discrete peak value that decays with the residual compressive stress. The lack of agreement between the inversely calculated K and the shape of K solutions derived from weight function methods demonstrated that, at a minimum, additional K modifications are needed in the 2-D method to accurately predict the crack growth and fatigue life. These K modifications may not be able to be computed via a closed form solution since they are most likely associated with modeling a 3-D problem (crack growth and residual stress distributions through the thickness are neglected or averaged) in 2-D.

To further explore the behavior of K during the crack growth, ΔK_{eff} was plotted versus number of cycles in Fig. 10. To achieve the slow crack growth of the experiment, the range of ΔK_{eff} was small and nearly constant over the majority of the life. The region of the da/dN versus ΔK curve responsible for ~88 % of the fatigue life is highlighted in Fig. 11. Together, Figs. 10 and 11 illustrate the reason for the extreme sensitivity of the K method seen in Fig. 5, as a small change in ΔK has a large effect on the crack growth rate.

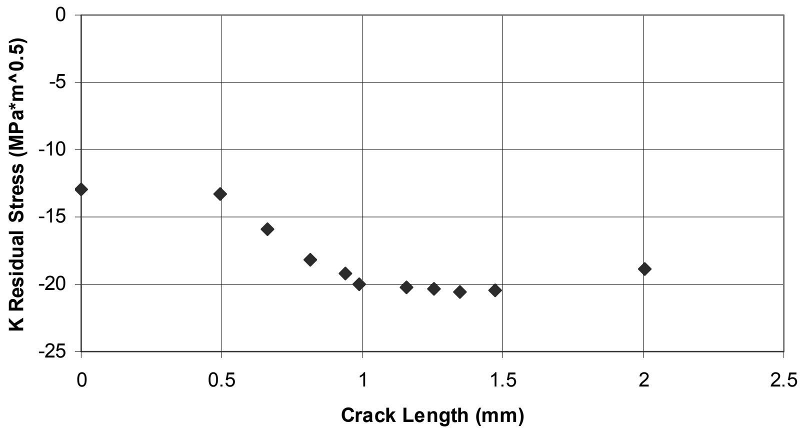

FIG. 9—*$K_{residual\ stress}$ from the AFGROW inverse analysis of current study.*

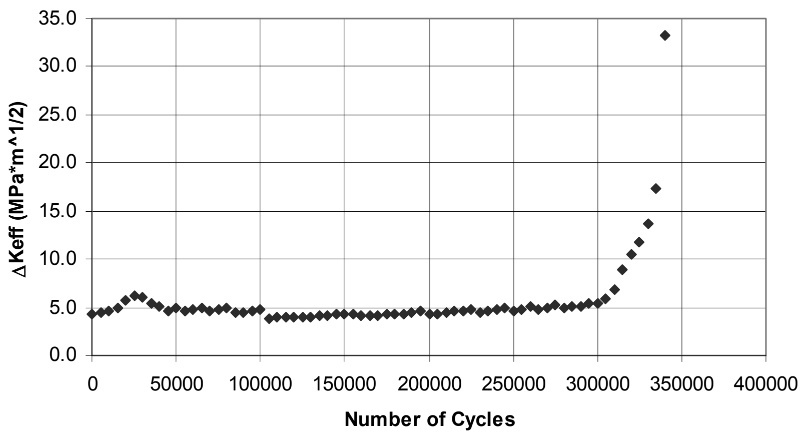

FIG. 10—*ΔK_{eff} from the AFGROW inverse analysis of current study.*

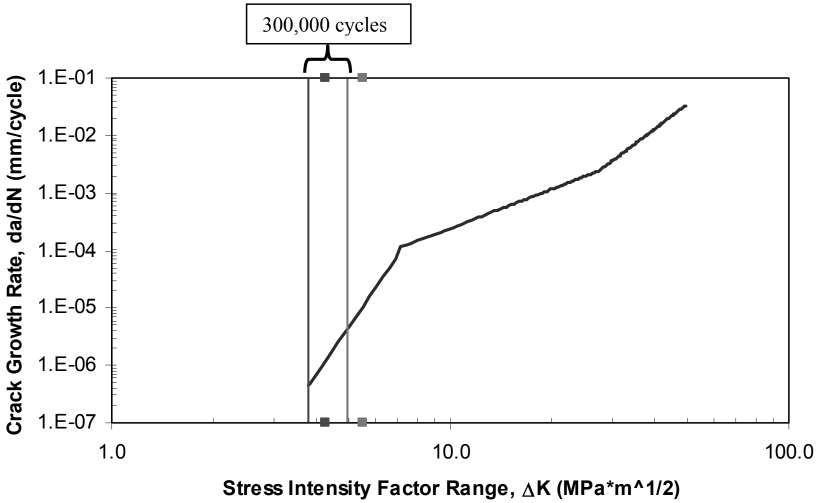

FIG. 11—*Material da/dN versus ΔK curve [5] highlighting range of ΔK_{eff} over 88 % of the fatigue life.*

In practice, the largest source of variability is associated with the estimation of the residual stress field used to calculate $K_{residual\ stress}$. As seen previously, a 1 % change in the $K_{residual\ stress}$ (and ΔK_{eff}) for this experiment resulted in much larger error in the fatigue life prediction.

Finite Element Analysis

The purpose of the FEA was to observe the crack mechanics (physical crack opening under load) and not the crack tip stress field. A ½ symmetry two-dimensional (2-D) plane stress finite element model was constructed simulating the test specimen used by FTI with a predetermined crack path as shown in Fig. 12. As mentioned previously, a residual hoop stress gradient is present through the thickness of a part, and this is not accounted for in a 2-D model. The decision to use a 2-D model has been made generally in most other studies and implementations of the K method to simplify the problem. Since the goal of the study was to evaluate the current methods, a 2-D model was used here to evaluate whether it adequately modeled the crack mechanics. The specimen thicknesses were on the borderline for plane stress and plane strain using a $2.5*(K_{Ic}/\sigma_{ys})^2$ relation, and the fast fracture surfaces of the specimens were indicative of plane stress. The plane stress model also yields a more conservative approach since the residual stresses are lower than in the plane strain model. An attempt was made to include a plain strain core as per Newman, et al. [7], but difficulties associated with stress gradients during the cold working operation could not be overcome in the current model.

The hole was cold worked by applying and then removing a uniform radial displacement to the hole. Elements were removed to capture the final ream operation. A crack was introduced and grown by removing boundary conditions along the face of the crack. To simulate contact with the mating crack surface during unloads, a rigid surface was placed along the crack plane. The model was subjected to an alternating pattern of crack growth generated by releasing boundary conditions followed by a load and unload step. The crack opening along the crack face was observed during the load for various crack lengths.

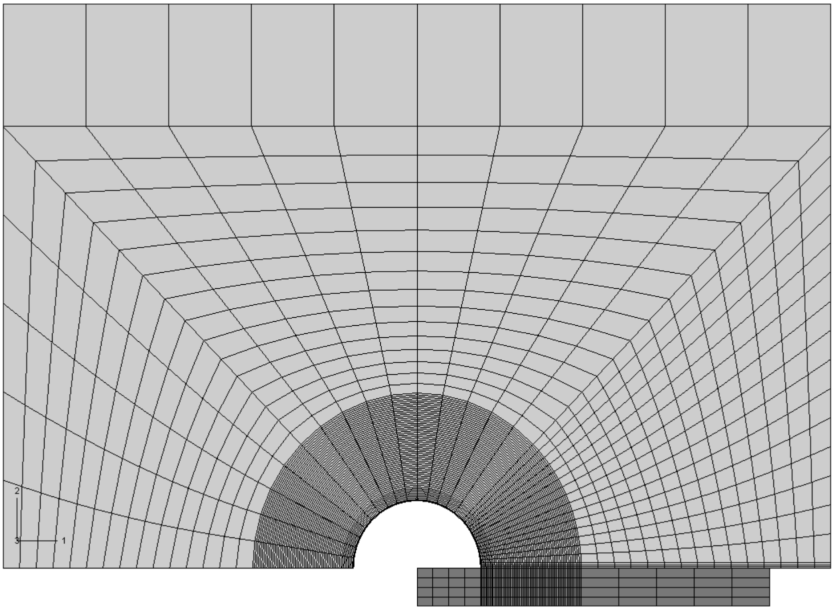

FIG. 12—*Two-dimensional FEA model of the fatigue specimen.*

The shape of the crack opening along the crack at different crack lengths is shown in Fig. 13. The rudimentary model used in this analysis indicated that the majority of the crack and the entirety of the crack tip remained completely closed under the 172 MPa load for crack lengths less than 1.88 mm. A small amount of opening was observed at the crack mouth. At crack lengths greater than 1.88 mm, the crack opened at both the edge of the hole and at the tip, while a considerable amount of the crack remained closed at the peak load.

Observations during the experiment showed that the crack grew continuously during the fatigue test and appeared to open and close at the crack tip throughout the test. This was contrary to 2-D FEA model results. As a result, it appeared that the 2-D model did not yield an accurate depiction of the crack mechanics. The differing crack growth on the exit and entry side in the experiment was another indication that the assumption of an average crack length in the 2-D FEA model was flawed and that a more general 3-D model is required.

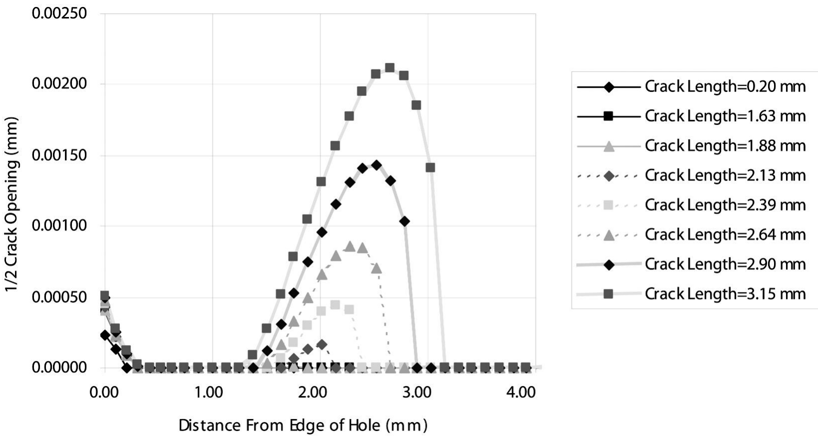

FIG. 13— Crack opening data from the FEA model for various crack lengths.

Discussion

The results indicate that the current 2-D $K_{residual\ stress}$ method for predicting crack growth from cold worked holes has several issues associated with a successful implementation. The shape of the $K_{residual\ stress}$ solution (determined inversely) required to match the crack growth curve is not consistent with the residual stress profile, and the prediction is highly sensitive to small changes in $K_{residual\ stress}$. 2-D FEA modeling of the crack around cold worked holes was also found to be flawed, as the results did not accurately model the crack mechanics.

These issues appear to be a result of imposing a 2-D solution onto a 3-D problem. The different crack lengths observed on the exit and entry face together with the through thickness variation of the residual hoop stresses are other good indicators that the 2-D methodology is not applicable in most cases, with the possible exception of thin materials.

In the 2-D case, a uniform through thickness crack has generally been treated as growing through a uniform residual stress field. The current experiment and others [3–5] have shown that crack growth on the entry side of the specimen is often significantly more than the crack growth observed on the exit side of the specimen. In the case of the current experiment, the crack grew significantly (~2.87-mm) more on the entry side than on the exit side. This difference occurred over a majority of the overall fatigue life. At the same time, 3-D models of the cold worked process have shown a significantly larger residual compressive stress in the center of the part than at the edges and a larger stress at the exit side than the entry side. The differences in the crack growth between the two surfaces and the abnormal delay in generating a through thickness crack may be attributable to the residual stress differences.

A crack in a cold worked hole typically initiates as a corner crack on the entry side of the part. In a non-cold worked situation, it quickly transitions to a through thickness crack. In the case of a cold worked hole, the residual stresses provide resistance to both crack growth radially from the hole and crack growth through the thickness. The resistance to crack growth increases through the thickness but decreases in the radial direction. The path of least resistance initially for a crack at the surface is radially where it grows into the diminishing residual compressive stress field. At some point, redistributions of the stress result in more crack growth through the thickness and on the exit side. 2-D methods are unable to capture this event and as a result are unable to accurately model the crack growth and crack mechanics. A move to a 3-D approach is required as illustrated in Fig. 14.

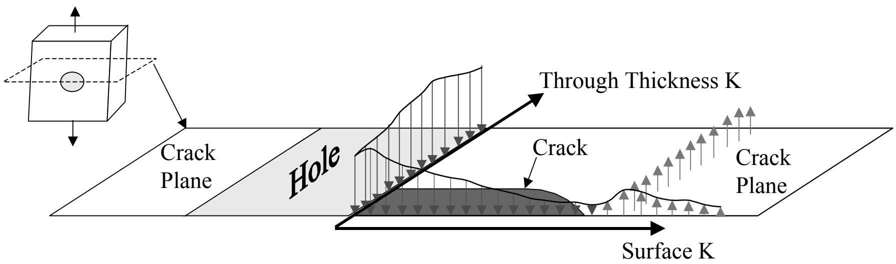

FIG. 14—*3-D approach to incorporating variable crack growth and residual stress through thickness.*

On a final note, underprediction of the crack growth during the majority of the fatigue life is common to many of the past studies. This underprediction is nearly as important as an accurate prediction of the fatigue life. Underprediction of the crack growth may result in removing and replacing parts earlier than required when the vast majority of life of the component remains. The current measure of effectiveness of a given prediction method should be expanded from a simple determination of the fatigue life to an accurate prediction of the entire crack growth curve.

Conclusions

The following conclusions can be made from this study:

- The inverse process was successful at generating the $K_{residual\ stress}$ required to match the crack growth curves of the experimental results provided here.
- The inverse process was useful as a tool to examine the $K_{residual\ stress}$ for a specific test result as used here. A larger number of specimens is required to develop a general empirical solution.
- The $K_{residual\ stress}$ required to match the crack growth curve appeared to be inconsistent with the residual compressive stress distribution indicating that either additional modifications are needed to the current 2-D K methodology to account for additional factors, such as variable through thickness stress distributions and crack growth rates, or a new methodology is needed.
- The current 2-D K methodology was found to be extremely sensitive to small differences in $K_{residual\ stress}$ and could result in significantly under or overestimating the fatigue life.
- The 2-D FEA model indicated that the crack did not open during a significant portion of the fatigue life, which was inconsistent with the crack growth results and indicated that the 2-D model was not physically representative of the crack.
- Cracks in this and other studies were found to initiate and propagate faster on the entry side of the specimen than on the exit side of the specimen.
- Changes to the current method must be made to more accurately model the mechanics of the crack due to the residual stress gradient through the thickness. These changes will

most likely require analysis of the crack front in two directions and include the through thickness variation of the residual compressive stress (A full 3-D analyses).

References

[1] Chandawanich, N. and Sharpe, W., Jr., "An Experimental Study of Fatigue Crack Growth Initiation and Growth from Cold worked Holes," *Engineering Fracture Mechanics*, Vol. 11, 1979, pp. 609–620.

[2] Cathey, W. H. and Grandt, A. F., "Fracture Mechanics Consideration of Residual Stresses Introduced by Cold working Fastener Holes," *Journal of Engineering Materials and Technology*, Vol. 102, 1980, pp. 85–91.

[3] Ball, D. L. and Lowry, D. R., "Experimental Investigation on the Effects of Cold Expansion of Fastener Holes," *Fatigue & Fracture of Engineering Materials and Structures*, Vol. 21, 1998, pp.17–34.

[4] Gaerke, J., Zhang, X., and Wang, Z., "Life Enhancement of Fatigue-Aged Fastener Holes using the Cold Expansion Process," *Proceedings of the Institute of Mechanical Engineers*, Vol. 214, Part G, 2000, pp. 281–293.

[5] Saunder, T. J. and Grandt, A. F., "The Effect of Edge Distance on Cold Working Fastener Holes," *Proceedings of the Fourth Joint DoD/FAA/NASA Conference on Aging Aircraft*, St. Louis, MO, 15–18 May 2000.

[6] *Damage Tolerance Deign Handbook – A Compiliation of Fracture and Crack Growth Rate for High Strength Alloys*, MCIC-HB-01R, University of Dayton Research Institute and Materials Laboratory, Air Force Wright Aeronautical Laboratories, Wright-Patterson AFB, December 1983.

[7] Newman, J. C., Booth, B. C., and Shivakumar, K. N., "An Elastic-Plastic Finite-Element Analysis of the J-Resistance Curve Using a CTOD Criterion," *Fracture Mechanics: 18th Volume, ASTM STP 945*, D. T. Read and R. P. Reed, Eds., ASTM International, West Conshohocken, PA, 1988, pp. 665–685.

Journal of ASTM International, Vol. 3, No. 5
Paper ID JAI12559
Available online at www.astm.org

William T. Fujimoto[1]

Modeling the Formation and Growth of Cracks from Cold-Worked Holes

ABSTRACT: First generation crack formation and crack growth predictive approaches for cold-worked holes—based on the growth of a single noninteracting crack in a stationary residual stress field—fail to account fully for the physical mechanisms by which cracks form and grow from cold-worked holes. This failure leads in many cases to large differences between predicted and actual lives. Factors not accounted for in first generation approaches include the following: 1. 3-D nature of residual stress field due to mandrel pull-through. 2. Multistage crack growth involving a progressively spreading system of cracks. 3. Multiple potential initial crack sites, and the effect of site upon the multistage crack growth path. 4. Relaxation of the residual stress field due to overloads/underloads, or due to cyclic reyielding from crack growth. 5. Interaction of the hole with adjacent structural elements for multilayer joints.A physics-based second generation methodology for accounting for these factors is described. This methodology separates into individual building blocks each of the various mechanisms controlling the formation and relaxation of residual stresses, and the nucleation and progression of a system of cracks. Because it explicitly models each of these mechanisms, it is capable of eliminating or reducing the uncertainty over the life improvement potential of the cold-working process, allowing the full potential of cold-working to alleviate the aging aircraft problem to be untapped.

KEYWORDS: residual stresses, cold-working, fatigue, fracture mechanics, weight function, stress intensity factors

Introduction

Cold-working of fastener holes is used extensively to increase the fatigue life and damage tolerance of mechanically-fastened joints in aircraft structural members. Life improvement factors of up to five or more are possible with holes which are cold-worked, while factors approaching 40 [1] are possible if cold-working is used in conjunction with interference fit fasteners. Clearly, if exploited to its full potential, cold-working can be a key element in a structural sustainment strategy to reduce life cycle costs via life extension, or in developing long life, low maintenance airframe members.

While the general principles by which cold-working can extend life are understood, exploiting the full potential of cold-working has been held back by a lack of a full understanding of the failure mechanisms in cold-worked holes. The life increase which is possible in multilayer aircraft joints is a function of many parameters, i.e., stress spectra, fastener system, % mandrel interference, edge distance, material properties, fastener clamp-up, restraint of secondary bending, surface finish and coating of the joint members, etc.

First generation approaches, such as the equivalent initial flaw size (EIFS) [2], or elastoplastic analyses based on two-dimensional solutions for the uniform expansion of a cylinder [3,4], either ignore the physics of the crack growth process, such as in the case of EIFS, or idealize the crack growth progress as involving a single crack growing from the edge of the hole in a stationary two-dimensional stress field which is unaffected by the growth of the crack.

Because the effects of many of the parameters controlling life are difficult to quantify, the life of a complex joint with cold-worked holes must usually be established by test. Testing is costly and time-consuming, and is only good for determining the life of the joint for a specific usage spectrum, not for optimizing the design for improved life, or for understanding how variations in usage can affect life. Depending on how these parameters interact, the actual life improvement factor for a joint with cold-

Manuscript received March 22, 2004; accepted for publication February 13, 2006; published online April 2006. Presented at ASTM Symposium on Residual Stress Effects on Fatigue and Fracture Testing and Incorporation of Results into Design on 19-21 May 2004 in Salt Lake City, UT; J. Bunch, Guest Editor.
[1] Advanced Structural Technology, Inc., e-mail: wfujimoto@advancedstructuraltechnology.com

worked holes versus one without cold-working may vary from little or no increase, to an increase of an order of magnitude or more.

In this paper, a physics-based approach for the total life prediction of joints with cold-worked hole is described. This approach accounts explicitly for each of the major mechanisms affecting the crack formation and crack growth lives, including relaxation of the residual stress field and the progressive growth of a system of cracks.

Key Factors Influencing Life

Key factors influencing life include the following:

- *3-D nature of residual stress field due to mandrel pull-through.*
- *Multistage crack growth involving a progressively spreading system of cracks.*
- *Multiple potential initial crack sites, and the effect of site upon the multistage crack growth path.*
- *Relaxation of the residual stress field due to overloads/underloads, or due to cyclic reyielding from crack growth.*
- *Interaction of the hole with adjacent structural elements for multilayer joints.*

A detailed discussion of the factors follows.

Through-the-Thickness Variations in Residual Stresses Due to The Directional Nature of Mandrel Pull-through—The through-the-thickness variations exist due to the directional nature of the cold-working process. In the split-sleeve cold-working method of Fatigue Technology, Inc. (FTI), the most popular method for airframe construction, an oversize tapered mandrel is pulled through the sheet by a pneumatic tool. A lubricated expandable split-sleeve is inserted in the hole prior to cold-working to prevent direct contact between the hole and the sliding mandrel. Upon pulling the mandrel through the hole, the hole is reamed to the final hole dimension. The directional process induces different residual stresses at the entrance surface, the midplane and at the exit surface.

Through-the-thickness variations in the residual stress field occur because the plate undergoes out-of-plane deformation during the mandrel pull-through process [5] and because of transverse shear stresses resulting from the diametral differences between the portion of the hole being expanded and the previously expanded portion of the hole, as shown schematically in Fig. 1. Figure 1 illustrates the rotation of a plate as a mandrel is pulled up through the hole. Figure 1(*a*) shows the rotation of the work-piece after the tapered "entry" ramp of the mandrel has entered the bottom of the hole. As shown in Fig. 1(*a*), the resultant pressure force acts below the midplane of the work-piece, causing an "upward" rotation of the work-piece. The opening of the hole due to work-piece rotation also reduces the contact pressure between the mandrel and the hole, since it reduces the effective interference. More importantly, high transverse shear stresses are induced as the loaded portion of the hole experiences yielding while the expansion of the hole is resisted by the elastic material along the unyielded portion of the hole. These transverse shear stresses act to reduce the residual hoop stresses imparted upon unloading, as the elastic spring-back resulting from the shear stresses is less than the elastic spring-back resulting from the compression of the deformed material.

The opposite occurs as the mandrel reaches the top of the hole, but the effects of work-piece rotation are ameliorated. As Fig. 1(*b*) shows, the resultant pressure force acts above the midplane of the work-piece, causing a "downward" rotation of the work-piece. The downward rotation "opens" the top of the hole, reducing the contact pressure between the mandrel and the hole. However, the high transverse shear stresses present during mandrel entry are not present during mandrel exit, due to the permanent expansion of the portion of the hole below the contact region. The permanent expansion of the material below the contact region reduces the shear stresses restraining expansion of the material near the exit surface. As a result, spring-back results primarily from elastic compression of the deformed material, not from transverse shear stresses. Thus, higher residual hoop stresses can be developed at the exit surface than at the entry surface.

Figure 2 from Forgues et al. [6] illustrates the variation through the thickness of the residual hoop stresses for a cold-worked 7475-T7351 aluminum plate with a W/D of 5 and a 4 % mandrel interference level. The residual stresses are shown at three stations through the thickness: along the mandrel entry

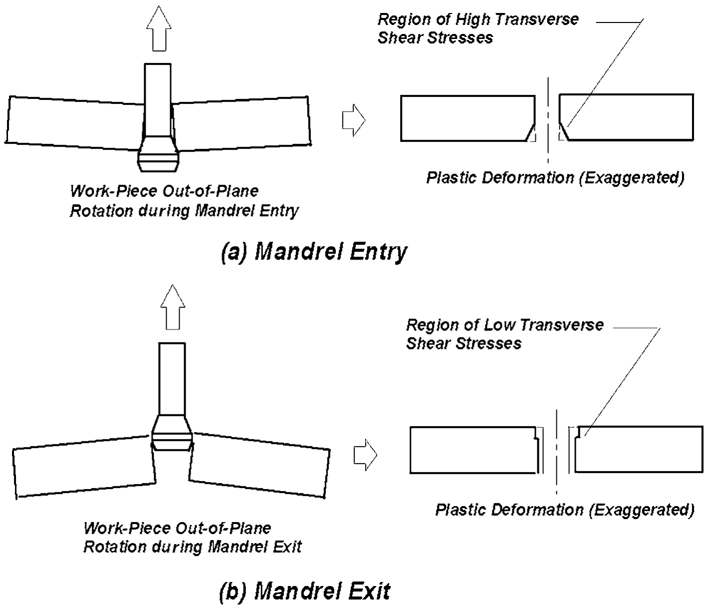

FIG. 1—*Out-of-plane plate rotation during mandrel pull-through.*

surface, at midsection, and along the mandrel exit surface. In obtaining these stresses, Forgues et al. used a 3-D axisymmetric ABAQUS finite element model. As Fig. 2 shows, Forgues et al. predicted that the residual tangential stresses at the entry surface are significantly lower in magnitude than at the midplane and at the exit surface. These results point to a significant reduction in the residual stresses at the entry surface, a fact independently confirmed by ANSYS 3-D analyses summarized in this paper.

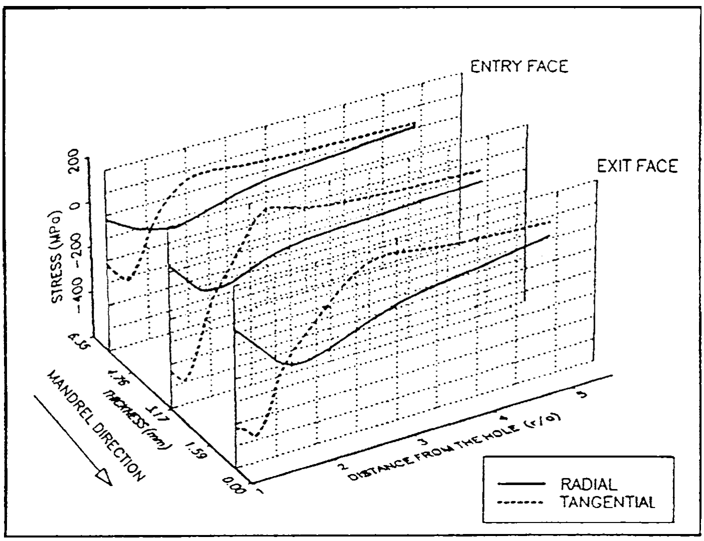

FIG. 2—*Analytically predicted residual stress distribution in cold-worked 7475-T7351 aluminum plate with a W/D of 5 and a 4 % mandrel interference level. Reproduced from 3-D axisymmetric numerical analysis and experimental study of the fastener hole cold-working process in Ref. [6].*

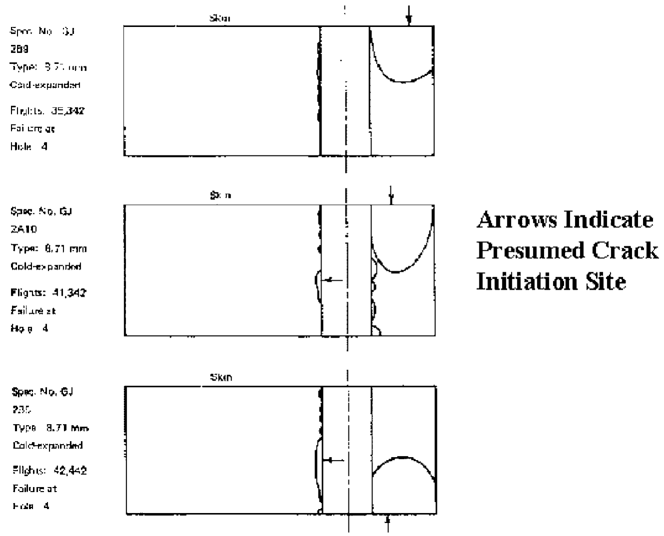

FIG. 3—*Experimentally determined fracture surfaces for 2014-T651 aluminum low load transfer specimens [7].*

Initial Cracking at Hole Edge versus Away from Hole and MultiStage Crack Growth—Most analytic simulations of crack growth from a cold-worked hole assume cracking at the edge of the hole. However, test data on cold-worked 2014-T651 aluminum low load transfer lap shear joint specimens which were tested in fatigue spectrum loading with a peak far field stress of 29.7 ksi, then examined after a crack had formed and grown, indicates that cracking can occur away from the hole [7], see Fig. 3. In Fig. 3, the fracture surface indicates that the primary crack nucleated away from the hole in the residual tension zone. Furthermore, the indications of secondary cracking at the hole edge are indicative of a multistage crack growth pattern where the secondary cracks will coalesce with the primary crack, leading to a single through-the-thickness crack. This secondary cracking indicates a relaxation of the residual stress field, leading to a loss of the residual compressive stress at the edge of the hole and the subsequent formation of secondary cracking. This relaxation can stem from two mechanisms. The primary mechanism is the inability of the cracked material to transmit the residual tension stresses needed to equilibrate the residual compression stresses, leading to a monotonic decay of the residual stress field as the crack grows [8]. The second mechanism is cyclic reyielding of the net section residual stress field due to crack tip plasticity.

Figure 4 summarizes the possible scenarios for multistage cracking following crack formation at the hole edge or away from the hole. Whether the crack nucleates at the hole edge or away from the hole is a function of the geometry, i.e., e/D, and the interference level, as well as the degree of secondary bending

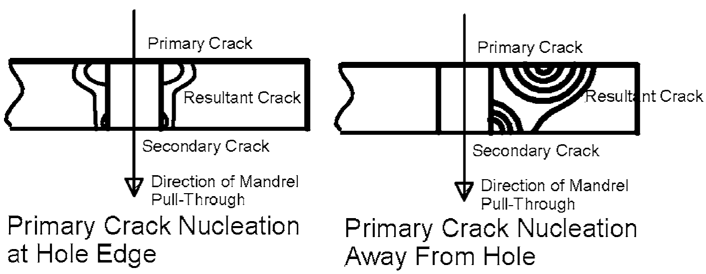

FIG. 4—*Possible multistage cracking scenarios.*

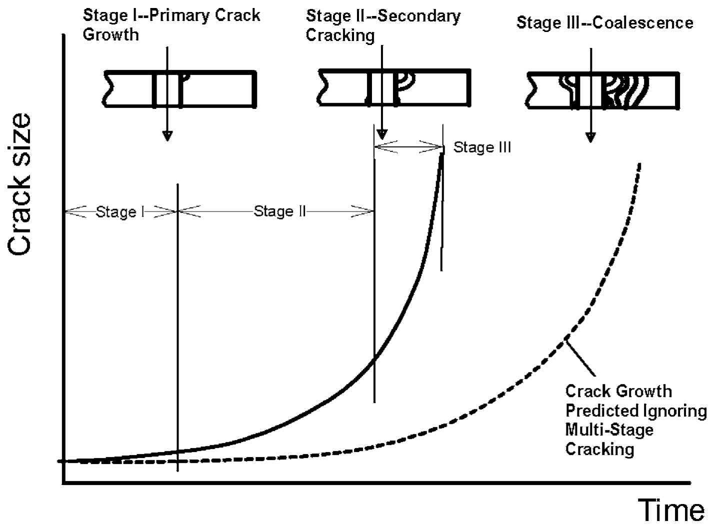

FIG. 5—*Multistage cracking at cold-worked hole.*

and the localized peaking of bearing stresses due to fastener tilting. In either case, formation of the primary crack is followed by formation of a secondary crack and the subsequent coalescence of the cracks into a single crack system. The consequence of this multistage crack growth is that the crack growth life can vary significantly from the life expected based on the assumption of a single noninteracting crack growing to failure, as shown schematically in Fig. 5.

Differences between an Isolated Hole and a Hole in a Multilayer Joint

Further complications arise when the crack is growing out of a hole which is part of a multilayer or multirow joint. Significant differences can exist between the life enhancement possible by cold-working an unloaded hole in a single layer plate and a loaded hole in a multilayer joint, due to the interaction of the crack with adjacent holes. Figure 6 shows a typical manufacturing splice at a frame bulkhead, where the longeron is terminated before the frame, then continued after the frame. Load continuity across the frame is provided by a doubler strap between the skin and the longerons. Figure 6 shows a hypothetical crack growth scenario where the primary crack initiates in the longeron at the hole edge at the faying surface with the doubler strap. As the primary crack grows through the short net section, secondary cracks can initiate at the hole at the back face due to the magnification of stresses along the back face as the primary crack grows, and away from the hole due to the residual tensile stresses from cold-working. These cracks can coalesce into a single macro crack which grows across the short net section to failure. The load redistribution to the uncracked net section as the crack system grows can lead to the formation of cracks on the opposite, uncracked side of the hole. As cracking progresses across the net section between the two holes, the redistribution of load from the cracked to the uncracked hole can cause the formation of a tertiary crack system at the opposite hole. This crack system will grow until it merges with the crack from the initially cracked hole, or until the layer fractures across its width. Because of this progressive spread of damage, the life of the joint may be significantly greater than the "life" of a single noninteracting crack growing through the short net section.

Further complicating the behavior of fatigue cracking in a multilayer joint is secondary bending caused by joint eccentricity. In a test program on joint specimens representative of the F-18 fighter, Evans [9] found a significant life reduction with secondary bending in multilayer joints, with little or no benefit from cold-working. Evans found that interference fit fasteners had to be used in conjunction with cold-working in order to achieve significant life increases.

In an analytical study, Fujimoto [10] noted that localized bearing peaking effects due to tilting of a fastener in a multilayer joint also can significantly lower the life of a cold-worked hole. In his study,

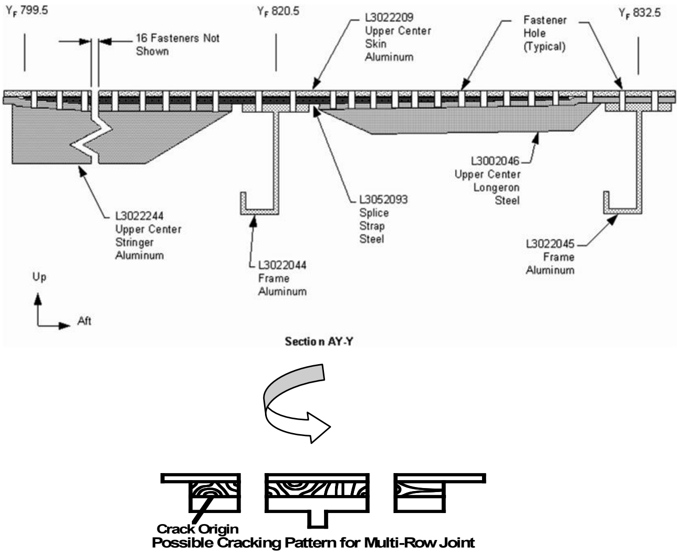

Figure 6. Notional Crack Growth Pattern in Multi-Layer Joint.

Fujimoto found a 20 % increase in the effective stress concentration factor for the hole and a 50 % reduction in the fatigue life when fastener tilting and the localized peaking of the stress field at the faying surface were accounted for.

Hence, determining the life of a multilayer joint with cold-worked holes requires treating the joint as a structural system, rather than as a single isolated hole with stationary boundary conditions.

A Second Generation Physics-Based Engineering Approach to Modeling Crack Nucleation and Growth

A second generation physics-based methodology for modeling crack nucleation and growth [5] has been developed to permit more accurate life predictions for multilayer joints with cold-worked holes. Cornerstones of the methodology are:

- Explicit Modeling of Mandrel Pull-through
- Tracking Multistage Crack Growth
- Accounting for Residual Stress Field Relaxation
- Accounting for Interaction of Hole with Fasteners and Adjacent Layers

The methodology is capable of explicitly accounting for each of the above factors. It is based upon:

- 3-D analytic/finite element modeling of cold-working.
- Stress field synthesis using method of strain invariance to track relaxation of residual stress field.
- Probabilistic fatigue analyses for identifying the most probable primary crack site.
- 3-D weight function for finding the stress intensity factors for crack growth analyses.
- Integration of a multilayer joint analysis program with cold-working analysis.

The following is a description of the major building blocks comprising the methodology.

ANSYS 3-D Finite Element Modeling of Cold-Working and Mandrel Pull-through

To determine these stresses, ANSYS three-dimensional finite element models were constructed to obtain correction factors for transforming a closed-form 2-D solution [5] into 3-D solutions. To capture the effect of the mandrel on the stresses, the mandrel pull-through process was explicitly modeled. In order to

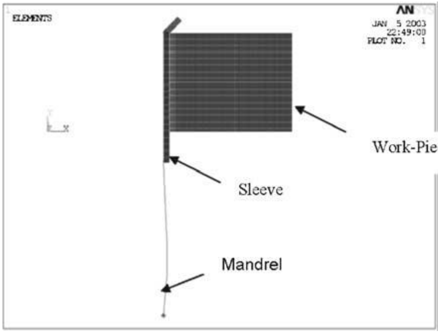

FIG. 7—*Axisymmetrix ANSYS model of work-piece with sleeve and rigid mandrel.*

simplify the modeling process, the rectangular plate was approximated by a circular annulus whose inner radius was equal to the hole diameter, and whose outer diameter was equal to the plate width, W. By reducing the geometry to an equivalent circular annulus, axisymmetric models, in which only half of the net section is explicitly modeled, could be used.

Figure 7 shows a typical axisymmetric model. The flared split sleeve was explicitly modeled in the model shown (although it was later removed in subsequent analyses to reduce the model size). The mandrel was modeled as a rigid surface with sharp corners[2] at the intersections of the mandrel entry and exit ramps with the mandrel flat. Mandrel pull-through was simulated by incrementally advancing the mandrel as a rigid body through the hole. Frictionless contact was assumed during pull-through.

In order to understand the effects of different modeling assumptions on the residual stresses, analyses were performed assuming both kinematic hardening and isotropic hardening.[3] In addition, various runs

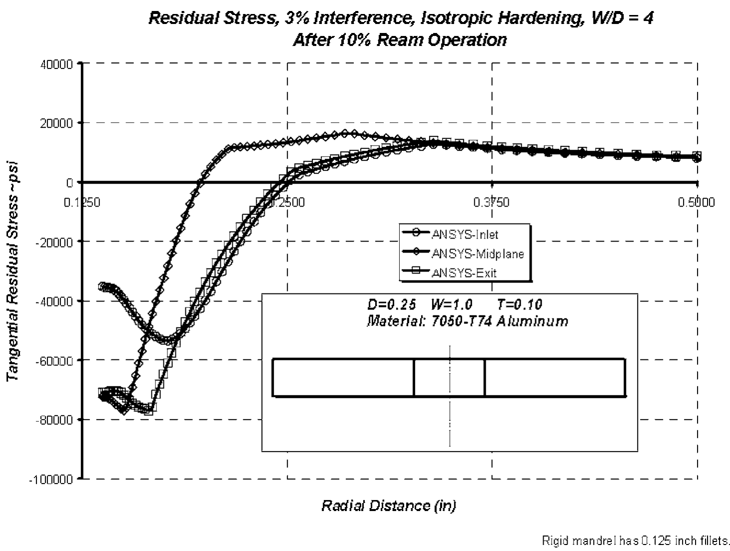

FIG. 8—*ANSYS 3-D residual tangential stresses in W/D=4 plate cold-worked to 3 % interference level, followed by 10 % ream.*

[2]Later models had rounded corners to eliminate the singularity caused by sharp corners.
[3]Only the results of the analyses assuming isotropic hardening are reported herein, to facilitate comparison with published finite element results in the literature.

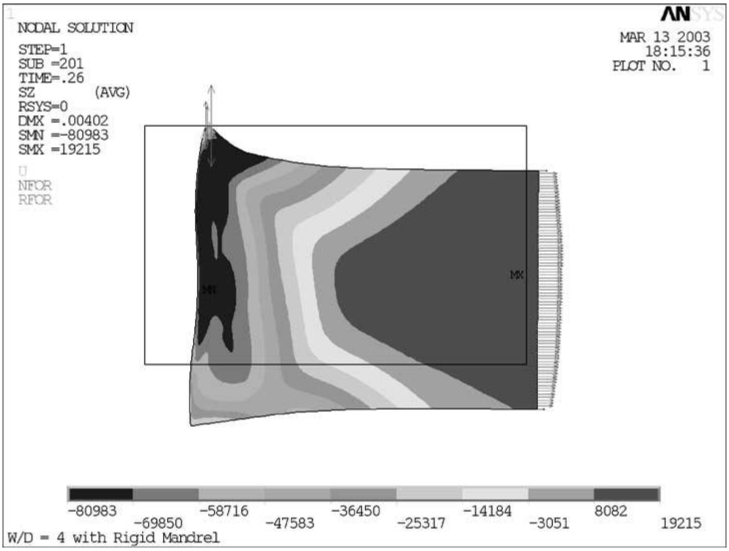

FIG. 9—*Contour plot of residual tangential stresses near hole edge, 0.10-in. thick W/D=4 7050-T74 Al plate cold-worked to 3 % interference.*

were made to examine the effects of the following: (1) mesh density, (2) penetrator stiffness, and (3) boundary conditions for restraining the work-piece during mandrel pull-through.

Typical residual stresses predicted by the model for the entry, exit, and midplane are shown in Fig. 8 for a 0.10-in. thick by 1.0-in. wide 7075-T74 Al plate with an 0.25-in. diam. hole which has been cold-worked to 3 % interference, followed by a 10 % post-ream. In determining these stresses, the "kill element" feature of ANSYS was used to remove the elements to simulate the post-ream, while retaining the residual plastic strains resulting from cold-working. A contour plot of the residual stresses in the vicinity of the hole is shown in Fig. 9.

From Fig. 8, it can be seen that the residual stresses along the entry surface are less than 50 % of the residual stresses along the midplane or at the exit surface, a result which agrees with the ABAQUS analysis of Forgues in Fig. 2. Figure 8 shows the same through-the-thickness distribution of the residual stresses as shown in Fig. 2: residual tangential stresses at the entry surface which are significantly lower in magnitude than at the midplane and at the exit surface.

Figure 9 shows a contour plot of the through-the-thickness variation of residual stresses in the vicinity of the hole. Figure 9 shows that the residual stress at the hole edge is constant through the thickness beginning at a point 25 % of the thickness from the mandrel entry side and extending to the exit side. From the entry side to a point at 25 % of the thickness, the residual stress shows a significant reduction due to the rotation of the work-piece. Furthermore, the plastic zone at both the entry and exit sides extend significantly further out than for the interior region.

Hence, both the ANSYS and ABAQUS 3-D finite element simulations point to a significant reduction in the residual stresses at the entry surface. However, it should be noted these results differ markedly from the published experimental results of Ozdemir and Edwards [8,11], which showed significantly lower residual stresses at both the entry and exit surfaces, and from the published finite element results of Pavier [12], which showed residual tensile, not compressive stresses at the intersection of the hole wall and the exit surface. Thus, a consensus on the through-the-thickness variation of residual stresses does not exist, leading to an uncertainty which needs to be resolved.

Relaxation of Residual Stress Field Due to Overloads/Underloads

The methodology explicitly accounts for the relaxation of residual stresses due to underloads or overloads. The relaxation of residual stresses has been shown by Ball and Doerfler [13] in an analytical and experi-

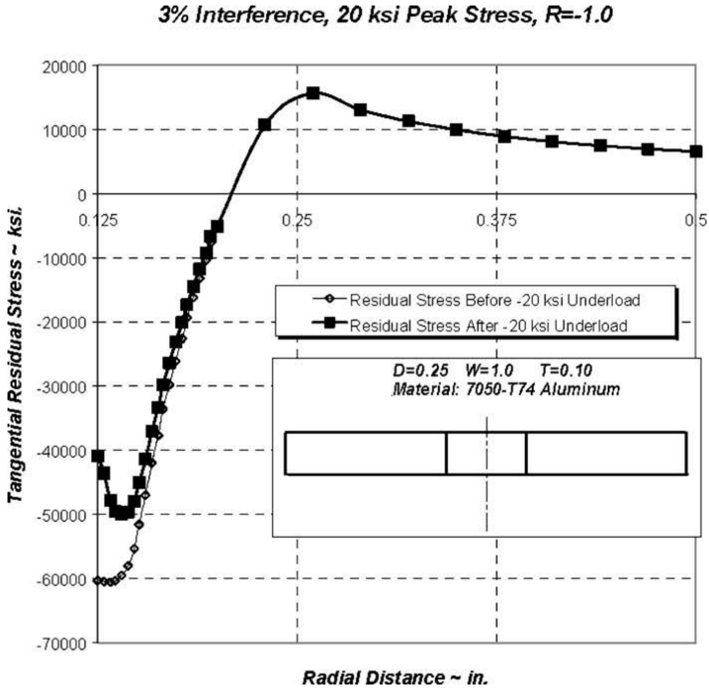

FIG. 10—*Method of strain invariance predicted relaxation of residual stresses due to compressive underload.*

mental study to cause major differences between the life expected, based on ignoring the relaxation, and the actual life. In Ball and Doerfler's work, ABAQUS was used to model the relaxation using the finite element method. In the methodology described herein, the method of strain invariance and the deformation theory of plasticity [14] were used to determine adjustments to the residual stresses resulting from the application of loading. In this approach, the solution for the residual stresses and strains are combined with the elastically determined strains from the applied loading to produce an approximation for the total strains resulting from the loading. The adjusted residual stresses and the residual strains can be obtained by superimposing the stresses and strains due to reyielding to the residual stresses and strains determined from the cold-working analysis. These residual stresses and strains then become the starting values for additional load cycles causing further reyielding, or for determining the relaxation of the residual stresses due to the growth of a crack into the residual tension zone.[4] Further details are available in Ref. [5]. This approach was used rather than an elastoplastic finite element analysis, as tracking the effects of overloads/underloads would have required a full three-dimensional model of the hole, rather than the axisymmetric model used for modeling cold-working. Since the effects of an overload or underload depend upon such variables at the ratio of the overload or underload to the prior load level and also upon the value of the e/D ratio (the ratio between the distance from the hole center to the free edge/hole diameter), elastoplastic finite element analyses would be impractical for use in a design oriented methodology. By using the method of strain invariance, the relaxation could be determined at run time for each overload/underload ratio in the loading spectrum and for the geometry of the joint.

Figure 10 shows an example of the residual stress adjustment obtained by the method of strain invariance for a hole which is cold-worked by uniform expansion of the hole. Figure 10 shows the residual tangential stresses in a W/D=4 plate of 7050-T74 aluminum which is subjected to a 3 % uniform

[4]All that is necessary to use the method of strain invariance with cracks is the elastic solution for the near tip stresses. These stresses may then be converted into strains and the strains added to the residual strains to serve as an approximation of the total strains resulting from the growth of the crack.

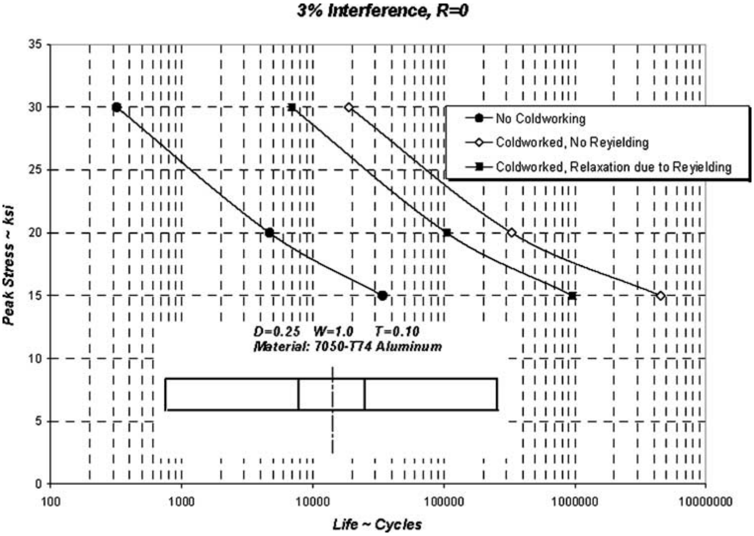

FIG. 11—*Effect of compressive underload on life of cold-worked 7050-T74 Al plate subjected to −20 ksi underload, followed by constant amplitude cycling at R=0.*

expansion of the hole and then subjected to a far field compression stress of −20 ksi followed by a far field tensile stress of +20 ksi. Also shown for comparison purposes are the residual stresses after cold-working, but before a −20 ksi underload. Since the residual stresses (in the absence of tensile overloads or compressive underloads) remain constant until a crack grows through the residual compressive stress field into the residual tension stress field, the residual stresses after cold-working, but before a −20 ksi underload, represent the residual stresses ignoring reyielding. Figure 10 shows that the compressive underload causes additional compressive reyielding near the hole edge which lessens the residual compressive stress at the hole edge by 20 ksi.

Figure 11 illustrates the effect of the relaxation due to reyielding on the fatigue life of the hole. As can be seen, the relaxation in residual stresses due to compressive reyielding can result in a significant reduction in the life of the member. Since most primary structural members for aircraft experience reversed loading, failure to account for this relaxation can lead to nonconservative estimates of life.

Multilayer Joint Analyses

The multilayer joint analysis program allows the bypass and bearing loads for each hole in a layer of a multilayer joint to be determined from a special finite element model of the joint [10]. In such a program, the fasteners can be represented by virtual fastener elements [15], which eliminate the need to explicitly model the hole or the fasteners. Using virtual fasteners, rather than an assemblage of solid elements to model a fastener, allows the fastener to be replaced by a special line element whose properties can be determined from a beam-on-elastic foundation model of the fastener. Bypass and bearing loads in the vicinity of the hole can be obtained from the finite element model of the joint, allowing the bypass stress, the fastener load, and the fastener rocking moment to be determined at each layer location. From this information, the 3-D variation of stresses in a layer for a fatigue or damage tolerance analysis can be predicted using stress field synthesis [5].

Probabilistic Fatigue Analysis for Finding the Most Probable Initial Cracking Location—Because of the various uncertainties and variabilities involved in the nucleation of a fatigue crack in a cold-worked hole, probabilistic fatigue analyses is necessary to find the most probable initial crack formation location, and to also track the probability of secondary cracking occurring at other locations. By performing a probabilistic analysis, rather than a deterministic analysis to identify the initial cracking location, the

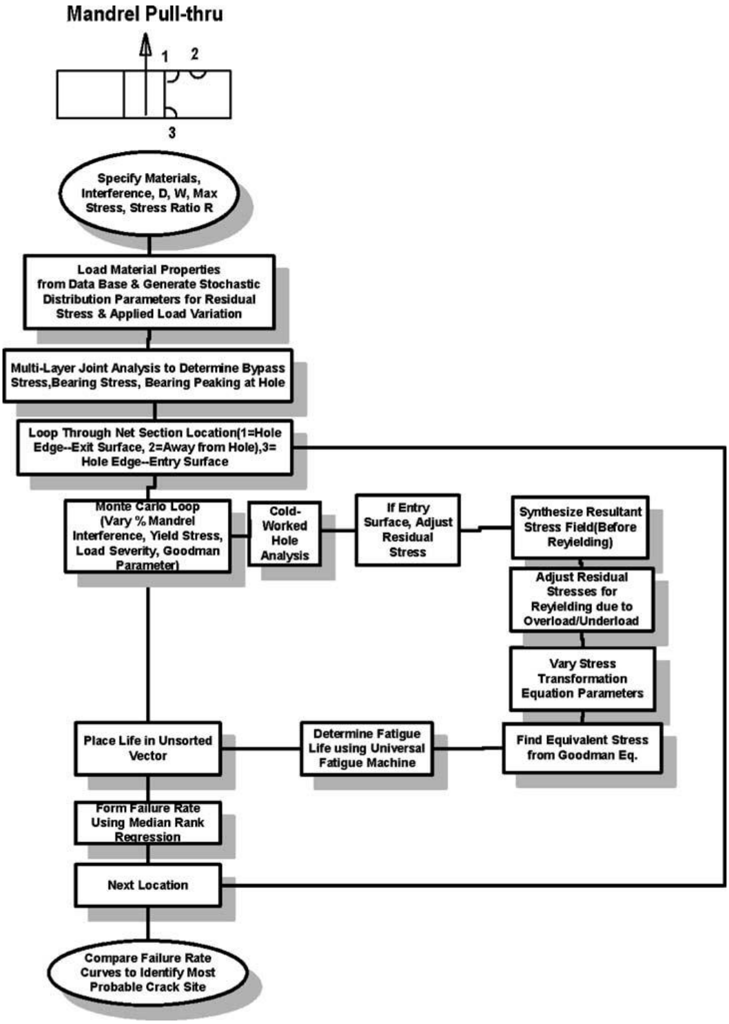

FIG. 12—*Flowchart for probabilistic fatigue analysis to identify most probable initial crack location and time to initial cracking.*

likelihood of initial cracking away from the hole can be estimated. This information, in turn, can be used to assess the risk of premature fatigue failures due to failure modes which are different than those used for establishing the expected life.

Figure 12 summarizes the architecture of *ProbabilityContour4,* a module developed for automating the probabilistic fatigue analyses. *ProbabilityContour4* uses the 3-D residual stress distribution determined by combining a two-dimensional solution for cold-working with three-dimensional correction factors from the finite element analyses to synthesize the stress field at the hole. It also accounts for the reduction in the residual stresses along the entry surface. The input to the module consists of the identifications for the plate and mandrel materials, the interference level, the hole diameter, D, the plate width, W, and the stress spectrum (currently the module is limited to constant amplitude loading with a specified stress ratio, R). With this information, the module extracts the mean material properties from the material database, along with the parameters for the assumed stochastic distribution for the interference level, the yield stress, and the elastic modulus.

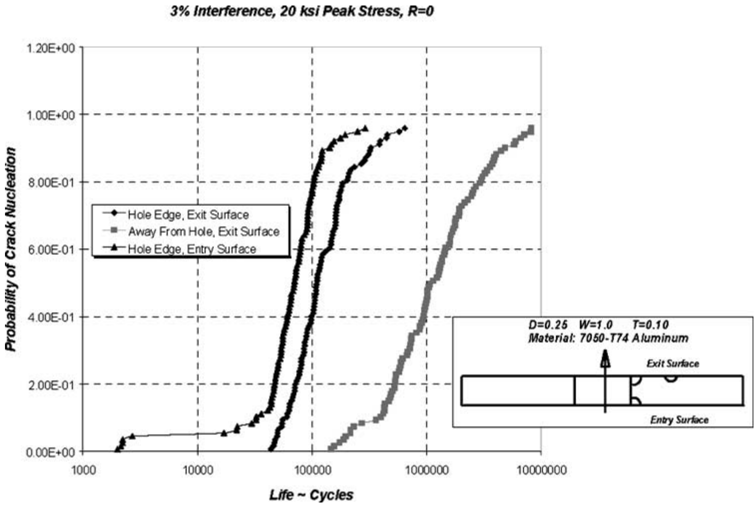

FIG. 13—*Failure rate curves generated using ProbabilityContour4.*

The module first calls the stress field synthesis subroutine *StressFieldSynthesizer* to form the elastically determined net section distribution of stresses and strains resulting from the applied loading.[5] The stress field synthesis program is linked to the multilayer joint analysis program, so that the secondary bending and the fastener bearing peaking gradient can be used in synthesizing a three-dimensional stress gradient.

Once the mean applied stress distribution has been determined, Monte Carlo simulation is used to determine the most probable location on the net section for initial crack formation. One hundred trials are used for each location on the net section. In the Monte Carlo simulation, the mandrel interference level, the material elastic properties and the yield stress, and the applied load severity factors (the factor by which the mean value is multiplied) are treated as stochastic variables with a Gaussian distribution and allowed to vary. Values of the parameters which correspond to the probability distributions assumed for the variables are generated by an inverse transform method [16] from random numbers generated by a random number generator.

For each trial, the residual stress field corresponding to the mandrel inference and yield strength is obtained from the cold-worked analysis routine. The steady stress level, and the vibratory stress amplitude for each maneuver in the usage spectrum is obtained by multiplying the mean applied stresses by the severity level for the trial and superimposing the applied stresses on the residual stress state.

The crack formation life corresponding to the equivalent stress amplitude is then found by a safe life fatigue analysis. As the lives are determined for each trial, they are written to an array. Once all the trials have been completed, the failure rate curves for each location are generated using the median rank regression method [17].

An example of failure rate curves generated using this module are shown in Fig. 13 for the exit surface hole edge, the exit surface away from the hole, and the entry surface hole edge[6] for a 7050-T74 aluminum member which is cold-worked to an interference level of 3 %, then subjected to constant amplitude cycling at a far field peak stress of 20 ksi and a stress ratio R of 0.

Failure rate curves such as shown in Fig. 13 can be used to identify the most probable initial cracking location. To compare the relative likelihood of cracking at a location other than hole edge at the entry surface, the median life of the hole edge on the entry surface can be divided by the mean life of the hole

[5]The stresses and strains in the x-direction (perpendicular to the net section) and in the y-direction (parallel to the net section) are synthesized from elastic stress field solutions for a hole in a finite width strip under bypass loading and bearing loading, respectively. These solutions are stored in multidimensional tables and read in during the start of the module.

[6]The failure rate was not generated for the entry surface, away from the hole, as this location would have significantly lower residual tension stresses than for the exit surface. Hence, for an unloaded hole, in the absence of secondary bending stresses, the probability of initial cracking here prior to initial cracking on the exit surface away from the hole would be very low.

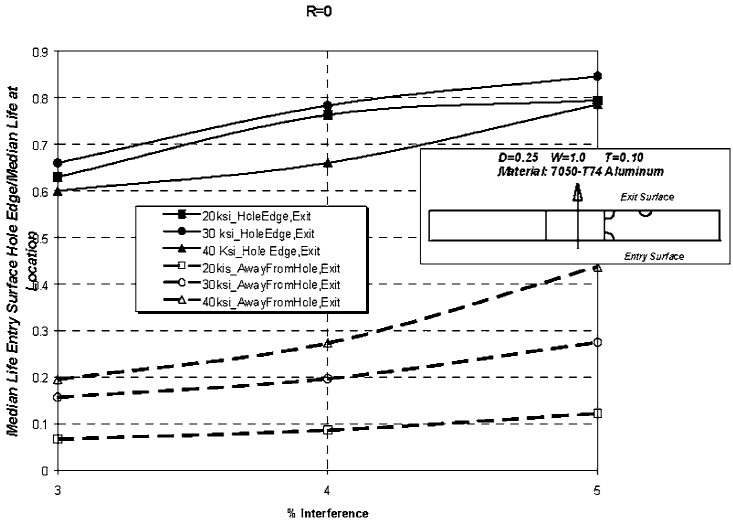

FIG. 14—*Likelihood of cracking on the exit surface versus cracking on the entry surface at the hole edge versus peak stress and interference for a 7050-T74 Al plate subjected to constant amplitude cycling at R=0.*

edge on the exit surface to serve as a measure of the likelihood of cracking occurring at the hole edge on the exit surface. A ratio greater than 1 is indicative of cracking initially occurring at the hole edge at the exit surface, while a ratio less than 1 is indicative of cracking initially occurring at the hole edge on the entry surface, where the residual stresses have been reduced by rotation of the work-piece during mandrel pull-through. Similarly, the median life of the hole edge on the entry surface can be divided by the mean life of the exit surface away from the hole edge to serve as a measure of the likelihood of cracking occurring at the exit surface away from the hole edge.

Figure 14 shows a carpet plot summarizing the nondimensional likelihood of cracking on the exit surface versus peak stress and interference for a 7050-T74 aluminum plate subjected to constant amplitude cycling at R=0. Figure 15 shows a carpet plot summarizing the nondimensional likelihood of cracking on the exit surface versus peak stress and stress ratio R for the same plate cold-worked to an interference level of 3 %.

The results summarized in Figs. 14 and 15 indicate that, regardless of stress level, interference, or load magnitude, the hole edge on the entry surface is predicted to be the most likely location for initial cracking for specimens with unloaded holes, with little likelihood of cracking occurring first on the exit surface away from the hole edge.[7] Furthermore, on the exit surface, it can be seen that the likelihood of cracking occurring first on the exit surface away from the hole is always less than at the hole edge, although it approaches the likelihood of cracking occurring at the hole edge for higher interference levels and stress levels. However, it should be noted that these results are only valid for specimens with normal e/D ratios and no secondary bending. Specimens with "shy" e/D ratios are more susceptible to cracking away from the hole, and thus may behave differently.

Since Figs. 14 and 15 predict cracking to occur at the hole edge for the lower stress levels and stress ratios close to 0 or less, findings which are in agreement with the test results of Cook and Holdway [18]. In their testing, Cook and Holdway subjected 7050-T76 aluminum unloaded hole cold-worked specimens to constant amplitude fatigue testing at R=0.1 and a peak stress of 26.7 ksi. Of the 16 specimens tested in fatigue, 62 % experienced initial cracking at the hole at either the entry or the exit surface, while the remainder of the specimens either experienced cracking at the grips, or experienced a combination of

[7]Even though the overall likelihood of initial cracking away from the hole edge was small, during the Monte Carlo simulations, numerous instances occurred where initial cracking was predicted to occur away from the hole. Hence, it must be emphasized that cracking away from the hole can occur on unloaded cold-worked holes, although the rate of occurrence, relative to the population, can be expected to be low.

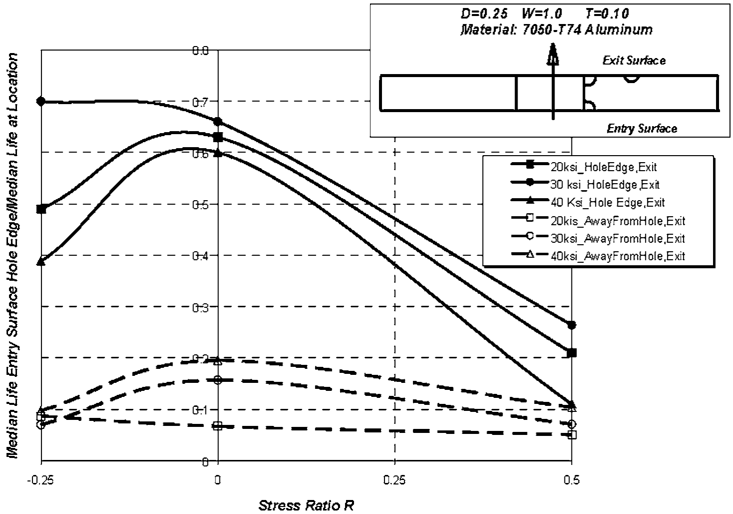

FIG. 15—*Likelihood of cracking on the exit surface versus cracking on the entry surface at the hole edge versus peak stress and stress ratio R for a 7050-T74 Al plate cold-worked to* 3 % *interference and subjected to constant amplitude cycling at R=0.*

cracking at the hole and the grips. In no case did cracking nucleate away from the hole in the residual tension zone. This finding is consistent with the probability contour plots of Figs. 14 and 15, which predicts that cracking at the hole edge is significantly more probable as cracking in the residual tension zone for the combination of R-ratio and peak stress.

Because *ProbabilityContour4* can also generate, as part of the Monte Carlo fatigue analysis to identify the most probable location for initial cracking, the failure rate curves relating the probability of cracking to service life, the modules can also be used to generate, for a specified probability level, the SN curves for cold-worked holes. Such curves can be used in a spectrum fatigue analysis for determining the life of a member for a specified reliability level.

The SN curves shown in Fig. 16 were generated using 50 % probability lives from the failure rate curves at each of the locations. The curves show that the crack formation life of the hole at the entry side is roughly half the life at the exit side due to the reduction of residual stresses. It should be noted that SN curves corresponding to a specified failure rate, i.e., 2 % probability of failure, can be generated by this technique simply by finding the lives corresponding to the specified failure rate. SN curves generated in this manner account for the variability in the cold-working process and in loads severity, variability in the accuracy of the equation used to transform the stress range into a form compatible with conventional SN or ε-N life curves, in addition to the variability of fatigue strength of the material. Thus, statistical protection against variability can be built into the fatigue analysis, as protection against unexpected premature failures.

Prediction of Stress Intensity Factors for Crack Growth

The stress intensity factors for crack growth analyses were determined from the hybrid 3-D weight function approach [19], a virtual crack approach which allows the stress intensity factor solutions to be obtained from the stresses in the uncracked member. In this approach, the Petroski-Achenbach approach [20] was extended to 3-D, allowing a weight function to be obtained from a single reference solution. Use of the Orynyak Green's function [21] for an embedded elliptical flaw subjected to a concentrated load as the fundamental term in the solution assured that the weight function formulation has the robustness necessary to handle the sharply bivariant stress field resulting from cold-working. The advantage to the use of the weight function is that the 3-D residual stress field for the unflawed member may be used directly for generating the stress intensity factor solution, without the need to explicitly model the crack tip in the

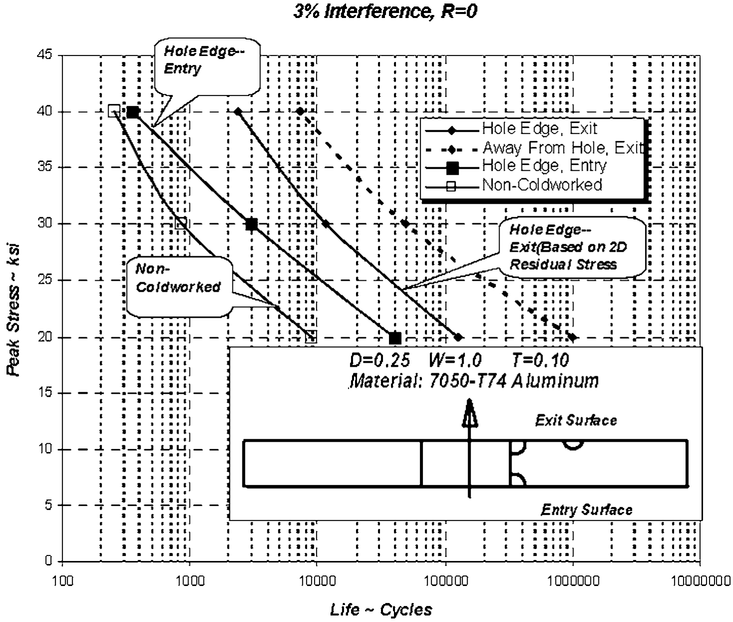

FIG. 16—*Fifty percent probability SN curves for potential initial crack locations for a 7050-T74 Al plate cold-worked to* 3 % *interference and subjected to constant amplitude cycling at R=0.*

finite element model. Thus, a crack growth analysis may be readily performed using the residual stresses from cold-working and the stresses from the applied loading for an unflawed member.

For a single corner crack initiating at the hole edge, the stress intensity factor is given by the following term:

$$K_{I_A} = 2\int_0^{y-a}\int_0^{x-c(y)} \sigma(x,y)m_A(x,y,a,c)dxdy$$

$$K_{I_C} = 2\int_0^{y-a}\int_0^{x-c(y)} \sigma(x,y)m_C(x,y,a,c)dxdy \tag{1}$$

where $\sigma(x,y)$ is the crack face stress, and $m_A(x,y,a,c)$ and $m_C(x,y,a,c)$ are the weight functions for the geometry for two degree-of-freedom crack growth, and are given by:

$$m(x,y,a,c) = m_o(x,y,a,c) + \frac{G(\eta)}{F(\eta)}\left[\left(1-\frac{R^2}{R_o^2}\right)m_o(x,y,a,c) + \frac{rR^2}{R_o^3}\frac{u_o(x,y,a,c)}{L\sqrt{\pi a}\dfrac{f_\phi}{E(k)}}\frac{\partial R_o(\eta)}{\partial R_o(\eta^*)}\right] + m(x,y,a,c)_{residual} \tag{2}$$

where $m_o(x,y,a,c)$ is the fundamental term in the expansion for the weight function, $u_o(x,y,a,c)$ is the crack opening displacement field for an embedded elliptical flaw under uniform tension loading, $F(\eta)$ is the nondimensionalized reference stress intensity factor solution, $G(\eta)$ is a geometry correction factor, and $m(x,y,a,c)_{residual}$ is a boundary-correction term associated with the derivatives of F and G. The reader is referred to Ref. [19] for a detailed explanation of the terms.

The weight function approach is particularly well suited for determining the stress intensity factors due to the residual stresses, as the crack face loading $\sigma(x,y)$ remains unaffected by the presence of the crack until the tip has extended into the residual tension stress field, and relaxation of the residual stresses occurs.

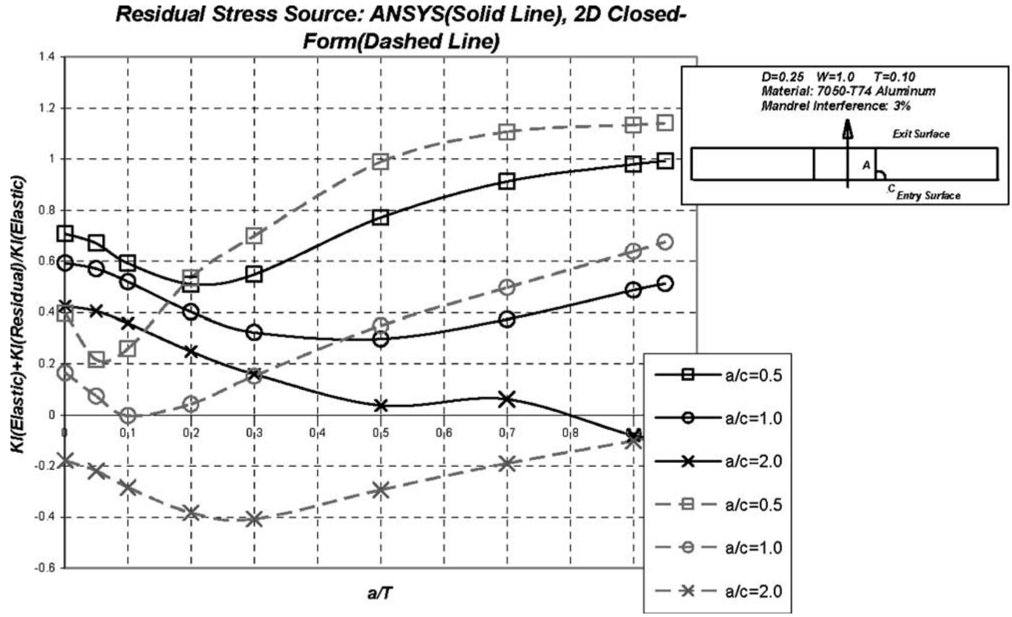

FIG. 17—*Maximum effective stress intensity factors at point C for corner crack growing from 0.1-in. thick by 1.0-in. wide 7050-T74 Al plate with 0.25-in. diam. hole cold-worked to 3 %, then subjected to 25 ksi far field stress.*

As an example of the power of the weight function approach, the residual stress intensity factors were computed using residual stress fields from a 2-D cold-working solution and from the 3-D ANSYS FEM solutions for a 0.1-in. thick by 1.0-in. wide 7050-T74 aluminum plate with a 0.25-in. diam. hole cold-worked to 3 % interference. The solutions were obtained in seconds for a variety of *a/c* and *c/R* configurations. The residual stress intensity factors were then combined with the stress intensity factors due to the applied loading of 25 ksi to determine the effective maximum stress intensity factor driving crack growth. Figure 17 shows a plot of the effective maximum stress intensity factor at point *C*, the intersection of the crack front with the plate surface, for corner crack growing from the edge of a cold-worked hole. Figure 18 shows a plot of the effective maximum stress intensity factor at point *A*, the intersection of the crack front with the hole wall.

In the figures, the nondimensional resultant stress intensity factor at points *C* and *A* are plotted as a function of *a/T* for cracks of aspect ratio $a/c=0.5$, 1.0, and 2.0. The nondimensional stress intensity factors were obtained by normalizing the resultant peak stress intensity factor (elastic stress intensity factor due to the applied load + residual stress intensity factor) by the elastic stress intensity factor due to the applied load. The curves with the solid lines were generated using the residual stress field generated by the ANSYS FEM solution of Fig. 8, while the curves with the dashed lines were generated using the residual stresses from the 2-D closed-form elastoplastic solution for cold-working. Values are shown for crack shape aspect ratios a/c of 0.5, 1.0, and 2.0 for a crack which is growing from the entry surface.

The results indicate that significant differences exist between the effective stress intensity factors based on 2-D or 3-D residual stress distributions, with the stress intensity factors based on the 2-D solution predicting significantly greater crack growth retardation from cold-working. For cracks with an aspect ratio a/c greater than 1.5, the nondimensional stress intensity factor obtained using the 2-D residual stress distribution becomes negative, indicating, for small cracks, no crack growth. In contrast, the nondimensional stress intensity factor obtained from the 3-D residual stress distribution would predict, for small cracks, crack growth, but at a significantly lower rate than expected in the absence of residual stresses.

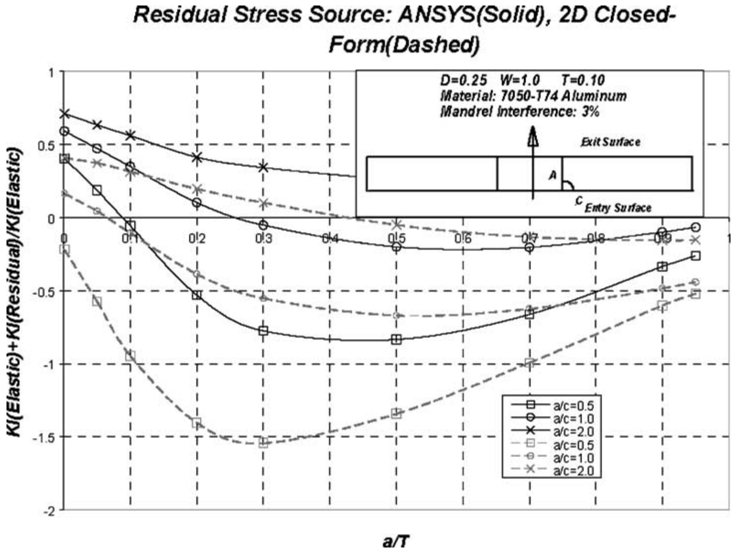

FIG. 18—*Nondimensionalized resultant peak stress intensity factors at point A for corner in 0.10-in. thick* $W/D=4$ *7050-T74 Al plate cold-worked to* 3 % *and subjected to constant amplitude cycling at a* $R=0$ *and max. Stress of 25 ksi.*

Since a major portion of crack growth is spent in this small crack region, it is apparent that use of 2-D residual stress distributions can lead to nonconservative estimates of the remaining life of a cold-worked joint, if the crack is growing from the mandrel entry surface.

Need for Further Development

The methodology discussed in this paper has only been developed to the point it can handle the growth of a single crack, although, as shown in Fig. 6, the life of a cold-worked hole in a multilayer joint can involve the nucleation and growth of a system of interacting cracks.

In order to handle the sequential damage progression of Fig. 6, further development is needed. Figure 19 shows a possible approach using a compounding approach. In the compounding approach, separate stress intensity factor solutions for the corner crack and for the surface flaw, as shown in Fig. 19, are superimposed. The interaction between the cracks can be accounted for using a crack interaction curve [5].

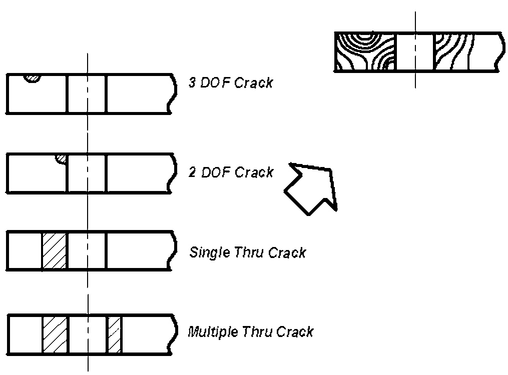

FIG. 19—*Synthesizing complex multistage crack growth from basic crack types.*

The cracks in Fig. 19 represent the basic building blocks from which complex multistage crack growth scenarios can be synthesized, including scenarios involving a primary crack which formed away from the hole in the residual tension zone, or cracks approaching each other. The stress intensity factor solutions for each crack configuration can be generated from the weight functions for a corner crack or a through crack, and for a surface crack away from the hole by numerical integration without the need to explicitly create a finite element model of the crack system.

Conclusions

The behavior of cracks nucleating and growing from cold-worked holes is complex, and governed by factors which have not been explicitly considered in the past. These factors should be accounted for in determining the crack nucleation or crack growth life to prevent nonconservative life estimates. First generation approaches for cold-worked holes based on 2-D residual stress solutions and on a stationary residual stress field may overestimate the life improvement potential of cold-worked holes. The primary reason is that the 2-D residual stress solutions ignore the "reduced" residual compressive stresses on the mandrel entry surface due to work-piece rotation during mandrel pull-through. This leads to the overestimation of the magnitude of the residual compressive stresses along the entry surface, leading to differences between the predicted and actual lives. In addition, first generation approaches also ignore the relaxation of the residual stress field which can occur due to reyielding from overloads or underloads, or due to crack growth into the residual tension zone. This can lead to further nonconservatism, especially for members subjected to a compression-dominated spectrum.

Because of these factors, a second generation approach which explicitly accounts for the 3-D nature of the residual stress field, residual stress relaxation, and multistage damage progression is necessary before the life of a member with cold-worked holes can be predicted analytically. A prototype second generation physics-based methodology has been developed but additional development and test validation is necessary.

Acknowledgments

The work described in this paper was performed under a Phase I SBIR grant from the Air Force Research Laboratory with Dr. Eric Tuegel as the Program Manager. The author is grateful to Dr. Tuegel for the opportunity to develop a rational model for cold-working and for the opportunity to make analytical testing of cold-worked holes achievable. The contribution of Mr. Antonio Portelinha in performing the finite element modeling of mandrel pull-through is also gratefully acknowledged.

References

[1] Finney, J. M., "Cold Expansion and Interference for Extending the Life of Multilayer Metal Joints," Aeronautical Research Lab, Research Report 17, 1993.
[2] MIL-A-83444, *Airplane Damage Tolerance Requirements*, USAF, 1974.
[3] Weiland, D. H., Cutshall, J. T., Burnside, O. H., and Cardinal, J. W., "Analysis of Cold-Worked Holes for Structural Life Extension," *FAA/NASA International Symposium on Advanced Structural Integrity Methods for Airframe Durability and Damage Tolerance, Part 2*, 1994, pp. 947–961.
[4] Rich, D. L. and Impellizeri, L. F., *Fatigue Analysis of Cold-worked and Interference Fit Fastener Holes, ASTM STP 637*, ASTM International, West Conshohocken, PA, 1977.
[5] Fujimoto, W., "Progress Toward Developing a 2nd Generation Crack Growth Prediction Methodology for Joints with Cold-Worked Holes," 2003 Air Force ASIP Conference, Savannah, GA, Dec. 2003.
[6] Forgues, S. A., Bernard, M., and Bui-Quoc, T., "3D Axisymmetric Numerical Analysis and Experimental Study of Fastener Hole Cold-working Process," *Computer Methods and Experimental Measurements for Surface Treatments*, M. H. Aliabadi and C. A. Brebbias, Eds., Computational Mechanics Publications, 1993.
[7] Mann, J. Y., Revill, G. W., and Lupson, W. F., "Improving the Fatigue Performance of Thick

Aluminum Alloy Bolted Joints by Hole Cold-Expansion and the Use of Interference-Fit Steel Bushes," ARL Structures Note *486*, Aeronautical Research Laboratories, Melbourne, Australia, 1983.

[8] Ozdemir, A. T. and Edwards, L., "Relaxation of Residual Stresses at Cold-worked Fastener Holes Due to Fatigue Loading," *Fatigue Fract. Eng. Mater. Struct.*, Vol. 20, No. 10, 1997.

[9] Evans, R. L., "The Influence of Secondary Bending on Fatigue Life Improvement in Bolted Joints," Research Report 14, AR-00808383, Aeronautical Research Laboratory, Australia, 1993.

[10] Fujimoto, W. T., "Analytical Testing of Joints with Cold-Worked Holes," Paper presented to 2001 Aging Aircraft Conference, Orlando, FL, Sept. 2001.

[11] Ozdemir, A. T. and Edwards, L., "3-D Residual Stress Distributions Around Split-sleeve Cold-Expanded Fastener Holes," *J. Strain Anal. Eng. Design*, Vol. 31, 1996, pp. 413–421.

[12] Pavier, M. J., Poussard, C. G., and Smith, D. J., "A Finite Element Simulation of the Cold Working Process for Fastener Holes," *J. Strain Anal. Eng. Des.*, Vol. 32, No. 4, 1997.

[13] Ball, D. L. and Doerfler, M. T., "Experimental and Analytical Studies of Residual Stress Field Evolution and Fatigue Crack Growth at Cold Expanded Holes," ASIP Conference, Savannah, GA, Dec. 2003.

[14] Mendelson, A., *Plasticity: Theory and Application*, Krieger Publishing Company, 1983.

[15] Fujimoto, W. T., "Application of the Virtual Crack Method to Damage Prediction in Multi-Loadpath Structure," Aging Aircraft Conference, New Orleans, LA, Sept. 2003.

[16] Mahadevan, S., "Monte Carlo Simulation," in *Reliability-Based Mechanical Design*, T. A. Cruse, Ed., Marcel Dekker, 1997.

[17] Abernethy, R. B., *The New Weibull Handbook*, 4th ed., Published and distributed by Robert, B. Abernethy, weibull@worldnet.att.net.

[18] Cook, R. and Holdway, P., "Residual Stresses Induced by Hole Cold Expansion," *Computer Methods and Experimental Measurements for Surface Treatments*, M. H. Aliabadi and C. A. Brebbias, Eds., Computational Mechanics Publications, 1993.

[19] Fujimoto, W. T. and Mettu, S., "A Weight Function Approach for Tracking the Growth of Surface and Radial Cracks Through Residual Stress Fields or Bi-variant Stress Fields," Paper presented to ASIP 2000 Conference, San Antonio, TX, Dec. 2000.

[20] Petroski, H. J. and Achenbach, J. D., *Eng. Fract. Mech.*, Vol. 10, 1978, pp. 257–266.

[21] Orynyak, I. V., Borodii, M. V., and Torop, V. M., "Approximate Construction of a Weight Function for Quarter-Elliptical, Semi-Elliptical and Elliptical Cracks Subjected to Normal Stresses" *Eng. Fract. Mech.*, Vol. 49, Sept. 1994, pp. 143–151.

Journal of ASTM International, June 2005, Vol. 2, No. 6
Paper ID JAI12569
Available online at www.astm.org

T. Honda,[1] *M. Ramulu,*[2] *and A. S. Kobayashi*[3]

Effect of Shot Peening on Fatigue Crack Growth in 7075-T7351

ABSTRACT: The effects of shot peening on fatigue crack growth in 7075-T735 single-edged notch bend (SENB) and three point bend (TPB) specimens are discussed. Fifty-one total fatigue tests were conducted with SENB and TPB specimens, which were machined from an 8.1 mm thick 7075-T7351 aluminum stock plate. All specimens were tested in the as-received or shot peened conditions, with crack perpendicular to the rolling direction, i.e., in the L-T direction. Fatigue tests of SENB specimens were conducted at a constant maximum load, stress ratios of R = 0.1 or 0.8, and to a pre-determined fatigue cycle or to failure. Crack growth rate was determined from the tunneling crack profile or by fractography. Peened surface roughness, subsurface microstructure, and micro-hardness profiles were also examined to evaluate their effect on crack growth rate. The TPB specimens were fatigued to failure at stress ratios of R = 0.1 or 0.8 and a S-N diagram constructed. Both the SENB and the TPB test results showed that severe shot peening (0.016A) slightly increased the fatigue life at low stress ratio of R = 0.1 but was found to be negligible at a high load ratio of R = 0.8. The stress concentration factor due to dimples generated by severe shot peening was estimated to be 1.14 and had negligible effect on the fatigue life. Grain distortion was observed to a depth range of 130–410 μm indicating the depth of the residual compressive stress layer developed for peening intensities of 0.004–0.016A, respectively.

KEYWORDS: fatigue, aluminum 7075-T7351, shot peening, residual stress, surface roughening

Introduction

Delayed crack initiation and the early stage of crack propagation in high strength steel components due to compressive residual surface and subsurface stresses, which are generated by shot peening, have been amply documented for nearly a century [1]. In contrast, comparable literature on the shot peening effects of aluminum is sparse [2] and contradictory at the best. Waterhouse et al. [3] and Pelloux et al. [4] showed that the rough peened surface of 7075-T6 specimens significantly degraded the fatigue life with only a net increase of 7 % in fatigue life. Small shot size, i.e., S170, which generated less compressive residual stress, however, resulted in a slight increase in fatigue life of peened 7075-T6 specimens due to the decreased surface roughness. They also found that the maximum compressive residual stress in 7075-T6 reverse bending specimens, which were shot peened with iron shots of S250, was 30 MPa at a surface depth of 30–50 μm. In contrast, Mutoh et al. [5] showed that crack growth rates in shot peened 7010 and 8090 aluminum alloys were significantly reduced at longer crack length, but this trend was reversed in cracks smaller than 0.3 mm. Sharp et al. [6–8] studied the shot peening effect of aluminum structural components and showed that a 140 % increase in fatigue life was possible under the "optimum peening treatment." The 140 % increase in fatigue life also reduced to 60 % for a re-peened surface. These contradictory results illustrate the competition between the residual compressive stresses generated by the shot peening process versus the elevated stress

Manuscript received 28 May 2004; accepted for publication 17 November 2004; published June 2005. Presented at ASTM Symposium on Residual Stress Effects on Fatigue and Fracture Testing and Incorporation of Results into Design on 19-21 May 2004 in Salt Lake City, UT.

[1] Senior Researcher, National Institute of Industrial Safety, Kiyose, Tokyo 204-0024, Japan.
[2] Professor, Department of Mechanical Engineering, University of Washington, Seattle, WA 98195.
[3] Emeritus Professor, Department of Mechanical Engineering, University of Washington, Seattle, WA 98195.

level due to the stress concentration and to the unavoidable roughened surface in a soft material, such as aluminum alloy. More recently, Ramulu et al. [9] applied water jet as an alternative to shot peening in order to reduce/eliminate the deleterious surface roughness generated by the shots while maintaining the compressive residual stresses. His results showed that an optimized, ultra-high pressure waterjet peening increased the fatigue life of 7075-T6 by about 20–25 %.

Most of the published literature on the shot peening effects on aluminum dealt with smooth cylindrical bars or the surface flaws generated from the peened surfaces, and very little has been reported on the shot peening of pre-cracked aluminum specimens. Zhu and Shaw [10], however, shot peened 7075-T6 aluminum compact specimens of thickness 12.7 mm at various locations along the pre-crack to study its effect on crack re-initiation and crack growth rate. While peening of the frontal region of the crack tip or along the crack wake showed only moderate retardation of crack growth, peening along the entire pre-crack length resulted in a marked improvement in retarding crack growth. Zhu and Shaw attributed the retardation effect to the induced crack closure in the crack wake and determined that the surface residual stress in the region ahead of the crack tip had negligible influence on the crack growth rate. The former crack closure is geometry and process dependent, while the latter surface residual stress is only process dependent.

The above brief literature review shows the lack of in-depth assessment of shot peening effect on the fatigue crack growth of aluminum specimens with a pre-existing crack. The exploratory study, which is presented in the following, addresses the effect of shot peening on fatigue crack growth in the presence of crack tip or corner singularities in 7075-T7351 aluminum specimens.

Experimental Procedure

Specimens

Three-point bend fatigue testing of 8.1 mm thick 7075-T7351 aluminum alloy, single-edged notch bend (SENB) and three point bend (TPB) specimens were conducted. These specimens and loading condition are a departure from the most commonly used cylindrical hourglass specimen tested in a rotating bending machine. Since the stress ratio of $R = -1$ in the rotating bend test imposes a repetitive and severe crack closure, SENB and bend specimens were used in this study for a positive stress ratio loading. Nine as-received specimens, 24 shot peened (Alman scale: 0.004A, 0.008A, 0.012A, and 0.016A) SENB, and 18 TPB specimens were tested with the crack perpendicular to the rolling direction, i.e., in the L-T direction. The entire surface on all sides of each specimen was shot peened to reduce, if not eliminate, crack closure, which would have been induced if shot peening was confined to the crack wake region of the SENB specimens [10]. The SENB and TPB specimens, as shown in Fig. 1, were machined from an 8.1 mm thick 7075-T7351 aluminum stock plate.

Shot Peening

Cast steel shots, shot size S 230-280, with a shot flow rate of 59–60 % bombarded all four sides of the aluminum specimens at Almen intensities of 0.004A, 0.008A, 0.012A, and 0.016A. Total peening time per side per specimen was 6 min. The cast steel shots were expected to generate a surface which was approximately twice as rough as that peened by glass beads [8].

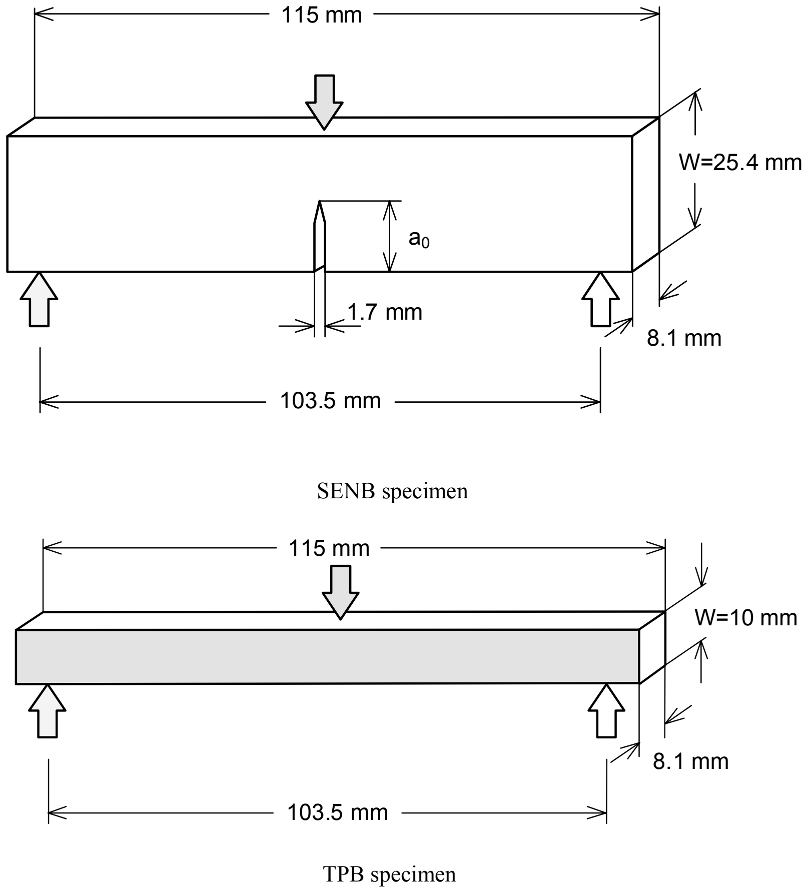

FIG. 1—*SENB and TPB specimens.*

Fatigue Testing

A 20 kN Instron servo hydraulic testing machine was used to fatigue the specimens in a three point bend fixture in lab air. A sine waveform was applied at 6 Hz with load ratio, R = 0.1 or 0.8. The crack tunneling profiles at failure were recorded in 33 SENB specimens, which were either fatigued to failure or fatigued to a predetermined number of cycles and fractured. The 18 as-received and shot peened (0.012A and 0.016A) TPB specimens (without pre-notching) were fatigued to failure at various stress levels, and a S-N diagram was constructed.

Surface Roughness

Surface roughness of the shot peened and as-received specimens was measured with a Federal Surfanalyzer model EAS-4400-W1 with a 5 μm diameter stylus probe. The traverse length of the probe was approximately 3 mm. The surface roughness was measured in 3–4 different locations in both the longitudinal and transversal directions on each sample. The statistical average roughness parameters are presented in terms of an average roughness, R_a, a root-mean square roughness, R_q, a peak-to-valley height, R_t, and a ten-point height, R_z.

Subsurface Integrity Analysis

Polished and etched 1.2 × 1.2 × 0.81 cm slices from the as-peened and fatigued specimens were viewed in a 400× microscope to study the subsurface grain structure of the as-received and shot peened specimens. Polished sectioned samples were also used to determine the through-thickness variation of micro-hardness using a Shimadzu M Vickers hardness tester with a 100-g load and a 15 s load time. Micro-hardness measurements were taken approximately every 20–30 μm to a depth of 100 μm and every 50 μm from a depth of 100–500 μm.

Fractography

The fracture surfaces of the as-received and shot peened specimens were sectioned and examined under a JEOL JSM-IC25S scanning electron microscope. Six SEM micrographs each were taken, approximately 150 μm from the specimen surface, 800μm apart, and also along the center line of the specimen at 1 mm intervals, between the starter crack and the final fatigue crack front. The mean striation spacing in these SEM micrographs were used to calculate the crack growth rate, *da/dN*.

Results

Thirty-three total SENB specimens, as-received and shot peened, were fatigued to 3000, 5000, 50 000, and 100 000 cycles and to failure at a constant maximum load of 1.73 kN, and two stress ratios of $R = 0.1$ or 0.8. Eighteen as-received and shot peened TPB specimens were tested at maximum stresses of 500, 400, 300, 250, 200, and 180 MPa and stress ratio of $R = 0.1$. Figure 2 shows typical photomicrographs of the fatigue fractured surfaces of shot peened SENB and TPB specimens. The peened (0.016A) SENB fractured surface in Fig. 2*a* shows that the crack origin was always from the starter crack, whereas in the TPB specimens in Fig. 2*b*, crack always initiated at one of the bottom corners of the bend specimen, due to folded voids caused by shot peening the corner.

Figure 3 shows the crack front profiles of the SENB specimens shot peened at 0.004A and 0.016A intensities and fatigued at stress ratios of $R = 0.1$ and 0.8. As expected, no significant difference is noted between the crack front profiles at failure of the as-received and shot peened (0.004A and 0.016A) SENB specimens at $R = 0.8$. However, the cycles to failure in the shot-peened specimens at 0.016A and 0.004A intensities were 25 and 7 % higher, respectively, than their as-received counterparts. Also, no significant improvement was found between the fatigue lives of the mildly shot peened (0.004A) and the as-received SENB specimens fatigued at $R = 0.1$. The influence of the shot peening intensity on the fatigue life of SENB specimen for $R = 0.8$ and 0.1 is summarized in Fig. 4. The data for $R = 0.1$ shows a very small increase in the number of cycles to failure with increasing shot peening intensity, while the corresponding data for $R = 0.8$ shows no change in fatigue life due to shot peening.

Figure 5 shows the SN curve of TPB specimens fatigued at $R = 0.1$. The lack of any significant difference in the fatigue lives of as-received and shot peened (0.012A, 0.016A) TPB specimens at $R = 0.1$ is consistent with the results in Fig. 3 for the SENB specimens fatigued at $R = 0.1$. However, the fatigue lives of shot peened, TPB specimens with polished sides and polished and rounded corners were slightly larger than those of the as-received or just shot peened TPB specimens.

Fatigue testing at $R = 0.8$, which would require fatiguing in excess 10^8 cycles, was not conducted due to the low cycling speed of the Instron testing machine. Nevertheless, the 10^2 order difference between the fatigue lives of SENB specimens tested at $R = 0.8$ and 0.1 is indicative of the high cycles required for constructing a S-N curve of TPB specimens fatigued at $R = 0.8$.

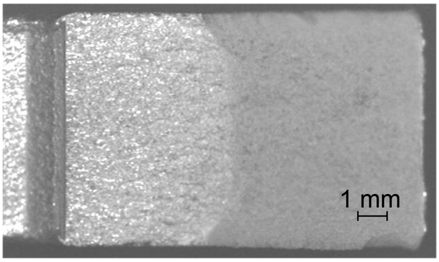

Failed at 6646 cycles (R = 0.1)

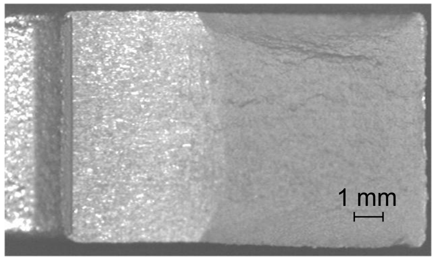

Failed at 229 449 cycles (R = 0.8)

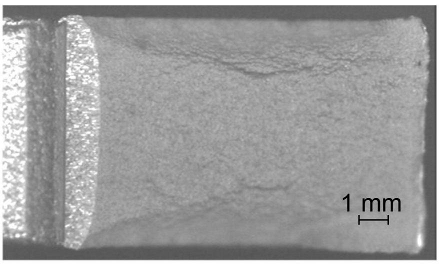

3000 cycles (R = 0.1)

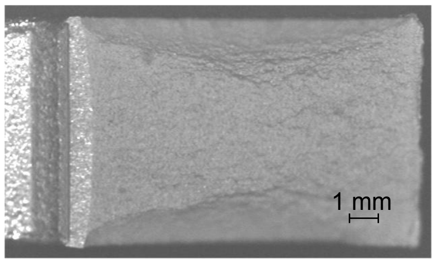

100 000 cycles (R = 0.8)

FIG. 2*a*—*Shot peened (0.016A) 7075-T7351 fractured SENB specimens.*

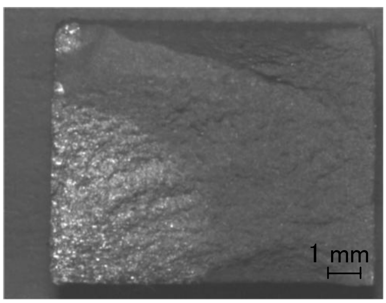

Failed at 25 076 cycles. $\Delta\sigma$ = 400 MPa.

FIG. 2*b*—*Shot peened (0.016A) 7075-T735 TPB specimen.*

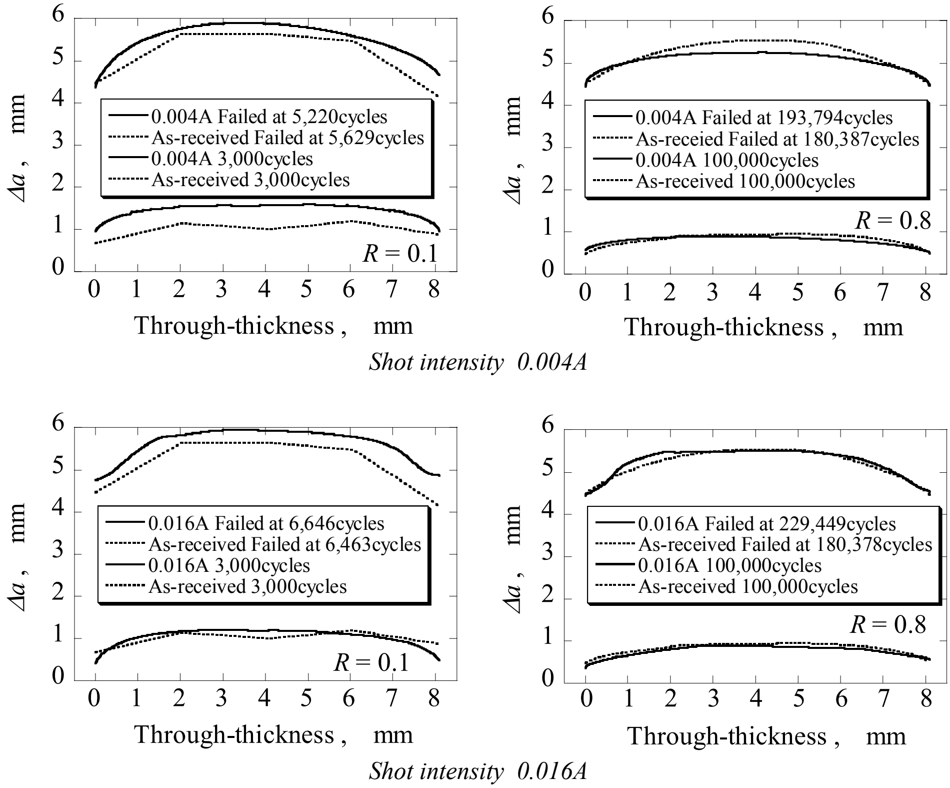

FIG. 3—*Crack front profiles of as-received and shot peened SENB specimens.*

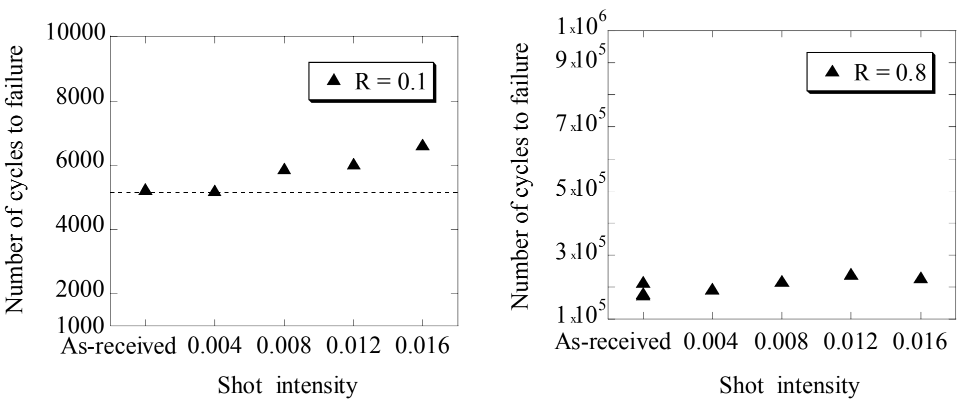

FIG. 4—*Fatigue life of shot- peened SENB specimens.*

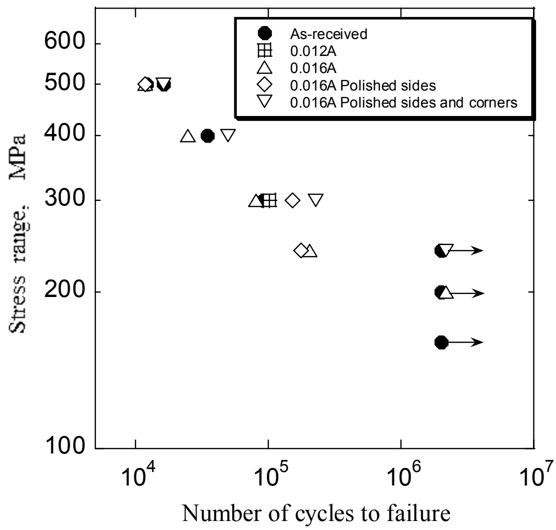

FIG. 5—*S-N curve for the as-received and shot-peened TPB specimens fatigued at R = 0.1.*

Surface Roughness

Figure 6 shows the increase in arithmetic mean roughness, R_a, and the peak to valley height, R_t, with increasing shot intensity. Both R_a and R_t increased with increased shot peening intensity as expected, thus leading to increased stress concentration which apparently offset the attendant increase in compressive residual surface stress. This stress concentration factor, SCF, for a 7075-T7351 plate shot peened at an intensity of 0.016A was estimated by the empirical formula of Li et al [11]:

$$K_t = 1 + 4\left(\frac{R_t}{S_p}\right)^{1.3}$$

where R_t = 10–30 μm, and the average distance between the peaks, S_p = 227–393 μm for peening intensities of 0.004 and 0.016A. The resultant stress concentration factor, K_t, was a negligible 1.06–1.15. In contrast, the stress concentration factor, K_m, at the machined notch tip of the SENB specimen with a measured tip radius 0.68 mm is 3.29, which overwhelmed the stress riser due to surface roughness. Once a starter crack initiates from the notch tip, a stress singularity of $1/\sqrt{r}$ dominates, and the surface roughness becomes a moot problem. Likewise, corner singularity of 1/r dominates the TPB specimen, when the peened specimen corners were not rounded and polished.

Surface Hardening

Figure 7 shows the subsurface non-dimensionalized micro-hardness (H_V / $H_{V\ base}$) variations in the as shot peened (0.004 A, 0.016A) specimens. While residual stress was not measured in this study, a 10 % increase in surface hardness was noted regardless of peening intensity. However, the influence of hardening layer can be surmised from the difference, if any, of the crack growth rate in this subsurface region of the as-received and shot peened SENB specimens.

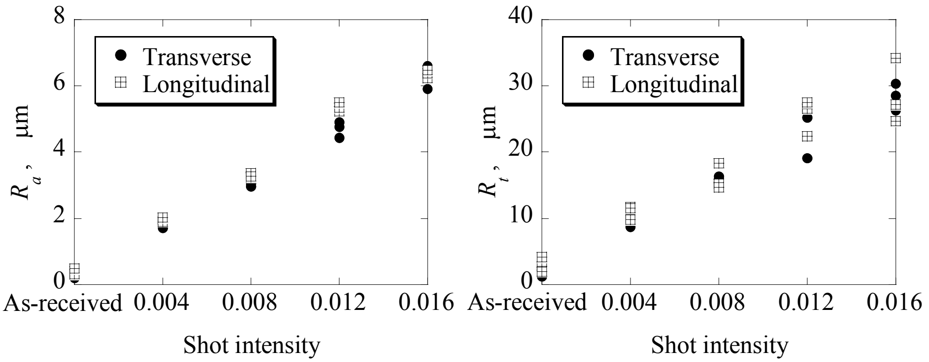

(a) *Arithmetic average surface roughness, R_a* (b) *Arithematic average peak-to-valley, R_t*

FIG. 6—*Arithmetic surface roughness and maximum indent height of shot-peened SENB specimens.*

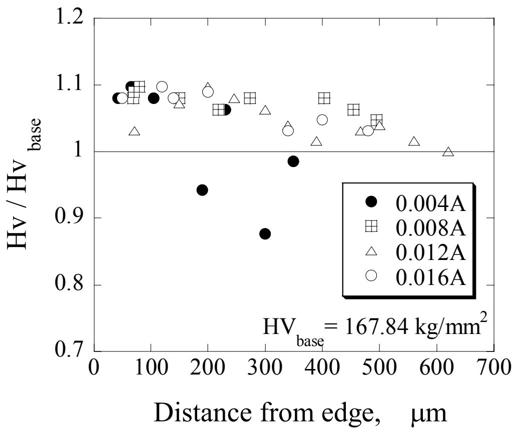

FIG. 7—*Subsurface Vickers micro-hardness distribution.*

Subsurface Micrographs

Figure 8 shows the subsurface micrographs of the as-received and shot peened (0.016A) SENB specimens. The surface clearly shows the indentations and foldings left by the impacted shots. Elongated and flattened grains dominated the subsurface of the peened specimen to an approximate depth of 400 µm. This depth coincides with the depth of the hardened layer identified by the micro-hardness in Fig. 7.

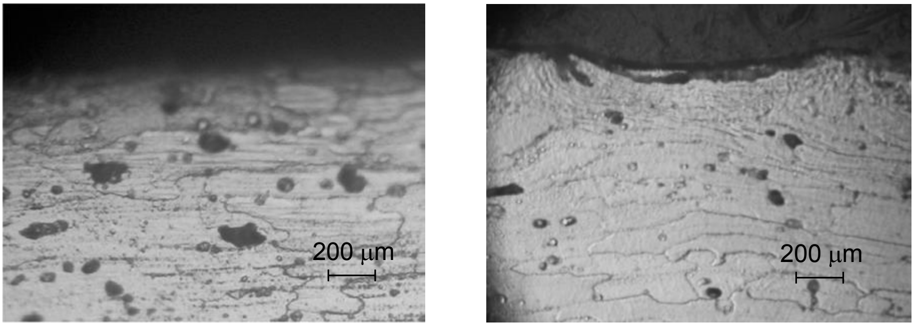

(a) As-received *(b) Shot peened (0.016A)*

FIG. 8—*Subsurface optical micrographs of as-received and shot-peened7075-T7351SENB specimens.*

Fractography

SEM photographs of the fracture surfaces of the SENB specimens were taken along a line 0.15 mm from to specimen surface and along the center line of the specimen. Figure 9 shows typical striation marks in SENB specimens, shot peened at 0.004A and 0.016 A and fatigued at R = 0.1. Δa relates to the fatigue crack extension at the point of observation. These striations were used to determine the crack growth rate, *da/dN*, at the locations of SEM photographs.

Figure 10 shows the *da/dN* versus ΔK relations at four locations along a line 150 μm from the left edge or within the surface hardening layer, and along the centerline of the SENB fracture surface. Little difference is noted between *da/dN* within the hardened layer and the central or mid-section of shot peened SENB specimens. Figure 11 is a composite of all *da/dN* data of as-received and shot peened SENB specimens. Despite the scatter in data, a slightly depressed *da/dN* of shot peened SENB specimens is observed in during the initial phase of crack extension, i.e., $\Delta a \approx 0.6 \sim 1$ mm. Beyond this initial phase of fatigue, shot peening had negligible or only minor effect on the crack growth rate.

Discussion

In order to relate the da/dN, which were determined by striation spacing, to the applied stress intensity, we estimated the crack driving force, i.e., the range of stress intensity factor, ΔK, at these locations by [12,13]:

$$S \propto \frac{\Delta G}{E}$$

or for plane strain conditions

$$S \propto (1-\nu^2)\left(\frac{\Delta K}{E}\right)^2$$

where S is the striation spacing, G is the strain energy release rate, υ is the Poisson ratio, and E is the modulus of elasticity. All striation data generated in the shot peened SENB fatigue crack fractographs and the striation spacing calculated by above equation were plotted and shown in Fig. 12. The excellent agreement between the predicted and SEM measurements can be seen when the proportionality constant for this material is 9.8, which is in good agreement with that of Kobayashi et al. [14] of $S = 9.4(1 - \nu^2)(\Delta K/E)^2$ and differed by a factor of 1.6 with that of Bates and Clark [12].

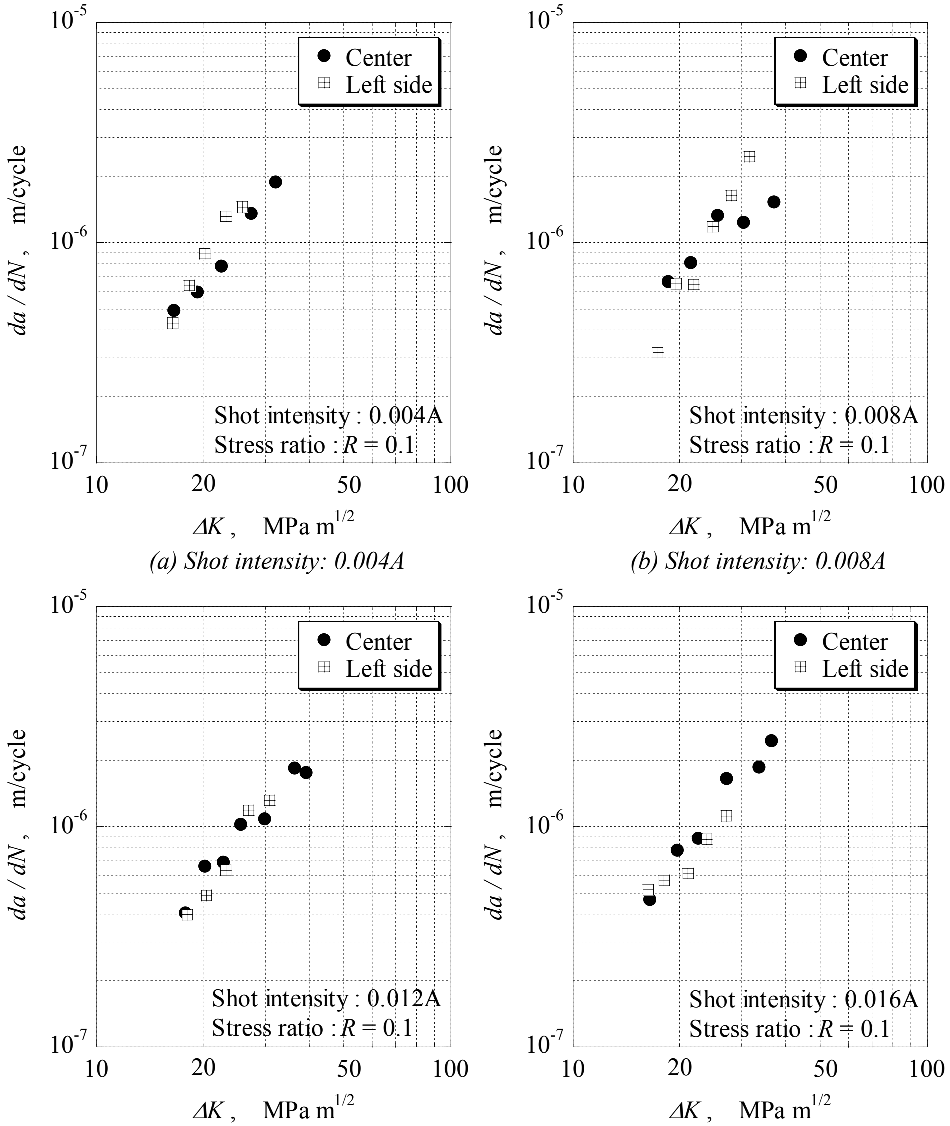

(a) Shot intensity: 0.004A

(b) Shot intensity: 0.008A

(c) Shot intensity: 0.012A

(d) Shot intensity: 0.016A

FIG. 10—*da/dN versus Δa in shot peened 7075-T7351 SENB specimens.*

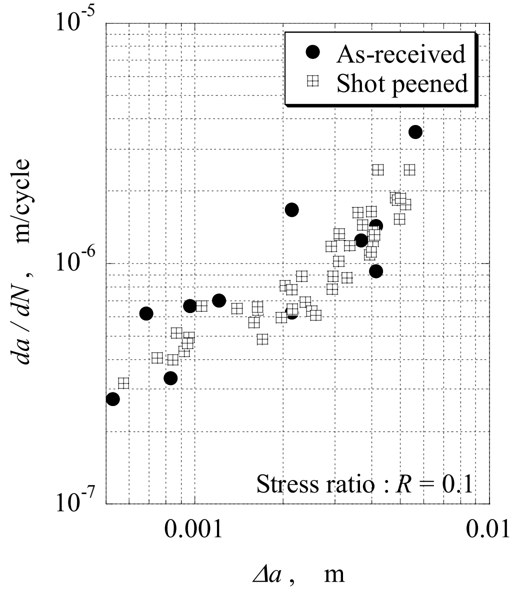

FIG. 11—*Crack growth rate in as-received and shot-peened (0.016A) 7075-T7351 SENB specimens.*

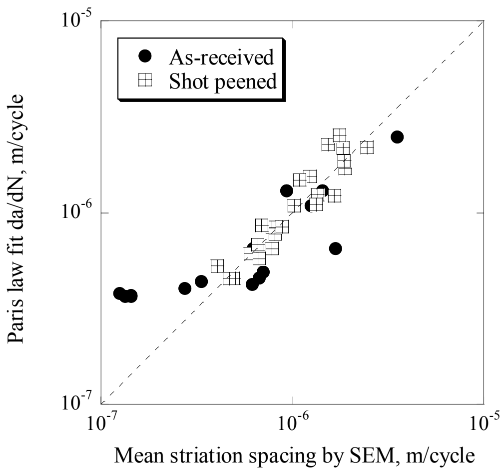

FIG. 12—*Correlation of calculate and SEM determined fatigue striation spacing in as-received and shot peened (0.016A)7075-T7351 SENB specimens.*

Reference [15] cites that shot peening of a rectangular cross-section cracked the sharp edge of the nitride steel specimen. Indeed, micrographs of the corners on tension side of the TPB specimens showed that the crack did initiate at a void in the fold generated by shot peening as shown in Fig. 13. Also shown for comparison is the micrograph of the as-received TPB specimen where the crack originated near the bottom center, despite the corner singularity. Two shot peened side surfaces of two TPB specimens were removed by polishing and fatigued to failure at maximum stresses of 500 and 300 MPa and $R = 0.1$. As shown in Fig. 14, the origin of the fatigue crack was near the bottom center of the shot peened surface. The data generated by these extra TPB specimens, with polished side surfaces and polished rounded corners, are superposed in Fig. 5. The extra data of polished sides falls within other data of as-received and shot peened TPB specimens. However, the polished sides with rounded corners improved the fatigue life at "300 MPa" by 149 % and 87 % in comparison with those of as-received and shot peened TPB specimens, respectively. Therefore, the life of shot peened TPB specimens was clearly dominated by the corner singularity of 1/r. For valid endurance data, care must thus be given in eliminating the corner singularity of shot peened TPB specimens.

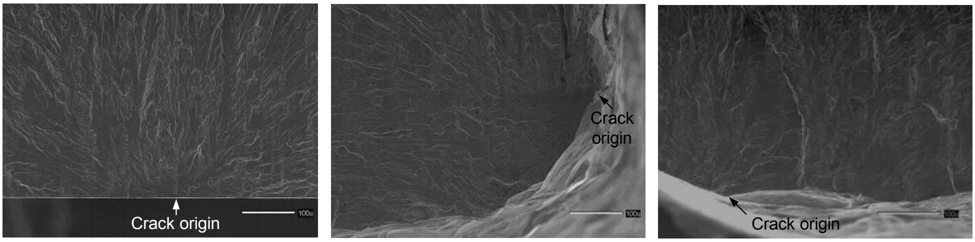

Failed at 34,644 cycles. *$\Delta\sigma = 400$ MPa* *(a) As received.*

Failed at 25,076 cycles. *$\Delta\sigma = 400$ MPA* *(b) Shot peened on all sides.*

Failed at 18,000 cycles. *$\Delta\sigma = 500$ MPa* *(c) Shot peened and rounded corners.*

FIG. 13—*Micrographs of tension side of as-received and shot peened (0.016A) TPB specimens.*

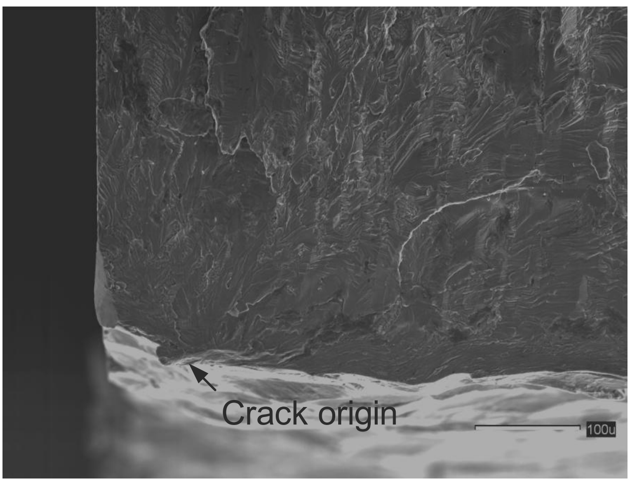

FIG. 14—*Micrograph of tension side of shot-peened (0.016A)TPB specimen with polished sides. Failed at 204 143 cycles. $\Delta\sigma = 240$ MPa.*

Conclusions

1. The distance between the significant peaks of the surface roughness profile of shot peened 7075-T7351 specimens was nearly equal to the diameter of the micro-dents caused by peening. The stress concentration factor at the machined notch tip of the SENB specimen overwhelmed the stress concentration generated by the peened surface textures.
2. The flattened grains near the surface of 7075-T7351 specimen resulted in increased micro-hardness of about 10 % and appeared to induce compressive surface stress. This probable presence of compressive surface stress had negligible effect on the crack front profile of shot peened 7075-T7351 SENB specimen.
3. The fatigue crack growth rate at the surface of a severely shot peened (0.016A) 7075-T7351 SENB specimen is not significantly different than that at the center of the specimen.
4. The fatigue lives of as-received and shot peened three point bend specimens are essentially identical. When the sides are polished and corners rounded, the fatigue lives at the lower stress range in shot peened specimens are larger than those of as-received specimens. Therefore fatigue lives in shot peened TPB specimens are dominated by corner singularity 1/r.

Acknowledgments

This research was supported by the National Institute of Industrial Safety, Japan. The authors thank Thomas P. Munson for his generous help in executing the experiments and in the data reduction processes.

References

[1] Niku-Lari, A., "Shot Peening," *First international Conference on Shot Peening*, Pergamon Press, New York, 1982, pp. 1–21

[2] Tosha, K., "Papers on Shot Peening Published in the World for the Last Thirteen Years," *The Seventh international Conference on Shot Peening*, Institute of Precision Mechanics, Warsaw, Poland, 1999, pp. 5–10

[3] Waterhouse, R. B., Noble, B., and Leaderbeat, G, "The Effect of Shot Peening on the Fretting-Fatigue Strength of an Age Hardened Aluminum Alloy (2014A) and Austenitic Stainless Steel," *Journal of Mechanical Working Technology*, Vol. 8, 1983, pp. 147–153.

[4] Pelloux, R. M. and Frabolot, M. C. "Effect of Shot Peening Methods on the Fatigue Behavior of Alloy 7075-T6," *First International Conference on Shot Peening*, Pergamon Press, 1981, pp. 445–451.

[5] Mutoh, Y., Fair, G. H., Noble, B., and Waterhouse, R. B., "The Effect of Residual Stress Induced by Shot Peening on Fatigue Crack Propagation in Two High Strength Aluminum Alloys," *Fatigue and Fracture of Engineering Materials and Structures*, Vol. 10, No. 4, 1987, pp. 261–272.

[6] Sharp, P. K., Clayton, J. Q., and Clark, G., "The Fatigue Resistance of Peened 7050-T7451 Aluminum Alloy – Repair and Re-Treatment of a Component Surface," *Fatigue and Fracture of Engineering Materials and Structures*, Vol. 17, No. 3, 1994, pp. 243–252.

[7] Sharp, P. K., Liu, Q., Barter, S. A., Baburamni, P., and Clark, G., "Fatigue Life Recovery in Aluminum Alloy Aircraft Structure," *Fatigue and Fracture of Engineering Materials and Structures*, Vol. 25, 2002, pp. 99–110.

[8] Sharp, P. K. and Clark, G., "The Effect of Peening on the Fatigue Life of 7050 Aluminum Alloy," DSTO-RR-0208, Department of Defence, Australia, March 2001.

[9] Ramulu, M., Kunaporn, S., Jenkins, M. G., Hashish, M., and Hopkins, J., "Fatigue Performance of Waterjet Peened Aluminum Alloy," *ASME Journal of Pressure Vessel Technology*, Vol. 123, No. 1, 2002, pp. 118–123.

[10] Zhu, X. Y. and Shaw, W. J. D., "Correlation of Fatigue Crack Growth Behaviour with Crack Closure in Peened Specimens," *Fatigue & Fracture of Engineering Materials & Structures*, Vol. 18, 1995, pp. 811–820.

[11] Li, J. K., Yao, M., Wang, D., and Wang, R., "An Analysis of Stress Concentrations Caused by Shot Peening and Its Application in Predicting Fatigue Strength," *Fatigue and Fracture of Engineering Materials & Structures*, Vol. 15, No. 12, 1992, pp. 1237–121.

[12] Bates, R. C. and Clark, W. G., "Fractography and Fracture Mechanics," *Trans. ASM*, Vol. 62, No. 2, 1969, pp. 380–389.

[13] Kawasaki, T., Yokobori, T., Nakanishi, S., Ogawara, Y., and Horiguchi, M., "Fractographical Study on Fatigue Crack Propagation in Structural Carbon Steel by Scanning Electron Microscopy," *Reports of the Research Institute for Strength and Fracture of Materials*, Vol. 6, No. 1, 1970, pp. 25–47.

[14] Kobayashi, H., Nakamura, H., and Nakazawa, H., "A Relation Between Crack Tip Blunting and the J-Integral," *Proc. of Third International Conference on Mechanical Behavior of Materials*, Pergamon Press, 1979, pp. 529–538.

[15] Coroccolo, D., Cristofolin, L., Bandini, M., and Freddi, A., "Fatigue Strength of Shot Peened Nitride Steel: Optimization of Process Parameters by Means of Design of the Experiment," *Fatigue & Fracture of Engineering Materials & Structures*, Vol. 25, 2002, pp. 695–707.

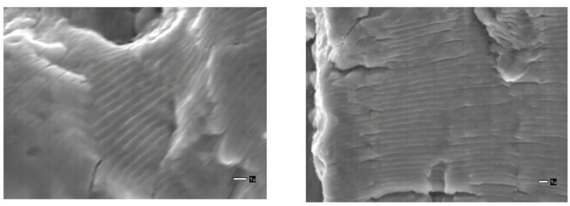

(a) Left side (?a = 1.6 mm) *(b) Center (?a = 2.0 mm)*

Figure 9a: Fatigure striations in a shot-peened (0.004A) 7075-T7351 SENB specimen fatigued at R =0.1.

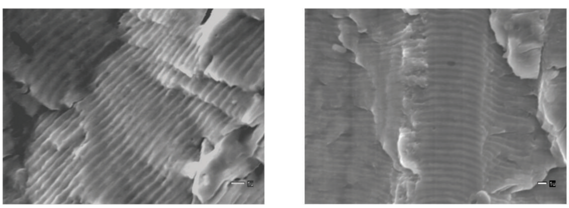

(a) Left side (?a = 1.6 mm) *(b) Center (?a = 2.0 mm)*

Figure 9b: Fatigure striations in a shot-peened (0.016A) 7075-T7351 SENB specimen fatigued at R =0.1.

ERRATUM: Figures 9a and 9b were omitted from the original online publication of this paper in the Journal of ASTM International. The online version of the paper now includes an erratum with a link to the figures. ASTM apologizes for the error and regrets any inconvenience to its readers.

Journal of ASTM International, Vol. 3, No. 5
Paper ID JAI12552
Available online at www.astm.org

Dennis J. Buchanan,[1] *Reji John,*[2] *and Noel E. Ashbaugh*[1]

Thermal Residual Stress Relaxation in Powder Metal IN100 Superalloy

ABSTRACT: Relaxation of shot peen induced compressive residual stresses due to thermal exposure was measured using X-ray diffraction. The material used in this study was a hot isostatically pressed (HIP) powder metal (PM) IN100 nickel base superalloy. A total of 14 IN100 samples were shot peened to an Almen intensity of 6A using MI-170-R shot with 125 % coverage. The sample dimensions were nominally 16×13×4-mm thick with an irradiated X-ray region of 8×5 mm. Residual stress measurements were made at the surface and at nominal depths of 12, 25, 50, 75, 125, 175, 250, and 350 microns. The shot peened samples were thermal exposed at two temperatures (650, 704°C) and a range of exposure times (0.5–300 h). Residual stress measurements on shot peened samples without thermal exposure were used as a basis for comparison. The relaxation of shot peened compressive residual stresses under purely thermal loading was examined. The residual stresses exhibited an initial rapid decrease on the surface and in the depth at both temperatures. However, continued thermal exposure produced little or no change in surface residual stresses while peak compressive stresses in the depth continued to relax with time at both temperatures. In all cases of this study the retained peak compressive residual stress after thermal exposure was greater than 50 % of the baseline value.

KEYWORDS: residual stress, shot peen, thermal exposure, thermal relaxation, stress relaxation, IN100, superalloy, X-ray, cold work

Introduction

Shot peening components to impart a compressive residual surface stress for retardation of crack initiation and crack growth has been employed for many years. Numerous studies have characterized the beneficial effects of compressive residual surface stresses on fatigue life for several aircraft alloys [1–5]. In design applications that utilize aluminum and titanium alloys, subjected to moderate temperatures and stresses, the residual stresses can be assumed to be stable with repeated cyclic stress controlled loading. In contrast, nickel-based superalloys are typically selected for applications where temperatures reach 70 % of the melting temperature and stresses approach the yield strength. Hence, under elevated temperature and high stress loading conditions plasticity and creep will alter the residual stress depth profile. Additional complications are caused by changes to the microstructure and mechanical behavior from shot peening and long term elevated temperature exposure.

Characterization of the initial residual stress and plastic strain depth profiles are required for accurate prediction of the evolution of stresses and plastic strains with applied thermal and mechanical loading. The accuracy of predictions depends on accuracy of the initial conditions, specifically the residual stresses and plastic strains. There are numerous variables that affect the residual stress and plastic strain depth profile. The elastic and inelastic material properties of the material itself have a pronounced affect on the resulting residual stresses and plastic strains. For example, machining and surface finishing processes prior to shot peening, such as grinding and polishing, all impart residual stresses into the component. The shot peening process itself has many variables that contribute to variability of imparted residual stresses: shot size, hardness, coverage and angle, just to name a few. There have been several empirical and physics-based models developed to determine the residual stress depth profile as a function of material properties and

Manuscript received May 24, 2004; accepted for publication February 13, 2006; published online March 2006. Presented at ASTM Symposium on Residual Stress Effects on Fatigue and Fracture Testing and Incorporation of Results into Design on 19–21 May 2004 in Salt Lake City, UT; J. Bunch, Guest Editor.
[1] University of Dayton Research Institute, 300 College Park, Dayton, Ohio, 45469.
[2] Air Force Research Laboratory, Materials and Manufacturing Directorate, AFRL/MLLMN, 2230, Tenth Street, Suit No. 1, Wright-Patterson Air Force Base, Ohio, 45433-7817.

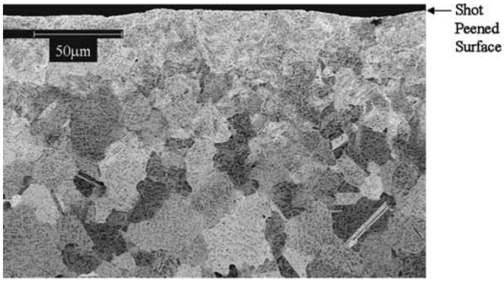

FIG. 1—*Cross section of IN100 as shot peened microstructure (no thermal exposure).*

shot peening parameters [6–9,17]. These models are useful for designers who wish to incorporate the beneficial affects of residual stresses for retardation of fatigue crack initiation and growth into life prediction. In some cases cyclic stress relaxation is incorporated into life prediction models to account for changing residual stress profiles and their effect on fatigue life. However, thermal relaxation of residual stresses is often overlooked or ignored. The failure to incorporate thermal residual stress relaxation could result in a nonconservative estimate of both fatigue crack initiation and crack growth resistance and, ultimately, a component that will not meet an expected design life.

The aim of this paper is to describe an experimental program developed using design of experiments (DOE) concepts coupled with experimental mechanics and analytical modeling to produce reliable experimental thermal residual stress relaxation data for a nickel-based superalloy, IN100. Further, this paper will present the experimental results and discuss observed thermal relaxation behavior as a function of temperature and exposure time.

Material

IN100 is a powder metal (PM) nickel-based superalloy with face centered cubic (FCC) structure and a nominal grain size of 20–25 μm, similar to the alloy described by Wusatowska-Sarnek et al. [10,11]. Scanning electron microscopy (SEM) analysis of the baseline (no exposure) and the extreme exposure (704°C @ 300 h) show no apparent differences in the microstructure. For example, there was no difference in grain size, no γ' coarsening, or no new phases present. However, there were obvious changes to the microstructure on all samples near the shot peened surface. Material deformation, cavities, and even embedded shot fragments were found on the surface of the samples. Figure 1 is a micrograph of a polished section of IN100. The top of the image was the shot peened surface of the material. The top 50 μm show a distinct change in microstructure resulting from the shot peening induced deformation. The bottom portion shows the interior and a typical representation of the microstructure and individual grains.

The monotonic true stress—true stain data for IN100 at temperatures (23, 650, and 704°C) are shown in Fig. 2. During the course of each tension test a low-stress (≈200 MPa) elastic loading cycle was performed at room temperature and at the intended test temperature. Fine ranges on the load cell and extensometer were used to accurately measure the elastic modulus during the elastic loading cycles. The elastic loading was performed multiple times to determine the repeatability of the modulus measurements. All tensile tests were performed in displacement control with the control signal generated by a 16-bit D/A function generator. The displacement rate in the elastic region ($<\sigma_y$) was nominally 0.007 mm/s and was increased by a factor of ten to 0.07 mm/s in the inelastic region to reduce the possible inclusion of time dependent behavior, creep, at elevated temperatures. A quartz-lamp heating unit with four-zone temperature control was used for the elevated temperature tension tests. Four K-type thermocouples were used to measure and control the temperature of the test specimen. Four-zone temperature control provided the capability to minimize the temperature gradients through the specimen thickness and along the loading axis of the specimen. Thermal profile maps on the specimen showed that the specimen was uniformly heated over the entire gage section of the specimen. Applied load, temperature, displacement, and extensometry data were collected during tensile tests. All tests were conducted in laboratory air using a computer controlled servo-hydraulic test system [12].

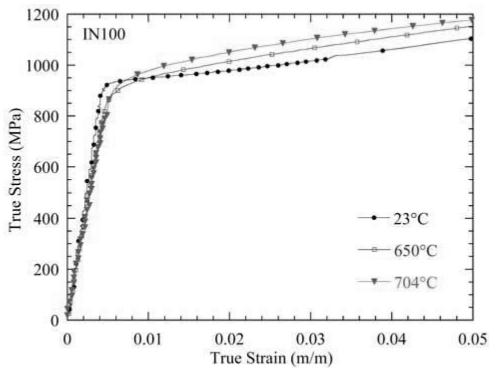

FIG. 2—*Monotonic true stress-true strain curves for IN100 at temperatures 23, 650, and 704°C.*

Specimen Design

Specimen design should not be trivialized as a simple task. For many standardized tests such as tensile, creep, and fatigue, the specimen geometry is specified in the testing standard to avoid the pitfalls of specimen design. Research projects with a significant experimental program should not be compromised by a poorly designed specimen geometry. The cost of raw material, machining, preparation, testing, and analysis of the data makes for a large financial investment that often cannot be repeated. In this study a great deal of effort was devoted to designing the specimen based on the mechanics of the shot peening process, the experimental testing program, and anticipated modeling efforts.

First and foremost was identification of all steps involved in the experimental procedures and the analytical analysis of the experimental X-ray diffraction (XRD) data to be collected. After identification of limiting factors such as material availability, size of test matrix, experimental and analytical requirements, a rectangular parallelepiped geometry was chosen. Final dimensions of the sample were based on the XRD experimental techniques and finite element (FE) analysis of residual stress profiles and layer removal simulations.

A three-dimensional FE model with quarter symmetry was used to provide insight for selecting dimensions of the sample. Based on residual stress depth profiles from another superalloy, IN718 [13,14] and typical shot peening specifications for turbine engine components [3], an Almen intensity of 6A was selected. A temperature profile was imposed on the FE model to produce a residual stress depth profile similar to that measured on IN718 [14] with an Almen intensity of 6A.

The in-plane dimensions were based on the grain size of the material, nominally 20–25 μm, the desired irradiated X-ray region (5×8 mm), the electropolishing region and the anticipated shot peened residual stress profile. The irradiated region was maximized to measure an average residual stress over as many grains as possible. A constant biaxial compressive residual stress was desired over the entire (5×8 mm) irradiated region. To achieve the constant biaxial compressive stress state over the entire irradiated region requires a surrounding border of material sufficiently wide to allow the normal stresses to decay to zero at the free surface. FE analysis was employed to determine the necessary amount of surrounding material. A 4 mm wide band of material was sufficient to have a uniformly stressed 5×8 mm measurement region. Figure 3 is a plot of the in-plane surface residual stresses (σ_{xx} and σ_{yy}) along a centerline from the center of the specimen to the edge of the specimen in the x-direction. The thick solid line represents half the length (4 mm) of the irradiated region in the x-direction. The solid circles and open rectangles are stresses in the x- and y-direction, respectively, as a function of distance in the x-direction. The stresses are equal in value and constant over the range of the XRD measurement region. Both stresses decrease in magnitude as they approach the edge of the sample. The stress in the x-direction changes rapidly as it approaches the free surface where it become zero. Figure 4 is a plot of the in-plane surface residual stresses (σ_{xx} and σ_{yy}) along a centerline from the center of the specimen to the edge of the specimen in the y-direction. This line is perpendicular to the line described in Fig. 3. The thick solid line represents half the width (2.5 mm) of the irradiated region in the y-direction. Both stresses decrease in

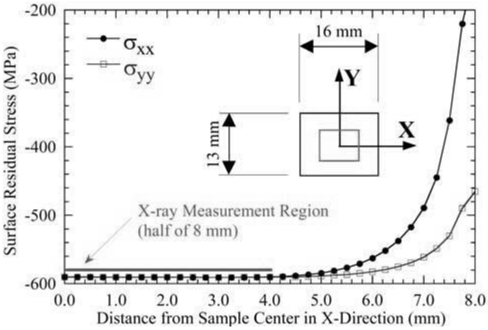

FIG. 3—*Profile of FE simulated surface residual stresses (σ_{xx} and σ_{yy}) from the center of sample to edge of sample in the x-coordinate direction.*

magnitude as they approach the edge of the sample. The stresses in the *y*-direction change rapidly as they approaches the free surface where they become zero.

XRD measurements are interpreted on the diffraction of radiation reflected from the surface and to a depth of approximately 10 μm for this material. Since the technique measures an average throughout a volume it was important to have a uniform stress field in the plane of the material. Nonlinear gradients in the plane of the stress field would not be captured and would produce erroneous errors in the measured residual stress. Using the assumption that the stress is equally biaxial and only varies as a function of the depth, corrections for volume averaging can be made for electropolishing and for subsequent depth measurements.

Another aspect considered was out-of-plane displacement associated with shot peening one side of the specimen at a time. A specimen that is too thin would produce an excessive amount of out-of-plane displacement and would violate assumptions made in the experiments and analysis. The FE model was used to determine the amount of out-of-plane deformation produced by shot peening a single side of the plate. The FE model was also used to simulate layer removal by electropolishing for depth measurements and the resulting out-of-plane displacement. Based on these analyses and recommendations from the shot peening vendor, Metal Improvement Company, Inc., of Blue Ash, OH, a specimen thickness of 4 mm was chosen.

Shown in Fig. 5 are the final specimen dimensions and cutout plan from the parent plate. The samples were taken from a 3×3 matrix of samples with the parent plate measuring 49 mm×40 mm×4 mm in size. In an effort to minimize the variation in shot peening from specimen to specimen the plates were shot peened first then split into the final sample dimensions via electrodischarge machining (EDM). Machining and shot peening the larger plates also reduced costs and made fixturing and shot peening profiles more repeatable.

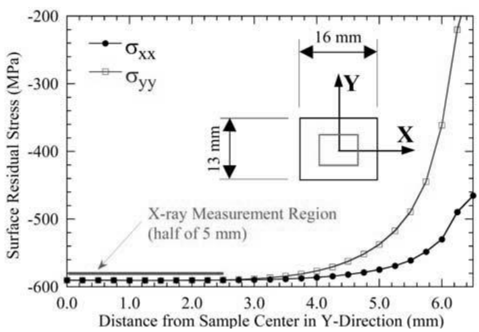

FIG. 4—*Profile of FE simulated surface residual stresses (σ_{xx} and σ_{yy}) from the center of sample to the edge of the sample in the y-coordinate direction.*

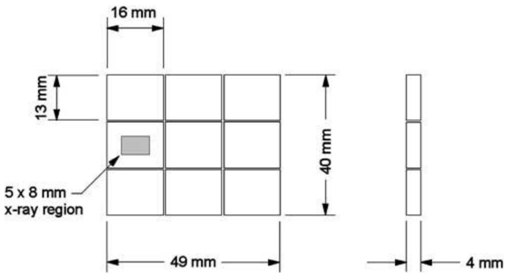

FIG. 5—*Schematic of cutout plan for shot peened plates of IN100 for thermal exposure and X-ray analysis.*

Shot Peening Conditions

The IN100 superalloy was shot peened to an Almen intensity of 6A−0+2 using a MI-170-R (SAE 170 max. cast steel shot, regular) shot with 125 % coverage. PEENSCAN® was applied prior to shot peening to verify complete coverage and uniformity over the entire surface of the plates [15]. A total of six plates were shot peened; only three were used for this study. The three plates (A2, B2, C1) used in this study, as listed in Table 1, were all shot peened at the same time. Both sides of the plates were shot peened simultaneously to reduce out-of-plane deformation often associated with shot peening a single side.

Test Conditions and Thermal Exposure Procedure

Thermal residual stress relaxation data in the literature [16–19] have shown that both temperature and exposure time have a significant affect on relaxation of stresses and reduction in cold work depth profiles. The stress relaxation rates are driven by material properties, temperature, residual stress, and cold work depth profiles. Exposure times and temperatures were selected on the basis of expected turbine engine operating conditions for this alloy.

To minimize specimen-to-specimen variations in thermal exposure each specimen was instrumented with a thermocouple and the temperature history logged on a strip chart recorder. This procedure was repeated for both exposure temperatures listed in Table 1. Recorded temperature measurements on specimens indicated that the specimens reached the desired exposure temperature in approximately nine min or less after insertion into the furnace.

Deformation mechanism maps (DMM) for nickel-based superalloys indicate that typical turbine engine operating temperatures are nominally 0.5 to 0.6 of the melting temperature, often called the homologous temperature. The homologous temperatures of IN100 for 650 and 704°C are 0.59 and 0.62, respectively. Therefore, residual stress relaxation was expected to occur at these two temperatures. In general, a homologous temperature of approximately 0.8 is an upper bound usage temperature for nickel-based superalloys.

TABLE 1—*Temperature and thermal exposure time matrix for IN100.*

Plate #	B2	C1	A2
	Temperature		
Exposure Time (h)	77°F	1200°F	1300°F
	23°C	650°C	704°C
0.0	x	x	x
0.5		x	x
1.0		x	x
3.0			x
10.0		x	x
100.0			x
300.0		x	x

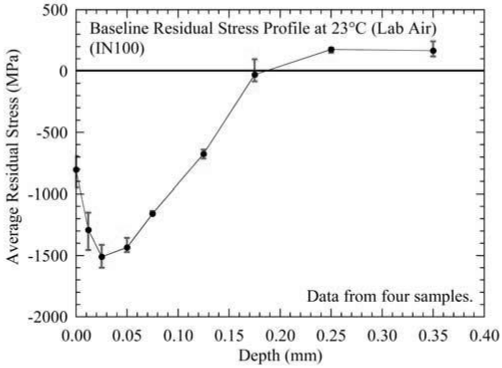

FIG. 6—*Repeatability of baseline residual stress distribution in IN100 at 23°C.*

X-Ray Stress Analysis

The X-ray elastic constant $E/(1+\nu)$ and the cold work calibration were experimentally measured on the same source of material as the test samples for the residual stress relaxation study. The X-ray elastic constant was measured on the crystallographic direction normal to the (311) plane of the FCC lattice. Determination of the elastic constant was completed using a thin rectangular beam under four-point bending in accordance with ASTM Test Method for Determining the Effective Elastic Parameter for X-Ray Diffraction Measurements of Residual Stress (E 1426) [20].

An empirical equation, based on a relationship developed by Prevéy [21], was used to relate the peak width at the half height of the diffraction peak to the percent cold work. This empirical relationship was established by XRD measurements on cylindrical samples deformed in compression to a range of cold work levels. For this residual stress relaxation study the cold work was determined using the width of the (311) diffraction peak at half-height and the empirically measured relationship. X-ray diffraction measurements for residual stress were completed in accordance with SAE J784a [22] using the diffraction radiation from the (311) planes.

The residual stress and cold work measurements were made at the surface and at nominal depths of 12, 25, 50, 75, 125, 175, 250, and 350 μm. Measurements were made in the direction of the short axis (13 mm) of the sample at the center of the sample face. The irradiated area over which the measurements were taken was 5×8 mm centered in the 13×16 mm sample dimensions. This provided a 4 mm border around the entire perimeter of the irradiated region for which the residual stresses to decay to zero at the free edge as discussed in the specimen design section and shown in Figs. 3 and 4.

Another opportunity to improve the consistency of the measured data and remove possible experimental uncertainties was with the electropolishing procedure for residual stress depth measurements. The entire surface of the sample was electropolished layer-by-layer. The stress corrections for layer removal were completed in accordance with the Moore and Evans [23] elasticity solution for flat plates. This avoided potential errors associated with stress gradients produced by pocket electropolishing.

Thermal Relaxation Results

Four baseline residual stress depth profiles with no thermal exposure were measured. Three of the depth profiles, one from each plate (A2, B2, C1), were measured by Lambda Research, Inc., and a fourth was measured elsewhere. Each profile was interpolated to a common set of nominal depths. The average residual stress and range of measurements are shown in Fig. 6. Overall, the peak compressive stresses and the overall response for all four samples were similar. The peak compressive residual stress always occurred within 50 μm of the surface, consistent with the changes in the microstructure as shown in Fig. 1.

Figures 7 and 8 show the residual stress and cold work depth profiles, respectively, for IN100 thermally exposed at 650°C for up to 300 h. These results were collected on five samples, all taken from plate

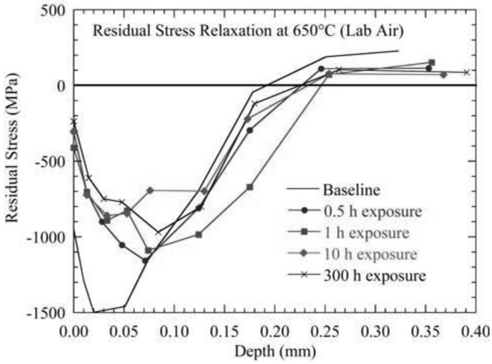

FIG. 7—*Residual stress distributions in IN100 versus exposure time at 650°C.*

(C1). A compressive surface residual stress of 250–400 MPa remained at the surface for all exposures. Stress relaxation was greatest at the free surface. The stress relaxation was less for the peak compressive stress. However, after 300 h of exposure to 650°C residual stress retention is approximately 65 %. There was also a shift of the peak compressive stress from 25 μm to approximately 75 μm. Below the free surface the residual stress profile did not follow the expected relaxation with increased exposure time. In particular, at a depth of 50 to 130 μm the 300-h exposure had a more compressive residual stress than the 10-h exposure. In contrast, there was a clear trend of decreasing cold work with increasing exposure time as shown in Fig. 8. The cold work profiles show a large change at the surface and to a depth of approximately 175 μm with increased exposure. This depth was coincident with where the stresses are below the monotonic yield strength of the material.

Figures 9 and 10 show the residual stress and cold work depth profiles, respectively for IN100 thermally exposed at 704°C for up to 300 h. These results were collected on seven samples, all from plate (A2). A compressive surface residual stress of 200–450 MPa remained at the surface for all exposures. Stress relaxation at the free surface was similar in magnitude to the relaxation that occurred at the peak compressive stress. After 300 h of exposure to 704°C residual stress retention is approximately 62 %. The cold work profiles show a large change at the surface and to a depth of approximately 130 μm with increased exposure. There was a clear trend of decreasing cold work with increased exposure time that was also observed at 650°C. The maximum stress relaxation and reduction in cold work was observed at the surface for both 650 and 704°C.

XRD of surface residual stress measurements have been proposed as a nondestructive method for characterizing the retained residual stresses in shot peened turbine engine components [24]. Figure 11 illustrates the difference in relaxation behavior of the surface versus the peak residual stress with exposure

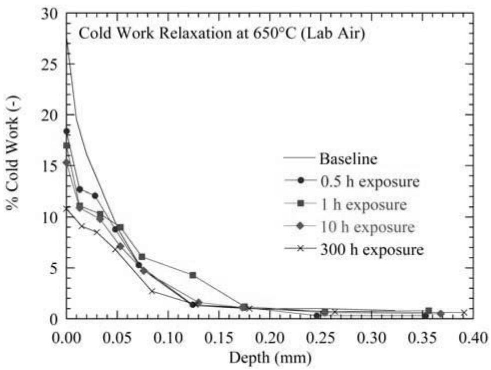

FIG. 8—*Cold work distributions in IN100 versus exposure time at 650°C.*

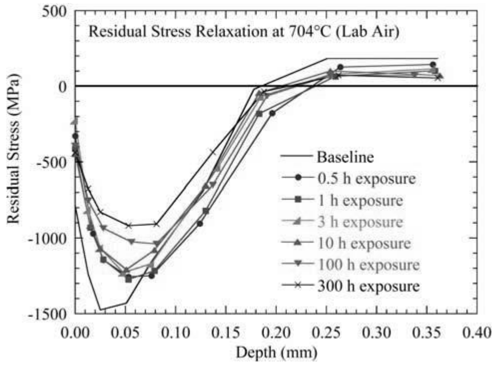

FIG. 9—*Residual stress distributions in IN100 versus exposure time at 704°C.*

time at 704°C. The data plotted in Fig. 11 include the raw surface measurement, corrected surface, and peak compressive residual stresses. The raw surface data are the as-measured surface value that represents the residual stress averaged to a depth of approximately 10 μm. The corrected surface data are computed values that can only be determined by making depth measurements and correcting the surface value based on the stress gradient into the depth. Finally, the peak compressive stress is the largest compressive residual stress in the depth. All three measures of residual stress were plotted versus exposure time. The raw and corrected surface residual measurements exhibited a rapid 450 MPa change in compressive residual stress while the peak compressive residual stress changed only 225 MPa with initial thermal exposure, approximately 30 min. Both the raw and corrected surface residual stress exhibit negligible change in the residual stress with increased exposure time after the initial change. However, the peak residual stress exhibited a continual reduction in compressive stress with increased exposure time. The raw surface residual stress overestimates the actual or corrected compressive residual stress on the surface for every exposure. Prevéy [21] has reported that the error between the raw and corrected surface residual stress was typically maximum at the surface. Therefore, any crack initiation predictions based on raw surface measurements will be nonconservative since they overestimate the actual compressive surface residual stress. In contrast, the raw surface residual stress measurement significantly underestimates the peak compressive residual stress in the depth. The peak compressive residual stress in the depth can retard crack growth and even stop small surface cracks from growing. In this case crack growth life predictions will be too conservative and the full benefit of residual stresses will not be incorporated into the life prediction. Clearly corrected and especially uncorrected (raw) surface residual stress measurements do not provide the capability for characterizing the relaxation of residual stress profiles, nor do they reflect the

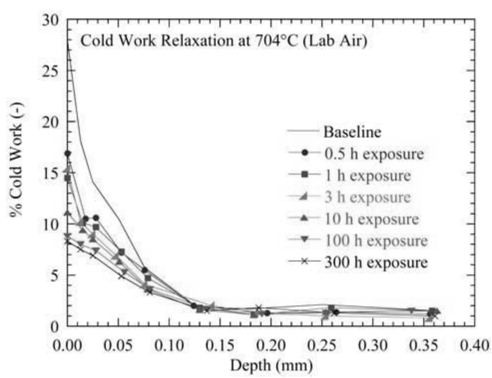

FIG. 10—*Cold work distributions in IN100 versus exposure time at 704°C.*

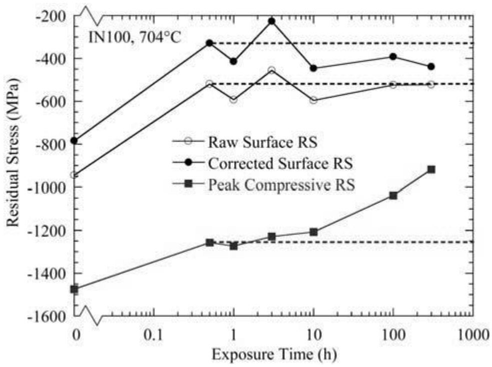

FIG. 11—*Surface and peak residual stresses with increasing exposure time at 704°C in IN100.*

same relaxation behavior of the peak compressive residual stress for the test conditions investigated in this study. Hence, raw surface measurements alone are no substitute for characterizing residual stress relaxation of residual stress depth profiles.

Discussion

The thermal residual stress relaxation depth profiles exhibited a rapid decrease with initial exposure that decreased with time. The relaxation rates and residual stress and cold work profiles were stress and temperature dependent. Surface residual stresses stabilized quickly, less than 1 h, whereas interior stresses continued to relax with increased exposure time. The difference in stress relaxation behavior between raw or corrected surface stresses and interior stresses precludes surface measurements as a single method for characterizing residual stress relaxation in shot peened materials with a stress gradient into the depth. The overestimate of beneficial compressive residual surface stresses resulting from raw surface measurements clearly provides a nonconservative estimate of crack initiation resistance. More importantly, without subsurface measurements the degree of nonconservatism cannot be determined. Also, surface measurements provided no indication of stress relaxation behavior of compressive stresses in the interior that occurred with increased exposure time. Clearly, XRD surface residual stress measurements alone do not properly characterize residual stress relaxation behavior for the test conditions in this study.

This difference in measured surface and peak residual stress relaxation behavior indicates that a simple scalar representation of residual stress alone is probably not sufficient for accurate modeling of the relaxation behavior of the entire depth profile. Full stress and plastic strain tensor information would be required to accurately model the complex relaxation behavior. The change in microstructure and material properties from shot peening, as a function of temperature and exposure time, contribute to the complexity of characterizing residual stress relaxation behavior.

Conclusions

This experimental investigation characterized the thermal residual stress relaxation of a powder metal IN100 superalloy. The shot peened samples were thermally exposed to two temperatures (650, 704°C) and a range of exposure times (0.5–300 h). The residual stresses exhibited an initial rapid relaxation on the surface and in the depth at both temperatures. However, continued thermal exposure produced little or no change in surface residual stresses while peak compressive stresses in the depth continued to relax with additional exposure time. After 300 h of exposure to 650 and 704°C residual stress retention was approximately 65 and 62 %, respectively. Comparisons of residual stress relaxation on the surface and in the depth demonstrated the inability of surface measurements to adequately characterize the relaxation behavior of the subsurface residual stress profile. In general, raw surface residual stress measurements are not a reliable method of characterizing residual stress relaxation, especially in the presence of subsurface stress gradients. Therefore, raw surface residual stress measurements alone should not be incorporated into a life prediction or life extension methodology to exploit the beneficial effects of compressive residual stresses on retardation of fatigue crack initiation and propagation when thermal residual stress relaxation is present. However, the results from this study do show that there is significant potential for taking credit, even if only partial, for shot peen residual stresses in life management of components.

Acknowledgments

This research was conducted at the Materials and Manufacturing Directorate, Air Force Research Laboratory (AFRL/MLLMN), Wright-Patterson Air Force Base, OH 45433-7817 under onsite contract number F33615-98-C-5214. The authors gratefully acknowledge the support of Dr. Leo Christodoulou of the Defense Advanced Research Projects Agency (DARPA) under DARPA orders M359-00 and M978-00. The thermal exposures and X-ray analysis were conducted at Lambda Research, Inc., of Cincinnati, OH under subcontract to the University of Dayton. The authors also acknowledge the SEM analysis of the shot peened samples by Dr. Kezhong Li and the finite element analysis by Dr. Steve Olson, both of the University of Dayton Research Institute.

References

[1] Scott, J. A., "The Influence of Processing and Metallurgical Factors on Fatigue," *Metal Fatigue: Theory and Design*, A. F. Madayag, Ed., John Wiley & Sons, Inc., New York, 1969.

[2] Jilia, R., Renzhi, W., and Xiangbin, L., "Investigation of Shot Peening Strengthening of René95 Powder Alloy," *Proceedings of the 6th International Conference on Shot Peening*, San Francisco, CA, 1996, pp. 338–347.

[3] Happ, M. B., Mourer, D. P., and Schmidt, R. L., "Residual Stress Analysis and LCF Test Results for Peened Bolt Hole and Dovetail Configurations," *Proceedings of ASM's Conference on Residual Stress—In Design, Process and Materials Selection*, W. B. Young, Ed., Cincinnati, OH, April 1987, pp. 127–136.

[4] Akber, J. A., Kyriacou, S., and El-Zafrany, A. M., "Effect of Shot Peening on the Fatigue Life of Axially Loaded Notched Components," *Proceedings of the 5th International Conference on Shot Peening*, Christ Church Oxford University, 1993, pp. 349–358.

[5] Gray, H., Wagner, L., and Lütjering, G., "Influence of Shot Peening Induced Surface Roughness, Residual Macrostresses and Dislocation Density on the Elevated Temperature HCF-properties of Ti Alloy," *Proceedings of the 3rd International Conference on Shot Peening*, H. Wohlfahrt, R. Kopp, and O. Vöhringer, Eds., Garmisch-Partenkirchen (FRG), 1987, pp. 447–457.

[6] Fuchs, H. O., "Approximate Analysis for Optimizing Prestress Treatments," *Analytical and Experimental Methods for Residual Stress Effects in Fatigue, ASTM STP 1004*, R. L. Champoux, J. H. Underwood, and J. A. Kapps, Eds., ASTM International, West Conshohocken, PA, 1988, pp. 13–20.

[7] Kyriacou, S., "Shot-peening Mechanics, A Theoretical Study," *Proceedings of the 6th International Conference on Shot Peening*, San Francisco, CA, 1996, pp. 505–516.

[8] Fathallah, R., Inglebert, G., and Castex, L., "Modeling of Shot Peening Residual Stresses and Plastic Deformation Induced in Metallic Parts," *Proceedings of the 6th International Conference on Shot Peening*, San Francisco, CA, 1996, pp. 464–473.

[9] Wohlfahrt, H., "A Model for Predicting Residual Stresses Produced by Shot Peening," *Proceedings of the European Conference on Residual Stresses*, E. Macherauch and V. Hauk, Eds., Translated from the German by Janet Mordike, Karlsruhe, 1983, pp. 347–364.

[10] Wusatowska-Sarnek, A. M., Blackburn, M. J., and Aindow, M., "Techniques for Microstructural Characterization of Powder-processed Nickel-based Superalloys," *Mater. Sci. Eng., A* 360, 2003, pp. 390–395.

[11] Wusatowska-Sarnek, A. M., Ghosh, G., Olson, G. B., Blackburn, M. J., and Aindow, M., "Characterization of the Microstructure and Phase Equilibria Calculations for the Powder Metallurgy Superalloy IN100," *J. Mater. Res.*, 18 (11), 2003, pp. 2653–2663.

[12] Hartman, G. A., Ashbaugh, N. E., and Buchanan, D. J., "A Sampling of Mechanical Test Automation Methodologies Used in a Basic Research Laboratory," *Automation in Fatigue and Fracture: Testing and Analysis, ASTM STP 1231*, C. Amzallag, Ed., ASTM International, West Conshohocken, PA,

1994, pp. 36–50.
[13] Prevéy, P., Hornbach, D., and Mason, P., "Thermal Residual Stress Relaxation and Distortion in Surface Enhanced Gas Turbine Engine Components," *Proceedings of the 17th Heat Treating Society Conference and Exposition and the 1st International Induction Heat Treating Symposium*, D. L. Milam et al., Eds., ASM Materials Park, OH, 1998, pp. 3–12.
[14] Prevéy, P., "The Effect of Cold Work on the Thermal Stability of Residual Compression in Surface Enhanced IN718," *Proceedings: 20th ASM Materials Solutions Conference and Exposition*, St. Louis, MO, October 10–12, 2000.
[15] *Shot Peening Applications*, 8th ed., Metal Improvement Company, Inc., a subsidiary of Curtiss-Wright Corporation, Paramus, NJ.
[16] Cao, W., Khadhraoui, M., Brenier, B., Guédou, J. Y., and Castex, L., "Thermomechanical Relaxation of Residual Stress in Shot Peened Nickel Base Superalloy," *Mater. Sci. Technol.*, Vol. 10, November 1994, pp. 947–954.
[17] Khadhraoui, M., Cao, W., Brenier, B., Castex, L., and Guédou, J. Y., "Experimental Investigation and Modeling of Relaxation Behavior of Shot Peening Residual Stresses at High Temperature for Nickel Base Superalloys," *Mater. Sci. Technol.*, Vol. 13, April 1997, pp. 360–367.
[18] Ahmad, J., Chandu, S., Kroupa, J., and Prevéy, P., "An Assessment of Residual Stresses Induced by Surface Treatments," *Proceedings of the 6th National Turbine Engine High Cycle Fatigue Conference*, HCF 2001, Jacksonville, FL, March 2001.
[19] Prevéy, P., "The Measurement of Subsurface Residual Stress and Cold Work Distributions in Nickel Base Alloys," *Proceedings of ASM's Conference on Residual Stress—In Design, Process and Materials Selection*, William B. Young, Ed., Cincinnati, OH, April 1987, pp. 11–19.
[20] Standard Test Method for Determining the Effective Elastic Parameter X-Ray Diffraction Measurements of Residual Stress, E 1426-98, Vol. 03.01, ASTM International, West Conshohocken, PA.
[21] Prevéy, P., "*X-ray Diffraction Residual Stress Techniques*," Metals Handbook, Metals Park: American Society for Metals, 1986, pp. 380–392.
[22] Residual Stress Measurement by X-Ray Diffraction, SAE J784a, M. E. Hilley, Ed., Soc. Auto. Eng., Warrendale, PA, Vol. 19, 1971.
[23] Moore, M. G., and Evans, W. P., "Mathematical Correction for Stress in Removed Layers in X-ray Diffraction Residual Stress Analysis," *SAE Trans.*, Vol. 66, 1958, pp. 340–345.
[24] Vukelich, S., Berkley, S., Russ, S., and Bradley, E. F., "Residual Stress Measurement and its Application to Achieve Predicted Full Life Potential of Low Cycle Fatigue (LCF) Engine Disks," The 9th International Symposium on Transport Phenomena and Dynamics of Rotating Machinery, Honolulu, Hawaii, February 2002.
[25] Vöhringer, O., "Relaxation of Residual Stresses," *Proceedings of the European Conference on Residual Stresses*, E. Macherauch and V. Hauk, Eds., Translated from German by Janet Mordike, Karlsruhe, 1983, pp. 47–80.
[26] Hoffman, J., Scholtes, B., Vöhringer, O., and Macherauch, E., "Thermal Relaxation of Shot Peened Residual Stresses in the Differently Heat Treated Plain Carbon Steel Ck 45," *Proceedings of the 3rd International Conference on Shot Peening*, H. Wohlfahrt, R. Kopp and O. Vöhringer, Eds., Garmisch-Partenkirchen (FRG), 1987, pp. 239–247.
[27] Schulze, V., Vöhringer, O., and Macherauch, E., "Thermal Relaxation of Shot Peened Residual Stresses in a Quenched and Tempered Steel 42 Cr Mo 4," *Proceedings of the 5th International Conference on Shot Peening*, Christ Church Oxford University, 1993, pp. 265–274.
[28] Standard Test Method for Verifying the Alignment of X-Ray Diffraction Instrumentation of Residual Stress Measurement, E 915-96, Vol. 03.01, ASTM International, West Conshohocken, PA.

Journal of ASTM International, May 2005, Vol. 2, No. 5
Paper ID JAI12558
Available online at www.astm.org

Hiroyuki Terada[1]

Stress Intensity Factor Analysis and Fatigue Behavior of a Crack in the Residual Stress Field of Welding

ABSTRACT: This paper deals with the behavior of a crack in the residual stress field induced by butt weld in a wide plate. It is known that the distribution pattern of residual stress is similar regardless of welding process, though the size and the magnitude of the residual stress depend largely on the welding process. Stress intensity factor and stress redistribution induced by the crack extension were calculated for a crack with arbitrary length and location. The stress redistributions caused by crack extension obtained by the present analysis showed good agreement with the experimental data. Fatigue crack propagation behavior in the residual stress field reported by Glinka was also examined from the ΔK point of view. In this paper, the effect of residual stress on the fatigue crack propagation rate is considered to be the effect of varying mean stress. The concept of ΔK_{eff}, where the effect of residual stress is accounted as the correction factor by the way of simple superposition, is shown to predict the crack growth rate with sufficient accuracy.

KEYWORDS: stress intensity factor analysis, crack, residual stress field, butt weld, stress re-distribution, fatigue crack, crack propagation, effective stress intensity factor

Introduction

The importance of the effects of residual stress on the fatigue and fracture strength of the welded joints of many machine parts and structural components has been recognized as well as that of material deteriorations by heat ingestion by welding. Consequently, many experimental studies on fatigue crack propagation behaviors or fracture strength and some analytical work have been carried out. References [1,2] list major summaries of this work. However, studies relating stress analysis and experimental results seems to be few [3,4], since the variation of residual stress or redistribution due to crack extension complicates the problem.

In the present paper, a stress analysis of a crack perpendicular to the welding bead in the residual stress field induced by butt weld in a wide plate was carried out using the Green function method. The distribution functions proposed by the author [5] and Tada and Paris [6], both of which satisfy all the physical requirements of the residual stress by welding were employed in the analysis. Concerning the residual stress to the welded structures, even if this stress relieves, it is impossible to remove the residual stress completely. And as a result, some residual stress, the distribution form of which is more or less similar to that of as welded, remains. Hence, the present results are also applicable to both the stress relieved joints and the as welded joints, either by gas tungsten arc welding, electron beam welding, or friction stir welding.

Manuscript received 27 July 2004; accepted for publication 2 November 2004; published May 2005. Presented at ASTM Symposium on Residual Stress Effects on Fatigue and Fracture Testing and Incorporation of Results into Design on 19-21 May 2004 in Salt Lake City, UT.

[1] Executive Director, Japan Aerospace Technology Foundation, c/o JAXA, 7-44-1, Jindaijihigashi, Chofu, Tokyo 182-8522, Japan.

Stress Intensity Factor Analysis

As for the distribution of the residual stress by welding, the author proposed the following equation to simulate σ_y [5] as shown in Fig. 1.

$$\sigma_y(x) = \sigma_0 e^{-0.5x^2}(1 - x^2) \tag{1}$$

where σ_0 is the maximum residual stress at welded center line.

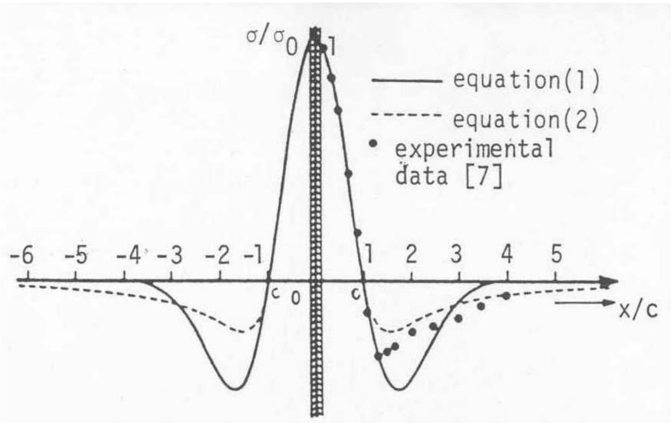

FIG. 1—*Residual stress distribution by welding and its assumed functions.*

Equation 1 satisfies all the physical requirements of residual stress which would be induced by butt weld of infinite plate [5]. Another equation satisfying those conditions was proposed by Tada and Paris [6] as shown by Eq 2.

$$\sigma_y(x) = \sigma_0(1 - x^2)/(1 + x^4) \tag{2}$$

The distribution of σ_y (x) is also shown by dashed line in Fig. 1. In Fig. 1, "c" is the characteristic length defined as the distance from the weld center line to the point where the residual stress changes its sign from tension to compression. Selection of the distribution function depends mainly on the observed form of compression side of residual stress distribution for each case. Residual stress distribution measured by Kanazawa et al. [7] is also presented in Fig. 1.

In this case, their experimental data of compressive stress region drop between the simulation curves given by Eqs 1 and 2. Once the distribution function is defined, the stress intensity factor K for a crack located in this field is calculated by Eq 3.

$$K\pm a = \frac{1}{\sqrt{\pi a}} \int_{-a}^{a} \sigma_y(\xi) \sqrt{\frac{a \pm \xi}{a \mp \xi}}\, d\xi \tag{3}$$

For a symmetric crack, stress intensity factor is evaluated by substituting Eq 1 or 2 into Eq 3. For the general case where the crack is eccentric to the welded line as shown in Fig. 2, the stress intensity factor is calculated by replacing x with (x + L) in σ_y equations [8].

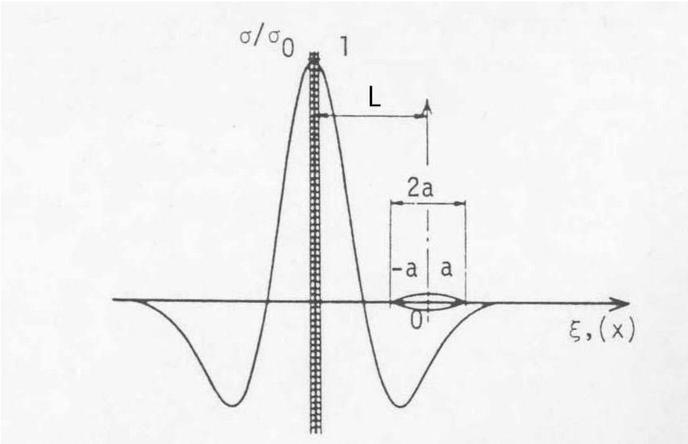

FIG. 2—*Eccentric crack in the residual stress field by welding.*

Here, L is the distance between the welded line and center of a crack normalized by the characteristic length defined by the length measured from the weld center line to the transition point (tension to compression) of original stress distribution. Evaluation of Eq 3 is conducted by using the following numerical integration formula [9].

$$\int_{-a}^{a} \sigma_y(\xi)\sqrt{\frac{a \pm \xi}{a \mp \xi}}\,d\xi = 2a\sum_{i=1}^{n} w_i \sigma_y(y_i) \tag{4}$$

where $y_i = \mp a(1-2x_i)$, $w_i = \dfrac{2\pi x_i}{2n+1}$, and $x_i = \cos^2\left(\dfrac{(2i-1)\pi}{2(2n+1)}\right)$.

As a matter of course, the existence of a crack in the residual stress field disturbs the original distribution patterns, as indicated by Eqs 1 or 2 in the vicinity of the crack. The redistributed stress normal to the crack line, $\sigma_{y,re}$ is calculated:

$$\sigma_{\mathrm{y,re}}(x) = \sigma_y(x) + \frac{a}{\pi\sqrt{x^2-a^2}}\int_{-a}^{a}\sigma_y(\xi)\left\{\frac{\sqrt{a^2-\xi^2}}{x-\xi} + \frac{\sqrt{a^2-\xi^2}}{x+\xi}\right\}d\xi \tag{5}$$

In the above equation, $\sigma_y(x)$ is the original residual stress distribution without a crack. Equation 5 is evaluated by following the numerical integration formula with sufficient accuracy for any crack length and eccentricity [10].

$$\int_{-a}^{a}\sigma_y(\xi)\frac{\sqrt{a^2-\xi^2}}{x \pm \xi}\,d\xi = a^2\sum_{i=1}^{n} w_i \frac{\sigma_y(at_i)}{x \pm at_i} \tag{6}$$

where, $t_i = \cos\frac{i\pi}{n+1}$, and $w_i = \frac{\pi}{n+1}\sin^2\left(\frac{i\pi}{n+1}\right)$.

Results and Discussion

Numerical Results of K and Stress Redistribution Analysis

The convergence of the numerical integrations of Eqs 4 and 6 is rapid for the wide range of crack size and eccentricity. Numerical results for the distribution function (Eq 1) converge faster than Eq 2. However, 10–20 terms of the polynomials of the numerical integration were sufficient to obtain the 5-figure accuracy for both functions.

As one of the calculation results, the relation of crack eccentricity and stress intensity factor of a crack with constant length is presented in Fig. 3.

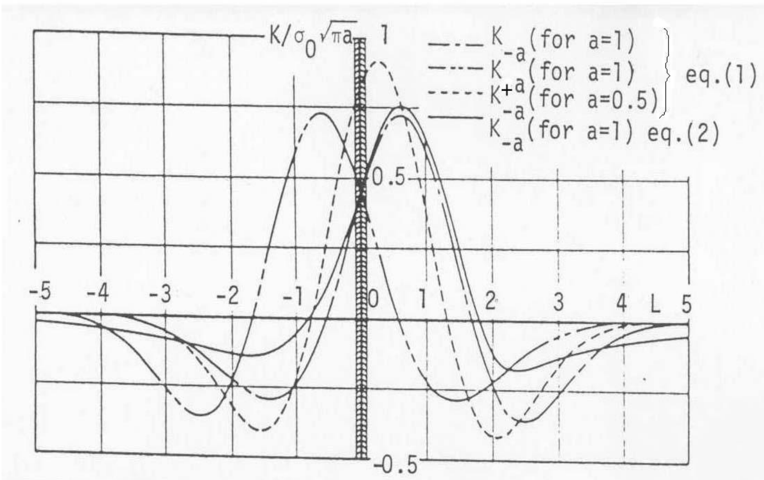

FIG. 3—*Effect of crack eccentricity on K (constant crack length).*

It should be noted that the maximum value is not obtained at L = 0 for the same crack size. The stress intensity factor becomes maximum when one of the crack tip has just crossed the welded line, namely, in that case the crack tip is surrounded by the higher stress of the original distribution. Stress intensity factor for a crack with various size and eccentricity are presented in Figs. 4 and 5 for distribution functions (Eqs 1 and 2), respectively. In Figs. 4 and 5, stress intensity factor K is defined by the following equation:

$$K = \sigma_0 \sqrt{\pi a}\, F_{res}$$

where F_{res} is the correction factor for residual stress.

The solid line indicates the stress intensity factor for the crack tip near the welded joint, while the dashed line corresponds to the remote side tip of the crack. Negative stress intensity factor becomes meaningful only when additional tensile loading other than residual stress is applied to the plate.

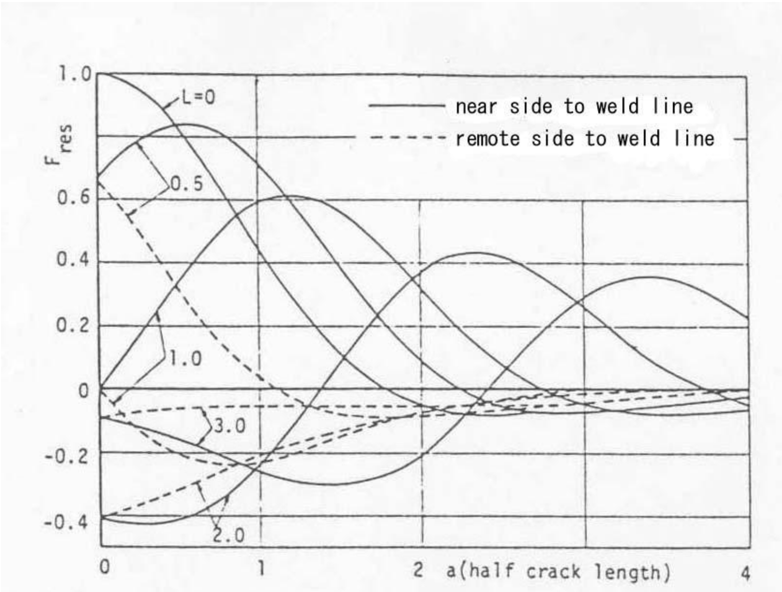

FIG. 4—*Relation of stress intensity factor, crack size, and eccentricity (Eq 1).*

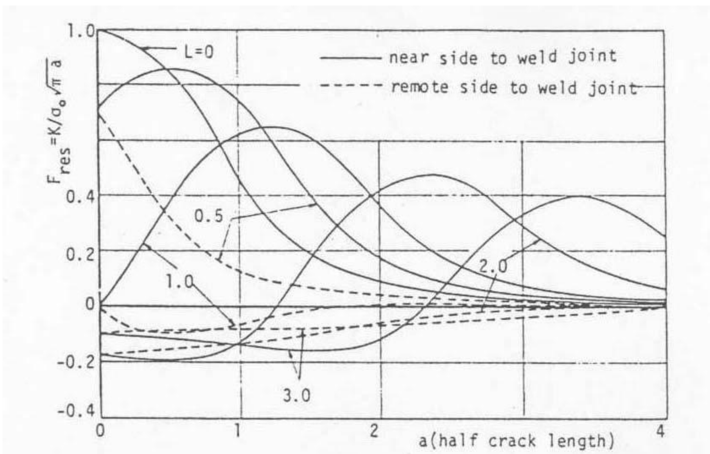

FIG. 5—*Relation of stress intensity factor, crack size, and eccentricity (Eq 2).*

An example demonstrating the effect of residual stress on the stress intensity factor for an extending crack with constant L is shown in Fig. 6. Stress intensity factor fluctuates as the crack extends across the welding line on account of residual stress, while in the case of absence of residual stress, it increases monotonically as indicated by the dashed line.

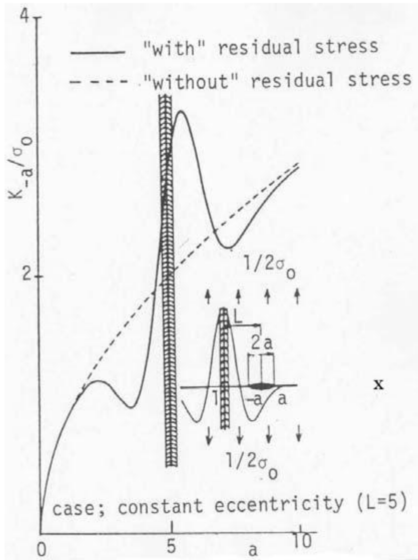

FIG. 6—*K for a crack approaching welded joint.*

Figures 7 and 8 demonstrate the redistribution form of $\sigma_{y,re}$ along the crack axis for a symmetric and an eccentric crack, evaluated for distribution function (Eq 2), respectively. In Figs. 7 and 8, λ is the crack length normalized by characteristic length "c". These results are obtained by numerical evaluation of Eq 5.

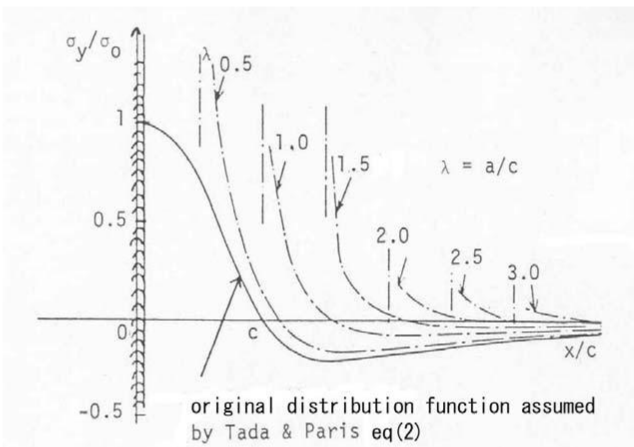

FIG. 7—*Crack extension and redistribution of σ_y (L = 0; symmetric crack).*

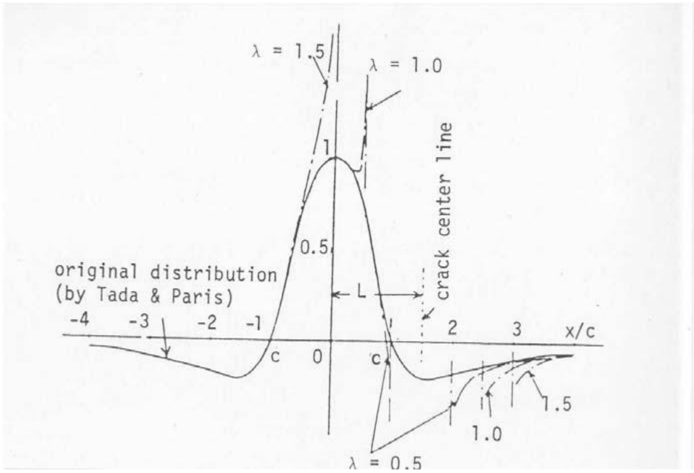

FIG. 8—*Crack extension and redistribution of* σ_y *(L=1.5; eccentric crack).*

The stress redistribution pattern for the symmetric crack in the residual stress field was observed by Kanazawa et al. [7]. Figure 9 shows the experimental results obtained by measuring the released strain with extending the saw cut [7]. Though the results presented in Fig. 7 are calculated for infinite plate, good correlation is observed with the experimental data.

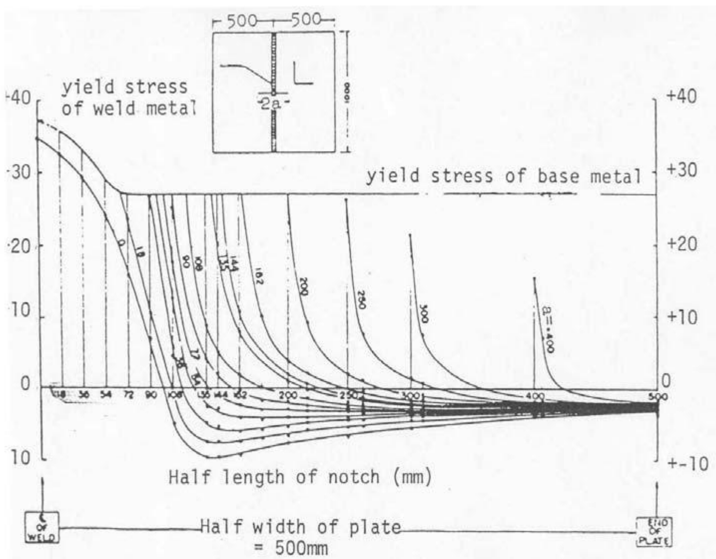

FIG. 9—*Effect of notch length on residual stress redistribution in notched specimen with longitudinal weldment [7].*

Effect of Residual Stress on Fatigue Crack Propagation

It is obvious that the residual tensile stress brings about unfavorable effect on fatigue crack propagation behavior as well as on fracture strength of the welded joints as might be anticipated from the results shown in Fig. 6.

In this study, the fatigue crack growth rate is considered primarily a function of ΔK. The effect of residual stress was accounted as a correction factor of ΔK in the following manner.

$$K_{eff} = \Delta K\left(1+\frac{\sigma_0}{\Delta\sigma}F_{res}\right), \text{ and } \Delta K = \Delta\sigma\sqrt{\pi a}\,F \tag{7}$$

where $\Delta\sigma$ is remotely applied fatigue stress, and F is the correction factor concerning the geometry of the cracked plate and is unity for an infinite plate.

Glinka [11] studied the fatigue crack growth rate of a symmetric crack perpendicular to the weld line. His results both for "with" and "without" residual stress are presented in Fig. 10, together with two prediction curves discussed by Nelson [3]. One of the predictions is based on the crack closure model. In Nelson's paper, the value of crack opening ratio "q" was directly referred from the results by Newman [12]. Crack closure model gives good estimation, but the results may greatly depend on the accuracy of the crack opening ratio q, and it is generally not easy to obtain the correct q for each material and testing. The singular points of the prediction curves by superposition approach, which might have arisen from the insufficient simulation of the residual stress, observed in Fig. 10, are also problematic because the stress distribution, and hence the stress intensity factor, has no singular properties as indicated in Figs. 3–5.

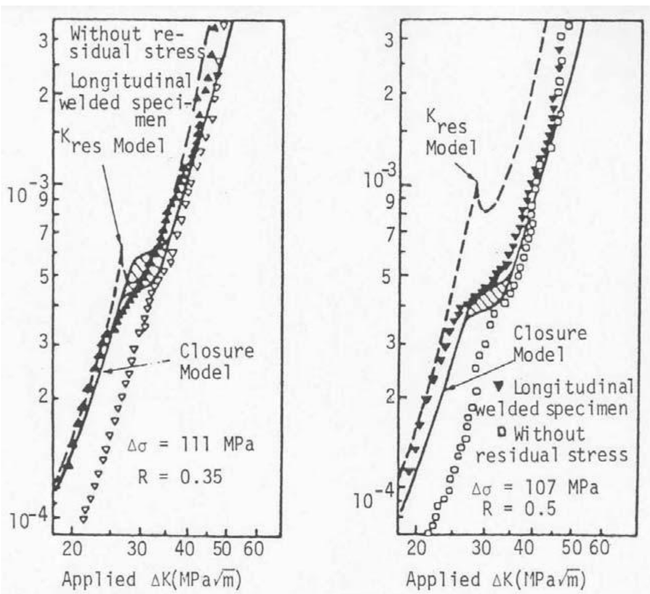

FIG. 10—*Comparison of crack growth rate predicted by a superposition approach and by a simple closure model with experimental data [11].*

In the present study, for simplicity, the author assumed the following Paris type equation for the experimental results given in Fig. 10, since the data corresponding to "without" residual stress can be simulated by straight lines in the log-log diagram for the range shown in the Figure.

$$\frac{d(2a)}{dn} = C\Delta K_{eff}{}^{\alpha} \tag{8}$$

Constants C and α in Eq 8 are determined from the experimental data of "without" residual stress (open symbols) in Fig. 10 as $C = 6.14\times10^{-11}$, and $\alpha = 4.5$ for $R = 0.5$, and $C = 1.36\times10^{-10}$ and $\alpha = 4.3$ for $R = 0.35$, respectively. In this case, ΔK_{eff} is read as ΔK because of no residual stress. The straight solid lines are those evaluated by using these constants. When we consider the effect of residual stress, we must evaluate ΔK_{eff} given by Eq 7. The residual stress distribution in this case is reported as Fig. 11 [12]. The maximum σ_y at weld center line, i.e., σ_0 (= 210 MPa) and the abscissa of transition point (x = 20 mm) were adopted to evaluate ΔK_{eff}. Equation 2 was used to calculate the correction factor for residual stress F_{res}. The results are presented by dashed curves in Fig. 12. These curves show good estimation of the effect of residual stress on the behavior of the fatigue crack propagation.

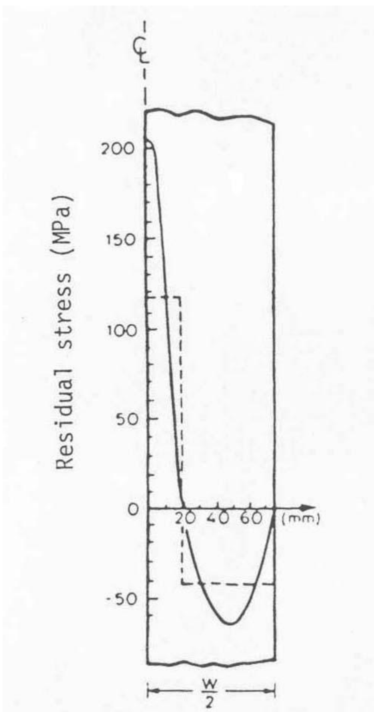

FIG. 11—*Residual stress distribution [11].*

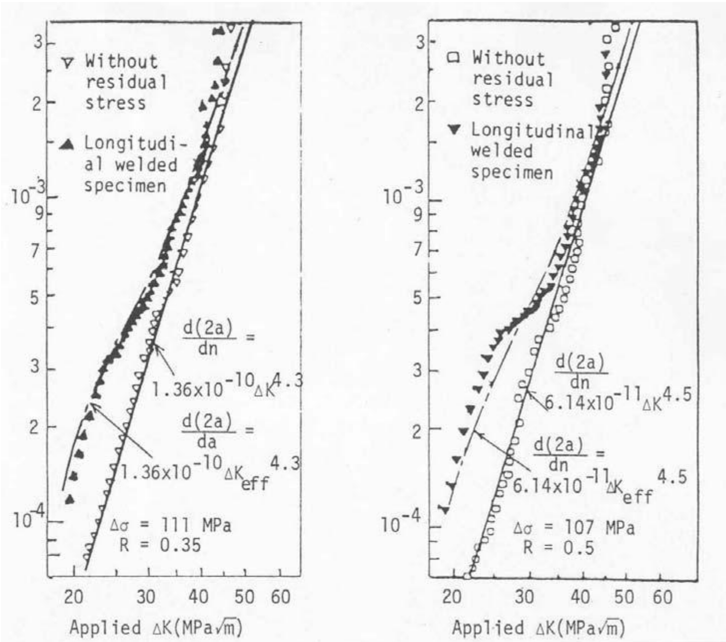

FIG. 12—*Comparison of crack growth rate estimated by present superposing method with experimental data [11].*

Concluding Remarks

Stress analysis was conducted on the crack perpendicular to the welding bead based on the Green function method. Initial stress distribution was assumed by simple closed form functions, which satisfy all the physical requirements peculiar to a butt welded joint in a wide plate. Those functions were proposed by the author and Tada and Paris independently. Stress analysis was carried out for these two functions.

Stress intensity factors for cracks with arbitrary size and eccentricity were calculated and presented in Figs. 3–5.

Existence and propagation of a crack disturb the original distribution form of residual stress in the vicinity of the crack. The stress redistribution was calculated and compared with the experimental results given by Kanazawa et al. The present results and experimental data showed good agreement.

By using the results of the present analysis, the effect of residual stress on the behavior of fatigue crack propagation was studied. Evaluation of fatigue crack growth rate of a crack perpendicular to the welded joints was conducted by the use of ΔK_{eff}, where the effect of residual stress is accounted as the correction factor to the conventional stress intensity factor range

$\Delta K\left(= \Delta\sigma\sqrt{\pi a}F\right)$. Estimation by ΔK_{eff} was compared with the experimental results obtained by Glinka, and present method was shown to give a good prediction.

References

[1] "Fatigue Testing of Weldments," *ASTM STP 648*, D. W. Hoeppner, Ed., 1978.
[2] "Residual Stress Effects in Fatigue," *ASTM STP 776*, J. F. Throop, and H. S. Reemsnyder, Eds., 1982.
[3] Nelson, D. V., "Effects of Residual Stress on Fatigue Crack Propagation," *ASTM STP 776*, 1982, pp. 172–188.
[4] Parker, A. P., "Discussion," to Ref. [3], *ASTM STP 776*, 1982, pp. 188–194.
[5] Terada, H., "An Analysis of the Stress Intensity Factor of a Crack Perpendicular to the Welding Bead," *Eng. Fract. Mech.*, Vol. 8, No.3, 1976, pp. 441–444.
[6] Tada, H. and Paris, P. C., "The Stress Intensity Factor for a Crack Perpendicular to the Welding Bead," *Int. J. Fracture*, Vol. 21, No. 2, 1983, pp. 279–284.
[7] Kanazawa, T., Oba, H., and Susei, S., "The Effect of Welding Residual Stress Upon Brittle Fracture Propagation (Rept. 2)," *Trans. Japan Soc. Naval Arch.*, No. 110, 1962, pp. 359–368.
[8] Terada, H. and Nakajima, T., "Analysis of Stress Intensity Factor of a Crack Approaching Welding Bead," *Int. J. Fracture*, Vol. 27, 1985, pp. 83–90.
[9] Abramowitz, M. and Stegun, A., "Handbook of Mathematical Function," Dover, Ed., 1954, p. 890.
[10] ibid., p. 889.
[11] Glinka, G., In: *Fracture Mechanics, ASTM STP 677*, 1979, pp. 198–212.
[12] Newman, J. C., Jr., "A Crack Closure Model for Predicting Fatigue Crack Growth Under Aircraft Spectrum Loading," NASA TM 81941, 1981.

Journal of ASTM International, September 2005, Vol. 2, No. 8
Paper ID JAI12546
Available online at www.astm.org

P. Prevéy[1] *and N. Jayaraman*[2]

A Design Methodology to Take Credit for Residual Stresses in Fatigue Limited Designs

ABSTRACT: High cycle fatigue (HCF) performance of turbine engine components has been known for decades to benefit from compressive surface residual stresses produced by shot peening. Recently laser shocking and low plasticity burnishing (LPB) have been shown to provide spectacular fatigue and damage tolerance improvement by introducing deep or through-thickness compression in fatigue critical areas. However, the lack of a comprehensive design method that defines the depth and magnitude of compression required to achieve a design fatigue life has prevented surface enhancement from being used for more than a safeguard against HCF damage initiation. The present paper describes a design methodology and testing protocol to allow credit to be taken for the beneficial compression introduced by surface enhancement in component design to achieve a required or optimal fatigue performance.
A detailed design method has been developed that relates the required fatigue life, the mean and alternating applied stresses, and the damage in terms of K_f to the residual stress at the fatigue initiation site required for the targeted HCF performance. The method is applied to feature specimens designed to simulate the fatigue conditions in the trailing edge of a first stage low pressure Ti-6-4 compressor vane to provide the optimal trailing edge damage tolerance. A novel adaptation of the traditional Haigh diagram to estimate the compressive residual stress magnitude for optimal fatigue performance is introduced. Fatigue results on blade-edge feature samples are compared with analytical predictions provided by the design methodology.

KEYWORDS: residual stress, design, Haigh diagram, fatigue, high cycle fatigue (HCF)

Introduction

Residual compressive stresses in metallic components have long been recognized [1–4] to enhance fatigue strength. Engineering components have been shot-peened or cold worked to create a surface layer of residual compressive stress with fatigue strength enhancement as the primary objective, or as a by-product of a surface hardening treatment like carburizing, nitriding, induction hardening, etc. Over the last decade, additional surface enhancement methods including LPB [5], laser shock peening (LSP) [6], and ultrasonic peening have emerged. These surface treatment methods have been shown to improve the fatigue performance of engineering components to different degrees.

LPB has been demonstrated to provide a deep (~1 mm) thermally and mechanically stable surface layer of high magnitude compression in various aluminum, titanium, and nickel based alloys and steels. Thermal and mechanical stability are obtained when compression is introduced with minimal cold working of the surface. A deep stable compressive residual stress state on the surface of these materials has been shown to be effective in mitigating fatigue damage due to foreign object damage (FOD) [7,8], fretting [9], corrosion fatigue [10], and corrosion pitting [11].

Manuscript received 20 April 2004; accepted for publication 8 March 2005; published September 2005. Presented at ASTM Symposium on Residual Stress Effects on Fatigue and Fracture Testing and Incorporation of Results into Design on 19-21 May 2004 in Salt Lake City, UT.
[1] President, Director of Research, Lambda Research, 5521 Fair Lane, Cincinnati, OH 45227.
[2] Director of Materials Research, Lambda Research, 5521 Fair Lane, Cincinnati, OH 45227.

Because the shallow layer of compression produced by shot peening is easily damaged and may not be retained in service, designers have used shot peening primarily for added safety and have not taken credit for the fatigue benefits in design methodology. In contrast, LPB and LSP produce thermally and mechanically stable compression over 1 mm deep, providing reliable mitigation of the fatigue debit of FOD, fretting, and corrosion pits. In high strength alloys, the original fatigue performance of the virgin material is achieved even in the presence of typical service generated defects. In the absence of compressive residual stresses, the allowable damage is generally limited to a fatigue notch sensitivity factor, k_f, on the order of 3. This design constraint leads to low allowable design stresses and hence much heavier sections.

Although mitigation of FOD, pitting, fretting, and corrosion damage has been demonstrated, a comprehensive approach to designing structures by taking specific design credit for surface compressive residual stresses has not been developed. Additional design factors including the compensatory tension necessary for equilibrium and distortion due to the introduction of residual compression into the structure must also be taken into account in this design process. This paper proposes a design approach suitable for structural alloys in high cycle fatigue and provides a specific case study of HCF behavior of Ti-6Al-4V feature specimens designed to simulate the stress conditions in an aircraft engine first stage compressor vane.

Stress-Life Analysis

The Haigh diagram [12], or constant fatigue life diagram, widely used to illustrate the effects of mean stresses on fatigue life, is shown in Fig. 1 as a map of the allowable stresses for a constant cyclic life in high cycle fatigue plotted as solid lines for a given alloy system. It is customary to plot the allowable alternating stress as the ordinate for a given mean stress on the abscissa, with the stress ratios $R = \sigma_{min}/\sigma_{max}$ shown as radial lines. The stress axes may be normalized with respect to the tensile strength of the material. The Haigh diagram, a convenient graphical representation to show the effects of mean stress, is usually prepared from experimental fatigue test results.

Effects of the notch fatigue sensitivity factor (k_f = unnotched σ_e / notched σ_e), where σ_e is the endurance limit or fatigue strength for a given life at R=-1, are also plotted as dotted lines in Fig. 1, again based upon experimental results. Although Haigh's fatigue tests included compressive mean stresses, the Haigh diagrams shown subsequently in the fatigue literature usually did not include the compressive mean stress range.

Fatigue life predictive models, including the Goodman, Gerber, and Soderberg constant life curves, can be plotted on the Haigh diagram as functions of alternating stress amplitude plotted against mean stress, as shown schematically in Fig. 2. Correspondingly,

$$\sigma_a = \sigma_e \{1 - \sigma_m / \sigma_{YS}\} \qquad \text{Soderberg} \qquad (1)$$

$$\sigma_a = \sigma_e \{1 - \sigma_m / \sigma_{UTS}\} \qquad \text{Goodman} \qquad (2)$$

$$\sigma_a = \sigma_e \{1 - (\sigma_m / \sigma_{UTS})^2\} \qquad \text{Gerber} \qquad (3)$$

where σ_a is the allowable alternating stress, σ_e is the fatigue strength at R ($\sigma_{min}/\sigma_{max}$) = -1, and σ_m is the mean stress at which the allowable alternating stress is to be determined. Thus, these predictive models give the allowable alternating stress for a predetermined cyclic life (say, 10^7 cycles) knowing only the fatigue strength in fully-reversed cyclic loading, the mean stress, and the yield or tensile strength of the material.

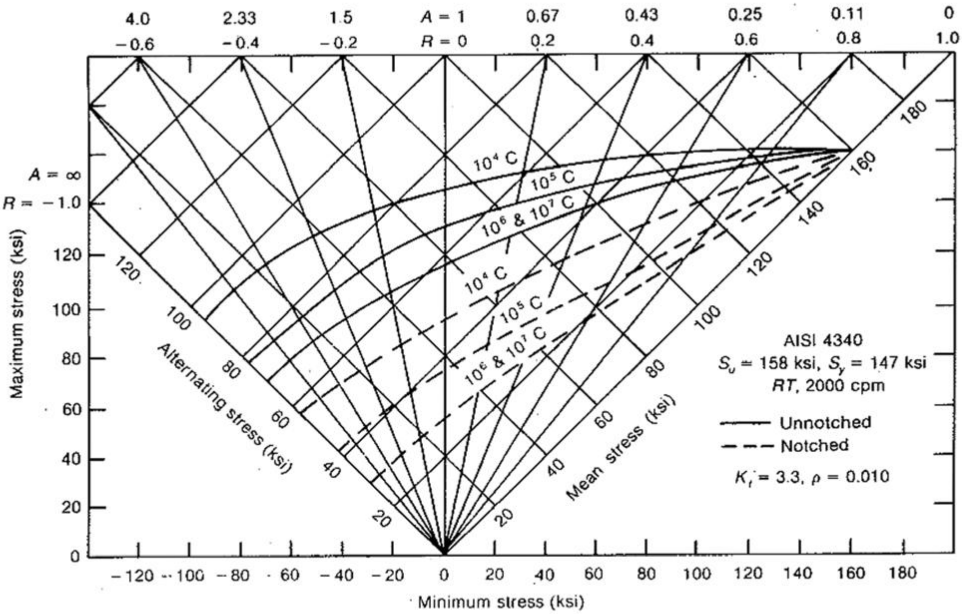

FIG. 1—*Haigh diagram for establishing influence of mean stress in fatigue for AISI 4340 steel for fatigue lives from 10^4 to 10^7 cycles, $k_f = 1$ and $k_f = 3.3$ [22].*

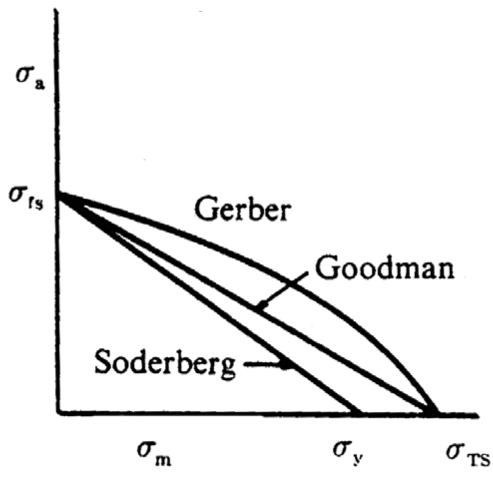

FIG. 2—C*onstant life curves for fatigue loading with nonzero mean stress [12].*

Early HCF experimental work attempted in the 1950s and 1960s with compressive mean stresses at R < -1 met with limited success primarily due to difficulties with specimen alignment when testing in compression [13–16]. Although test methods have improved, and perhaps due to the primary interest in tensile mean stresses in design, the literature contains few HCF data for high negative R suitable to extend the Haigh diagram into the compressive mean stress region. O'Conner and Morrison [13] constructed a Haigh diagram for an alloy steel, shown in Fig. 3, with a triangular bounding region to indicate the limits of applied alternating stress, for both tensile and compressive mean stress, up to the yield strength stress limits.

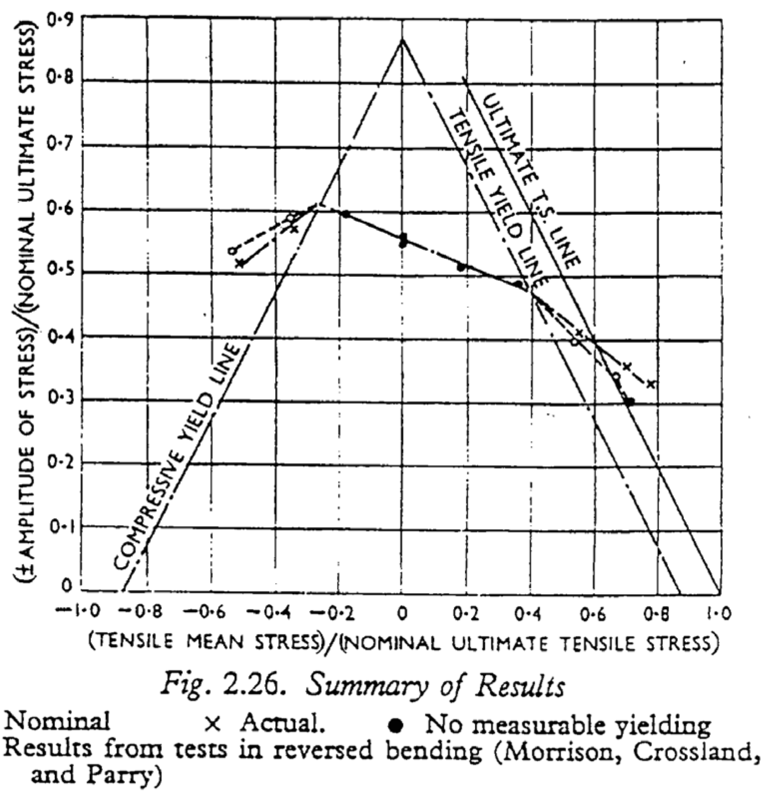

FIG. 3—*Haigh diagram for alloy steel showing yield strength limits in both tension and compression [13].*

Because of the limited availability of data for R < -1, Haigh diagrams are seldom used to predict the fatigue performance under compressive mean stresses. Engineering design approaches that include compressive mean stresses as part of the global structurally applied stresses are rare. Therefore, other than for academic curiosity, there has not been a serious need for fatigue predictions under compressive mean loads. The lack of reliable fatigue life prediction methods has further limited the ability to take credit for compressive residual stresses in design.

With the recognition of the fatigue improvement achievable with surface enhancement treatments, there is a need for predicting fatigue behavior with compressive mean stresses. In the following section, the application of a simple stress-strain function to unify available HCF data for different R-ratios and k_f values is developed. The resulting fatigue design diagram is a modified Haigh diagram extended to include compressive mean stresses. The proposed fatigue design diagram: (a) enables prediction of fatigue behavior in the presence of damage, (b) enables prediction of fatigue behavior in the presence of both damage and residual stresses, and (c) more importantly, provides a design guideline to determine the compressive residual stress magnitude needed to achieve a target damage tolerance. The fatigue design diagram provides a design tool to allow credit to be taken for residual compressive stress distributions in the design of fatigue critical components.

Model Development

Smith, Watson, and Topper [17] (SWT) suggested a single stress-strain function,

$$\sqrt{(\sigma_{max}\varepsilon_{alt}E)} = \text{constant} \tag{4}$$

to combine the effects of mean stress and alternating stress. They demonstrated that this function, when plotted against $\log(N_f)$, effectively unified the fatigue results for tensile and compressive mean stresses in SAE1015 steel, 2024-T4 Al alloy, SAE4340 steel, and 24S-T3 Al alloy. Assuming that elasticity conditions dominate high cycle fatigue (and therefore, $\varepsilon_{alt}E = \sigma_{alt}$,) Fuchs and Stephens [18] considered application of the stress function,

$$\sqrt{(\sigma_{max}\sigma_{alt})} = \text{constant} \tag{5}$$

in place of the stress-strain function in HCF. Additionally, the effect of notches can be included by considering the Neuber's rule expressed in terms of $k_f \leq k_t$ for the practical range of design where $1 < k_t < 4$,

$$\sigma\varepsilon = k_f^2 S_e \tag{6}$$

where σ and ε represent the notch root stress and strain, S and e represent the nominal stress and strain, and k_t is the tensile notch sensitivity factor. The combination of the stress function, $\sqrt{(\sigma_{max}\sigma_{alt})}$ and Neuber's rule in the essentially elastic HCF stress range leads to a new stress function

$$k_f\sqrt{(S_{max}S_{alt})} = \text{constant} \tag{7}$$

Since $S_{max} = S_{mean} + S_{alt}$, the unifying stress function including the notch effects can be written as

$$k_f^2(S_{mean} + S_{alt})S_{alt} = \text{constant} \tag{8}$$

In the limiting case of $k_f = 1$ and $S_{mean} = 0$, the stress function is simply S_e^2, where S_e is the nominal fatigue strength under fully-reversed cyclic loading (R = -1) conditions. Therefore,

$$k_f^2(S_{mean} + S_{alt})S_{alt} = S_e^2 \tag{9}$$

Based on the above analysis, it is possible to theoretically construct a series of Haigh diagrams for various k_f values, simply based upon a single fatigue strength value, S_e for the material. Further, the series of lines when plotted within the bounds of the yield strength triangle provides the engineering design limits. Fuchs and Stephens, when plotting this triangle, chose to use the cyclic yield stress for the maximum allowable alternating stress at the apex of the triangle. Because the allowable stress limits are much less than either yield strength in HCF limited designs, for the purposes of the present discussion, the difference between the yield limits is not significant, and the exact location of the yield boundaries are of interest only at extreme design limits.

The fatigue design diagram for Ti-6Al-4V is presented in Fig. 4 as a plot of S_{alt} versus S_{mean}, with the yield strength triangle indicating the elastic limits. Fatigue strength data from Aerospace

Structural Metals Handbook [19] for k_t ($\approx k_f$) values of 1 and 2.82 are plotted for R of –1, 0, and 0.5 in Fig. 5. The results from 4-point bending fatigue tests conducted at Lambda Research are also plotted. For the sake of reference, constant R lines for R = 0.1, R = -1 and R = -2 are also plotted.

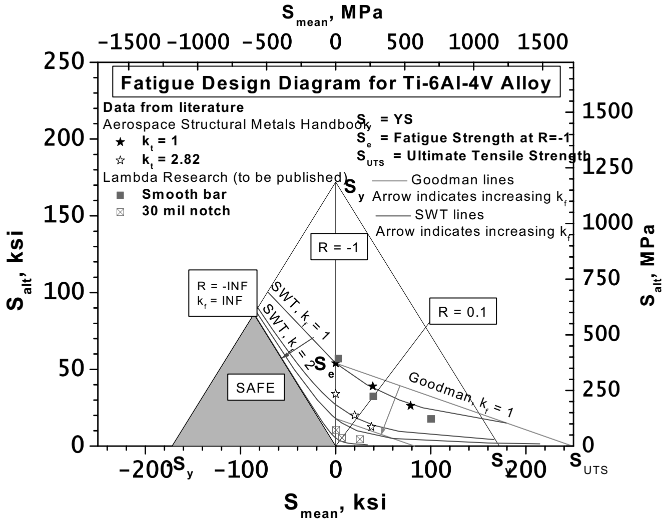

FIG. 4—*Fatigue design diagram for Ti-6Al-4V showing allowed alternating and mean stresses for* 10^7 *cycle life for different R-ratios and fatigue notch sensitivity factors* k_f.

Goodman lines for $k_f = 1$ and $k_f = 3$ were constructed using the endurance limit at R = -1 and true fracture strength value from the Aerospace Structural Metals Handbook [19]. Similarly, the modified SWT lines are plotted using the above equation and the single fatigue strength value, S_e at R of –1 for the smooth bar. The modified SWT line for $k_f = 2$ shows a substantial debit in fatigue performance. The lines for $k_f = 3$ and beyond practically converge in both the compressive and tensile mean stress regimes. For $k_f \geq 5$, and for the limiting notch condition (k_f approaching ∞), the modified SWT line coincides with R = $-\infty$ in the compressive mean stress region, and shows practically no allowable alternating stress in the tensile mean stress regime. In the region to the left of the R = $-\infty$ line, the part is entirely in compression throughout the loading cycle. If the assumption that fatigue damage and failure by crack propagation (mode I crack propagation) is not possible in the absence of a cyclic tensile stress component, then there exists a safe triangular region where no fatigue damage is possible. This triangular region is marked "SAFE" in the fatigue design diagram.

For the sake of completeness, additional data from ML and ASE[20] from the HCF annual Report Section 2.2 are shown in Fig. 5. As seen in this figure, there is general agreement between different sources of fatigue data in the mean stress regime corresponding to R ≥ 0, while in the mean stress regime with R < 0, there is some significant scatter in the data, and the modified SWT line is conservative, in that it under-predicts the fatigue strength.

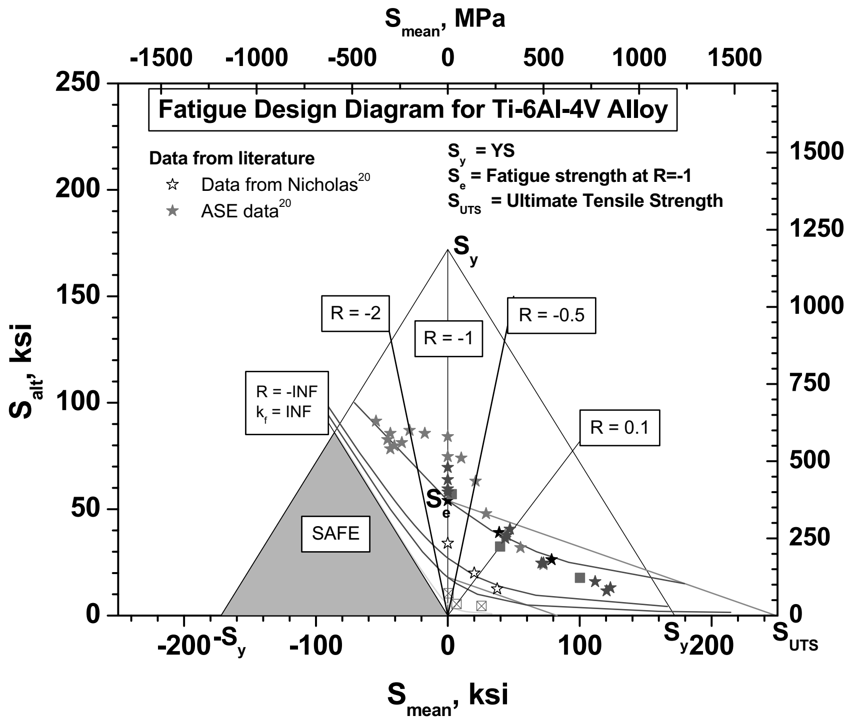

FIG. 5—*Same as Fig. 4, with the inclusion of additional experimental data (smooth bar results) from [20], showing reasonable agreement for* $R < -2$ *and* $R > -0.5$.

Prediction Method

In using this fatigue design diagram to estimate the allowable mean and alternating stresses, only the stresses in the region where fatigue damage initiates are of interest. For example, if fatigue damage initiation occurs at a corrosion pit, FOD, or other surface damage, the local stresses in the affected region are of interest, including the immediate sub-surface region. The knowledge of the applied stresses, R, and the depth of damage to be tolerated (and resulting k_f) are needed to determine the appropriate surface residual stress magnitude for a successful design. In the absence of a specified target depth of damage tolerance, the maximum possible damage tolerance may be assumed.

In this section, a hypothetical case is discussed with the help of a magnified section of the fatigue design diagram from Fig. 6*a*. Let us assume that the part is subjected to fatigue loading at an R = 0.1. The modified SWT line for $k_f = 1$ (no surface defects) predicts a nominal mean stress of 300 MPa (44 ksi) and a nominal alternating stress of 250 MPa (36 ksi) plotted as point A in Fig. 6*a*. In the presence of defects such that $k_f = 3$, these stresses drop to nominally 106 and 87 MPa (15.4 and 12.6 ksi), respectively, moving the allowed operating point to point B along the R = 0.1 line. In order to achieve full mitigation of the damage and restore the fatigue strength in the presence of the $k_f = 3$ conditions, the surface mean stress (residual plus applied) must be moved into higher compression along the k_f = 3 modified SWT line up to the point C. The difference in the mean stress of point C with respect to point B (i.e., the distance BD in Fig. 6*a*) represents the amount of surface compressive residual stress needed to fully mitigate the surface damage. This compressive residual stress magnitude is needed at the point of fatigue crack initiation at the bottom edge of the damage.

In a second example, consider a fatigue loading condition of R = -1. Under this condition, (Point A in Fig. 6*b*) the modified SWT line for k_f = 1 (smooth surface) predicts a S_{alt} of 370 MPa (54 ksi) with a zero mean stress. For the limiting FOD condition as k_f approaches infinity, corresponding to even a modest size crack or notch, the fatigue strength becomes negligible (Point B in Fig. 6*b*). In order to fully mitigate even this extreme condition, residual compression can be introduced into the surface at the depth of the FOD or crack tip sufficient to move along the $k_f = \infty$ modified SWT line to point C. Again, the difference in the mean stress of Point C with respect to Point B (i.e., the distance BD in Fig. 6*b*) represents the amount of surface compressive residual stress, nominally –400 MPa (-58 ksi), needed to fully restore the fatigue strength with the damage present. Again, this compressive residual stress must exist in the region covering the tip of the defect or crack from which fatigue cracks will originate.

Case Study of Mitigating FOD in Blade-Edge Simulation Feature Specimens

The following examples are taken from a study involving a HCF of blade-edge feature specimens designed to simulate the fatigue conditions experienced by the edge of a compressor vane in a turbine engine. Figures 7*a* and *b* show two specimen designs for HCF testing at R = 0.1 and –1, respectively, chosen to investigate the effect of stress ratio on HCF behavior. All HCF tests were run at room temperature in 4-point bending on a Sonntag SF-1U fatigue machine at 30 Hz with the specimens loaded in the hard-bending mode (edges, not sides, under maximum stress). FOD was simulated with electrical discharge machining (EDM) notches ranging from 0.25–2.5 mm (0.010–0.100 in.) deep machined into the edges of the specimens as shown in Figs. 7*a* and *b*.

The specimen edges were LPB treated to impart through-thickness compressive residual stresses. Residual stresses were measured by x-ray diffraction methods, and the residual stress distributions are plotted in Fig. 8. This figure shows the full residual stress map as a function of distance (chord-wise) from the edge of the specimen at the various depths indicated. Subsurface measurements were obtained by electrochemical polishing to remove layers up to the mid-thickness of the specimen before x-ray measurements, and the results were corrected for stress relaxation. The minimum compression occurs at mid-thickness, and fatigue failure initiated from this region. In Fig. 8, the residual stress results are shown spanning the LPB treated region and into the region of compensatory tension developed behind the LPB processed regions. The maximum compensatory tension of 220 MPa (~32 ksi) occurs in the mid plane of the specimen just behind the LPB processed region. Compensatory tensile stresses near the surface are lower. A discussion of the incorporation of compensatory tension into design is presented later in this paper.

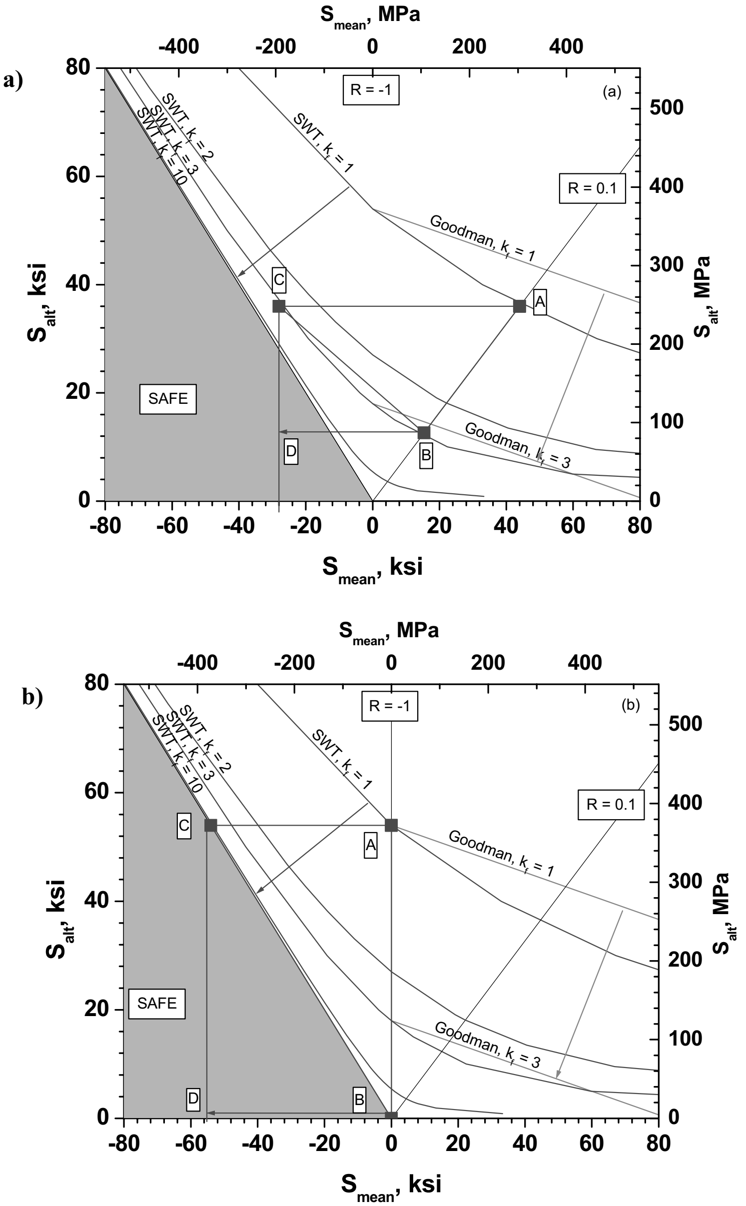

FIG. 6—*Magnified sections of the fatigue design diagram illustrating the fatigue design process with residual stresses in the presence of defects (FOD, pits, or cracks): (*a*) illustrates the effect of compressive stress (BD) to mitigate k_f = 3 for a fatigue condition of R = 0.1, and in (*b*) the effect of compressive stress (BD) to mitigate a k_f= ∞ is shown.*

a)

b)

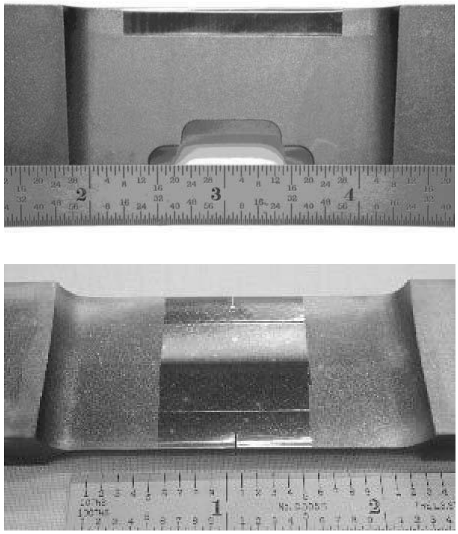

FIG. 7—(a) *Single Edge Blade (SEB) and (*b*) Double Edge Blade (DEB) feature specimens used for simulation of HCF damage in the trailing edge at R = 0.1 and –1, respectively.*

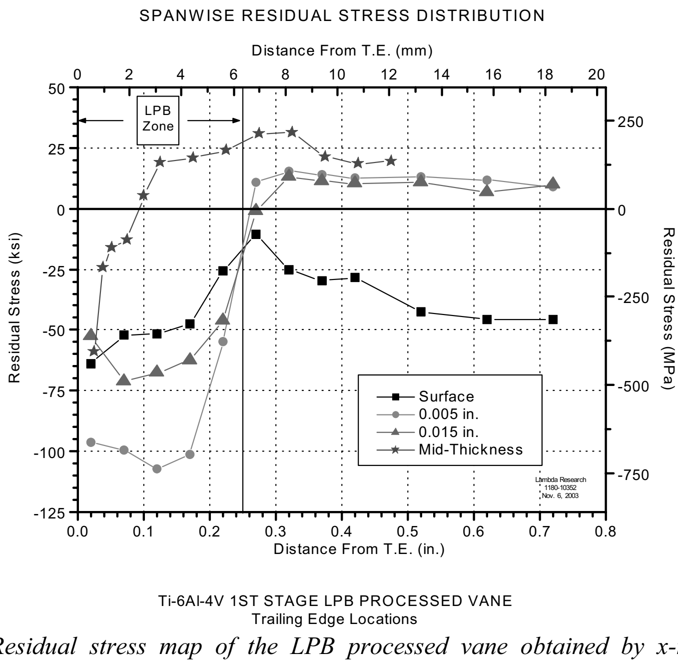

FIG. 8—*Residual stress map of the LPB processed vane obtained by x-ray diffraction measurements of the spanwise residual stress at various distances from the trailing edge and depths from the surface.*

The HCF test results are shown in Fig. 9 as S-N plots for both single-edge samples tested at R = 0.1 and double-edge samples tested at R = -1. Although HCF tests were performed for a variety of FOD depths, for the sake of brevity and clarity, only the results from FOD of 0.5 mm (0.020 in.) depth are presented. In the presence of 0.5 mm deep FOD, the baseline (untreated) fatigue strengths at R = 0.1 and –1 are nominally 70 and 105 MPa (10 and 15 ksi), respectively. As indicated in Fig. 9, none of the LPB treated specimens with 0.5 mm FOD tested at either stress ratio failed from the FOD. The fatigue performance of the LPB treated specimens was substantially better than the baseline specimens for either stress ratio and sample design, indicating that the LPB treatment largely mitigated the adverse effects of the 0.5 mm deep FOD. However, most of the specimens failed by sub-surface crack initiation from the mid-plane, or in regions of the specimen away from the FOD as shown in Figs. 10*a* and *b*. The variation in the depth and location of the fatigue initiation introduced scatter into the results, in spite of the presence of simulated FOD. Estimates of the 10^7 cycle fatigue strength corresponding to the two dominant failure modes (initiation from FOD versus sub-surface initiation), are shown as upper-bound and lower-bound S-N curves for the experimental data in Fig. 9. The fatigue strength for LPB treated specimens with a 0.5 mm (0.020 in.) FOD at R = 0.1 was estimated to be nominally 725 MPa (105 ksi), and at R = -1, nominally 380 MPa (55 ksi). The corresponding fatigue strengths for subsurface failure initiation are estimated to be nominally 480 and 310 MPa (70 and 45 ksi), respectively.

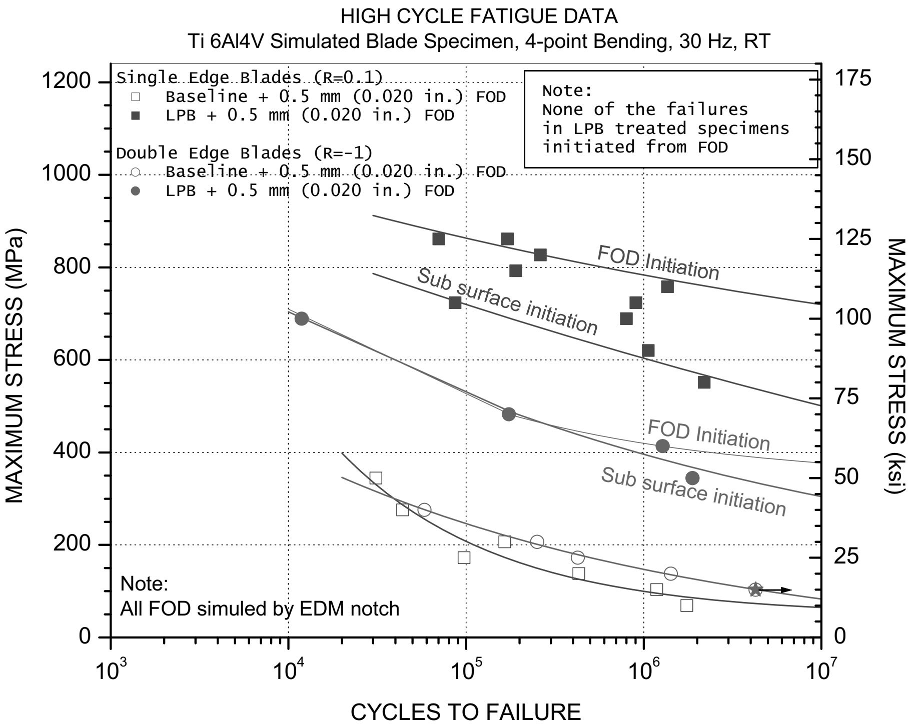

FIG. 9—*HCF test results for the blade edge simulation feature specimens.*

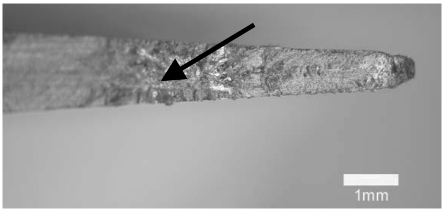

(a)

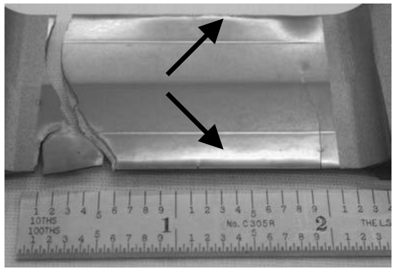

(b)

FIG. 10—*(*a*) Optical fractograph of a SEB feature specimen with LPB treatment showing crack initiation from sub surface regions (arrow). LPB + 0.5 mm (0.020 in) FOD, R = 0.1,* σ_{max} *= 690 MPa (100 ksi),* N_f *= 800 038 cycles. (*b*) Failure of a DEB feature specimen with LPB treatment showing initiation in a remote area in spite of the presence of 0.5 mm (0.020 in.) FOD (arrows) on both edges of the specimen, R = -1,* σ_{max} *= 480 MPa (70 ksi),* N_f *= 174 315 cycles.*

The baseline fatigue strengths, plotted on the fatigue design diagrams as Points B in Figs. 11*a* and 12*a*, correspond to nominal fatigue notch sensitivity factors, k_f, of 10 and 3.4, respectively. This difference in k_f for the same notch size may be attributed to the fatigue cycling conditions (tension-tension for R = 0.1, and tension-compression for R = -1). Now, given the least compressive residual stress of -413 MPa (-60 ksi) produced by LPB at mid-thickness and the 0.5 mm (0.020 in.) FOD depth, the points B can be translated to points C along the respective modified SWT lines. Positions C in Figs. 11*a* and 12*a* represent the actual stress state at the tip of the FOD. The allowed applied stresses are then given by the points E that represent the predicted fatigue performance of these specimens with the additional compressive residual stress indicated by the shift from B to D along the means stress axis. The measured fatigue strengths (from Fig. 9) of 725 MPa (105 ksi) for R = 0.1 and 380 MPa (55 ksi) for R = -1, in the absence of compensatory tension, are plotted in Figs. 11*a* and 12*a* as points F (Actual).

However, none of the LPB treated specimens actually failed from the EDM simulated FOD. The failures originated from sub-surface crack initiation at the depth where the compensatory tensile stresses were maximum. The fatigue strengths associated with this damage mechanism for R = 0.1 and R = -1 are estimated to be 480 MPa (70 ksi) and 310 MPa (45 ksi), respectively. When the maximum sub-surface compensatory tension at 220 MPa (32 ksi) at mid-thickness of the specimen is introduced into the fatigue design diagram analysis, the fatigue performance predictions are presented in Figs. 11*b* and 12*b*. Here, since there are no preexisting flaws from which the cracks initiate, the effective k_f is considered to be 1, and therefore the modified SWT line corresponding to a $k_f = 1$ was used for this analysis. Starting from the baseline positions of "B" in both Figs. 11*b* and 12*b*, and accounting for the mid-thickness compensatory tension of 220 MPa (32 ksi), corresponding to distance BD in Figs. 11*b* and 12*b*, the stress state is translated to positions C. Since the entire specimen is subjected to fatigue cycling at R of 0.1 and –1, the predicted fatigue strengths with the subsurface compensatory tension are marked by points E in Figs. 11*b* and 12*b*. Again, in both Figs. 11*b* and 12*b*, the corresponding measured fatigue strengths of 480 MPa (70 ksi) and 310 MPa (45 ksi) are also indicated by points F (Actual).

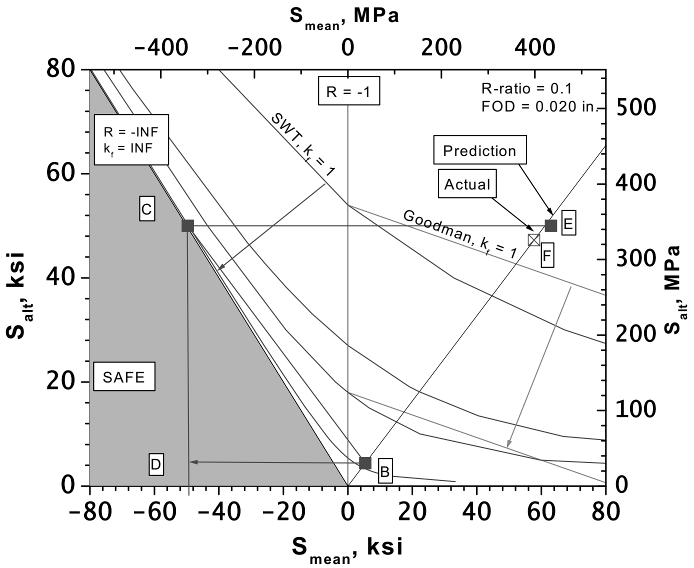

(a)

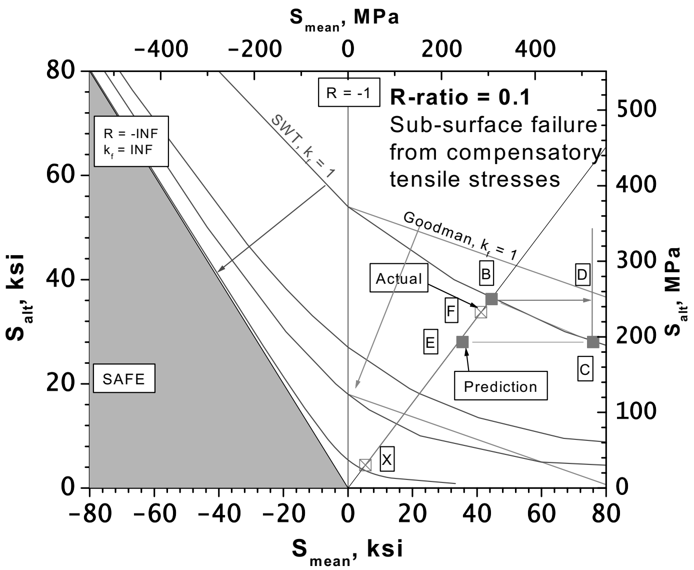

(b)

FIG. 11—*Validation of the design methodology for LPB treated specimens fatigue tested at an R-ratio of 0.1. The design analysis is performed (*a*) using in FOD initiated failure process and (*b*) using subsurface failure initiation process.*

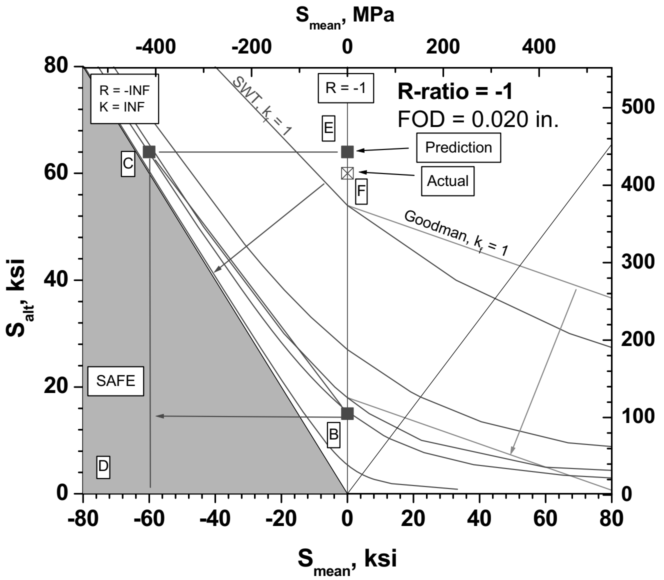

(a)

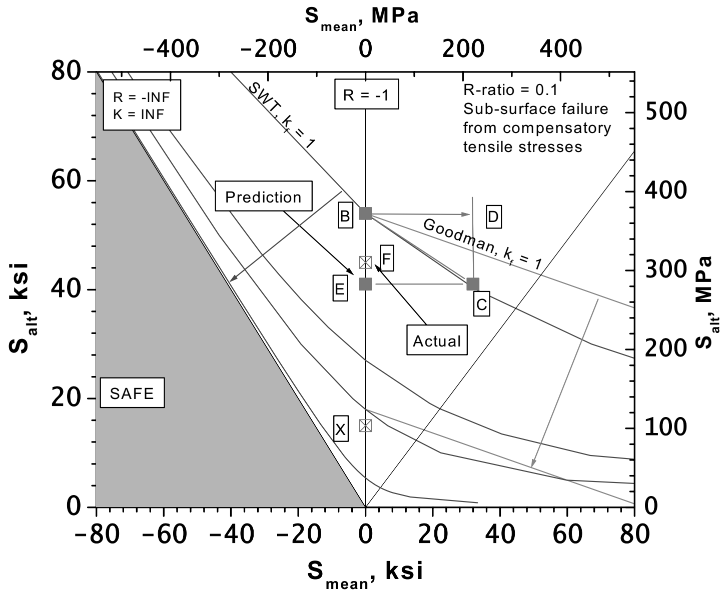

(b)

FIG. 12—*Validation of the design methodology for LPB treated specimens fatigue tested at an R-ratio for –1. The design analysis is performed (*a*) using in FOD initiated failure process and (*b*) using subsurface failure initiation process.*

It is evident from these figures that the predicted fatigue strengths are lower than the predictions from 11a and 12a. Therefore, the preferred failure mechanism is sub-surface crack initiation, as observed in testing. It is also evident that in the absence of the compressive residual stresses, the fatigue strengths would have been 10 ksi and 15 ksi, respectively, plotted as points X in Figures 11b and 12b. Even with sub-surface crack initiation from the region of maximum compensatory tension, the fatigue strengths of the specimens with LPB treatments were increased by a factor of 3 and 5 times for R = -1 and R = 0.1, respectively.

The differences between predictions and actual fatigue results are on the order of the accuracy of the underlying residual stress and fatigue data, and may be attributed to cumulative error in both the residual stress measurements and fatigue test data. Additional analyses of Ti-6Al-4V and other alloy systems are currently under way to further validate this predictive design procedure.

Summary and Conclusions

A fatigue design method based upon a modified SWT model for unifying fatigue data under various conditions of stress ratio, R, and fatigue notch sensitivity factor, k_f, have been developed [21]. A Fatigue Design Diagram (modified Haigh Diagram) has been developed defining the allowed alternating stress for given applied and residual mean stresses in both the net tensile and compressive mean stress regions. A series of modified SWT lines for various notch sensitivities, k_f, allows the prediction of safe zones. The fatigue design methodology allows the determination of the amount of residual compression that must be introduced into the surface at the depth of fatigue crack initiation to achieve optimum fatigue strength for a given damage state specified by the notch sensitivity, k_f. The method further allows the prediction of surface or subsurface fatigue initiation based upon the measured residual stress field. The proposed fatigue design methodology provides a means to incorporate surface compressive residual stresses imparted through various surface treatments like laser shock peening, low plasticity burnishing, etc., into component design for maximum fatigue benefit. The model has been validated through experimental results for Ti-6Al-4V for R = -1 and 0.1.

Acknowledgments

The authors wish to gratefully acknowledge constructive discussions and review provided by Dr. Gary Halford of NASA, Glenn Research Center, and Dr. Theodore Nicholas of the Air Force Institute of Technology, which have contributed to the development of this paper.

References

[1] Frost, N. E., Marsh, K. J., and Pook, L. P., *Metal Fatigue*, Oxford University Press, 1974.

[2] Fuchs, H. O. and Stephens, R. I., *Metal Fatigue In Engineering*, John Wiley & Sons, 1980.

[3] Berns, H. and Weber, L., "Influence of Residual Stresses on Crack Growth," *Impact Surface Treatment*, S.A. Meguid, Ed., Elsevier, 1984, pp. 33–44.

[4] Ferreira, J. A. M., Boorrego, L. F. P., and Costa, J. D. M., "Effects of Surface Treatments on the Fatigue of Notched Bend Specimens," *Fatigue, Fract. Engng. Mater., Struct.*, Vol. 19, No. 1, 1996, pp. 111–117.

[5] Prevéy, P. S., Telesman, J., Gabb, T., and Kantzos, P., "FOD Resistance and Fatigue Crack Arrest in Low Plasticity Burnished IN718," *Proceedings of the 5th National High Cycle Fatigue Conference*, Chandler, AZ, March 2000.

[6] Clauer, A. H., "Laser Shock Peening for Fatigue Resistance," *Surface Performance of Titanium*, J. K. Gregory, et al., Eds., TMS Warrendale, PA, 1996, pp. 217–230.

[7] Prevéy, P., Jayaraman, N., and Ravindranath, R., "Effect of Surface Treatments on HCF Performance and FOD Tolerance of a Ti-6Al-4V Vane," *Proceedings 8th National Turbine Engine HCF Conference*, Monterey, CA, April 2003.

[8] Prevéy, P. S., et al., "The Effect of Low Plasticity Burnishing (LPB) on the HCF Performance and FOD Resistance of Ti-6Al-4V," *Proceedings: 6th National Turbine Engine High Cycle Fatigue (HCF) Conference*, Jacksonville, FL, March 2001.

[9] Shepard, M., Prevéy, P., and Jayaraman, N., "Effect of Surface Treatments on Fretting Fatigue Performance of Ti-6Al-4V," submitted to *International Journal of Fatigue*.

[10] Jayaraman, N., Prevéy, P. S., and Mahoney, M., "Fatigue Life Improvement of an Aluminum Alloy FSW with Low Plasticity Burnishing," *Proceedings 132nd TMS Annual Meeting*, San Diego, CA, March 2003.

[11] Prevéy, P. S. and Cammett, J. T., "The Influence of Surface Enhancement by Low Plasticity Burnishing on the Corrosion Fatigue Performance of AA7075-T6," to appear in *International Journal of Fatigue*.

[12] Suresh, S., *Fatigue of Materials*, Cambridge University Press, 2001, pp. 226–227.

[13] O'Connor, H. C. and Morrison, J. L. M., *International Conference on Fatigue*, Institution of Mechanical Engineers, 1956, pp. 102–109.

[14] Woodward, A. R., Gunn, K. W., and Forrest, G., "The Effect of Mean Stress on the Fatigue of Aluminum Alloys," *International Conference on Fatigue*, Institution of Mechanical Engineers, 1956, pp. 158–170.

[15] Findley, W. N., "Experiments in Fatigue Under Ranges of Stress in Torsion and Axial Load from Tension to Extreme Compression," Vol. 54, ASTM International, West Conshohocken, PA, 1954, pp. 836–846.

[16] Howell, F. M. and Miller, J. L., "Axial-Stress Fatigue Strengths of Several Structural Aluminum Alloys," ASEM, Vol. 55, 1955, pp. 955–968.

[17] Smith, K. N., Watson, P., and Topper, T. H., "A Stress-Strain Function for the Fatigue of Metals," *Journal of Materials*, Vol. 5, No. 4, Dec. 1970, pp. 767–778.

[18] Fuchs, H. O. and Stephens, R. L., "Metal Fatigue," John Wiley & Sons, New York, 1980, p. 153.

[19] *Aerospace Structural Metals Handbook*, 3704.

[20] Nicholas, T. and Maxwell, D. C., "Mean Stress Effects on the High Cycle Fatigue Limit Stress in Ti-6Al-4V," *Fatigue and Fracture Mechanics: 33rd Vol., ASTM STP 1417*, W. G. Reuter and R. S. Piascik, Eds., ASTM International, West Conshohocken, PA, 2002.

[21] Patent pending.

[22] Dieter, *Mechanical Metallurgy*, MIL-HBDK-5, 3rd ed., U.S. Dept. of Defense, McGraw-Hill, Figure 12-9, 1986, p. 386.

Journal of ASTM International, March 2005, Vol. 2, No. 3
Paper ID JAI12565
Available online at www.astm.org

Alex S. Redner,[1] *Ennio Mognato,*[2] *and Matteo Schiavonato*[2]

Correlation Between Strength and Measured Residual Stress in Tempered Glass Products

ABSTRACT: U.S. and European Standards for strength and residual stresses in tempered glass are reviewed. Experimentally established correlation between the strength and nondestructively measured residual surface stress is demonstrated.

KEYWORDS: strength of glass residual stress, specifications of tempered glass

Introduction

Architectural and automotive glass manufacturing volume increased substantially in the last 20 years. The complexity of design and overall glazed surface easily explains the increase in automotive glass production volume. In the case of the building industry, even an untrained eye can easily observe the evolution of architectural concepts. A fully glazed curtain wall is now a commonplace appearance, emphasizing the most desirable aspects of glass selection: illumination of interiors combined with excellence of outdoor views, color, simplicity of shapes, and the ability to provide heat shielding.

Architectural glazing is subjected to complex loading, including dynamic pressure, thermal loading, impacts, and vibration. Failure of glass generally has dangerous consequences, and changes in glazing specifications were historically influenced by liability decisions, both in the United States and abroad.

One should notice the striking difference between the mechanical properties specification of metals or plastics and glass. In metallic structures, the strength of material is specified and used in the design of structures. Strength is considered as a material property, routinely tested and shown in product descriptions. In the case of glass, residual stresses are specified as the key parameter describing the expected material properties and strength. In metals and plastics, chemical composition and impurities are of prime concern and the maximum elongation or ductility are required properties. These parameters are not usually specified for glass. Moreover, the residual compressive stresses on the surface are of prime interest.

Tempering Process

In order to develop residual compressive stress on all surfaces, glass is subjected to the tempering process, consisting of:

Manuscript received 15 March 2004; accepted for publication 11 January 2005; published March 2005. Presented at ASTM Symposium on Residual Stress Effects on Fatigue and Fracture Testing and Incorporation of Results into Design on 19-21 May 2004 in Salt Lake City, UT.
[1] Strainoptic Technologies Inc., North Wales, PA 19454, USA.
[2] Stazione Sperimentale Del Vetro, Marghera, Venezia 30175, ITALY.

- Heating to a uniform temperature (approximately 650°C), bringing the surface to a viscous state,
- Fast quenching, using cold air jets.

During the quenching process, a severe temperature gradient develops and the surfaces of the glass cool faster than the midlayers. Once the material returns to room temperature, a parabolic residual stress distribution develops (shown in Fig. 1), with compressive stress (–) on surfaces and along edges, balanced by tensile stress (+) in the midplane.

The speed of cooling and the resulting temperature gradient near the surface determine the intensity of compression surface stresses. The residual surface stress must be kept within a narrow range and measured, to satisfy the material specifications.

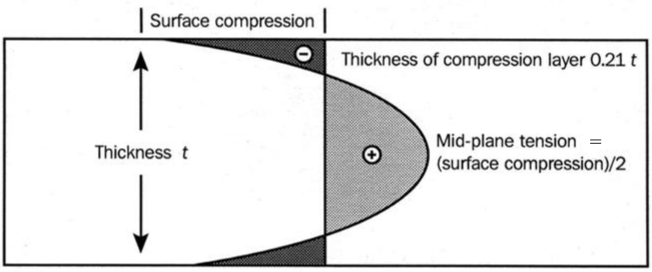

FIG. 1—*Stress distribution in tempered glass*.

Residual Stress and Strength of Tempered Glass

The strength of soda-lime flat glass produced in a continuous "float" process is measured using 4-point bending samples. The bending strength test is described in the ASTM Test Method C158[3] [1] practiced in the United States, and in an equivalent European Standard EN1288 [2].

In the Unites States and Europe, several grades of flat glass are separately defined and specified:

1. *"Annealed" Glass* emerging from the float process has very low residual stress. The range of bending strength of the float glass is 40–70 MPa as reported by several authors over a period of many years. The scatter of test results is significant, and a large number of samples are needed to obtain statistically valid results.
2. *Heat-Strengthened (HS) and Fully Tempered (FT) Glass*. The specifications for HS and FT glass are shown in Table 1. One can see the fundamental difference between the U.S. specifications ASTM C 1048 [3] based on residual surface stress, and the definitions based on strength and fragmentation incorporated in European Standards EN1863-1 [4] and EN12150-1 [5]. It is not possible to discuss the differences between these specifications without first establishing the correlation between the residual stresses and the strength. In fact, it is not possible to practice the Factory Production Control (FPC)

[3] The full title of all test methods referenced herein is shown at the end of this paper.

required by EN12150-2 [5] and EN1863-2 [4] without first developing the correlation, whenever FPC is based on compressive stress measurement.

3. *Safety Glass* is used for all glazing in the automotive industry and is also extensively used in buildings, in locations where glass breakage in large shards or particles could result in serious lacerations to people. Tempered glass and laminated glass offer the desired performance. It should also be noted that in Europe fully tempered glass must comply with the fragmentation test.

A theoretical derivation based on principles of fracture mechanics, published recently by Gulati [6], shows that particle size is related to midplane tension, and therefore, can be correlated to surface compression. Experimental correlations between residual surface stress and particle size were published by Jacob [7] and Joehlin [8]. Specifications for "safety" glass define the impacting tool, size of particles expressed as number of particles within a 50 mm × 50 mm square (typically used in the automotive industry and in European Standard EN12150-1 [5]), or maximum weight of 10 largest particles as defined by ANSI Z97.1 [10].

Particle size requirements are frequently changing. However, a correlation to tempered glass surface stress is excellent. Experimental work demonstrates that when residual surface stress exceeds 90–100 MPa (13 000–14 500 psi), particles will be sufficiently small to satisfy most safety glass classification requirements. Producers of tempered glass need to be concerned also with an excessive level of residual stress. While a large surface compression assures strength and particle size requirements, it is always combined with a large midplane tension. However, foreign particles or inclusions, if present within this tensile layer, can produce spontaneous fracture [11]. Also, excessive overheating can adversely affect the flatness and optical quality of glass.

The safety glass fragmentation test is a destructive test, involving an impactor, particle count, and documentation. This test is mandatory in European Standards. It is a costly procedure involving loss of material and judgmental interpretation. Quality control using surface stress measuring is a nondestructive process described in ASTM C 1279 [12], yielding quantitative nonsubjective results in minutes.

Correlation of Bending Strength and Residual Stresses on the Surface of Heat-Treated Glass

Table 1 provides a summary of U.S. and European Standards. There is some similarity between these specifications, and also some fundamental differences. ASTM C 1048 [3] directly requires the manufacturer to assure that the glass has the residual stress within a range, assuming that the strength is sufficiently increased to fulfill the needed design stress requirements.

In contrast, the European Standards EN1863-1 [4] and EN12150-1 [5] mandate a minimum bending strength together with fragmentation performance to ensure safety. Measuring bending strength is a lengthy and expensive process. The test requires a specimen size that is not the same as production sizes. The daily production test must be carried out using nondestructive surface stress measuring test associated with a fragmentation test on a sample with fixed dimensions. The correlation performed by the producing factory or an accredited laboratory is a burden on the manufacturer.

TABLE 1—*Strength and residual stress specifications for architectural soda lime glass.*

Standard Specification	Heat Strengthened Type HS Strength	Heat Strengthened Type HS Residual Stress	Fully Tempered Type FT Strength	Fully Tempered Type FT Residual Stress	Safety Fragmentation
ASTM C1048	2× stronger than annealed	24–52 Mpa (3500–7500 psi)	4× stronger than annealed	69 Mpa min. (10 000 psi min)	N/A
ANSI Z97.1					yes
EN 1863	70 Mpa min	Established by correlation			yes
EN 12150			120 Mpa min	Established by correlation	yes
EN 12600					yes

Correlation Between Residual Stress and Strength Using Experimental Data

The test data used to establish the correlation were obtained from tests conducted to certify products in accordance with European Standards.

An extensive experimental program was conducted at Stazione Sperimentale del Vetro located in Venice, Italy, aimed at establishing a correlation between the surface stress and the strength measured using the method described in EN1288-3 [2]. The stress measurements were collected from tests executed to certify products according to European Standards. Only data from samples that fulfilled fragmentation requirements were used. Strength measurements were performed using a Tiratest TT Universal testing machine, equipped with a 4-point bending fixture described in EN1288-3 [2]. All tests were conducted at room temperature 23 +/– 5°C and humidity levels ranging between 40 and 70 %.

Stress at rupture was calculated from the standard bending formula, corrected for the dead weight of the sample, as shown in Appendix 1.

Surface stresses were measured using a Grazing Angle Surface Polarimeter (GASP), manufactured by Strainoptic Technologies, Inc., and calibrated using a calibrated tempered glass sample. The location and number of points are specified in [3–5].

The test results were accumulated over a three-year period, using samples 360mm × 1100mm from 15 different production plants. The materials tested included both coated and uncoated glass, with the thickness ranging from 4 mm to 19 mm, satisfying HS and FT fragmentation classifications. Table 1 shows the strength requirements of these products.

Approximately 500 specimens were tested to evaluate conformity to EN12150-1 [5] and EN1863-1 [4].

The data presented in Figs. 2–4 include approximately 300 samples. Most of the tested items were fully tempered (FT), with approximately 80 samples falling in the heat strengthened (HS) range. We have also included samples that were not heat-treated, tested as received from the float-line process. Most of the samples had smooth-ground edges, without visible chips.

During the 4-point strength test, some fractures originated at edges, as opposed to the central region. It was noted that, for coated glass, the strength is affected by the position of the coated face (tensile or compressive). Figure 2 shows results from all 300 samples, including coated and uncoated glass, not segregated by origin of fracture. The influence of the coating is now under investigation, and will be published in the near future. To eliminate this variable, only clear float glass was included in Figs. 3 and 4.

Figure 3 illustrates the correlation between the strength and surface compression using the results of uncoated glass only, regardless of the fracture origin, while Fig. 4 shows only samples with fractures originating in the central region. The difference is not significant, but easily understandable, considering that the edges were not polished, and also that surface compression on edges was not measured. The increase in the Coefficient of Determination, R^2, shows a greatly improved correlation when data are validated correlating fracture to stress in the region where the stress is measured. We hope to include the edge compression correlation to edge fractures in future research.

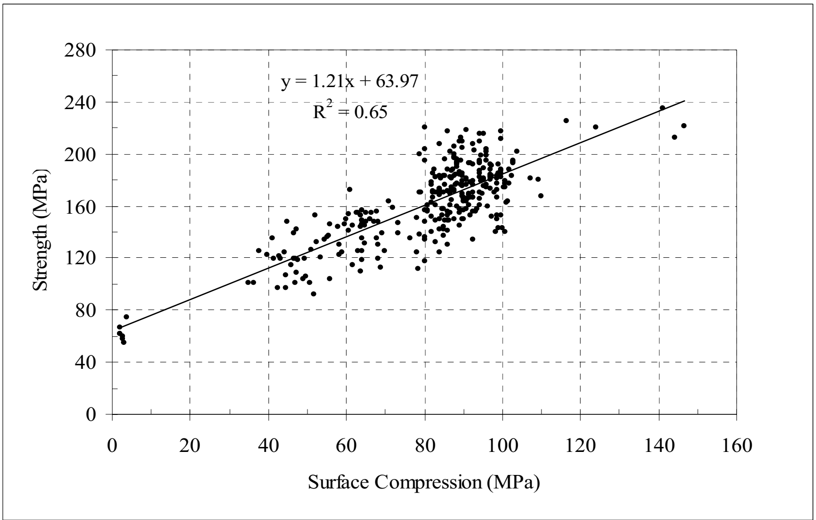

FIG. 2—*Bending strength versus residual surface stress, includes all samples.*

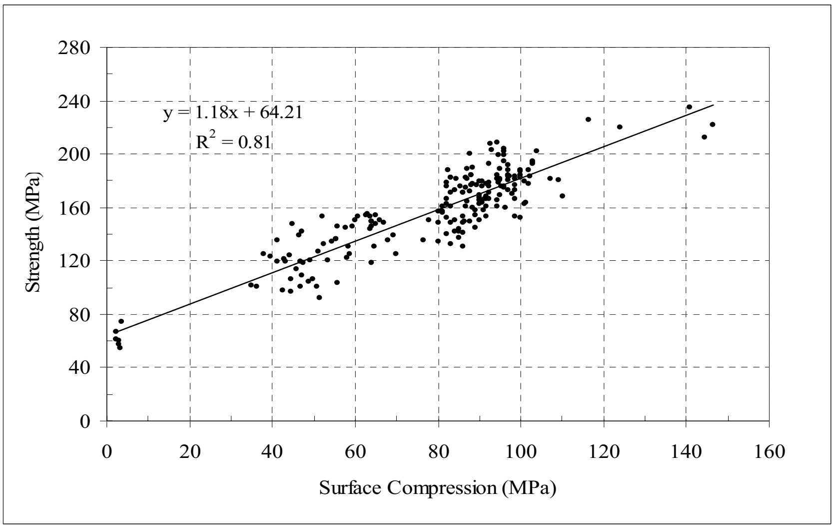

FIG. 3—*Bending strength versus residual surface stress, includes central and edge fractures, uncoated samples only.*

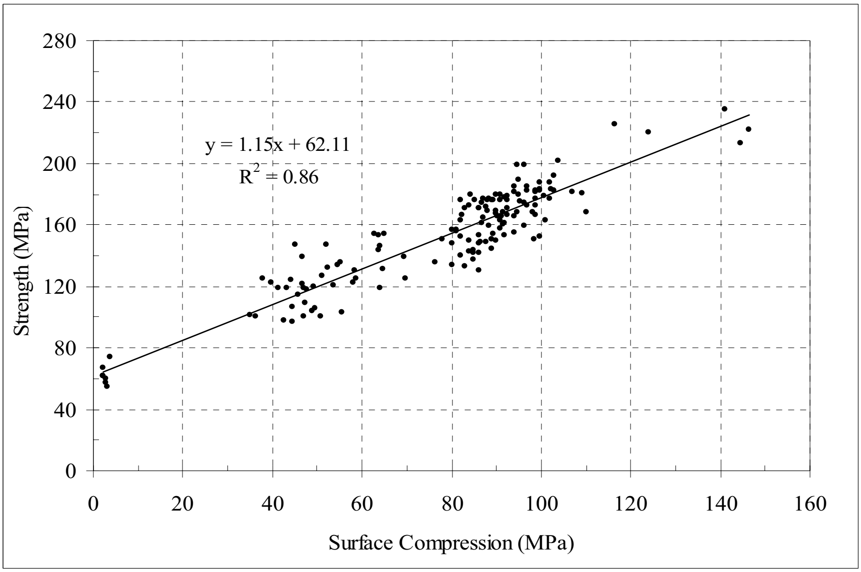

FIG. 4—*Bending strength versus residual surface stress, edge fractures excluded, uncoated samples only.*

Results and Conclusions

Residual Stress in Heat-Strengthened Glass (HS)

The Heat-Strengthened glass (HS) is defined in ASTM C 1048 [3] as "generally" twice as strong as annealed glass, heat treated to assure surface compressive residual stress between 24 and 52 MPa. In ASTM specification C 1048, the strength of annealed glass is not referenced or specifically stated. Extrapolating the strength (Figs. 2–4) to zero surface compression, the average strength of annealed glass is approximately 60 MPa (8700 psi) and the scatter of experimental data ranges between 50 and 75 MPa (7000 and 10 900 psi), well in agreement with generally accepted practices.

The increase in strength is shown in Figs. 2–4 to be proportional to the residual stress. A 24 MPa (3500 psi) surface compression will add approximately 1.18×24 (Fig. 3) to the strength, making a total strength of approximately 90 MPa, which is certainly insufficient to assure a strength that is "double" that of annealed glass. To assure the "double" strength (120 MPa), minimum surface compression of 50 MPa (7250 psi) is required.

The presently mandated level was set up to satisfy "stay in frame when broken" criteria, but no break pattern is mandated. Indeed, extensive research performed on 66 samples by Joehlin [8] demonstrated that there is NO RELIABLE CORRELATION between the surface stress and fragmentation pattern for stresses typically present in HS glass.

The European Standard EN1863-1 [4] defines the HS glass as a "material within which permanent residual stresses were induced, and exhibiting prescribed fracture characteristics." The residual stress level is not defined, but a minimum strength is set to be 70 MPa. Examination of Figs. 2–4 shows that the residual surface compression required to assure a 70

MPa (10 150 psi) strength is fairly low. In all samples that passed the conformance test (Fig. 2), the surface compression was equal or higher than 35 MPa (5000 psi). Since the EN1863-1 [4] standard also required a fragmentation test, setting up an upper limit of acceptable surface compression, a range of 35–60 MPa (5000–8200 psi) assures conformance with both strength and fragmentation requirements. This range is very close to the ASTM range of required surface stress.

Fully Tempered (FT) and Safety Glass

The differences between ASTM C 1048 [3] and EN12150-1 [5] specifications are significant. The fully tempered, or kind FT, is defined in C 1048 as "up to four times as strong as annealed glass," and also as having a minimum surface compression of 69 MPa (10 000 psi), or edge compression not less than 67 MPa (9600 psi).

An average examination of Figs. 2–4 suggests that the residual surface stress of 69 MPa (10 000 psi) will result in strength in excess of 140 MPa, which is approximately two times higher than annealed glass (higher than required by EN12150).

The ASTM C 1048 [3] specification also states that a glass meeting ANSI Z97.1 [10] or CPSC Safety Glass criteria will also meet the FT specifications.

The break pattern specified by ANSI Z97.1 [10] is based on a maximum weight of ten largest particles collected after the sample is shattered using a 100-lb punching bag. (This specification is presently in the process of revision.) Data from field-testing performed by producers demonstrate that the surface stress needed to assure the conformance with ANSI Z97.1 [10] specifications should be greater than 100 MPa. At this surface stress level, the strength exceeds 130 MPa, considering the data scatter.

The European Standard EN12150-1 [5] defines tempered glass as "thermally toughened soda-lime silicate safety glass within which a permanent stress has been included in order to increase its strength and prescribed fragmentation characteristics."

Fragmentation is defined by the number of fragments counted within a 50 mm × 50 mm mask, and the minimum number of particles is specified in Table 2.

TABLE 2—*Minimum count of particles in 50 × 50 mm area.*

Glass Type	Nominal Thickness mm	Minimum Particle Count
	3	15
Float and Drawn Sheet	4–12	40
	15–19	30
Patterned	4–10	30

Correlation between the number of particles and residual stresses was extensively studied in the past [7] [11]. The results of our test data confirm this information.

Mechanical strength required in EN12150-1 [5] is 120 MPa. In Figs. 2–4, it is easy to see that when the surface stress exceeds 85 MPa, all data points consistently show a strength that is higher than 120 MPa.

Although there is no upper strength or residual stress limit, excessively high tempering temperature will usually introduce higher residual stress and additional optical distortion. A surface compression between 85 and 100 MPa (12 300 and 14 500 psi) will satisfy both strength and fragmentation requirements.

General Conclusions

The research reported was based on a very large number of tested samples.
From the accumulated test data, it can be concluded that:

- The strength of heat-treated flat glass increases linearly as the surface stress increases.
- A general relationship between the bending strength of heat-treated glass and residual surface stress has a form:

(Bending Strength) = (Strength of annealed glass) + (C) × (Measured Surface Compression).

The experimentally demonstrated coefficient for float glass $C = 1.18$.

- The scatter of data points in Figs. 2–4 is greatly reduced when the results obtained from coated glass samples and edge-cracked samples are separated.
- In coated glasses, we have noted that mechanical strength depends on which surface is in tension, resulting in a substantial scatter (Fig. 2). In Fig. 3 we have plotted only uncoated float glass specimens, including both central and edge fracture origins. The fit quality R^2 becomes substantially better.
- The scatter and the quality of fit can be expressed by the **Coefficient of Determination** R^2. It represents the fraction of variability in y that can be explained by the variability in x. If the regression line perfectly fits all the observed data points, then $R^2 = 1.00$. Thus, R^2 is a relative measure of the "goodness" of fit of the observed data points to the regression line.
- In Fig. 4, the edge-cracked samples were not included. Here we obtain an excellent straight line fit. In this plot the edge-surface cracks are not influencing the data. To include edge strength, we must consider that the residual stress along the edge is uniaxial, while in the central region the residual surface stresses are biaxial in nature. Additional understanding of correlation between the edge fracture and the edge stress remains to be established.
- Strength can be reliably predicted from the measured surface residual compressive stress.
- The strength versus residual stress relation is independent of the thickness within the reported range, permitting substantial cost savings to producers, using nondestructive Factory Production Controls.
- Additional research is needed to correlate reliably edge-fracture to edge stress. This work is now in progress and the results will be reported in the near future.

Acknowledgments

The authors would like to acknowledge the contributions of G. I. Negri and F. Comiati to the successful completion of data acquisition and the test program.

References

[1] ASTM Standard C 158: Test Method for Strength of Glass by Flexure, *Annual Book of ASTM Standards*, Vol. 15.02, ASTM International, West Conshohocken, PA.
[2] EN1288, European Standard: Glass in Building—Determination of Bending Strength of

Glass, CEN, Rue de Stassart 36, Brussels B1050, Belgium.
[3] ASTM Standard C 1048-97b: Specification for Heat-Treated Flat Glass—Kind HS, Kind FT Coated, and Uncoated Glass, *Annual Book of ASTM Standards*, Vol. 15.02, ASTM International, West Conshohocken, PA.
[4] EN1863 European Standard: Glass in Building—Heat Strengthened Soda-Lime Silicate Glass (Part 1 and Part 2), CEN, Rue de Stassart 36, Brussels B1050, Belgium.
[5] EN12150 European Standard: Glass in Building—Thermally Toughened Soda-Lime Silicate Glass (Part 1 and Part 2), CEN, Rue de Stassart 36, Brussels B1050, Belgium.
[6] Gulati, S. T., "Frangibility of Tempered Soda-Lime Glass Sheet," *Proceedings*, *GPD*, Tampere, Finland, September 1997, pp. 72–76.
[7] Jacob, L., "Manufacturing Constraints, Performance Characteristics, Benefits and Limitations of Using Tempered Glass in Buildings," *Proceedings*, *GPD*, Tampere, Finland, June 2003, pp. 58–61.
[8] Joehlin, S. W., "Test Examine the Relationship of Break Pattern and Stress Levels in Heat-Strengthened and Tempered Glass," *Glass Magazine*, March 1999.
[9] EN12600 European Standard: Glass in Building-Pendulum Test and Impact Test Method and Classification of Float Glass, CEN, Rue de Stassart 36, Brussels B1050, Belgium.
[10] ANSI Z97.1: Safety Performance Specifications and Methods of Test for Safety Glazing Materials Used in Buildings, ANSI, 1819 L Street NW, Suite 600, Washington, D.C. 20036.
[11] Jacob, L., "A Critical Review of Impact Testing and Classifications of Safety Glass for Use in Buildings," *Proceedings*, *GPD*, June 2001, pp. 268–273.
[12] ASTM Standard C 1279: Test Method for Non-Destructive Photoelastic Measurement of Edge and Surface Stresses in Annealed, Heat Strengthened and Fully Tempered Flat Glass, *Annual Book of ASTM Standards*, Vol. 15.02, ASTM International, West Conshohocken, PA.

Appendix 1—Calculated Stresses for 4-Point Bending Fixture

The strength measurements were performed using a TIRATEST TT2750 Universal Dynamometer, using a four-bending fixture described in EN1288-3. The most important parameters are: the rate of increasing of bending stress, (2 ± 0.4 MPa/s), the geometry of test frame, and the environmental conditions (23 ± 5°C and 40 % ≤ RH ≤ 70 %). The stress at rupture was calculated from equations:

$$\sigma_{bB} = k\left[F_{\max} \cdot \frac{3 \cdot (L_s - L_b)}{2 \cdot B \cdot h^2} + \sigma_{bG}\right]$$

$L_b = (200 \pm 1)$ mm	distance between the upper supports
$L_s = (1000 \pm 2)$ mm	distance between the lower supports
$E = 70 \times 10^3$ N/mm^2	Elastic modulus
$\sigma_{bG} = \dfrac{3 \cdot \rho \cdot g \cdot L_s^2}{4 \cdot h}$	bending stress due to the weight of the specimen
$k = 1$	Central breakage (the origin of fracture is in a central part of specimen and in the part of glass between the upper supports).
$k \neq 1$	Edge breakage (the origin of fracture is on the edge and in the part of glass between the upper supports).

In this last case ($k \neq 1$), k depends on the deflection of the specimen at its center (y/h).

$$\frac{y}{h} = \frac{3 \cdot F_{\max}}{4 \cdot E \cdot B \cdot h^4} \cdot \left[\frac{L_s^3}{3} + \frac{L_b^3}{6} - \frac{L_s \cdot L_b^2}{2}\right]$$

The numerical value of k is obtained from a graph shown in EN1288-3.

Journal of ASTM International, January 2006, Vol. 3, No. 1
Paper ID JAI12551
Available online at: www.astm.org

Nathan J. Horn[1] *and Ralph I. Stephens* [2]

Influence of Cold Rolling Threads Before or After Heat Treatment on High Strength Bolts for Different Fatigue Preload Conditions

ABSTRACT: SI grade 12.9 high strength steel bolts were used to investigate the fatigue behavior of bolt threads rolled before/after heat treatment using two different thread profiles and two different high preload values. Bolts were 3/8 UNRC-16 (coarse) and 3/8 UNRF-24 (fine) and preloads were taken as 75 and 90 % of proof stress. Axial forces were applied through the nut. Axial and transverse residual stresses near the thread root were measured using X-ray diffraction. Most fracture surfaces contained crescent-shaped cracks and SEM evaluation indicated all fatigue crack growth regions contained multiple facets with no striations. Rolling after heat treatment caused little to no increase in fatigue resistance for the coarse threads. However, the fine threads finite fatigue life increased by factors of 2 to 5 and fatigue strengths based on S_a at 10^7 cycles increased by 40 and 50 % for the 90 and 75 % of proof stress preload, respectively. These are significant increases considering the very high preloads or R-ratios. The greater preload gave better fatigue resistance when based on the maximum stress, S_{max}, and lower fatigue resistance when based on the alternating stress, S_a. Based on S_{max}, fatigue strengths at 10^7 cycles for 90 % of preload were equivalent to or greater than the actual proof stress. S_{max} at 10^7 cycles for fine threads rolled after heat treatment with 75 % of proof stress was also greater than the actual proof stress. The above results can be attributed to different thread root radii, thread region smoothness, original residual stress from rolling after heat treatment, and residual stress relaxation from the high preloads.

KEYWORDS: Fatigue, Axial, Bolts, Preload, Residual Stress, High Mean Stress, High R-Ratio.

Introduction

Over the years, much research has been done to find ways to increase the fatigue performance of threaded fasteners. Some of these discoveries, however, resulted in an increase in the wear on tooling used in the manufacturing process. For example, it was shown that rolling the threads of a bolt after heat treatment increased the fatigue resistance by adding residual compressive stresses to the thread root [1]. However, the damage accrued by the die in the rolling process was greatly increased by rolling the harder metal. The increased wear on tooling,

---

Manuscript received April 5, 2004; accepted for publication Aug. 9, 2005; published Jan. 2006. Presented at ASTM Symposium on Residual Stress Effects on Fatigue and Fracture Testing and Incorporation of Results into Design: 19–20 May, 2004, Salt Lake City, UT.
[1] Research Assistant, Mechanical and Industrial Engineering Department, The University of Iowa, Iowa City, IA 52242. USA.
[2] Professor, Mechanical and Industrial Engineering Department, The University of Iowa, Iowa City, IA 52242, USA.

as well as increased production time, labor, and energy consumption resulted in a more expensive fastener. At the time the increased fatigue resistance was recognized, the small degree of preload typically used in bolt testing was not representative of the installation preload used at that time, and is even less representative of that used today. Researchers found that by tightening fasteners to a level that introduces significant local plastic deformation at the root of the thread, the scatter in clamping force in a bolted connection was significantly reduced [2].

The torque-turn method or what is sometimes referred to as the "torque-to-yield" method was introduced to create a more consistent clamping force. This method has almost entirely replaced tightening of a bolt to a specified torque value in fatigue critical bolted connections such as connecting rods. The torque-turn method began to be more readily used by American automotive manufacturers in the mid 1980s. It has been shown that there is little change in the fatigue resistance of the fastener compared to those tightened to a specified torque value. Using this tightening method that introduces preloads nearing gross plasticity across the section of the bolt, and the cyclic nature of the loading on the fastener, there is some ambiguity as to whether the beneficial residual compressive stresses gained by rolling the threads after heat treatment are relaxed. This relaxation, if it occurs, would result in the loss of the extra fatigue resistance sought by the introduction of residual stresses in the thread root.

The quantity of literature dealing with fatigue in axial loaded threaded fasteners is vast. Many sources were found with preload or mean stress influence and the benefits of residual compressive stresses, that result from rolling the threads onto the fastener after heat treatment rather than machining, grinding, or rolling threads before heat treatment [1–13]. Nearly all the literature indicated benefits from rolling threads after heat treatment were due to residual compressive stresses induced at the thread root. A few mentioned that benefits also come from the quality of the surface created by rolling threads after heat treatment. Contradictions on handling preload or mean stress in axial loaded threaded fasteners were common. For example, recommendations to use Soderberg, Modified Goodman, or Gerber models for mean stress implies the allowable alternating stress fatigue limit will depend on the mean stress. Others stated alternating stress fatigue limits are independent of mean stress. This later model appears to be more realistic for bolt threads rolled before heat treatment and is emphasized in the generic Haigh diagram for notched conditions [14] and Verein Deutscher Ingenieure, VDI, 2230 guidelines for SI grade 8.8 and above [3]. For SI grade 8.8 and above, VDI 2230 guidelines with threads rolled after heat treatment provide a quantitative equation that shows the alternating stress fatigue limit at low mean stress will be greater than that for roll before heat treatment, but this benefit will decrease in a linear manner as the mean stress approaches the yield strength, at which time all benefits from rolling after heat treatment will be eliminated. This brings out the important aspect of residual stress relaxation when gross yielding occurs in the threads. If this is in fact the case, the extra money spent on these methods of increasing residual stresses would be a waste.

An axial loaded bolt research program, of which the first portion is covered in this paper, is one proposed by Caterpillar (CAT) to quantify the amount of benefit gained by rolling threads after heat treatment compared to rolling the threads before heat treatment, as well as to determine if a preload exists at which the benefit deteriorates due to the relaxation of the residual stresses induced by rolling the threads after the heat treatment process. The bolt research program has been expanded and coordinated by the Society of Automotive Engineers Fatigue Design and Evaluation, SAEFDE, committee as part of its comprehensive high mean stress/R-ratio fatigue program [15]. The objectives of this research were/are to be evaluated by testing four different bolt series with two different thread profiles. Extensions of this research are being conducted at the University of Iowa and several other laboratories. The direct objectives of this portion of the study were to test the specimens monotonically, determine the proof loads of each bolt series, as well as generate eight stress-life (S-N) curves from testing at two preload values representative of those used in real life, in a fatigue situation. The intended preloads to be tested were 75 and 90 % of the proof stress of the bolt. These preloads were chosen based on experience of personnel at CAT as well as the experience of the authors of this paper. Throughout fatigue testing, cyclic creep/ratcheting was monitored and the fracture surfaces were examined macroscopically to solidify a qualitative understanding of the failure modes. Representative short and long life specimens were selected and evaluated macroscopically and microscopically using a Scanning Electron Microscope (SEM). These results were then used to more closely determine whether the mode of failure at these high preloads was fatigue and whether the mode of failure would change to fatigue combined with cyclic creep/ratcheting or just cyclic creep/ratcheting at higher loads. Following testing with two preload levels, and fractographic evaluation, the benefits of rolling threads after heat treatment compared to those rolled before heat treatment were qualitatively and quantitatively evaluated.

Bolt Material, Manufacturing, Thread Profile, K_t, and Residual Stress

The bolts tested in this research are categorized as SI grade 12.9. They were made of SAE 8640 alloy steel with the composition listed in Table 1. The SI grade was selected due to the increasing usage of metric bolts in the ground vehicle and aerospace industries. However, bolts with the Unified National Radius Coarse (UNRC) 3/8-16 and the Unified National Radius Fine (UNRF) 3/8-24 threads were chosen by the bolt manufacturer, based upon the availability of the machine and tools used to manufacture the bolts. The bolts tested in this study were Class 2A fasteners that specify the amount of tolerance deemed acceptable for the manufacturing of these bolts. All threads were cold rolled using reciprocating flat, free-roll dies. The nuts are categorized as a Hex Thick Grade 8+ Class 2B. These nuts were selected due to their common usage in applications associated with high strength bolts similar to the type being tested in this research.

TABLE 1—*Composition of 8640 Bolt material.*

C	Mn	P	S	Si	Ni	Cr	Mo	Cu
0.40	0.90	0.012	0.012	0.230	0.58	0.53	0.21	0.08

Sn	V	Al	N	B	Ti	Nb
0.001	0.001	0.023	0.0070	0.0007	0.003	0.001

Two different categories of bolts of each thread type were tested. One category was heat treated after the thread rolling process, and the other was heat treated prior to the thread rolling process. Many bolts are made by thread rolling before the heat treatment process. This is the norm unless the purchaser specifies the roll after heat treatment specifically. The cost for rolling threads after heat treatment is a 20–40 % increase over the bolts rolled before heat treatment. This increase in price is due to the increased labor, die wear, and cold rolling the under-head fillet. Rolling the under-head fillet is usually done on roll after heat treatment bolts because the roll after heat treatment threads are considered to have more fatigue resistant threads, and thus, the most fatigue critical region is often diverted to the under-head fillet [1]. For these roll after heat treatment bolts, the under-head fillet was shot-peened prior to rolling for greater convenience rather than cold rolled.

The root radii of each group of bolts were measured at two locations on one specimen from each group. The measurements were taken on two adjacent threads at a location near the center of the threaded section of the bolt. The average of the two values is contained in Table 2. The scatter of measurements within each group ranged from +/– 0.001 to +/– 0.004 mm. A photograph of two of the fine thread series are contained in Fig. 1 with Part (a) being the roll before heat treatment specimen and Part (b) the roll after heat treatment specimen (heat treatment has been abbreviated as HT). It is important to note the root radii of the roll after heat treatment specimens (Group 3 and 4) were in all cases 5 to 15% larger than that of the roll before heat treatment specimens (Groups 1 and 2). This resulted from a different set of dies being used to roll the threads of the bolts heat treated before the thread rolling process than was used on the threads of the bolts rolled before heat treatment. It must be noted that the root radii values for all of the bolts tested are within the standards set forth by the American Society of Mechanical Engineers for the minimum root radius [16].

TABLE 2—*Average root radii for each bolt group.*

	Average Root Radius (mm)
Group 1 (Coarse Roll Before HT)	0.195
Group 2 (Fine Roll Before HT)	0.159
Group 3 (Coarse Roll After HT)	0.226
Group 4 (Fine Roll After HT)	0.204

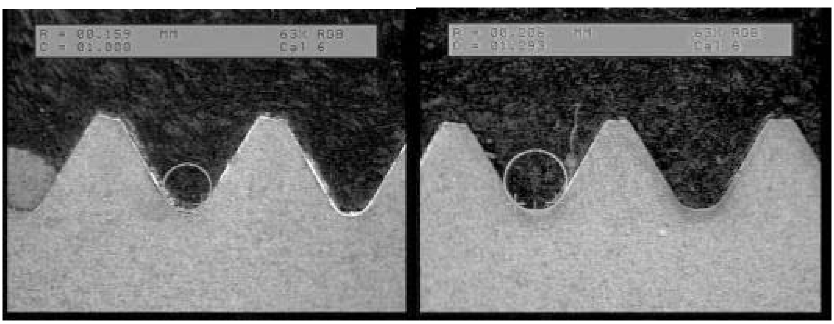

a) Roll Before HT b) Roll After HT

FIG. 1—*Thread root radius profiles, fine thread series (provided by John Deere Technical Center, Moline IL).*

Stress concentration differences resulting from the aforementioned difference in root radius are not easily quantified. An extensive 3D finite element analysis (FEA) would have to be conducted to determine the actual stress concentration effect on the bolts in this research. The complexity of the finite element work is difficult for many reasons commonly stated in the literature; most of these difficulties include nut/bolt interaction variation and their differences. Another is the extent of plasticity at the root of the notch, particularly at high preload values, that virtually eliminates the validity of placing much confidence in an elastic K_t value. It has been shown that bolted joint alterations such as a change in nut material and engaged thread length (thickness of nut), as well as amount of thread filling (depth of thread engagement), have significant effects on the stress concentration at the critical region studied in this research [17]. Even though it is recognized that the validity of an elastic K_t value is low, a simplified axis-symmetric FEA model was completed to get a general idea of the effect the geometry difference will have on the local stress/strain behavior in the bolt groups. It should be noted prior to reviewing the finite element analysis results that these are an approximation of geometric stress concentration effects only. The effects described by this FEA model should be comparable or conservative when compared to those acting at the root of the thread. The result of the FEA was a K_t value of 4.67 for the roll after heat treatment fine thread series (Group 4) while the roll before heat treatment fine thread series (Group 2) had a K_t of 4.23, a difference in stress concentration of approximately 10 % for the fine thread specimen.

Figure 2 shows the fine thread grain structure around the root of the thread. The altered grain flow at the root of the notch resulting from the cold working after heat treatment is visible, Fig. 2*b*, and much different than that of the roll before heat treatment specimens, Fig. 2*a*. The lack of grain flow on the roll before heat treatment specimens is what would be expected to result from the recrystallization of the material and the through depth heat treatment. This should relax the residual stresses from the cold rolling and eliminate the directional grain flow at the root of the notch. The coarse thread grain structure/flow was essentially the same as for the fine thread. Micro-hardness versus depth from the thread root converted to Rockwell C, *Rc*, hardness values are plotted versus depth from thread root in Fig. 3 for the fine thread series. The results show a slight increase in hardness toward the surface of the roll after heat treatment specimens, Fig. 3*b*, and are consistent with what would be expected for bolts with residual compressive stresses at the thread root. The solid lines at *Rc* = 40 are the average core hardness values. Similar results exist for the coarse thread series.

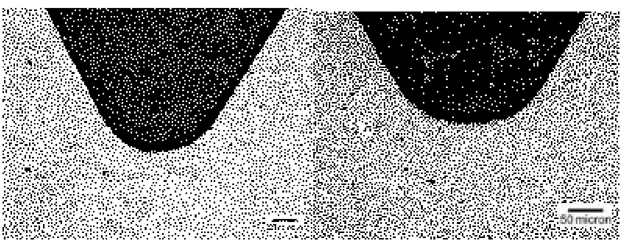

a) Roll Before HT b) Roll After HT

FIG. 2—*Grain flow micrographs, fine thread series (provided by John Deere Technical Center, Moline IL).*

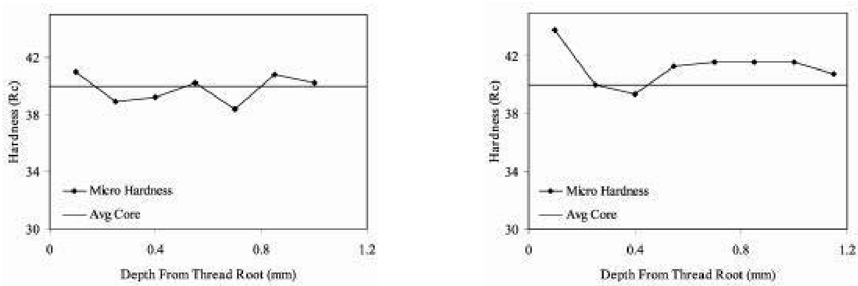

a) Roll Before HT b) Roll After HT

FIG. 3—*Hardness versus depth from the root of the thread, fine thread series, (Provided by John Deere Dubuque and Lake Erie Screw).*

Figure 4 contains plots of the axial and tangential residual stresses, Figs. 4*a* and 4*b* respectively, taken at the surface as well as two depths of 0.051 and 0.127 mm (0.002 and 0.005 in.) below the surface of the thread root for each series of bolt. An X-ray diffraction technique and electropolishing was used to obtain these values after the majority of the threads were machined off. The roll before heat treatment specimens (Groups 1 and 2) have essentially no residual stresses, which coincides with what is expected of a component recrystallized, quenched, and tempered after cold working. Also, note the axial surface residual stress on the coarse roll after heat treatment (Group 3) is slightly tensile, while at 0.05 mm the axial residual stress is about 250 MPa in compression. Rolling after heat treatment is performed primarily to increase the magnitude of the axial residual compressive stress that is expected to increase the fatigue resistance of the bolt. The bolt manufacturer had no explanation for this lack of residual compressive stress on the surface of the coarse roll after heat treatment fastener; however, the specimens were later found to contain thread laps that are considered detrimental to fatigue resistance. The fine thread series rolled after heat treatment (Group 4) had a surface residual compressive stress of 255 MPa, which is only 23 % of the proof stress. The tangential components of the residual stresses on the roll after bolts (Groups 3 and 4) were always compressive at the locations evaluated and were much larger in magnitude than the axial component, particularly for coarse rolled after heat treatment (Group 3).

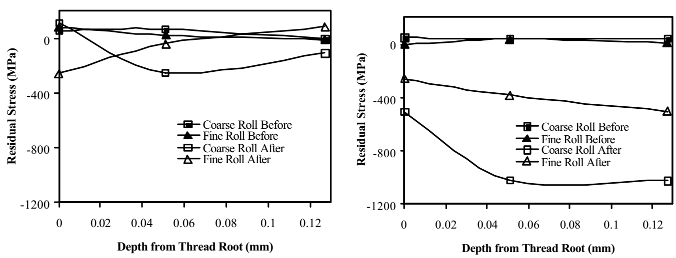

a) Axial Direction b) Transverse Direction

FIG. 4—*Residual stress versus depth from root of the thread (Provided by Ford Motor Company via Proto manufacturing Ltd.).*

Test Procedures and Monotonic Tension Results

Figure 5 shows the grip design used in this testing. The alloy selected for the body of the grips was SAE 8630. This alloy, in its annealed state, is relatively ductile, and fatigue resistant. Since the axial load was transferred through the nut, a high contact stress from the under-head surface of the bolt/nut was expected and a hardened tool steel insert was used to protect the body of the grips from this stress. The horizontal, 25.4-mm (1.0-in.) hole on the upper grip was incorporated to ease in the loading and unloading of each specimen. All testing was performed on a closed loop servo-hydraulic test system. Two types of room temperature testing were conducted in this research. First, monotonic testing needed to be conducted to determine the tensile properties of the bolts. The fatigue testing was conducted next using a percentage of the proof stress quantified in the monotonic tests as a constant minimum stress. All monotonic fractures occurred in the thread region away from the nut, while all fatigue fractures occurred at the first thread of the bolt/nut interface.

FIG. 5—*Photograph of grips used during testing*.

The fatigue testing conducted in this research was of constant amplitude sinusoidal waveform. Fatigue tests were conducted at a frequency of 30 Hz for short life specimens (lives expected to be less than 5×10^5 cycles) and 60 Hz for long life specimens (lives expected to be greater than 5×10^5 cycles). These values were used based on a study of the accuracy and frequency response of the test system at representative forces that was conducted at the beginning of this test program. Fatigue tests were terminated when fracture resulting in two pieces occurred, or at 10^7 cycles where run-out was assumed. All fatigue test data fell within 10^4 to 10^7 cycles. Stress-life plots were obtained by keeping the minimum stress constant at 75 or 90 % of the proof stress and varying the maximum stress, to obtain stress-life (S-N) plots. This constant preload testing is different than most fatigue testing that is usually conducted at a constant mean stress, or constant R-ratio. This method was utilized to depict more accurately the preloading that bolts will encounter in their typical applications. For constant amplitude loading, the R ratio is defined by Eq 1 with S_{min} and S_{max} representing the minimum and maximum applied stress, respectively.

$$R = \frac{S_{min}}{S_{max}} \quad (1)$$

The resultant average tensile properties from triplicate monotonic tensile tests for a given bolt group are contained in Table 3. The ultimate strengths and proof strengths were calculated using the tensile stress area, A_t, that is the same for both the ASME and SAE bolt standards [16, 18]. These converted values are 50.000 mm^2 and 56.645 mm^2 for the coarse and fine thread series, respectively. The average tensile proof stress from the roll before heat treatment monotonic tests was taken as 1100 MPa and was used to determine the preload or minimum stress used in all fatigue tests. However, the proof stresses for roll after heat treatment are closer to 1000 MPa indicating roll after heat treatment lowered the proof stress by about 10 %. The decision to base the preload as a percentage of 1100 MPa was made for better comparative continuity.

TABLE 3—*Average monotonic properties for each bolt group.*

	Group 1	Group 2	Group 3	Group 4
	Coarse Roll Before HT	Fine Roll Before HT	Coarse Roll After HT	Fine Roll After HT
S_{proof} (MPa)	1103	1082	996	974
S_u (MPa)	1277	1277	1306	1301

Two resultant monotonic force versus ram-displacement curves are shown in Fig. 6. The variability within each group was small (less than 5 %), except for the proof stress of Group 4 that had a larger variability on the scatter (about 9 %). The variability in the individual ultimate strength values was less than 2 % for all four-bolt groups. The average ultimate strength for each bolt group is about 1300 MPa indicating roll before/after heat treatment had little affect on the ultimate strength contrary to that for proof stress. All four-bolt groups satisfied minimum proof stress and ultimate strength requirements for SI 12.9 bolts, which are 970 and 1220 MPa respectively.

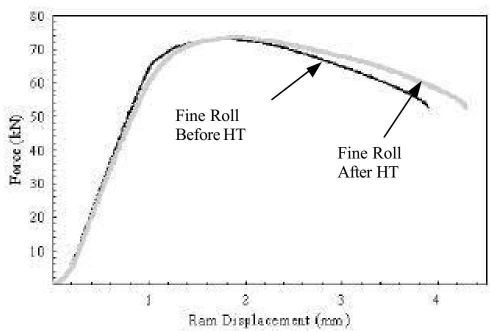

FIG. 6—*Representative monotonic force versus ram displacement curves for fine thread series rolled before and after heat treatment.*

There are many different aspects to compare, based on the amount of data generated in this research. Each of the following sections will describe the results on the basis stated in the title of the subsection. Each of the following selections of data are plotted on a semi-log scale. The best fit lines contained in the semi-log stress life plots were fit using a least squares regression power function.

Influence of Roll Before/After HT for 75 and 90 % S_{proof} for Coarse and Fine Threads

Experimental fatigue results from the tests conducted on the Unified National Rolled Coarse (UNRC) thread profile 3/8-16 for S_{min} equal to 75 and 90 % of S_{proof} are shown in Figs. 7*a* and 7*b*, respectively. In these figures the stress amplitude is located on the left vertical axis and the maximum stress is on the right vertical axis. In each of these figures, on the right hand axes S_p locates the reference 1100 MPa proof stress. The two curves in each of Figs. 7*a* and 7*b* converge at long life and are interpreted as no benefit from rolling coarse threads after heat treatment at long life. In the finite life region (less than 10^6 cycles) the roll after HT fatigue lives have up to about a factor of 2 increase in life, which is considered a small difference.

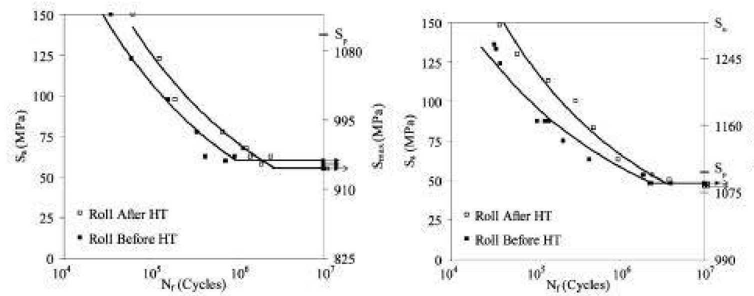

a) 75% of Proof Preload b) 90% of Proof Preload

FIG. 7—*Influence of roll before/after HT, coarse thread series.*

Experimental fatigue results for the Unified National Rolled Fine (UNRF) thread profile 3/8–24 are shown in Figs. 8*a* and 8*b* for 75 and 90 % preload, respectively. Note on these plots the increased fatigue resistance at all lives for the roll after HT. This includes run-outs at 10^7 cycles and the finite life region where increases in fatigue life range from factors of 2 to 5. The fatigue strengths of both coarse and fine threads at 10^7 cycles based on both S_a and S_{max} are given in Table 4 along with the actual average proof stresses. Rolling after HT with the coarse threads caused zero increase in these fatigue strengths, while 40 and 50 % increases occurred for fine threads for preloads of 90 and 75 % S_{proof}, respectively, based on S_a. For 90 % proof preload all fine thread fatigue strengths based on S_{max} and 10^7 cycles were either very close to, or higher than, the actual S_{proof}. Values of R-ratio for all tests with 75 or 90 % proof stress ranged from 0.73 to 0.91 with run-out values ranging from 0.84 to 0.91. These high R-ratios are indicative of the high preload desired in bolted connections.

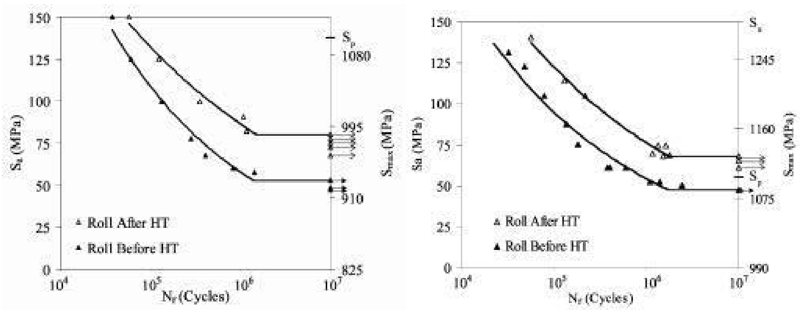

a) 75% of Proof Preload b) 90% of Proof Preload

FIG. 8—*Influence of roll before/after HT, fine thread series.*

TABLE 4—*Fatigue strength based on run-outs (10^7 Cycles).*

	S_a 75%	S_a 90%	S_{max} 75%	S_{max} 90%	Actual S_p
Coarse Roll Before HT (MPa)	60	48	945	1090	1103
Coarse Roll After HT (MPa)	55	48	935	1090	996
Fine Roll Before HT (MPa)	53	48	930	1090	1082
Fine Roll After HT (MPa)	90	68	985	1126	974

Comparison of Coarse/ Fine Fatigue Resistance for Roll Before/After Heat Treatment

Figures 9*a* and 9*b* demonstrate a comparison between the fine and coarse threads for the rolled before heat treatment series (with negligible residual stresses) at the 75 and 90 % of proof preloads, respectively. Based on the trends of these curves, it is seen that both coarse and fine threads have similar fatigue resistance based on the stress calculated using the tensile stress area A_t. This lack of significant difference between the same grade bolt of the coarse and fine thread series coincides with statements in literature that selection of thread pitch is more dependent on ease of assembly/reliability on the assembly line [19]. However, Figs. 10*a* and 10*b* for the rolled after heat treatment show a slightly different trend with the fine threads having better fatigue resistance than the coarse threads. This is attributed to the local notch geometry conditions and/or the higher axial surface compressive residual stress in the fine roll after heat treatment threads.

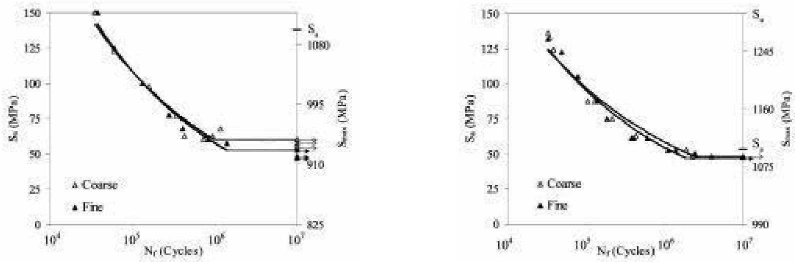

a) 75% of Proof Preload b) 90% of Proof Preload

FIG. 9—*Comparison of coarse and fine threads, roll before HT*.

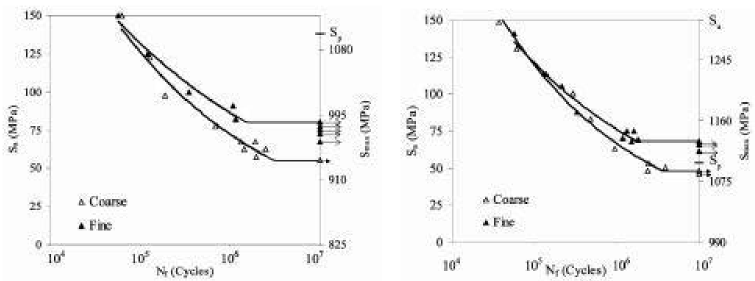

a) 75% of Proof Preload b) 90% of Proof Preload

FIG. 10—*Comparison of Coarse and Fine Threads, Roll After HT*.

Effect of Preload Based on Stress Amplitude, S_a, for Coarse and Fine Threads

Figures 11 and 12 contain plots of stress amplitude versus life for each group of bolts with the roll before heat treatment group shown in (a) and the roll after heat treatment group shown in (b). Figure 11 is that of the coarse thread series and Fig. 12 is that of the fine thread series. Each plot contains data for both preload values to aid in comparison of preload influence on the stress amplitude versus life curves. For all four bolt series, the fatigue resistance at 75% proof preload is equal to, or better than, 90% proof preload. The fatigue strengths at 10^7 cycles for 75% proof preload are increased between 10 and 25% relative to that for the 90% proof preload. The higher proof preload is accompanied by a higher R-ratio. This same deleterious higher R-ratio effect based on S_a was noted in the previous SAEFDE high R-ratio findings [15].

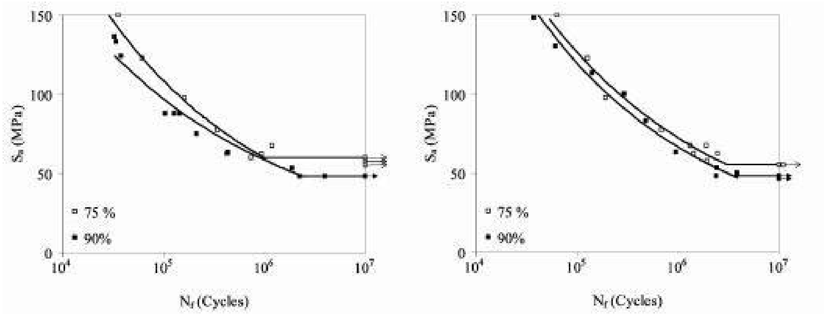

a) Roll Before HT b) Roll After HT

FIG. 11—*Effect of preload based on S_a, coarse threads*

.

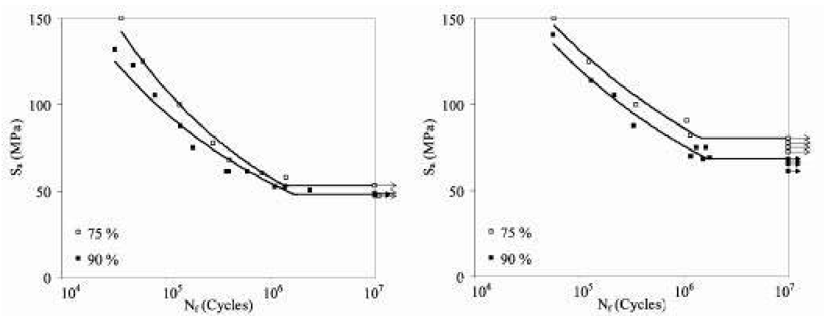

a) Roll Before HT b) Roll After HT

FIG. 12—*Effect of preload based on S_a, fine threads*.

When viewed on a stress amplitude versus life plot (Figs. 11 and 12), the conclusion that higher preload is detrimental to the axial fatigue behavior of fasteners can be drawn. Due to the nature of the loading on externally threaded fasteners, and the minimal preload relaxation in these high strength fasteners, one would expect the alternating stress versus life plot to be more important than the S_{max} versus life plots. What is not being taken into account in these plots is the importance of the consistent clamping force needed in high strength bolt applications. Examples include that of the engine bearing oil film importance, another is in head bolt applications. A consistent high clamping force is needed in internal combustion engines to maintain a head gasket seal during the combustion of the air/fuel mixture in each cylinder. Without this high clamping force, the combustion pressure will not be turned into rotational energy and will actually be diverted into either the next cylinder or into the cooling system. Therefore, it is made known that consistent adequate clamping force for the application as well as strength high enough to prevent joint opening is of utmost importance when bolts of the type tested in this research are used. If a bolt is used with a great enough strength to keep a joint from opening, the fatigue portion of the problem will most likely take care of itself. It is common sense that if joint opening occurs the forces on the fastener will increase due to the impact forces created during the opening and closing of the joint. Upon this occurrence fastener failure will almost surely occur. The magnitude of difference between the 75 and 90 % of the proof stress preloads in each individual bolt category is negligible when this critical clamping force importance is taken into consideration.

Effect of Preload Based on Maximum Stress, S_{max}, for Coarse and Fine Threads

Figures 13 and 14 also show the effect of preload on the stress life diagrams, but here with the maximum stress plotted on the vertical axis. Figure 13 is that for the coarse thread series, and Fig. 14 is that for the fine thread series. As expected from ref 15, for all bolt series, the greater preload or greater R-ratio consistently demonstrates the greater maximum stress versus life curve. For fatigue strengths at 10^7 cycles, these increases were about 15 %. For each series of bolt shown in these diagrams the shortest life specimen in the 90 % of proof preload is very close to the ultimate strength of the bolt. If the preload were increased from this 90 % of proof level, the finite life end of the curve will tend to become horizontal or the overall slope will demonstrate a decrease in slope from left to right.

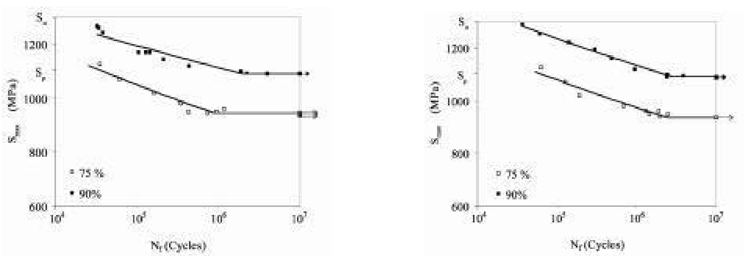

a) Roll Before HT b) Roll After HT

FIG. 13—*Effect of preload based on S_{max}, coarse threads.*

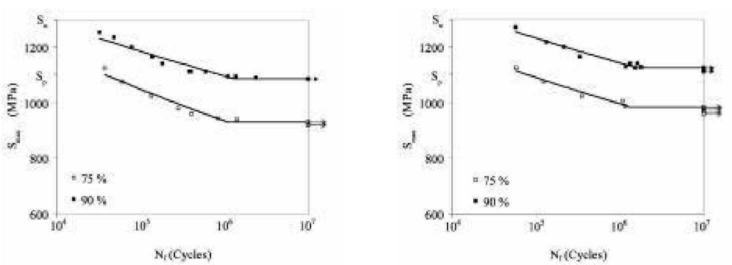

a) Roll Before HT b) Roll After HT

FIG. 14—*Effect of preload based on S_{max}, fine threads.*

Cyclic Creep/Ratcheting

Throughout the duration of tests conducted, the peak ram displacements were recorded to quantify cyclic creep/ratcheting. Three representative curves of peak ram displacement versus applied cycles, one of a short life specimen, one of a mid-life specimen, and one of a run-out have been selected for both preloads and each fine thread series bolt group and are contained in Fig. 15 with the 75 % preload located on the plots (a) and (b) and the 90 % preload plots (c) and (d) with the left plots (a) and (c) being for the fine thread series rolled before heat treatment and the right plots (b) and (d) being for the fine thread series rolled after heat treatment. The results that follow for the fine threads were very similar to those for the coarse threads. It must be noted that these curves are shown on a semi-log plot, and therefore, half-life is located just a short distance from the final fracture point or run-out. The short, vertical "tail" on the short and mid-life cyclic creep/ratcheting plots is evidence of a quickly accelerated crack growth just prior to fracture as would be expected with a high preload value, and then sudden fracture. As shown in Fig. 15*a* and *b*, the tests at the 75 % preload had little or no cyclic creep/ratcheting throughout the life of each specimen.

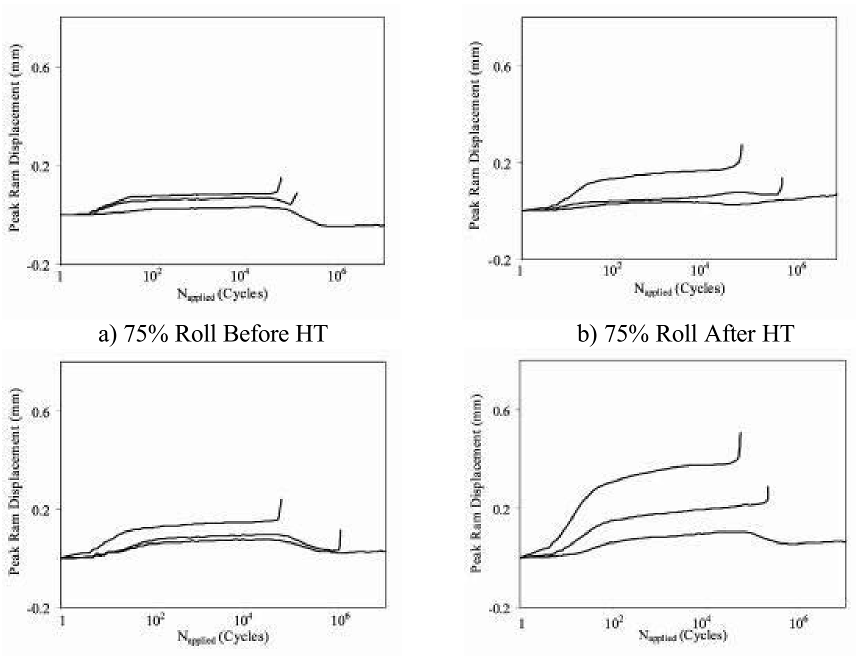

a) 75% Roll Before HT

b) 75% Roll After HT

c) 90% Roll Before HT

d) 90% Roll After HT

FIG. 15—*Representative peak ram displacement versus applied cycles, fine thread series.*

Figure 15*c* and *d* show three representative peak ram displacement versus cycles behavior (each) for fine thread specimens at the 90 % preload. Nearly all of the 90 % preload long-life specimens show little or no evidence of cyclic creep/ratcheting. However, the peak ram displacement versus cycles for the short life and some of the mid-life specimens did show some signs of cyclic creep/ratcheting. This is not surprising once it is understood that for the fine thread series rolled after heat treatment, the entire set of specimens in the so called 90 % preload category underwent loading of which the entire stress range was above the actual proof stress of the bolt. This category of tests with 90 % preload was actually run at a preload value equal to 102 % of the actual proof stress of the bolt group, which was 974 MPa. This happened resulting from the 1100 MPa proof stress assumption mentioned earlier and will be discussed more in depth later in the paper.

The creep/ratcheting observation conducted throughout this testing has demonstrated a small increase in the amount of creep/ratcheting experienced across the life only during tests at the higher, 90 %, preload with shorter fatigue lives. Creep/ratcheting appeared to have some effect on the short life roll after heat treatment groups at the so called 90 % of the proof stress preload level based on the peak ram displacement versus applied cycles plots. It is interesting to note that the longer life specimens did not show signs of cyclic creep/ratcheting and yet the alternating stress life plots for the 75 and 90 % preloads have only small differences in alternating stress values for a particular life. This leads one to believe that somewhat higher preload values could possibly be used without a significant falloff in long life fatigue resistance. The maximum stress values for the short life specimens at 90 % of the proof stress preload are very close to the ultimate strength of the individual bolt groups. Because of this, the short life stress amplitude magnitudes will probably decrease for any higher preloads tested. The only question to be answered by the higher preload testing will be how high of a preload can be used with a resulting S-N diagram which still has some slope (i.e., not just random failures/horizontal S-N plots).

Fractography

As mentioned previously, all fractures occurred at the first thread of the bolt/nut interface. Upon completion of testing, the fracture surfaces of each specimen were examined with the naked eye and with an eyepiece of ×10 magnification. After this macroscopic observation was completed, one monotonic fracture surface from each group, as well as a representative short life and long life fatigue specimen from each group at both 75 and 90 % of proof minimum stresses, were selected for further evaluation. Macroscopic evaluation was once again performed, this time using the SEM at a magnification of ×40. Following this macroscopic evaluation in the SEM, each specimen was thoroughly evaluated at ×1500 magnification.

The monotonic fractures all grew from the outside of the bolts with the exception of the fine thread series rolled before heat treatment. All of the monotonic microscopic evaluation revealed ductile dimpling throughout the entirety of the fracture surface, which includes both the transverse and shear lip regions.

Figures 16 through 19 each contain an (a) electron macrograph at ×40 magnification, combined with two electron micrographs of (b) fatigue crack growth (FCG) and (c) final fracture (FF) regions under ×1500 magnification. Under macroscopic observation the area of fatigue crack nucleation, FCG, and FF regions were readily obvious and are marked on the figures.

Ratchet mark(s) were always evident in both of the groups rolled prior to heat treatment as shown in Figs. 16*a* and 18*a* indicating multiple crack nucleation sites. The groups rolled after heat treatment, however, did not always show ratchet mark(s) at long life as shown in Fig. 19*a*. When viewed at ×1500, FCG regions for each category of bolt showed fatigue facets. No striations or beach marks were visible in the fatigue crack growth regions. The FF regions for each of the specimens showed ductile dimpling on the transverse fracture plane, as well as the region where the final fracture switched to the shear plane. These observations are exactly what would be expected of a typical fatigue fracture where significant ductility exists.

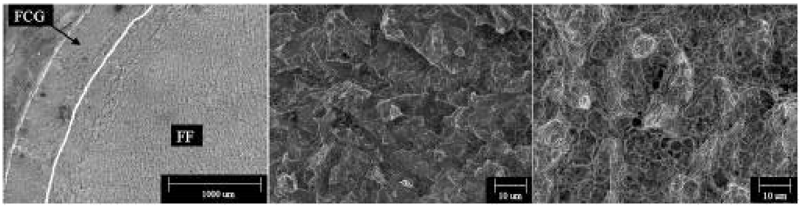

a) Macro b) FCG c) FF

FIG. 16—*Fracture surface, roll before HT, short life specimen.*

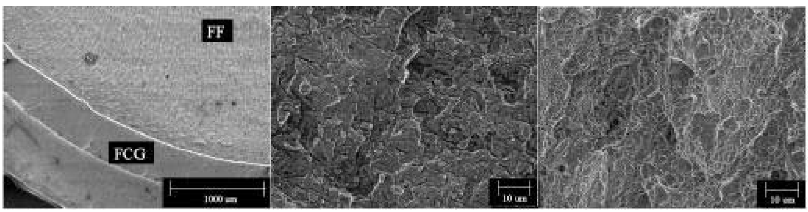

a) Macro b) FCG c) FF

FIG. 17—*Fracture surface, roll after HT, short life specimen.*

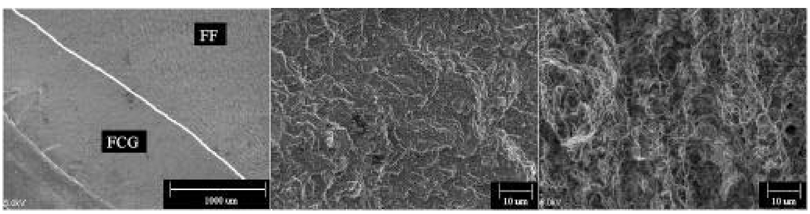

a) Macro b) FCG c) FF

FIG. 18—*Fracture surface, roll before HT, long life specimen.*

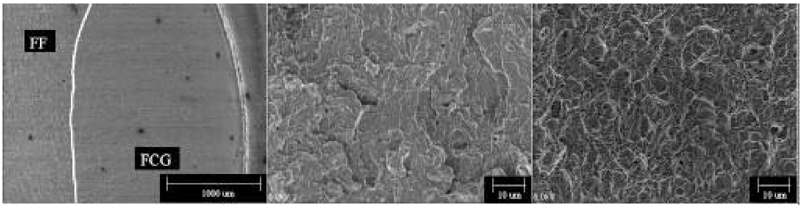

a) Macro b) FCG c) FF

FIG. 19—*Fracture surface, roll after HT, long life specimen.*

The fatigue specimens were separated into two categories, short and long life. The fractographic differences between the two preload categories within each group were negligible. The roll before heat treatment specimens showed a significantly larger number of crack nucleation sites than those rolled after heat treatment, with some long life fatigue specimens rolled after heat treatment showing no ratchet marks. Because of this, the first crack nucleation site was difficult to pinpoint. Crescent shaped fatigue cracks grew almost entirely around the short life specimens, but the amount of circumference decreased as the length of life of the bolt increased. The shape of the FCG region was for the most part crescent shaped, but some of the longest life specimens began to make the transition to a straight edge crack front or to that of a thumbnail shape. The depth of the crescent shaped cracks prior to final fracture varied from about 0.5 mm to 2 mm. Thumbnail crack depths varied from about 2 mm to 4 mm.

Fractography revealed that all of the fracture surfaces of specimens that underwent fatigue loading had failures that were fatigue in nature. However, this does not rule out cyclic creep/ratcheting and fatigue interaction that can sometimes be difficult to identify with fractography alone. Important and beneficial information gathered from the fractography portion of this research was the fact that there were a significantly lower number of ratchet marks on the roll after heat treatment groups compared to that on the roll before heat treatment bolts. This occurred across the span of lives tested, and was consistent at both preload values and thread profiles and was most likely due to the smoother thread notch root regions from rolling after heat treatment.

Proof Stress Assumption

For the experimental testing, a constant proof stress was assumed for all four series of bolts. This assumption could be looked upon as a good or bad way to compare results depending on the purpose of the evaluation. In industry, from the bolt manufacturer's point of view, this comparison would be considered useful. The manufacturer wants to have a quantification of the benefit in fatigue life a purchaser could expect when purchasing a bolt that is more expensive because it was rolled after the heat treatment. In this case, a purchaser may be expecting to use the same torque or torque turn method for tightening of each bolt. For this situation, the assumption of constant preload would be a good one. From this point of view, the conducted research has provided the manufacturer with a quantitative benefit explanation they can provide to their customers of increased fatigue resistance created by the rolling of the threads after heat treatment (based on fine thread series).

From the point of view of the more technologically advanced purchasers, who do testing and research of their own, this comparison is not necessarily the best. The high-end purchasers usually define a minimum proof stress value they expect from the bolt manufacturer when purchasing a large lot of bolts. For this reason, the bolt research groups would like to be able to decide the preload that should be used for the lot of bolts just purchased. In this case the bolts, which were received from the manufacturer, will have a proof stress somewhat higher than the value they specified or from the minimum standard value. In order to calculate the preload which is optimal for the lot of bolts that were just purchased, they will have to monotonically test some of the bolts to determine the average proof stress. Once the proof stress is determined the company would like an easy method to determine the optimal preload or tightening (torque-turn procedure) that should be used on the entire lot of bolts. In this case it would be nice to determine the optimal preload value that will maintain the most consistent clamping force yet will still retain high fatigue resistance.

One thing this research demonstrates is that a simple proof test determination may not be possible when trying to create a general rule of thumb for optimal preload value on bolts manufactured with the threads rolled after as well as rolled before heat treatment process. In fact, each type of bolt (rolled before or after heat treatment) may need to have different rules of thumb for determination of the best preload to be used. It is difficult at this point, within the limited amount of testing conducted, to make any predictions as to this optimal preload value that should be used.

Discussion of the Influence of Manufacturing Process

Table 5 provides the percent benefit of fatigue strength at 10^7 cycles between the bolts rolled before and after heat treatment for each of the thread series for preloads of 50, 75, and 90 % of the proof stress. Benefits in life and fatigue strength due to rolling threads after heat treatment that were quantified in this research can be attributed to three primary aspects/properties that were altered/added due to the change in the manufacturing process:

1. Increases in residual stresses,
2. Differences in stress concentration from geometry,
3. Differences in stress concentration from the increased quality of the surface finish on the roll after heat treatment specimens.

These three effects combine to provide the separation in the S-N diagrams for the comparative groups.

TABLE 5—*Roll after heat treatment benefits in fatigue strength (10^7 cycles).*

	Stress Amplitude		
Preload Level (%)	50	75	90
Coarse (%)	8	-9	0
Fine (%)	67	50	40

The idea that the increases in fatigue resistance may have come partially from the surface finish is based on the decrease in the number of crack nucleation points evident in the long life roll after heat treatment versus the roll before heat treatment specimens. One may argue that this could occur due to the surface axial compressive residual stresses, but if this were the case, the coarse threads rolled after heat treatment with the tensile axial residual stress on the surface would have shown more nucleation points and been detrimental in life throughout the span of the S-N diagrams when compared to the roll before heat treatment of the same thread series. Neither of these were the case, therefore, a smaller number of crack nucleation sites in the roll after heat treatment bolts is accepted to demonstrate a better quality of surface finish at the root of the notch.

Based on the experimental results generated during this research, it appears the compressive residual stress increase expected from the rolling of threads after heat treatment has a lesser effect on the fatigue resistance of the fastener at realistic higher preload values. Further evaluation in this SAEFDE research program will result with a solid explanation and quantification of the high preload fatigue behavior of these high strength bolts, as well as a good indication of the preloads where the residual stresses begin to play a more significant part in an increased fatigue life.

Summary and Conclusions

1. Based on standard thread area, A_t, the monotonic and fatigue properties for the coarse and fine threads roll before heat treatment were similar. The roll after heat treatment coarse and fine monotonic properties were also similar, but the fatigue resistance was better for the fine threads.
2. The bolt failure mechanisms were always fatigue crack nucleation and growth from the first thread at the nut/bolt interface. Multiple nucleation sites as indicated by multiple ratchet marks dominated the roll before heat treatment specimens. These multiple nucleation sites did not occur in the roll after specimens due primarily to a smoother notch root radius region. Fatigue cracks were primarily crescent in shape, but for a few specimens at longer lives the crack tended to become more of a straight edge crack and occasionally thumbnail in shape. Fatigue crack growth regions always contained fatigue facets with no beach marks or striations, and final facture regions always contained ductile dimples. Cyclic creep/ratcheting only occurred with the 90 % proof stress and primarily at the shorter lives. This did not influence the fracture surface appearance.
3. Rolling after heat treatment increased the fatigue resistance for the fine threads at all lives, but only a little for the coarse threads at finite lives. These results were attributed to different thread radii, thread region smoothness, near surface residual compressive stresses, and possible residual stress relaxation from the high preloads. The increased fine thread fatigue resistance depended on the preload magnitude where fatigue strengths at 10^7 cycles increased 50 % for a preload of 75 % proof stress and 40 % for a preload of 90 % proof stress. These are still significant fatigue strength increases despite the high preload stresses and high R-ratios.
4. Based on fatigue resistance using the alternating stress, S_a, the higher preload, or higher R-ratio, was detrimental. However, when based on maximum stress, $S_{\max}$, the higher preload, or higher R-ratio, was beneficial.

Acknowledgments

The authors would like to thank Jeffrey Nash at Caterpillar for information on bolt usage and testing at Caterpillar, Steve Vass at Lake Erie Screw for providing all bolts/nuts, Al Conle at Ford for providing the residual stress measurements, and Gregory Werner and James Wong from John Deere for providing the thread profiling and microhardness measurements. This cooperation was possible through the Society of Automotive Engineers Fatigue Design and Evaluation, SAEFDE, committee.

References

[1] Bickford, J. H., An Introduction to the Design and Behavior of Bolted Joints, 3rd ed., Marcel Dekker, New York, 1995.

[2] Finkelston, R. J., "Preloading for Optimum Bolt Efficiency," Assembly Engineering, 1974, pp. 24–28.

[3] Heston, A. W., "VDI Joint Design Procedures" in Handbook of Bolts and Bolted Joints, J. H. Bickford and S. Nassar, eds., Marcel Dekker, New York, 1998, pp. 317–340.

[4] Walker, R. A. and Finkelston, R. J., "Effect of Basic Thread Parameters on Fatigue Life," SAE paper 700851, Society of Automotive Engineers, Warrendale, PA, 1970.

[5] Finkelston, R. J. and Kull, F. R., "Preloading for Optimum Bolt Efficiency," Assembly Engineering, August 1974, pp.24–28.

[6] Witte, E. C., "Combating Fatigue Failure in Bolts," Plant Engineering, 1977, pp. 127–131.

[7] Finkelston, R. J. and Wallace, P. W., "Advances in High-Performance Mechanical Fasteners," SAE paper 800451, Society of Automotive Engineers, Warrendale, PA, 1980.

[8] Crispell, C., "New Data on Fastener Fatigue," Machine Design, 1982, pp. 71–74.

[9] Kull, F. R., "Bolt Fatigue" in Handbook of Bolts and Bolted Joints, edited by J. H. Bickford and S. Nassar, Marcel Dekker, New York, 1998, pp. 699–707.

[10] Novak, G. J. and Patel, T., "Thread Lubricants" in Handbook of Bolts and Bolted Joints," J. H. Bickford and S. Nassar, eds., Marcel Dekker, New York, 1998, pp. 43–55.

[11] Technical Reference Guide, Industrial Fasteners Institute, Cleveland, OH.

[12] Juvinal, R. C. and Marshak, K. M., Fundamentals of Machine Component Design, John Wiley & Sons, New York, 2000.

[13] Ifergane, S., "The Effect of Manufacturing Processes on the Fatigue Lifetime of Aeronautical Bolts," Engineering Failure Analysis, 2001, Vol. 8, pp. 227–255.

[14] Stephens, R. I., Fatemi, A., Stephens, R. R., and Fuchs, H. O., Metal Fatigue in Engineering, 2nd ed., Wiley Interscience, Hoboken, NJ, 2000.

[15] Stephens, R. I., Pals, T. J., Karadag, M., and Vantiger, T. R., "The Effect of Tensile Mean Stress on Fatigue of Unnotched and Notched SAE 1045 Steel," SAE paper 2003-01-0912, Society of Automotive Engineers, Warrendale, PA, 2003.

[16] ASME Standard B1.1: Unified Inch Screw Threads, ASME, New York, NY, 2002.

[17] Dragone, E., "Effect of Nut Compliance on Screw Thread Load Distribution," Journal of Strain Analysis, 1990, Vol. 25, No. 3, pp. 147–150.

[18] SAE Standard J429: Mechanical and Material Requirements for Externally Threaded Fasteners, Society of Automotive Engineers, Warrendale, PA, 1999.
[19] Anon, "Thread Forms and Torque Systems Boost Reliability of Bolted Joints," Product Engineering, Vol. 48, No. 12, 1977, pp. 37–41.

Journal of ASTM International, February 2006, Vol. 3, No. 2
Paper ID JAI12547
Available online at www.astm.org

L. Edwards,[1] *M. E. Fitzpatrick,*[2] *P. E. Irving,*[3] *I. Sinclair,*[4] *X. Zhang,*[5] *and D. Yapp*[6]

An Integrated Approach to the Determination and Consequences of Residual Stress on the Fatigue Performance of Welded Aircraft Structures

ABSTRACT: Although residual stress in welded structures and components has long been known to have an effect on their fatigue performance, access to reliable, spatially accurate residual stress field data has been limited. Recent advances in neutron and synchrotron X-ray diffraction allow a far more detailed picture of weld residual stress fields to be obtained that permits the development and use of predictive models that can be used for accurate design against fatigue in aircraft structures. This paper describes a fully integrated study of the three-dimensional residual stress distribution accompanying state-of-the-art fusion welds in 2024-T4 aluminum alloy, and how it is affected by subsequent machining and service loading. A particular feature of this work has been the development of techniques allowing the nondestructive evaluation of the residual stress field in the full range of specimens used to provide the design data required for welded aircraft structures and the integration of this information into all aspects of damage tolerant design.

KEYWORDS: residual stresses, fatigue, damage tolerance, structural integrity, welded aircraft structures

Introduction

Research into cost saving of aircraft metallic members and components is a continuous process in the aerospace industries. Weight saving through design modification of aircraft is being undertaken to support cost reduction programs and to face the challenge of 21st century mass air transportation [1]. Welding instead of mechanical fastening has been identified as one of the major tools for cost reduction, in terms of weight reduction and by production cost saving through substitution of assemblies and built-up structures by formation of an integral structure. However, unlike mechanical fastening, welding leads to

- An integral structure with a single load path construction.
- Creation of microstructure near the fusion and heat affected zone (HAZ) with changed grain structure and strength.
- Formation of potential sources of initiating defects not present in the wrought alloy.
- Creation of local and global residual stress fields.

All these factors, in particular the creation of a variable residual stress field across the weld, would have a profound influence on the fatigue life of the welded metallic members and components. The civil aircraft design specification demands damage tolerance characteristics in safety critical parts. Therefore, before implementation of such process change it is necessary to establish the fatigue crack growth behavior under the influence of the variable distribution of residual stress that exists following welding. The relationship between the fatigue crack growth in the welded microstructure and the distribution of the residual stress field is the most essential input for the damage-tolerant, fail-safe design of the safety critical components [2].

Manuscript received January 7, 2005; accepted for publication August 24, 2005; published December 2005.

[1] Professor of Structural Integrity, Dept of Materials Engineering, Open University, Milton Keynes, UK, MK7 6AA.
[2] Senior Lecturer, Dept of Materials Engineering, Open University, Milton Keynes, UK, MK7 6AA.
[3] Professor of Damage Tolerance, School of Industrial and Manufacturing Sciences, Cranfield University, Cranfield, Bedfordshire MK43 0AL.
[4] Reader, School of Engineering, Southampton University, Southampton, UK, SO17 1BJ.
[5] Senior Lecturer, School of Engineering, Cranfield University, Cranfield, Bedfordshire, UK, MK43 0AL.
[6] Senior Lecturer, School of Industrial and Manufacturing Sciences, Cranfield University, Cranfield, Bedfordshire, UK, MK43 0AL.

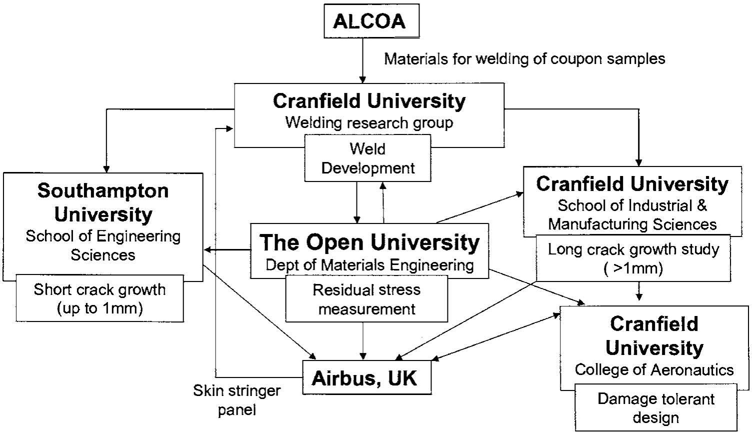

FIG. 1—*WELDES project partners and structure.*

This paper describes the work of an integrated program, WELDES (weld processing design and durability of welded aircraft assemblies), on the determination and consequences of residual stress on the fatigue performance of welded aircraft structures. The breadth of partners and their main functions are shown in Fig. 1.

The factors controlling fatigue initiation and crack growth in welds are relatively well understood, and the importance of residual stress, HAZ hardness, and microstructure is well known. However, access to reliable, spatially accurate residual stress field data has previously been limited. The development of dedicated neutron and synchrotron X-ray diffraction techniques for the measurement of residual stress has opened up the possibility of acquiring high quality, accurate data which can be used reliably in predictive structural integrity models. However, acquisition of high quality, reliable residual stress data is of optimum use only if it is used to influence both process design and subsequent damage-tolerance data collection and use. This latter point is particularly important, as when one is dealing with residual stress fields, similitude no longer automatically exists between laboratory fracture-mechanics specimens and fabricated components and structures.

Thus, in the present program a fully integrated study has been undertaken of the full residual stress distribution associated with state-of-the-art fusion welds in 2024-T4 and 7150-T651 aluminium alloys, and how they are affected by subsequent machining and service loading. A particular feature of this work has been the development of techniques allowing the nondestructive evaluation of the residual stress field in the full range of specimens used to provide the design data required for welded aircraft structures. This has included small bend specimens used to study initiation and short fatigue crack growth, middle tension M(T) and compact tension CT specimens used to study long fatigue crack growth, and large integral welded double stringer/skin mockups used to investigate the likely failure mode of welded wing-skin assemblies.

The resulting residual stress data have been combined with relevant microstructural data in the fatigue modeling process. Initiation behavior has been studied using replica techniques to monitor the initiation and growth of cracks from interdendritic pores in the weld HAZ. Initiation of small fatigue cracks occurred virtually from the first cycle at defects in the microstructure and thus models for the growth and linkage of the microcracks, including the role of residual stress, were developed and fatigue initiation behavior (defined as the life to a crack of 1 mm) has been accurately calculated from knowledge of intrinsic crack growth rates and HAZ characteristics. Factors controlling macroscopic fatigue growth rates have been investigated using constant ΔK tests. The changes in growth rate as the cracks cross the weld have been determined and related to the changes in the residual stress field, hardness, and microstructure within the HAZ. Large-scale skin-stringer mockups have been manufactured and fatigue tested and the implications of the results of the program have been assessed. Both 2024-T4 (lower wing skin) and 7150-T651 (upper wing skin) candidate welds have been studied but only the 2024-T4 work will be described here.

Weld Processes Studied

The processes studied in this work were metal inert gas (MIG) welding and variable polarity plasma arc (VPPA) welding. Although MIG welding has been in extensive use for various defence and space research application for many years, because of flexibility and low cost, its application has been restricted in the civil aviation industry, as the high strength heat treated 2XXX and 7XXX aluminium alloys used were regarded as unweldable via this process [3].

2024-T4 alloy is a widely known Al–Cu–Mg alloy used extensively in aircraft fuselages and lower wing skin-stringer panels. This is a high-strength, age-hardened alloy and is characterized by its superior damage tolerant characteristics [2]. The alloy has been typically regarded as unweldable because of its compositional range whereby it is prone to hot cracking. Recent advances in welding technology and the use of 2319 filler wire, however, have made it possible to weld 2024-T4 to aviation standard [4].

The dominant cause of generation of residual stress in a weld is the unequal expansion and contraction of the weld metal and the surrounding heat affected zone. The fusion welding process causes intense local heating in the weld metal region and the heat is conducted into the surrounding metal. At this high temperature the metal yields under compression due to the cooler surrounding material. During cooling, uneven contraction between the yielded and nonyielded region gives rise to tensile residual stress along the welding direction.

VPPA welding is a more recently developed process. It has been used for a number of critical applications like the space shuttle external fuel tank [5], and also in structural welding of the international space station by the United States of America's National Aeronautics and Space Administration (NASA) where the weld joint has to withstand the harshest external atmospheric condition [6]. The process is much favored because of its capability to weld relatively thick sections in a single pass, and also for the relatively low distortion of the welded parts that allows for high dimensional accuracy after further machining.

The application of either of these processes in safety critical components in civil aviation, however, requires complete understanding of fatigue crack growth characteristics under the changed microstructure and residual stress field. This would form an important design input for safety critical structures to exhibit damage-tolerant, fail-safe characteristics [2].

Any subsequent machining of the welded component is likely to change the residual stresses within it. As the fracture mechanics specimens that are used to measure material fatigue crack propagation characteristics are, by necessity, smaller than the welded structures they are intended to represent, they also contain significantly different residual stress profiles. Thus, the nondestructive evaluation of the residual stress fields in the full range of specimens used to provide the design data required for welded aircraft structures is essential if fully representative damage tolerance data is to be obtained.

Weld Processes Development

The MIG process forms an arc between a filler wire and parent plate. VPPA uses a nonconsumable tungsten electrode, and can be used with filler wire or without (autogenous welding). These processes were used to make butt welds in flat coupons, and to weld skin-stringer panels in 2024-T4.

The welded coupons were then used for detailed evaluation of microstructure, tensile, and small-scale fatigue properties, and residual stress evaluation. Large skin-stringer panels were subsequently designed, fabricated, and manufactured, and their residual stress profiles were non-destructively evaluated before full-scale fatigue testing. The material used was 2024-T4 Al-4.4%Cu-1.5%Mg T351 supplied as 12.7 mm thick plate. The MIG filler metal was 5039 Al-2.8%Zn-3.8%Mg. In general, fusion welding of aluminium alloys is regarded as difficult since they are susceptible to porosity because of the evolution of hydrogen during welding, and also to solidification cracking because of the wide solidification range in some alloys. The MIG welds were produced in the flat position (plate horizontal) using a two-pass procedure (Fig. 2). The VPPA welds were produced by welding vertically up (plate vertical) in a single pass.

The VPPA process produces a "keyhole"—the plasma pressure generates a cavity completely through the plate to be welded, and the molten weld metal flows round the keyhole to form the weld. The welded coupons were 240 mm by 500 mm by 12.7 mm. For both MIG and VPPA, good quality welds were produced, with an absence of gross defects, either large pores, or large solidification cracks. However, the MIG welds did contain a high density of small (50–200 μm) gas pores, and small (20–50 μm) interden-

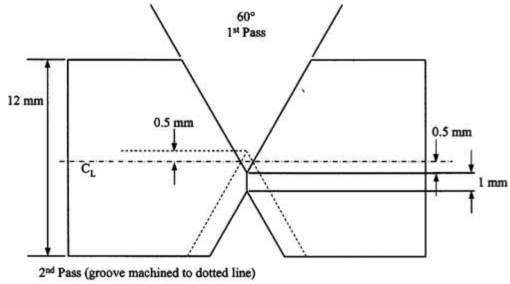

FIG. 2—*Schematic showing cross section of plate preparation for MIG Welding.*

dritic defects. In contrast, the VPPA welds were essentially defect-free. There were some interdendritic defects in the weld metal on micro-examination, but these were less than 20 μm in length, smaller, in fact, than the intermetallics in the parent material.

This is a remarkable outcome for arc welding of aluminium. It is thought that the presence of the keyhole and the flow of weld metal round the keyhole are responsible for this result. The MIG welding could be performed at relatively low heat input, 0.93 kJ/mm, whereas for the VPPA welding the heat input was higher at 4 kJ/mm. This results in a slower thermal cycle for VPPA compared to MIG, and this produces a wider and softer heat affected zone (HAZ) in the VPPA welds compared to the MIG welds.

Skin-stringer panels were manufactured using the VPPA process only. There were a number of differences in the weld when compared to the flat plate coupons. In particular, as the effective heat sink is quite asymmetric, owing to the proximity of the weld center line to the doubler, the HAZ width differed on either side of the weld. The final 1.2 m long as-welded and machined skin stringer panel is shown in Fig. 3. The weld is located approximately at one third of the height of the stringer. A detailed description of the geometry is given later in this paper.

Residual Stress Measurement

Residual stresses are difficult to account for in structural integrity calculations for several reasons: they are introduced and evolve throughout a range of production stages; they affect fatigue crack initiation and growth rates; they may evolve as a consequence of in-service loading; and perhaps most importantly, residual stresses have been traditionally difficult to determine reliably and accurately. These problems become acute when dealing with stress fields arising from welding. Residual stresses are critically dependent upon welding parameters, heat input, number of weld passes, and the properties of the material(s) being welded. Accurate determination of residual stresses is not simple. Methods such as hole drilling are destructive and reliable methods for the determination of residual stresses deep within structures and components have only recently become available.

Thus, a robust methodology was developed for determining nondestructively the residual stress field in these aluminium alloy welds for aerospace applications using state of the art techniques. The method combines rapid data acquisition from synchrotron X-ray diffraction, coupled with the high penetration of

FIG. 3—*As-fabricated and machined skin stringer panel.*

TABLE 1—*Samples and residual stress measurement technique used.*

Sample	Dimensions (mm)	Source
As -welded	240×280×12	Neutron and synchrotron
Machined to 7 mm	240×280×7	Neutron and synchrotron
Short crack coupons	100×90×7	Synchrotron
MT coupons	380×80×7	Neutron
Skin stringer panels	1240×350×80	Neutron

neutron diffraction to build up a profile of the residual stress. The measurement methods employed for a given task depended on the size and scale of both the specimens and the residual stresses present as summarized in Table 1.

As may be seen from Table 1 the main techniques used were:

Neutron Diffraction

Neutron diffraction is now a well-established method for the measurement of elastic strain in crystalline materials [7]. It has been applied to a wide range of materials and problems, and a draft International Standards Association (ISO) standard for its use is now in circulation [8]. Neutrons have high penetration into most materials, and hence it is possible to make measurements up to several tens of cm inside structural components so it has the advantage that large specimens can be studied (Fig. 4).

Synchrotron X-ray Diffraction

Synchrotron X-ray diffraction is a relatively new technique for strain measurement [7]. Using high-intensity X-ray beams it is possible to obtain highly detailed strain maps inside components in as little as an hour, much faster than is possible with neutron diffraction. The method has a drawback in that for most samples one strain component cannot be measured in depth, because a grazing incidence of the beam is needed that gives an overly large path length for sensible measurement. As a result, we have developed a method that combines the high speed and resolution of the synchrotron X-ray method with the ability of neutrons to give all strain components [9].

Thus, the precise technique used depended on the size of the specimen. In the small three-point bend specimens of dimensions 80 by 80 by 7 mm^3, used to study fatigue crack initiation and crack growth up to 1 mm, the near-surface residual stresses were determined using laboratory and synchrotron X-ray diffraction alone. Conversely, the large skin-stringer panels were measured only using neutron diffraction.

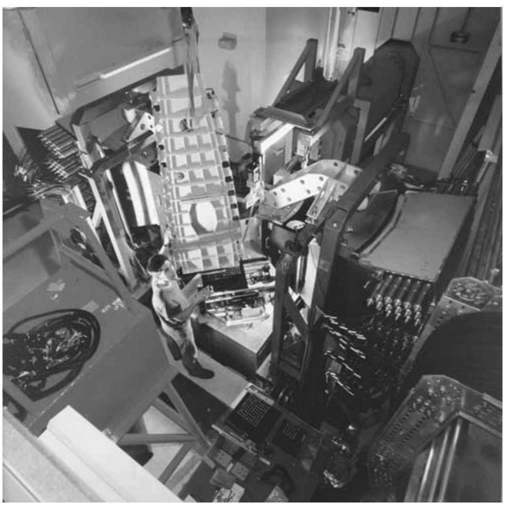

FIG. 4—*Installing a large wing rib sample on the ENGIN-X neutron stress diffractometer [10].*

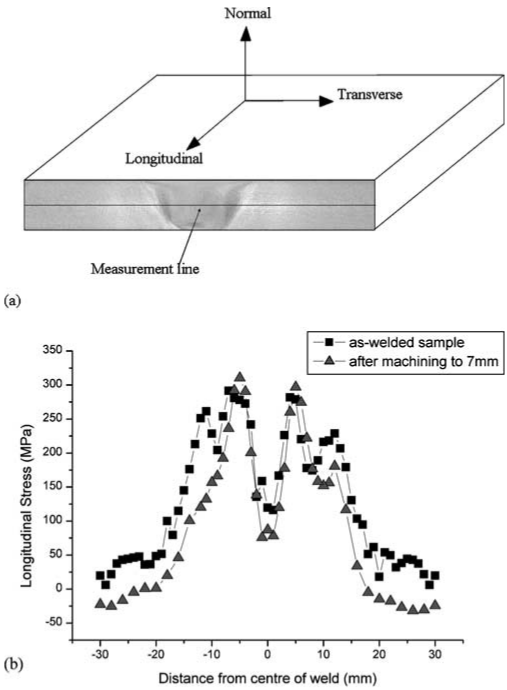

FIG. 5—*(a) Schematic showing the measurement geometry in the weld coupons and strain measurement directions and (b) longitudinal residual stresses in a 2024-T4 welded coupon before and after machining the thickness from* 12 to 7 mm.

The residual stress profiles in the remaining intermediate size specimens were measured using a novel combination of neutron and synchrotron X-ray diffraction in both the as-welded and machined-to-thickness conditions.

Weld Coupon Stresses

The as-welded coupons were 0.5 m long, 12 mm thick, and 186 mm wide. Typically a section 280 mm long was cut from this original coupon and the longitudinal, transverse, and normal strains were measured at its center point on a plane perpendicular to the weld. The geometry of the weld and the specific strain directions measured are as schematically shown in Fig. 5(*a*). On the reasonable assumption that these three directions are principal strain directions, all three stresses were then calculated using Hooke's Law. For brevity, only the longitudinal stresses are presented here. After this measurement the specimen was then machined down to 7 mm thickness and the stresses were remeasured. Figure 5(*b*) illustrates the longitudinal stress re-distribution that was found on the center line of a 2024-T4 MIG welded specimen as a result of this mechanical processing. As can be seen from Fig. 5(*b*), the peak stresses are not changed after machining but the width of the central area containing the tensile residual stresses is slightly reduced. Note that the residual stress directions are related to both the weld direction and plate geometry and these definitions apply to all measurements given in this paper. The error on each of the stress measurements shown in Fig. 5 is of the order of $\pm$10 MPa. Unless otherwise plotted on the graph this value may be taken to be the error of all stress measurements reported here.

Typical Residual Stress Results

Complete cross-sectional mapping of the full stress tensor was carried out for many of the welds and fracture mechanics specimens involved in this study; details of both the methods used and the results

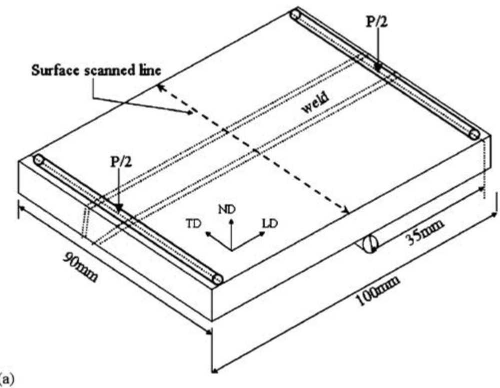

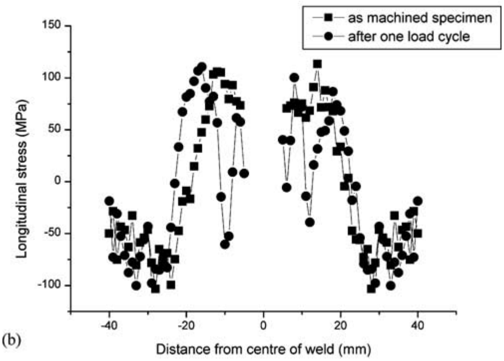

FIG. 6—*(a) Schematic figure showing test, weld, and measurement geometry of three point bend small fatigue crack growth specimen. (b) Near-surface longitudinal residual stresses in the 2024-T4 VPPA sample before and after the application of the first load cycle.*

obtained are published elsewhere [9,11–16]. Here, for brevity, line measurements of longitudinal stress will be reported. For the small fatigue crack specimen, which is loaded in bending, near-surface measurements will be presented. For all the other specimens, the longitudinal residual stresses across the middle of the specimen perpendicular to the weld will be presented as described in schematic diagrams which accompany each measurement described in this paper.

Small Fatigue Crack Specimens

The three-point bend small fatigue crack growth specimens had dimensions 80 mm by 80 mm by 7 mm [Fig. 6(*a*)]. The near-surface residual stresses in both the as-prepared specimens and after the application of the first tensile stress cycle (300 MPa), were determined [17]. As can be seen from the 2024-T4 VPPA results shown in Fig. 6(*b*), (where the stresses are measured using an effective gage volume covering a depth of 500 mm centerd at a depth of 650 mm below the tensile surface) stress redistribution does occur on first loading as relatively high stresses (in this case 300 MPa) are often used in short fatigue crack growth testing.

Long Fatigue Crack Specimen Stresses

Long fatigue crack growth propagation rates across the weld were monitored in two specimen types. Most of the testing was performed on 300 by 80 by 7 mm middle tension [M(T)] panels. Some comparison testing was also carried out on 7 mm thick compact-tension (CT) specimens with $W=70$ mm. The preparation of the 80 mm wide M(T) samples from the 186 mm wide, 7 mm thick weld coupons further

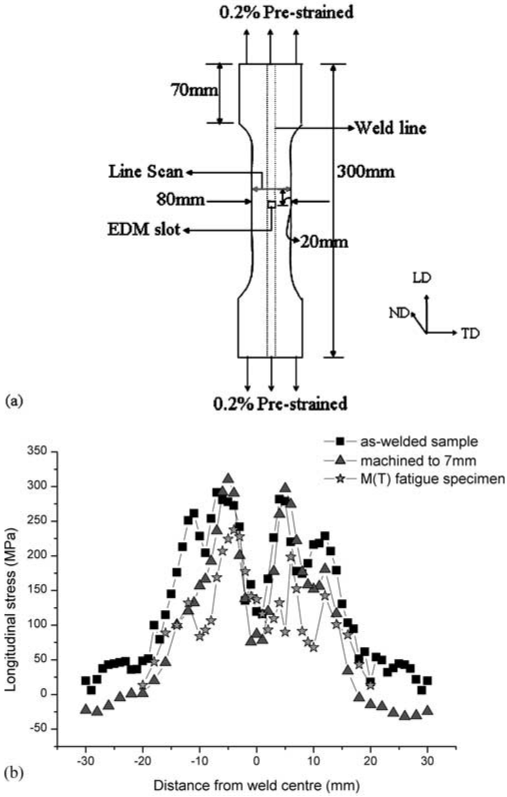

FIG. 7—*(a) Schematic of M(T) specimen showing weld and measurement geometry. (b) Longitudinal stresses in 2024-T4 MIG M(T) long fatigue crack growth specimens.*

relieved the longitudinal residual stress as can be seen from Fig. 7 which shows the stress evolution in the production of a 2024-T4 M(T) specimen. It can be seen that while reducing the thickness of the original welded plates from 12 to 7 mm had little effect on the peak longitudinal stresses, reduction of the transverse width of the plates resulted in a drop in peak longitudinal stress of nearly 150 MPa. The production of the CT specimens caused an even larger redistribution, caused principally by the introduction of the notch. Figure 8 plots the longitudinal stress in a 2024-T4 MIG CT specimen. It can be seen by comparison of this figure with Fig. 7 that there are significant changes in both the size and shape. The introduction of the notch in the CT specimen has caused the residual stresses to be no longer symmetric with respect to the weld. There is a substantial reduction in the peak tensile longitudinal stress from 225 to 130 MPa and the crack tip now sees a compressive longitudinal stress of 50 MPa.

Skin-Stringer Fatigue Specimen Stresses

The skin-stringer fatigue specimen, which was designed in this study using the data obtained from the as-welded coupon stresses, is very large (1240 by 170 by 77 mm) and thus can only be measured using the latest state-of-the-art neutron diffractometers such as the ENGIN-X diffractometer at ISIS pictured in Fig. 4 [10]. The design of this specimen is discussed later in this paper but a schematic figure of the specimen cross section showing the position of the welds is shown in Fig. 9(*a*). The longitudinal residual stress measured along the web and doubler of the 2024-T4 VPPA skin-stringer fatigue specimen [see schematic Fig. 9(*b*) for the positions of the two measurement lines] are shown in Fig. 9(*c*). It can be seen that the longitudinal stress in the web is asymmetric with respect to the weld and the peak stress (150 MPa) occurs

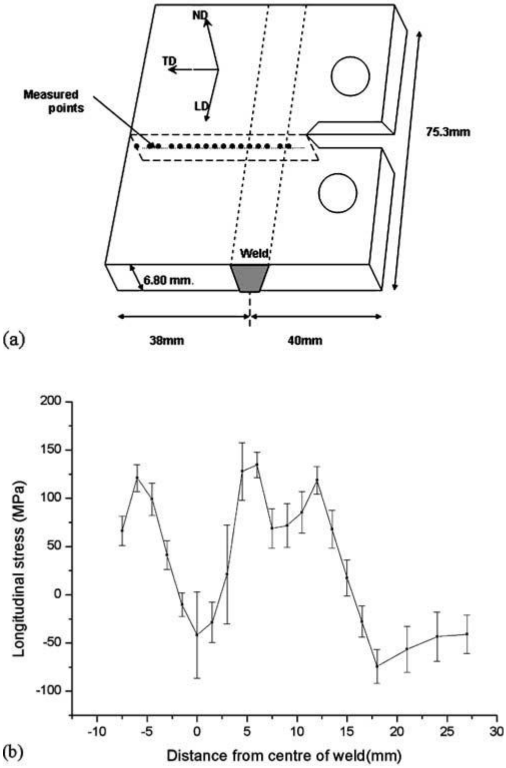

FIG. 8—*(a) schematic of specimen showing weld and measurement geometry of 2024-T4 MIG W* =70 mm *CT specimen (b) measured longitudinal residual stress along the crack line.*

away from the skin toward the top of the stiffener. On the other side of the stiffener weld, near to the skin, the peak longitudinal stress is lower (100 MPa), a value consistent with that found across the doubler. The lower stresses found on the skin side of the weld are probably the result of lower temperatures being achieved there during welding due to the whole skin acting as a heat sink.

Short Fatigue Crack Initiation and Growth

The initiation and growth of short fatigue cracks was studied in three-point bend loading (using the 80 by 80 by 7 mm^3 sample and loading geometry described in Fig. 6(*a*), at constant cyclic load amplitudes and a *R* ratio (minimum stress/maximum stress) of 0.1. Samples were loaded in the longitudinal orientation (i.e., parallel to the weld line), consistent with the final skin-stringer demonstrator structure. Scanning electron microscopy (SEM), transmission electron microscopy (TEM), optical microscopy, hardness mapping, and differential scanning calorimetry were also used to elucidate the local microstructural conditions of the regions in and around the welds (particularly identifying the competition between ageing, overageing, resolutionizing, and reprecipitation occurring across the HAZ).

It was found that several fatigue crack initiation processes may occur within the welds and associated HAZs, each with its own implications for performance/lifing. Fatigue life of the MIG welds was seen to be controlled by fusion zone behavior, determined by the combined effects of interdendritic defect size, crack coalescence, and residual stresses. Quantitative analysis showed that while interdendritic defects in the MIG weld were distinctly smaller than the gas bubbles (up to ~50 μm for the interdendritic defects, as opposed to ~200 μm for the bubbles), the interdendritic defects were more prominent initiation sites (consistent with their angular morphology and damaging colocation of intermetallic particles at the sharp

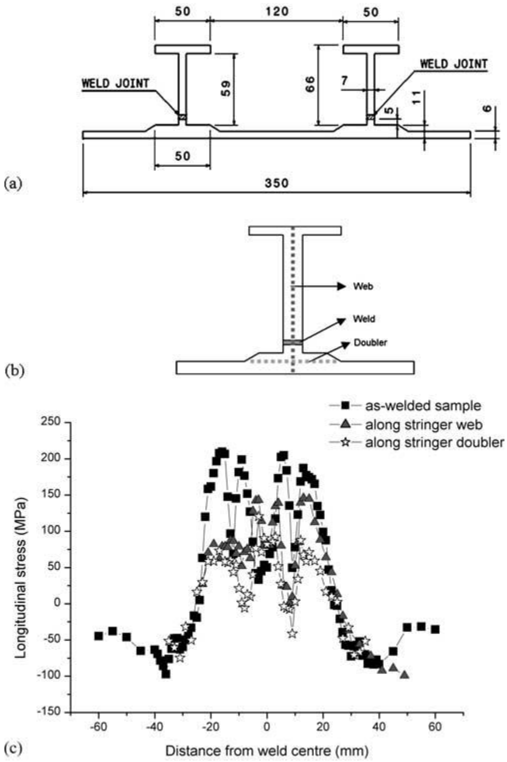

FIG. 9—*(a) Cross section of skin stringer design, (b) measurement lines, (c) longitudinal residual stresses in the web and doubler of the 2024-T4 VPPA skin stringer fatigue specimen.*

corners formed by neighboring dendrite arms), see Fig. 10. In the VPPA welds, the fusion zone presented a much finer, lower density of crack initiating defects, and although crack initiation was indeed seen in the fusion zone, failure was controlled by cracks forming at the peak residual stress location of the HAZ. Such cracks were associated with the intrinsic defect population of the parent material (intermetallic particle clusters).

Within MIG weld samples it was noted that failure of the weld was dominated by multiple crack formation and coalescence, with no single dominant crack appearing until cracks coalesced right across the fusion zone (a distance of the order of 10 mm) and started to propagate into the weld heat affected zone (HAZ), see Fig. 11. In contrast, little influence of crack-crack interactions was seen in failure of the VPPA welds.

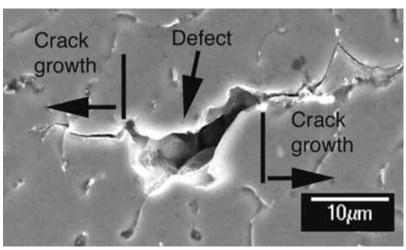

FIG. 10—*Typical crack initiation seen at small/acicular interdentric defects of MIG weld fusion zone.*

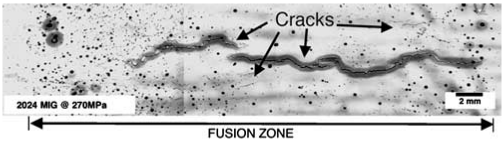

FIG. 11—*Multiple crack interaction/coalescence across MIG weld fusion zone.*

In the context of fatigue life to 1 mm total crack length, a micromechanical model has been developed for the MIG fusion zone and VPPA HAZ. The model considers the probability of initiation and the density/distribution of pores (or intermetallic particles) within a given microstructure. A Monte Carlo approach was used to simulate microstructural influence on crack initiation and crack densities. A microstructural model of short crack growth rates was then used [18], considering the local influences of grain size and flow strength on failure. The incidence of crack interactions is considered via a simple geometrical method [19]. The crack growth rate part of the modeling approach was calibrated via "subsized" coupon testing, where small bend bars (3 by 1.5 mm in cross-section, 25 mm long, see Fig. 12) were taken from specific regions of the welds: at this scale, the samples represented essentially homogeneous material that could be considered residual-stress-free as they were significantly smaller than the wavelength of the measured stress distribution. The influence of residual stress on weld failure was then considered purely in terms of crack closure via a simple closure model (going from a closure-free initial growth to steady-state long crack behavior). Predictions with and without residual stress (RS) effects were made by including the longitudinal residual stress measured at the crack initiation site after the first load cycle. Initiation actually occurred where the longitudinal residual stress was highest in Fig. 7; so the value taken was 100 MPa.

Overall it was found that the initiation/short crack fatigue behavior of both the VPPA and MIG welds could be reasonably well predicted, and Fig. 13 shows the prediction for VPPA welded 2024-T4.

Long Fatigue Crack Growth

Measurements of fatigue crack growth rates at constant load amplitude were performed on samples with three size scales: CT samples with a W dimension of 70 mm, M(T) panels 380 mm long and 80 mm gage length width with the weld on the center line, and a 1.2 m long skin—stringer panel with the stringer welded to the skin longitudinally. The three types of samples have been described when reporting their residual stress profiles earlier. Sample thickness in CT and M(T) samples was 7 mm: this was the skin thickness in the skin-stringer panel. The effects of mean stress, weld process, and alloy type on fatigue crack growth rates were systematically studied. In compact tension (CT) and middle tension [M(T)] specimens, crack lengths were monitored using a precision dc electrical potential technique. In skin-stringer panels an automated video system was used.

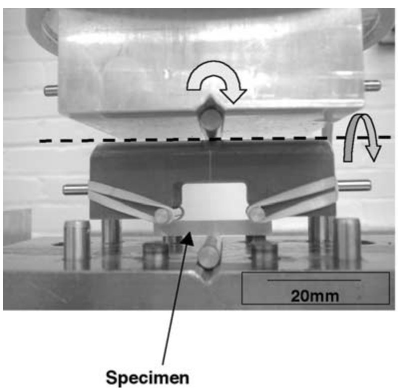

FIG. 12—*Subsize fatigue testing, showing test specimen and self-aligning bend fixtures.*

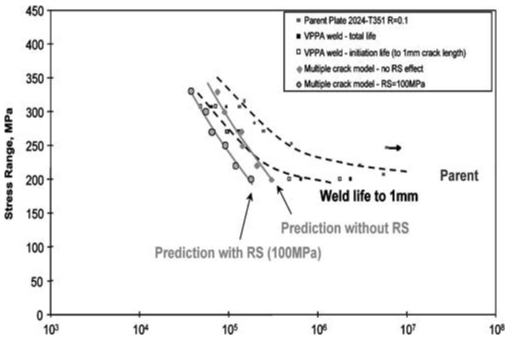

FIG. 13—*Comparison of experimental and predicted fatigue lives for VPPA welded 2024-T4: Weld life and predictions are particularly shown for a crack length of* 1 mm.

All welds were loaded parallel to their longitudinal axis, with cracks growing across them. This orientation will be relevant to aircraft applications, but it results in cracks growing across widely varying residual stress fields, accompanied by changes in microstructure and hardness. A conventional constant load range fatigue crack growth test will therefore not exhibit similitude, as crack tips at different values of stress intensity range ΔK will be subject to different crack tip conditions. Therefore additional testing was performed in which the ΔK was maintained constant with crack length, allowing the effect of changes in residual stress and microstructure on crack growth rates at a constant value of ΔK to be determined. A selection of the data gathered on the welded samples which illustrate the influence of residual stress follows.

Effect of Residual Stress on Fatigue Crack Growth Rates in Welds

Figure 14 compares fatigue crack growth rates for VPPA welded 2024-T4 with those of parent plate. Data for the welded samples is at R values of 0.1 and 0.6, and shows that there is little effect of tensile mean stress in the presence of tensile residual stresses, and second, that crack growth rates in the welded samples are accelerated with respect to the parent plate by a factor of up to a factor of 10. Tests conducted at a constant value of $\Delta K = 6$ MPam$^{1/2}$ confirm that the acceleration is maintained at approximately this level up to 25 mm from the weld line.

The dramatic influence of residual stress on weld crack growth rates is further illustrated by a comparison of growth rates produced in constant $\Delta K = 6$ MPa m$^{1/2}$ in the M(T) panels and in the CT samples.

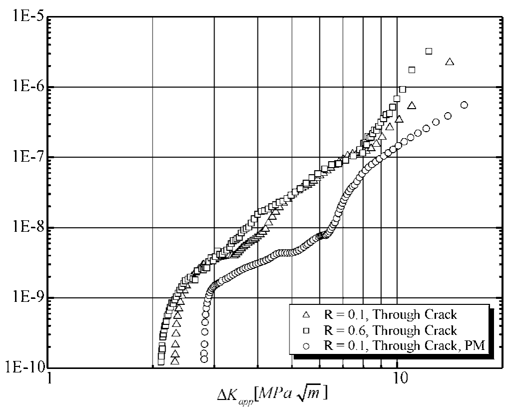

FIG. 14—*da/dN vs* ΔK *for VPPA welded 2024-T4, tested at* R=0.1 *and 0.6 in M(T) samples with* 2 mm *starting defect in center of the weld line. Comparison with parent plate at* R=0.1

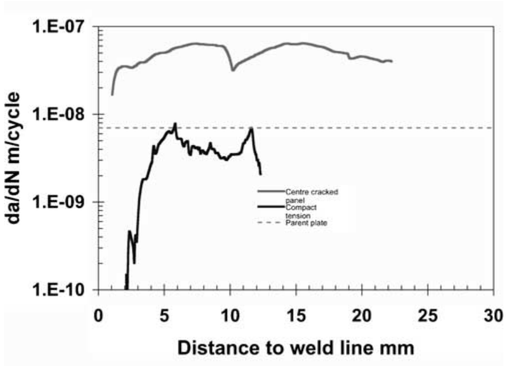

FIG. 15—*Comparison of growth rates measured in CT and M(T) samples of 2024-T4 with identical VPPA welds at a constant* ΔK *of* 6 MPa-$m^{1/2}$, R=0.1.

This is shown in Fig. 15; M(T) panels, as shown in Fig. 7, produce substantial tensile residual stresses on the weld line, whereas CT samples, a shown in Fig. 8, possess a compressive residual stress on the weld line. The growth rates in the tension residual stress field vary between 2×10^{8} and 7×10^{8} m/cycle, depending on distance from the weld line, whereas in the compact tension samples, growth rates declined to less than 10^{10} m/cycle as the crack approached the weld line, and at a maximum only achieved 7×10^{9} m/cycle—a factor of 10 slower than that in the M(T) sample with an identical weld. 7×10^{9} m/cycle is the parent plate da/dN for a ΔK value of 6 MPa $m^{1/2}$. As the welds in the two samples were virtually identical, the differences in growth rate must be due to residual stresses arising from welding and modified by the sample preparation processes.

Fatigue crack growth rates produced on testing the 2024-T4 skin-stringer panel with a defect introduced on the weld line were similar to those measured in the much smaller center cracked panel, when compared on the basis of stress intensity factor. Figure 16 shows da/dN versus ΔK for crack growth rate measured on the 2024-T4 skin-stringer panel and those measured on the center cracked panel. There is only a small overlap in the two sets of data, but the linkup is smooth with only a little scatter. This is perhaps surprising in view of the differences in residual stresses in the two samples; however, in both cases the stresses are tensile, and the crack is originating within the weld line in both samples. The CT samples demonstrate more profound changes in growth rate when the residual stresses are compressive.

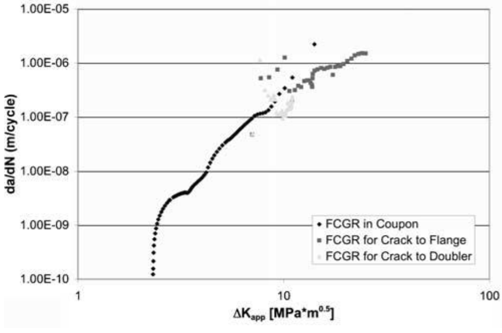

FIG. 16—*Comparative fatigue crack growth rates in the skin stringer panel and the MT long crack growth specimens.*

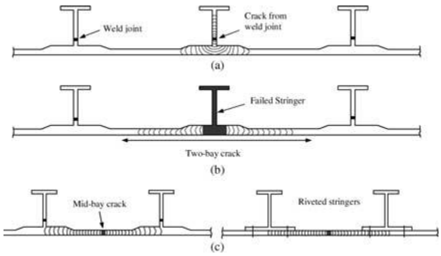

FIG. 17—*Failure scenarios: (a) Stringer failure due to flaws in weld join; (b) cracking under a broken stringer; (c) midbay skin cracks from a discrete damage source, maintenance-holes, or connection fastener holes to the ribs.*

Implications for the Design, Fail Safety and Damage Tolerance of Aircraft Wing Panels

The main objectives of this work are to develop analysis approaches to predict fatigue crack growth that include the influence of welding residual stress and to explore fail-safety design options for integral/welded stringer panels. A global-local approach combining linear elastic fracture mechanics (LEFM) with the finite element method (FEM) has been employed to investigate the influence of the measured residual stress fields and fatigue crack growth rates on the design of putative welded aircraft wing structures. Initial work performed included the design of the welded skin-stringer panels for fatigue testing, crack growth analysis of the CCT specimens, and fail-safety and damage tolerance analysis of welded stringer panels. Due to space constraints only some conclusions of the latter two studies will be reported here. The main function of this section is to illustrate how the residual stress measurements can be included in a holistic design model of the damage tolerance of welded aircraft structures. Details of fail-safety (residual strength) and damage tolerance analysis (fatigue crack growth and inspection) can be found in [20].

Design of Two-Stringer Welded Wing Skin Panels for Fatigue Testing

The design constraints (decided by the WELDES consortium) were that the weld joint in the stringer should be in the web close to the skin panel and the thickness of all weld samples are 7 mm (after post-weld machining). In addition, the panel had to be capable of being tested in the available 1 MN fatigue-testing machine. An "I" section was adopted to represent the wing's lower covers, in order to make comparisons with similar built-up designs. The final design configuration was shown in Fig. 9(*a*). The stringer to skin area ratio (A_{st}/bt) is defined as the ratio of the stiffener cross-section area (A_{st}) to the product of the bay width (b) and skin thickness (t). It is 1.03 for the tension panel.

Damage Tolerance and Fail-Safety Analysis of Welded Stringer Panels

Welded stringer panels behave like integrally machined panels; both are unitized structures without redundancy structural members. In contrast, the mechanically fastened (built-up) panels are desirable in terms of fail-safety criterion since the stringers are effective crack stoppers. However, the integral and welded panels are becoming increasingly popular due to much reduced manufacturing cost and considerable weight savings. It is necessary and timely to investigate the fail-safety and damage tolerance aspects of this kind of stringer panel.

The first failure scenario considered was crack initiation and subsequent propagation from the weld joint at the stringer web [Fig. 17(*a*)]. The welded joint has high tensile residual stresses and local micro-structural change resulting in lower fatigue strength (crack initiation aspect) and faster crack growth rate (crack propagation aspect). Another important failure mode is a crack propagating in the panel skin, e.g., crack under a broken stringer in Fig. 17(*b*) and a midbay skin crack in Fig. 17(*c*).

For built-up panels the bolted stringers act as effective crack stoppers to arrest these cracks. However, the welded or integral stringers are not so effective; they will slow down the crack growth rate as the crack tip approaches an integral stringer due to the integral fastening system being completely rigid hence reducing the stress intensity factor (K), but these stringers will not act as crack stoppers. Analyses were performed for both damage tolerance (crack growth life) and fail-safety (residual strength and large crack

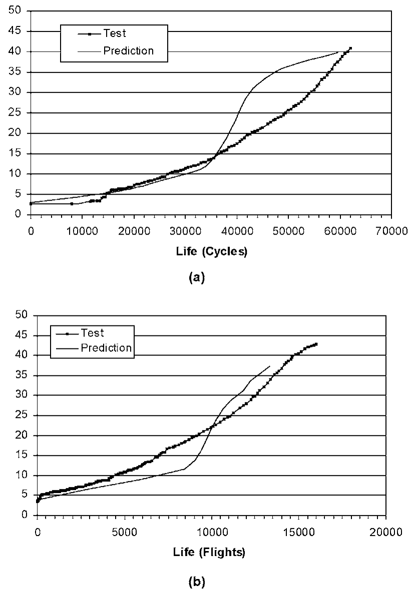

FIG. 18—*Stringer web cracking from the weld joint—predicted fatigue crack growth life and comparison with test results. (a) Tension panel under CAL (*S_{max}=88 MPa, R=0.1*); (b) tension panel under aircraft service load spectrum* (S_{max}=138 MPa).

capability) aspects. The stress intensity factor (K) versus crack length relation for the skin-stringer panels was established by finite element analysis (FEA). FEA was then used to calculate crack closure induced changes to derive ΔK_{eff}, taking into account extra plasticity effects arising from local softening in the HAZ and weld residual stress effects. In this first approach, crack opening stress is assumed to be a function of the stress ratio (R) and welding residual stress and *not* related to geometry. For a given structure, once the ΔK and the crack opening stress are found, fatigue life prediction was carried out for a given load spectrum using the AFGROW software package. This approach works well for the constant amplitude loading cases. For variable amplitude loads, an alternative approach was used. The welding residual stress distribution was simply input into the AFGROW code that calculates the residual stress intensity factor by either GAUSSIAN integration or weight function methods and then predicts fatigue crack growth life. Life prediction by both methods is demonstrated below.

Life Prediction Results

For the two-stringer panel, we assumed that one stringer has a defect at the weld joint with the total length of 6 mm. This flaw could be caused by fatigue process and the local residual tensile stresses or an initial weld defect. So this is a real threat to welded structural panels under the damage tolerance design concept. The crack is supposed to grow simultaneously toward the stringer upper flange and the skin doubler. This was simulated by moving the two crack tips in both directions simultaneously. The virtual crack closure technique (VCCT) was used to calculate the strain energy release rate that was then converted to a stress intensity factor (SIF). Figure 18 shows the life prediction results under constant amplitude and aircraft service loading spectra, respectively. The agreement with the test results is reasonably good for this complex problem. Further work is necessary to address the effect of residual stress relaxation and redistribution owing to crack growth. This may improve the accuracy of life prediction.

Conclusions

The WELDES project has uniquely integrated the powerful recent developments in non-destructive residual stress measurement using neutron and synchrotron X-ray diffraction with the damage tolerance data acquisition and design necessary to implement welded aircraft structures. Significant new knowledge has been obtained and a mechanism for dealing with the loss of similitude that occurs when residual stresses are present in structures has been developed. It is shown that if accurate reliable residual stress data is available then adequate predictions of the fatigue life of welded structures can be made.

References

[1] Heinz, A., Haszler, A., Keidel, C., Moldenaur, S., Benedictus, R., and Miller, W. S., "Recent Developments in Aluminium Alloys for Aerospace Applications," *Mater. Sci. Eng., A* 280(2), 102–107 (2000).

[2] Fitzpatrick, M. E. and Edwards, L., "Fatigue Crack/Residual Stress Field Interactions and Their Implications for Damage-Tolerant Design," *J. Mater. Eng. Perform.* 7(2), 190–198 (1998).

[3] Mendez, P. F., "New Trends in Welding in the Aeronautic Industry," *Proceedings of the Conference "New Trends for the Manufacturing in the Aeronautic Industry*," Publ. Hegan/Inasmet, San Sebastian, Spain, 2000.

[4] Angus, W. Thomas, "Parameter Development for the Mig Weldings of High Strength Aerospace Aluminium Alloys," *Ph.D thesis*, School of Industrial and Manufacturing Science Cranfield University, 2002.

[5] Nunes, A. C., Bayless, E. O., Jones, C. S., Munafo, P. M., Biddle, A. P., Wilson, W. A., Nuflez, A. C., and Bayless, E. O., "Variable Polarity Plasma Arc Welding on the Space Shuttle External Tank," *Weld. J. (Miami, FL, U. S.)* 63(9), 27–35 (1984).

[6] Woodward, H., "International Space Station-Welding Will Be Out of This world," *Weld. J. (Miami, FL, U. S.)* 75(3), 34–40 (1996).

[7] Withers, P. J. and Webster, P. J., "Neutron and Synchrotron Strain Scanning," *Strain* 37(1), 19–25 (2001).

[8] ISO/TTA 3:200I, "Polycrystalline Materials—Determination of Residual Stresses by Neutron Diffraction."

[9] Stelmukh, V., Edwards, L., Santisteban, J. R., Ganguly, S., and Fitzpatrick, M. E., "Weld Stress Mapping Using Neutron and Synchrotron X-Ray Diffraction," *Mater. Sci. Forum* 404–407, 599–604 (2002).

[10] Daymond, M. R. and Edwards, L., "A Fully Refined Diffractometer Designed Specifically for the Measurement of Stress," *Neutron News* 15, 24–29 (2004).

[11] Stelmukh, V., Edwards, L., and Ganguly, S., "Full Stress Tensor Determination in a Textured Aerospace Aluminium Alloy Plate Using Synchrotron X-Ray Diffraction," *Textures Microstruct.* 35(3–4), 175–183 (2003).

[12] Zhang, Y., Fitzpatrick, M. E., and Edwards, L., "Cross-Sectional Mapping of Residual Stresses in a VPPA Weld Using the Contour Method," *Acta Mater.* 52(17), 5225–5232 (2004).

[13] Stelmukh, V. and Edwards, L., "Optimizing Neutron Strain Scanning by the Use of Electron Backscatter Diffraction," *Microscopy and Analysis* 91, 2002, pp. 15–18.

[14] Ganguly, S., Fitzpatrick, M. E., and Edwards, L., "Use of Neutron and Synchrotron X-ray Diffraction for Non-destructive Evaluation of Weld Residual Stresses in Aluminium Alloys," *J. Neutron Res.* 11, 219–225 (2004).

[15] Ganguly, S., Fitzpatrick, M. E., and Edwards, L., "Comparative Neutron and Synchrotron X-Ray Diffraction Studies to Determine Residual Stress on an As-Welded AA2024 Plate," *Mater. Sci. Forum* 490, 223–228 (2005).

[16] Pratihar, S., Stelmukh, V., Hutchings, M. T., Fitzpatrick, M. E., Stuwe, U., and Edwards, L., "Measurement of the Residual Stress in MIG Welded 2024-T351 and 7150-T651 Compact Tension Samples," *Mater. Sci. Eng.* to be published.

[17] Lefebvre, F., Ganguly, S., and Sinclair, I., "Micromechanical Aspects of Fatigue in a MIG Welded Aluminium Airframe Alloy," *Mater. Sci. Eng., A* 397, 338–354 (2005).

[18] Edwards, L. and Zhang, Y. H., "Investigation of Small Fatigue Cracks. II. A Plasticity Based Model of Small Fatigue Crack Growth," *Acta Metall. Mater.* 42(4), 1423–1431 (1994).

[19] Hünecke, J. and Schöne, D., "Short Crack Behaviour in a Low Carbon Steel under Fatigue Loading," *Proc Fatigue 2002*, edited by A. F. Blom, ISBN 19015372853, 2002, pp. 2021–2028.

[20] Zhang, X. and Li, Y., "Damage Tolerance and Fail Safety of Welded Aircraft Wing Panels," *AIAA J.* 43(7), 1613–1623 (2005).

Journal of ASTM International, June 2005, Vol. 2, No. 6
Paper ID JAI12564
Available online at www.astm.org

Ajit K. Roy,[1] *Anand Venkatesh,*[2] *Satish Dronavalli,*[2] *Vikram Marthandam,*[2] *Douglas Wells,*[3] *Farida Selim,*[4] *and Ronald Rogge*[5]

Residual Stress Measurements in Welded and Plastically Deformed Target Structural Materials

ABSTRACT: Transmutation of spent nuclear fuels (SNF) is currently being considered to transform long-lived isotopes to species with relatively short half-lives and reduced radioactivity through capture and decay of minor actinides and fission products. This process is intended for geologic disposal of SNF for shorter durations in the proposed repository at the Yucca Mountain site. The structural material (Type 304L stainless steel/Alloy EP-823) surrounding the transmutation target will be subjected to welding operation and plastic deformation during fabrication, which could induce residual stresses in it. Destructive ring-core, and nondestructive x-ray diffraction, neutron diffraction, and positron annihilation spectroscopic techniques were used to evaluate residual stresses in welded and cold-worked specimens of both materials. The results indicate that, in general, for a welded specimen consisting of Alloy EP-823 and Type 304L stainless steel on opposite sides, compressive and tensile residual stresses were observed in the former and latter materials, respectively. However, a welded specimen consisting of only Alloy EP-823 on both sides showed tensile residual stresses. The extent of residual stresses in cold-worked specimens was enhanced with increased level of cold-reduction. In case of a bent specimen, compressive and tensile residual stresses were noticed in the convex and concave sides, respectively.

KEYWORDS: transmutation, martensitic alloys, residual stress, positron annihilation spectroscopy, neutron diffraction, ring-core

Introduction

When subjected to tensile loading beyond a limiting value, metals and alloys can undergo plastic deformation resulting in lattice defects, such as voids and dislocations. These imperfections may interact with the crystal lattice, producing a higher state of internal stresses characterized by reduced ductility. Residual stresses can also be developed in welded structures due to rapid rate of solidification and dissimilar metallurgical microstructures between the weld and base metals. Development of these internal stresses is often influenced by incompatible permanent strains resulting from thermal and mechanical operations associated with plastic

---

Manuscript received 25 March 2004; accepted for publication 2 March 2005; published June 2005. Presented at ASTM Symposium on Residual Stress Effects on Fatigue and Fracture Testing and Incorporation of Results into Design on 19–21 May 2004 in Salt Lake City, UT.
[1] Associate Professor, Department of Mechanical Engineering, University of Nevada, Las Vegas, 4505 Maryland Parkway, Box 454027, Las Vegas, NV 89154.
[2] Graduate Student, Department of Mechanical Engineering, University of Nevada, Las Vegas, 4505 Maryland Parkway, Box 454027, Las Vegas, NV 89154.
[3] Associate Professor, Department of Physics, Idaho State University, Campus Box 8106, 785 S. 8th Ave., Pocatello, ID 83209.
[4] Post Doctoral Researcher, Department of Physics, Idaho State University, Campus Box 8263, 785 S. 8th Ave., Pocatello, ID 83209.
[5] Senior Research Officer, National Research Council, Neutron Program for Materials Research, Building 459, Chalk River Laboratories, Chalk River, Ontario, CANADA, KOJ 1JO.

deformation. These types of operation can produce premature failures in engineering metals and alloys unless these residual stresses are relieved by specific thermal treatments commonly known as stress-relief operations.

During transmutation of spent nuclear fuels, the structural materials surrounding the target, such as molten lead-bismuth-eutectic, may experience a significant amount of residual stresses due to plastic deformation and welding. Therefore, characterization of residual stresses in plastically-deformed and welded candidate target structural materials seems appropriate. The destructive ring-core (RC) method has been used to estimate residual stresses based on the strain relieved during the coring operation. Simultaneously, non-destructive techniques, including positron annihilation spectroscopy (PAS), neutron-diffraction (ND), and X-ray diffraction (XRD), have been used to characterize residual stress in austenitic and martensitic stainless steels that were subjected to either cold-deformation or welding operations. The test materials were cold reduced by 7 and 11 % of their plate thickness. In addition, plastic deformation in rectangular beams was produced by three-point-bending. Welded specimens consisting of similar and dissimilar structural materials on both sides were also evaluated for residual stress characterization. The comprehensive results including the metallographic evaluations are presented in this paper.

Experimental

Materials tested include austenitic Type 304L Stainless Steel and martensitic Alloy EP-823. Their chemical compositions are shown in Table 1. Experimental heats of both materials were melted by vacuum-induction-melting practice. They were subsequently forged and rolled into plate materials of desired dimensions. These materials were then heat treated prior to the machining of the test specimens. Type 304L SS plates were austenitized at 1850°F for 1 h followed by air cooling, thus producing a fully austenitic microstructure. Alloy EP-823 was austenitized at a similar temperature followed by an oil quench. The quenched plates were subsequently tempered at 1150°F followed by air-cooling. This type of thermal treatment produced fully-tempered martensitic microstructure without any retained austenite.

TABLE 1—*Chemical composition of materials tested (wt%).*

Bal – Balance.

Material	Elements (wt %)															
	C	Mn	P	S	Si	Cr	Ni	Mo	Cu	V	W	Cb	B	Ce	Al	Fe
Alloy EP-823	0.17	0.54	0.005	0.004	1.11	11.69	0.65	0.7	0.01	0.34	0.6	0.26	0.005	0.08	0.02	Bal
Type 304L SS	0.02	1.63	0.003	0.005	0.40	18.20	9.55	0.03	0.03	…	…	…	…	…	0.01	Bal

A part of the heat-treated plates was further plastically deformed by cold rolling to reduce the plate thickness by approximately 7 and 11 %. Some of the heat-treated rectangular beams were deformed by three-point bending to produce a gradual residual stress gradient along the length. Prior to deformation, these beams were electropolished to remove the surface cold work resulting from the machining operation. The center of these beams was displaced 1.5 in. during the bending process. The outer supports were separated by 10 in. Welded specimens consisting of similar and dissimilar metals (Alloy EP-823 and Type 304L stainless steel) on opposite sides were prepared using the gas-tungsten-arc-welding (GTAW) method. The specimens' configurations are shown in Fig. 1. Four different techniques, namely γ-ray induced PAS, XRD, ND, and RC methods were used to characterize the residual stresses induced in the test specimens due to plastic deformation and welding.

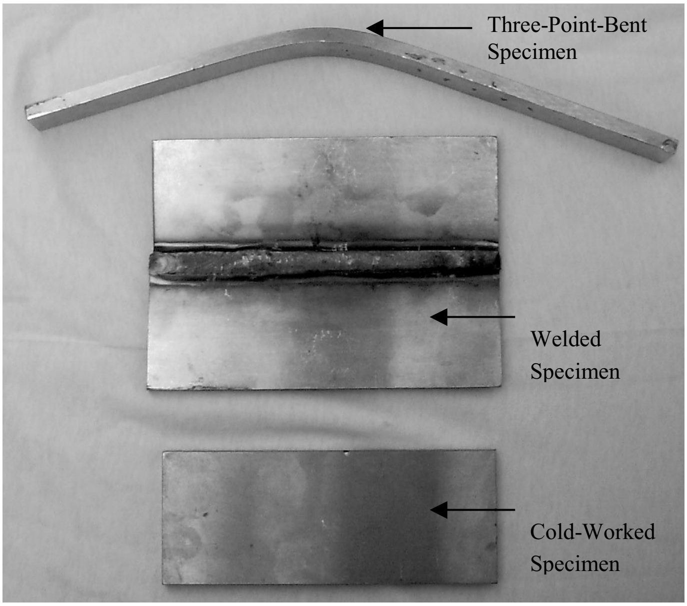

FIG. 1—*Test specimen configurations.*

Positron Annihilation Spectroscopic Technique

Positron Annihilation Spectroscopy (PAS) is a well-established non-destructive technique to characterize defects in materials [1]. However, the conventional PAS technique uses slow positron beams or wide energy spectrum beams from radioactive sources. The thickness of samples under investigation is severely limited by the range of the impinging positrons embedded inside the sample [2]. The technique used in this investigation employed high penetrability γ-rays to extend positron annihilation spectroscopy into thick samples and to enable characterization of stress, strain, and defects in materials of interest. The collimated bremsstrahlung beam from a linear accelerator (6 MeV pulsed Linac) was used to create positrons inside the test specimen via pair production (Fig. 2). This photon beam has a wide energy spectrum up to 6 MeV. No photon-induced activation was involved in this process. Each positron generated by this technique was thermalized and annihilated with one of the sample electrons emitting two annihilated photons having 511 keV energy back to back. These annihilated photons were recorded by a high-energy resolution HPGe detector, and the resultant data were analyzed in terms of three line shape parameters, namely S, W, and T (Fig. 3), of the 511 keV annihilation peak [2,3]. The residual stresses developed in the test specimens were qualitatively analyzed using these three parameters.

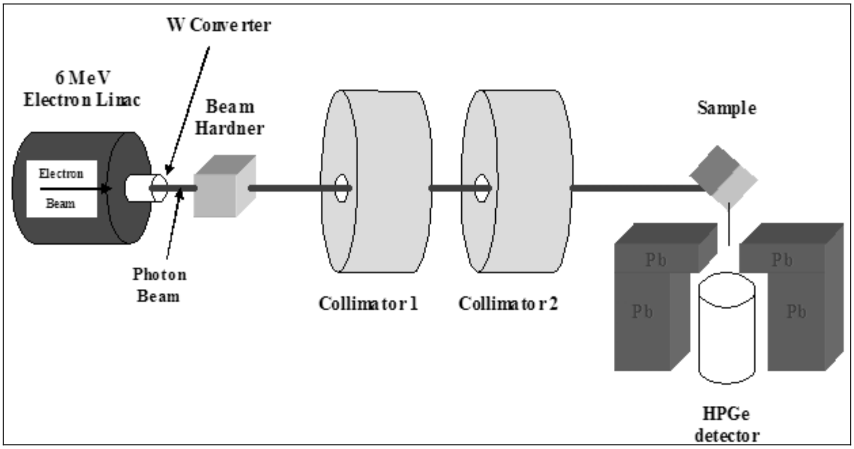

FIG. 2—*PAS test setup.*

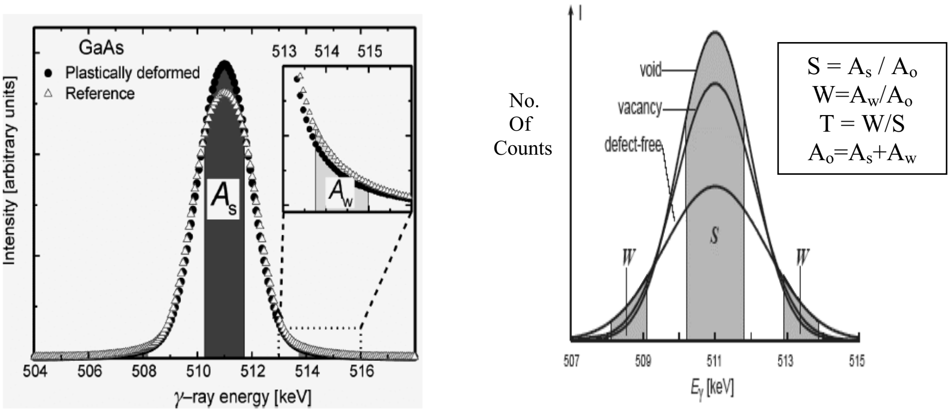

(a) (b)

A_s = Area of the central region of the peak
A_w = Area of the wing region of the peak
A_o = Total area of the peak

FIG. 3—*Characteristics of 511 KeV γ –ray energy spectrum.*

X-Ray Diffraction Technique

The X-Ray Diffraction (XRD) technique exploits the fact that when a metal is under stress (applied or residual), the resulting elastic strains cause the atomic planes in the metallic crystal structure to change their spacing. Since metals are composed of atoms arranged in a regular three-dimensional array to form a crystal, most metallic components of practical concern consist of many tiny crystallites (grains) randomly oriented with respect to their crystalline arrangement and fused together to make a bulk solid. When such a polycrystalline metal is subjected to stress, elastic strains are produced in the crystal lattice of the individual crystallite. The XRD method can measure these interatomic spacings, which are indicative of the elastic strain in the specimen. Changes in the interatomic spacing can, therefore, be related to the elastic strain in the material and, hence, to the stress [4]. This technique involves repeated scanning of a selected peak with the specimen orientated at an increasing angle to the incident beam (Fig. 4). The x-ray beam is directed onto the sample surface at a location of interest. The diffracted beam is detected by a position sensitive proportional counter. The angular position (2θ) of the diffracted beam is used to calculate the distance (d-spacing) between parallel planes of atoms using the Bragg's law. A series of measurements made at different x-ray beam approach angles (ψ) are used to fully characterize the d-spacing. The slope of the least squares fit on a graph of the d-spacing versus $\sin^2 \psi$ is used to calculate the stress.

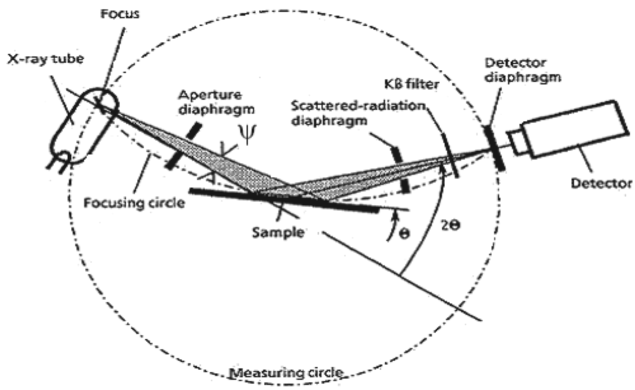

FIG. 4—*Conventional XRD testing technique.*

Neutron Diffraction Technique

Like other diffraction techniques, the Neutron Diffraction (ND) method relies on elastic deformations within a polycrystalline material that cause changes in the spacing of the lattice planes from their stress-free value. Although stress measurement by the XRD method is a well established technique, it is practically limited to near-surface stresses [5–7]. Measurements by ND are carried out in much the same way as with XRD, with a detector moving around the sample, locating the positions of high intensity diffracted beams. The greatest advantage that neutrons have over x-rays is their capability to penetrate into greater depths that make them suitable for measurements at near surface depths of around 0.2 mm down to bulk measurements of up to a few centimeters. With high spatial resolution, ND can provide complete three-dimensional strain maps of engineered components. This is achieved through translational and rotational movements of the component. In a typical neutron diffraction experiment, a collimated neutron beam of certain wavelength is diffracted at an angle of 2θ by the polycrystalline sample, which passes through a second collimator and reaches the detector (Fig. 5). The slits of the two collimators define the 'gauge' volume, the cross-section of which can be as small as 1 mm × 1 mm and, in special cases, even smaller. The interplanar distance, *d*, can be evaluated using the

Bragg's law, and the corresponding lattice strain can be evaluated. The stress values can, therefore, be determined from these strain readings using appropriate mathematical formulae. This method of stress evaluation, with the capacity for collecting large quantities of data (via position sensitive detectors) over the whole surface and depth (depending on the thickness of the sample) has made ND a particularly useful technique for the validation of theoretical and numerical models [8,9].

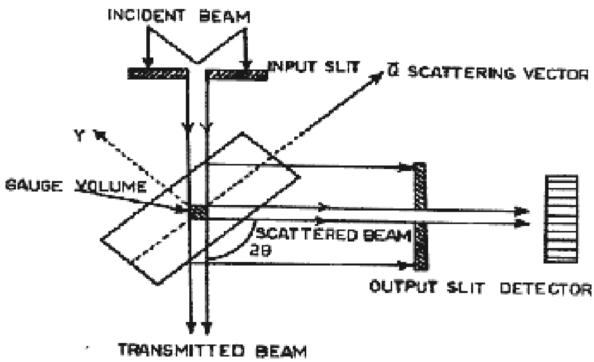

FIG. 5—*ND experimental setup.*

Ring-Core Technique

The ring-core (RC) method is a mechanical/strain gage technique employed to determine the principal residual stress as a function of depth in polycrystalline and/or amorphous material. This method involves the localized removal of stressed material using an incremental ring coring (mechanical dissection) device and measurement of strain relief in the adjacent material [10]. Strain gage rosettes are usually employed to measure the relieved strains. The method used in this study consisted of dissecting the desired location by a nominally 0.25-in. diameter plug containing the strain gages (Fig. 6). A total nominal depth of 70×10^{-3} in. was cut by this plug at increments of 2×10^{-3} in. The relieved strain measurements were made on the surface of the material remaining inside the ring. The residual stresses existing in the material before ring coring were calculated from the measured relieved strains.

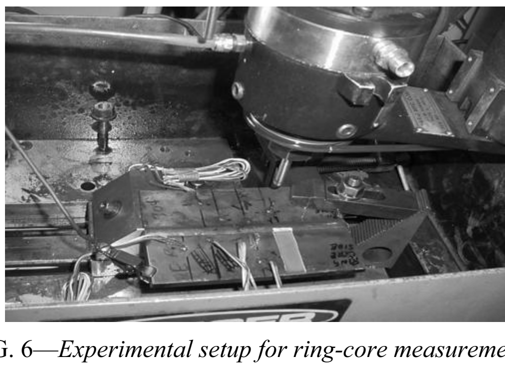

FIG. 6—*Experimental setup for ring-core measurements.*

Results and Discussion

The characterization of residual stresses was carried out using all four techniques mentioned earlier. A comparative analysis of the residual stresses measured using these techniques has been preferred to validate the resultant data.

PAS Data

The PAS data on the cold-worked specimens of Type 304L SS revealed reduced values of T-parameter with increasing degree of cold work (Fig. 7). The control specimen, which had no cold reduction, showed the highest T-value. These results suggest that the magnitude of the T-parameter is inversely proportional to the degree of cold-reduction. Interestingly, the extent of reduction in the T-parameter for this alloy was more pronounced between 7 and 11 % cold reduction compared to that of Alloy EP-823 within the same cold reduction range, as illustrated in Fig. 8. The insignificant reduction in the T-parameter for Alloy EP-823 may be attributed to the enormous amount of stress initially needed to cause plastic deformation during cold rolling of Alloy EP-823. However, as appreciable amount of plasticity was achieved by 7 % reduction in thickness, this material was relatively free to enable dislocations to move through the lattice, thus needing less stress to produce additional reduction in thickness beyond 7 %.

XRD Data

Measurement of residual stresses by the XRD technique was carried out on welded specimens consisting of similar (Alloy EP-823/Alloy EP-823) and dissimilar (Alloy EP-823/Type 304L SS) metals. The residual stress distribution in the former configuration was found to be predominantly tensile in nature. Tensile stresses were as high as +15 ksi (103.4 MPa) near the weld. In contrast, the residual stress in the Alloy EP-823 side of the Alloy EP-823/Type 304L SS sample was compressive along the fusion line up to a nominal distance of 1 in. Maximum compressive stress of –35 ksi (241.3 MPa) was observed near the fusion line (Fig. 9). This variation in the nature of stress distribution (tensile versus compressive) can be attributed to the difference in the rate of solidification among the two base materials and the weld material during rapid heating and cooling of the welded specimen. XRD measurements were not possible on the welded Type 304L SS specimen due to its coarse-grained microstructure.

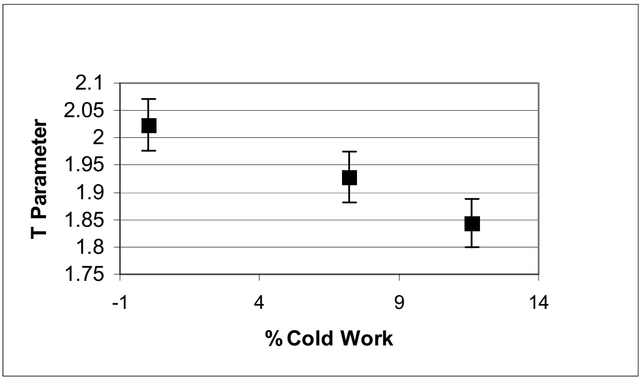

FIG. 7—*PAS measurements on type 304L SS cold-worked specimens.*

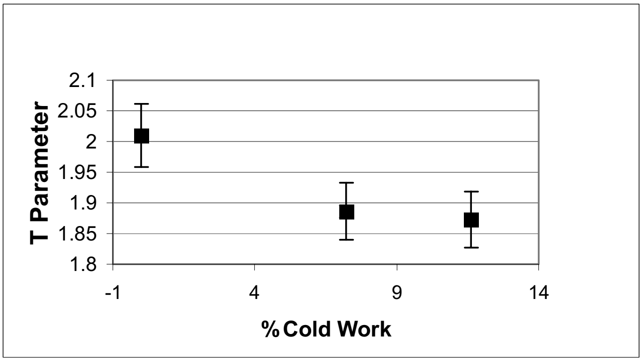

FIG. 8—*PAS measurements on alloy EP-823 cold-worked specimens.*

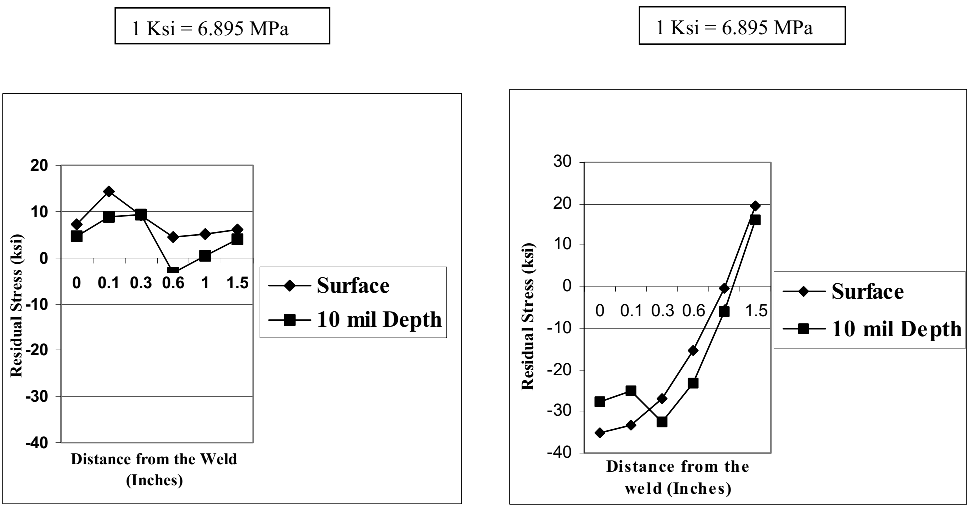

(a) (b)

FIG. 9—*XRD Measurements on:* a*) Alloy EP-823 / Alloy EP-823 and* b*) Alloy EP-823 / Type 304 L SS welded specimen (measured on the alloy EP-823 side only).*

Stress measurements performed on the bent specimen of Alloy EP-823 by the XRD method revealed compressive residual stresses in the convex side and tensile residual stresses on the concave side of the bent specimen (Fig. 10). The magnitude of the maximum residual stress was approximately $\pm$40 ksi (275.8 MPa) at the bent region, with varied stress levels away from the center, as expected.

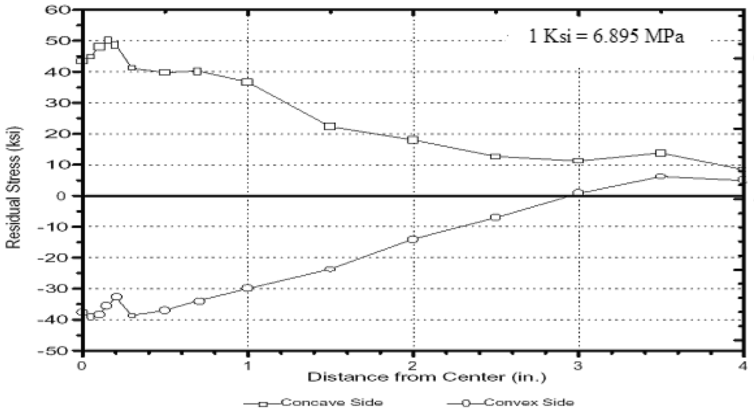

FIG. 10—*XRD measurements (longitudinal) on EP-823 three-point-bent specimen.*

Comparison of ND and RC Data

The results of residual stress measurements on a welded specimen consisting of Alloy EP-823 and Type 304L SS by neutron diffraction (ND) and ring-core (RC) techniques are illustrated in Figs. 11 and 12. The analyses of these data have been performed considering individual measurements either on the Alloy EP-823 side or on the Type 304L SS side using both techniques for comparison purposes. For the EP-823 side of this welded specimen, there is a clear indication that the residual stresses measured by either technique near the fusion line were compressive in nature (Figs. 11*a* and 11*b*). On the contrary, the measured residual stresses on the Type 304L SS side were tensile in the vicinity of the fusion line, as shown in Figs. 11*c* and 11*d*. The observations made from these analyses may be attributed to the different rates of solidification during the welding process involving Alloy EP-823 and Type 304L SS, which are characterized by different chemical composition, thermal treatment, and the resultant metallurgical microstructures.

The analyses of residual stresses measured by either technique at a distance of 1.0 in. from the fusion line indicate that the residual stresses on the EP-823 side (Figs. 12*a* and 12*b*) gradually became more positive, indicating the development of reduced compressive stresses away from the fusion line, as expected. Conversely, the measured residual stresses on the Type 304L SS side by both techniques gradually became more positive, indicating increased tensile stresses away from the fusion line up to a certain depth, as shown in Figs. 12*c* and 12*d*. However, beyond certain depth, the ND technique showed gradual increase in residual stresses while the RC measurements showed more or less similar values of residual stresses. The reason for this inconsistent behavior on the Type 304L SS side of the welded specimen at a distance of 1.0 in. from the fusion line is unexplainable. Additional experimental data may shed some light on this behavior. Nevertheless, in general, the data generated by both techniques showed similar patterns.

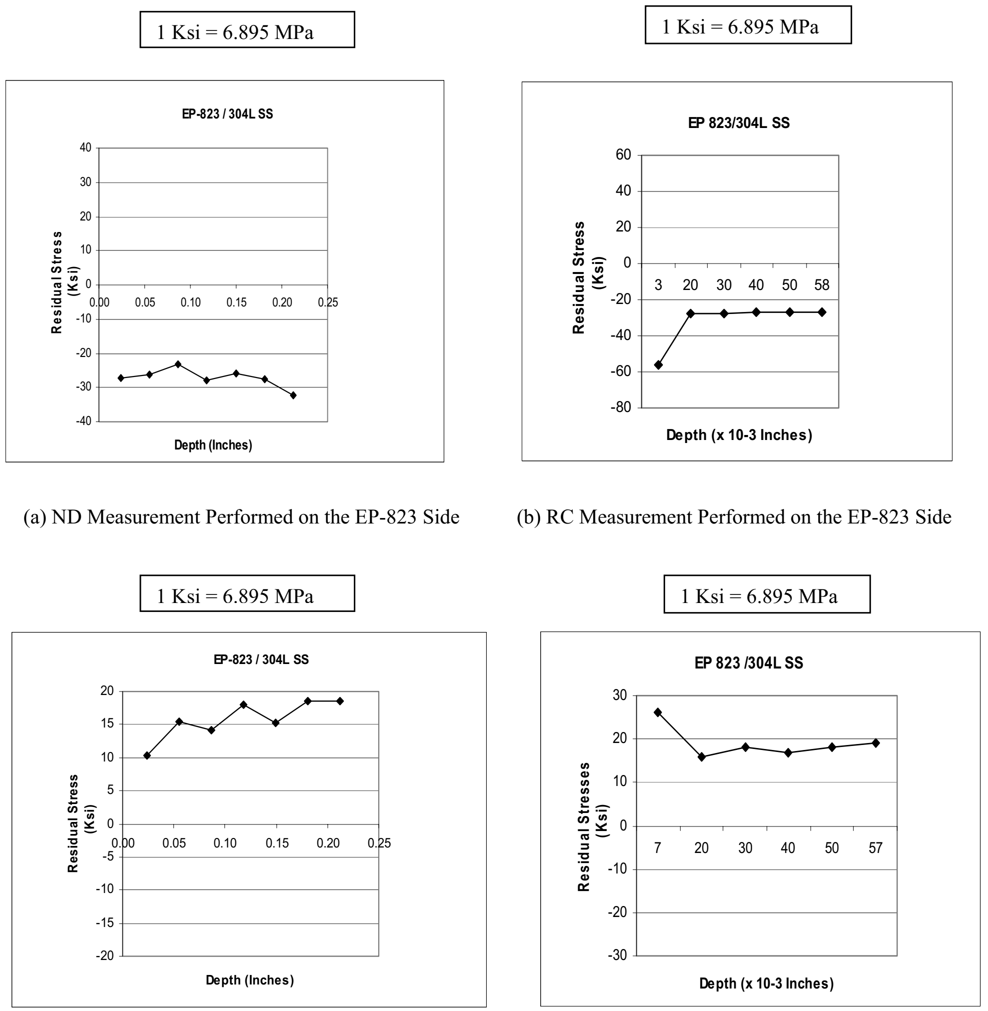

(a) ND Measurement Performed on the EP-823 Side

(b) RC Measurement Performed on the EP-823 Side

(c) ND Measurement Performed on the 304L SS Side

(d) RC Measurement Performed on the 304L SS Side

FIG. 11—*Residual stress measurements by ND and RC methods on Alloy EP-823 /Type 304L SS welded specimen adjacent to the fusion line.*

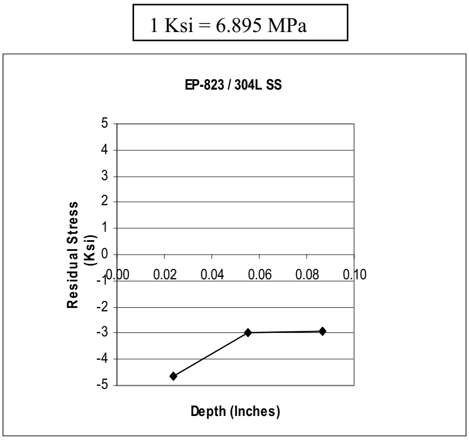

(a) ND Measurement performed on the EP-823 Side

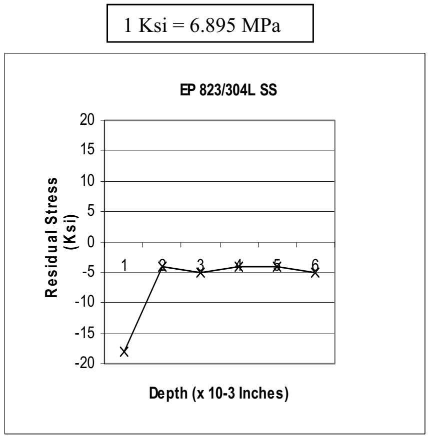

(b) RC Measurement performed on the EP-823 Side

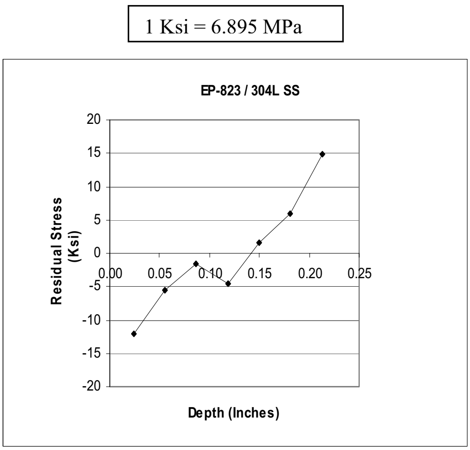

(c) ND Measurement performed on the 304L SS Side

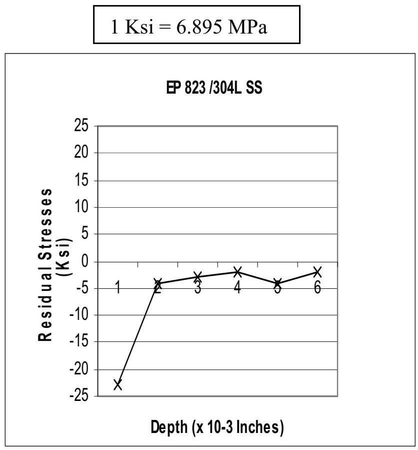

(d) RC Measurement performed on the 304L SS Side

FIG. 12—*Residual stress measurements by ND and RC methods on Alloy EP-823 / Type 304L SS welded specimen (measured at a distance of 1 in. away from the fusion line).*

Metallography

The test specimens were examined by optical microscopy to analyze their metallurgical microstructures. Further, the difference in microstructure was also analyzed for a welded specimen consisting of Alloy EP-823, Type 304L SS, and the filler material, as shown in Figs. 13*a* and 13*b*.

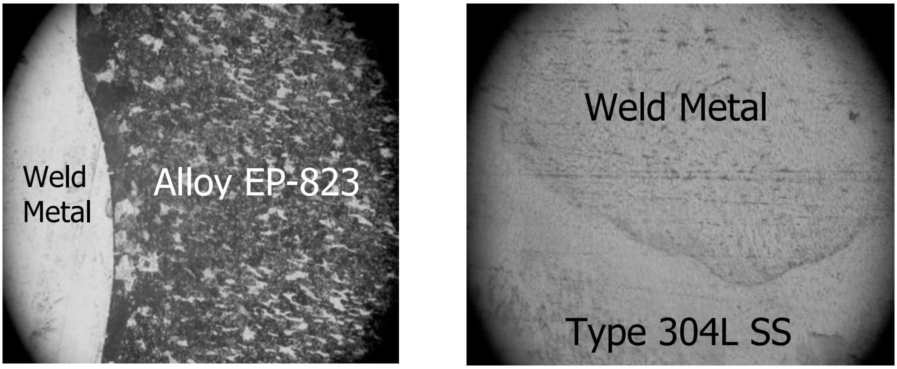

(a) Alloy EP-823, and Weld Metal, Etched (10×) (b) Type 304L SS, and Weld Metal, Etched (10×)

FIG. 13—*Optical micrographs of alloy EP-823/Type 304L SS welded specimen.*

Summary and Conclusion

The residual stresses generated in Alloy EP-823 and Type 304L SS due to cold deformation, bending, and welding have been characterized by both destructive and non-destructive methods. While the ring-core method is a destructive technique, three other techniques such as positron annihilation spectroscopy, neutron diffraction, and x-ray diffraction constitute non-destructive methods for residual stress evaluation incorporated in this investigation. The significant conclusions drawn from this study are summarized below.

- For both alloys, the magnitude of the line shape parameter, T, as evaluated by the PAS technique was gradually reduced with increased level of cold deformation. The reduced T value is an indication of increased residual stress due to cold reduction.
- Residual stresses measured by the XRD method on a welded specimen consisting of Alloy EP-823 only were tensile. However, compressive stresses were observed on the Alloy EP-823 side of Alloy EP-823 / Type 304L SS welded specimen.
- XRD data obtained on a bent specimen of Alloy EP-823 showed compressive residual stresses on the convex side, while tensile stresses were observed on the concave side.
- A comparative analysis of residual stresses measured on the Alloy EP-823 side of a welded specimen (Alloy EP-823/Type 304L SS) by the ND and RC methods revealed compressive stresses at or away from the fusion line by both techniques. On the contrary, the residual stresses measured near the fusion line of the Type 304L SS side of this specimen were tensile in nature. Some discrepancy, however, was noticed at some distance away from the fusion line.

Acknowledgments

This work was funded through the University of Nevada, Las Vegas, Transmutation Research Program administered by the Harry Reid Center for environmental studies (U.S. Department of Energy Grant No. DE-FG04-2001 AL67358). Acknowledgment is also made to Dr. Anthony Hechanova, Director, Transmutation Research Program. Thanks and appreciation are also extended to Dr. Stuart A. Maloy of Los Alamos National Laboratory for his help in specimen preparation.

References

[1] Selim, F. A., Wells, D. P., Harmon, J. F., Kwofie, J., Spaulding, R., Erickson, G., et al., "Bremssstrahlung-Induced Highly Penetrating Probes for Non-Destructive Assay and Defect Analysis," *Nuclear Instruments and Methods in Physics Research A*, Vol. 495, No. 2, 2002, pp. 154–160.

[2] Kumar, A. P., Lynn, K. G., and Welch, D. O., "Characterization of Defects in Si and SiO2–Si Using Positrons," *Journal of Applied Physics*, Vol. 76, No. 9, 1994, pp. 4935–4982.

[3] Hautojarvi, P. and Vehanen, A., *Positrons in Solids*, Springer Verlag, New York, 1979, pp. 1–20.

[4] Clayton, O. R., "Residual Stress Measurements," *ASM Handbook – Mechanical Testing and Evaluation*, Vol. 8, ASM International, Ohio, 2000, pp. 898–899.

[5] Martukanitz, R. P. and Howell, P. R., "Neutron Diffraction Studies of Welds of Aerospace Aluminum Alloys," *Nondestructive Evaluation and Material Properties III*, The Minerals, Metals and Materials Society, Warrendale, PA, 1997, pp. 89–95.

[6] SAE, "*Residual Stress Measurement by X-Ray Diffraction*," SAE J784a, 2nd ed., Society of Automotive Engineers, Warrendale, PA, 1972.

[7] Ismail, I. C. and Cohen, J. B., *Residual Stress Measurement by Diffraction and Interpretation*, Springer-Verlag, New York, 1987.

[8] Kandil, F. A., Lord, J. D., Fry, A. T., Grant, A. V., "*A Review of Residual Stress Measurement Methods – A Guide to Technique Selection*," NPL Report MATC(A) 04, National Physical Laboratory, February 2001.

[9] Albertini, G., Bruno, G., Carrado, A., Fiori, F., Rogante, M., and Rustichelli, F., "Determination of Residual Stresses in Materials and Industrial Components by Neutron Diffraction," *Measurement Science and Technology*, Vol. 10, No. 3, 1999, pp. 56–73.

[10] Keil, S., "Experimental Determination of Residual Stresses with the Ring-Core Method and an Online Measuring System," *Experimental Techniques*, Vol. 16, No. 5, 1992, pp. 17–24.

Journal of ASTM International, April 2006, Vol. 3, No. 4
Paper ID JAI12568
Available online at www.astm.org

Edward J. Kingston,[1] *Danut Stefanescu,*[2] *Amir H. Mahmoudi,*[2] *Chris E. Truman,*[2] *and David J. Smith*[2]

Novel Applications of the Deep-Hole Drilling Technique for Measuring Through-Thickness Residual Stress Distributions

ABSTRACT: This paper presents novel applications of the deep-hole drilling technique for residual stress measurement in components. The results outline the versatility of this technique for application in complex situations such as residual stress measurement in very thick components, components with difficult access to the measurement location, very large components, components requiring high spatial resolution, and components requiring detailed near surface residual stress distribution. The deep-hole drilling measurements were compared with results obtained using other measurement techniques. Excellent agreement was found between the results.

KEYWORDS: residual stress, measurement methods

Introduction

A variety of techniques exist that allow measurement of residual stresses and they are usually subdivided into three categories. Nondestructive techniques such as x-ray diffraction and neutron diffraction enable several measurements to be made at the same spatial point. The semidestructive techniques, such as surface hole drilling, deep-hole drilling, and ring coring, only damage a small part of the specimen and thus permit further measurements at different locations. Finally, destructive techniques, such as layering, completely destroy the specimen. In this paper, application of the novel deep-hole technique to samples of different sizes, shapes, and materials is described. This technique measures the distribution of residual stresses through sections of interest, particularly those where other techniques cannot be easily applied.

The deep-hole technique consists of drilling a hole through a specimen and trepanning a core containing the hole. The hole diameter is measured before and after trepanning and the changes in diameter are used to calculate the residual stresses. Zhdanov and Gonchar [1], Beaney [2], and Jesensky and Vargova [3] developed initial studies using the deep-hole drilling technique. Zhdanov and Gonchar [1] examined residual stresses in steel welds using large reference holes and cores, i.e., 8 and 40 mm respectively. Beaney [2] used gun drilling to provide smooth and straight reference holes of 3.175 mm diameter. The core was then trepanned by electrochemical machining. The change in the hole diameter was measured using strain gages fixed onto two parallel beams fixed together and drawn along the hole. Jesensky and Vargova [3] used two blind-drilled holes on the opposite faces of the specimen and strain gages placed inside the two holes and on the two faces. After trepanning two cores of 32 mm diameter in the component, residual stresses in the three directions could be determined. The method developed by Beaney [2] was updated by Proctor and Beaney [4] who used capacitance gages to measure the change in hole diameter instead of strain gages. Smith and Bonner [5] and George et al. [6], and George and Smith [7,8] have significantly improved these procedures. Leggatt et al. [9], Smith and Bonner [5], Bouchard et al. [10], and George et al. [11] also carried out numerous calibration studies. Recently DeWald and Hill [12] made improvements of the data analysis method. A review of the standard procedure currently used for residual stress measurement in components is given in the next section.

Manuscript received May 28, 2005; accepted for publication October 24, 2005; published online January 2006. Presented at ASTM Symposium on Residual Stress Effects on Fatigue and Fracture Testing and Incorporation of Results into Design on 19-21 May 2004 in Salt Lake City, UT; J. Bunch, Guest Editor.
[1] VEQTER Ltd., University Gate East, Park Row, Bristol, BS1 5UB, UK.
[2] Department of Mechanical Engineering, University of Bristol, University Walk, Bristol, BS8 1TR, UK.

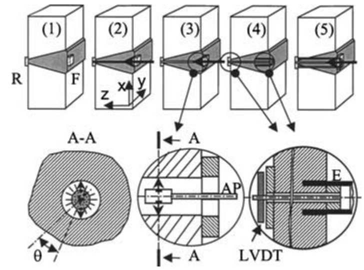

FIG. 1—*Schematic of the deep hole drilling technique. (1) Attach front (F) and rear (R) bushes, (2) Gun drill a reference hole, (3) Measure the reference hole diameter using an air probe (AP), (4) Trepan a coaxial core around the reference hole using a tubular EDM electrode (E) and measure core length change using a linear variable differential transformer (LVDT), (5) Remeasure the reference hole diameter using an air probe.*

Previous calibration studies have shown that the deep-hole drilling (DHD) technique is a reliable experimental technique for obtaining residual stress distributions in components. The technique has determined residual stresses in complex situations, where other techniques are less suited. In this paper some of the most recent and novel applications of the deep-hole drilling technique are presented. The case studies demonstrate the versatility of this technique to measure residual stress distributions in very thick components, components with difficult access to the measurement location, in-situ measurement for full-scale components with highly non-uniform residual stress distribution requiring high spatial resolution, and components with rapidly varying residual stresses requiring detailed near surface residual stress measurements.

Review of the Deep-Hole Drilling Technique

The DHD technique introduces a reference hole through the thickness of a component. The distortion of the hole in the radial direction is measured after a cylinder (i.e., core), coaxial to the reference hole, is extracted from the component. This distortion allows determination of the residual stress distribution in planes normal to the axis of the reference hole using elasticity theory. The axial distortion of the cylinder containing the reference hole can also be measured during trepanning of the cylinder. Trepanning is carried out by electrodischarge machining (EDM), which in turn introduces thermal effects. Measurement of the axial distortion, once any thermal effects are removed from data, provides information about the out-of-plane residual stress. In order to determine the thermal component of the axial deformation of the core, the temperatures of the sample, EDM fluid, and the ambient conditions are measured during trepanning using thermocouples. The various stages of the deep-hole drilling technique are illustrated in Fig. 1. The method of analyzing strains to convert to residual stresses is briefly summarized here. George et al. [6] and George and Smith [7,8] give further details.

In the DHD technique the radial displacements $\Delta d(\theta,z)$ of the reference hole, having an initial diameter d_0, are measured, after core trepanning, as a function of angle θ and through-thickness position z. For a three-dimensional data analysis the total axial deflection $\Delta H_t(z)$ of the trepanned core is also measured as a function of the through-thickness position z. By measuring the core temperature during trepanning the thermal contribution $\Delta H_{th}(z)$ to the total axial deflection can be estimated. The axial deflection $\Delta H(z)$, due to mechanical release of the strain, can be obtained for each increment of the trepanned depth ΔH_{av} from the difference between the total and thermal axial deflections. The hoop and axial strains $\varepsilon_{\theta\theta}(\theta,z)$ and $\varepsilon_{zz}(z)$ along the core are related to the in- and out-of-plane relaxed residual stresses σ_{xx}, $\sigma_{yy}\tau_{xy}$, σ_{zz} by (George et al. [6], George and Smith [7,8])

$$\varepsilon_{\theta\theta}(\theta,z) = \frac{\Delta d(\theta,z)}{d_0} = \quad \frac{1}{E}[\sigma_{xx}f(\theta,z) + \sigma_{yy}g(\theta,z) + \tau_{xy}h(\theta,z) \quad \nu\sigma_{zz}] \tag{1a}$$

TABLE 1—*Summary of components.*

Component name	Material and Young's modulus, E, GPa	Basic dimensions, mm	Measurement depth, mm	Estimated error in residual stress, MPa
Forged roll	Steel, 206	Diameter, 435, length, 830	435	±30
Rail section	Steel, 209	Length 600, height, 172, width, 150	172	±30
Submarine structure	Steel, 210	Diameter 6600, height 2360	35 & 31	±30
Friction welded tube	Titanium, 110	Outside diameter 60, length 140	20	±15
Punched plate	Aluminum, 70	Length 62.5, width, 60, depth, 15	15	±10

$$\varepsilon_{zz}(z) = \frac{\Delta H(z)}{\Delta H_{av}} = \frac{1}{E}[\sigma_{zz} \quad \nu(\sigma_{xx} + \sigma_{yy})] \tag{1b}$$

where $f(\theta, z)$, $g(\theta, z)$, and $h(\theta, z)$ are functions of angle θ and depth z(Garcia Granada et al. [13]).

If radial displacement measurements are obtained at m angles, a least-squares fit to the measured strains can be used to determine the stresses. For each through-thickness position z, Eq 1 can be rewritten in matrix form as

$$\overline{\varepsilon} = [M]\overline{\sigma} \tag{2}$$

where the strain and stress vectors $\overline{\varepsilon}$ and $\overline{\sigma}$ are

$$\overline{\varepsilon} = [\varepsilon_\theta(\theta_1, z), \varepsilon_\theta(\theta_2, z), \ldots, \varepsilon_\theta(\theta_m, z), \varepsilon_{zz}(z)]^T \tag{3a}$$

$$\overline{\sigma} = [\sigma_{xx}(z), \sigma_{yy}(z), \tau_{xy}(z), \sigma_{zz}(z)]^T \tag{3b}$$

and the compliance matrix $[M]$ is given by

$$[M] = \begin{bmatrix} f(\theta_1, z) & g(\theta_1, z) & h(\theta_1, z) & \nu \\ f(\theta_2, z) & g(\theta_2, z) & h(\theta_2, z) & \nu \\ \vdots & \vdots & \vdots & \vdots \\ f(\theta_m, z) & g(\theta_m, z) & h(\theta_m, z) & \nu \\ \nu & \nu & 0 & 1 \end{bmatrix}. \tag{4}$$

Therefore, the optimum residual stress vector $\hat{\sigma}$ can be obtained by

$$\hat{\sigma} = [M]^* \overline{\varepsilon} \tag{5}$$

where $[M]^*$ is the pseudoinverse or Moore-Penrose inverse matrix of the compliance matrix and is defined as

$$[M]^* = ([M]^T[M]) \ ^{1}[M]^T \tag{6}$$

The residual stress distribution through the thickness is obtained by using Eq 5 at each measurement position z.

Case Studies

In this section results obtained using the deep-hole drilling technique on a range of components of different material and size will be illustrated.

Components

The deep-hole drilling technique was used to perform residual stress measurements on several different types of components. These components illustrate the versatility of the deep-hole drilling technique to measure accurately residual stress distributions in complex situations such as in very thick components *(forged roll)*, in sections with varying thickness (*rail section*), components with difficult access to the measurement location *(mock-up submarine T specimen)*, very large components *(full scale submarine structure)*, components requiring high spatial resolution *(Ti-alloy friction stir welded cylinder)*, and components requiring detailed near surface and interior residual stress distributions *(punched aluminum plate)*. The components are summarized in Table 1, and a brief description of the components is given below. The

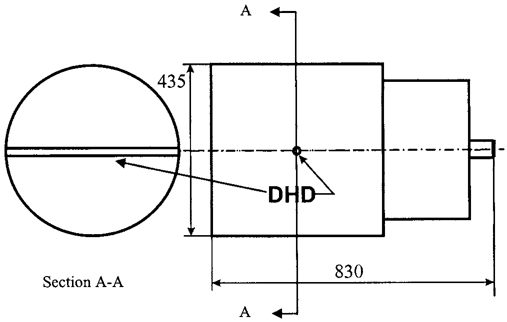

FIG. 2—*Schematic diagram of the forged "mini" steel roll. The DHD location was through the center of the forged roll. All dimensions in millimetres.*

case studies are ordered in terms of the measurement depth, starting with the forged roll, which requires the deepest measurement.

Forged "mini" roll: The overall arrangement of the forged steel roll is shown in Fig. 2. This roll represented a mini mockup and was forged from a solid martensitic steel billet and weighed approximately 830 kg. The term "mini" is therefore used very loosely. The real rolls supplied to the milling industry vary in size from 80–460 tons. After forging, the roll was reheated and water spray quenched, a process that is used traditionally to provide the required microstructure and hardness of material close to the surface of the roll. The DHD method was applied after the quenching operation.

Rail section. A 600 mm long section of European UIC60 rail was examined. A schematic of a section through the rail illustrating the dimensions is shown in Fig. 3. The DHD method was applied at the midlength of the rail and through the thickness, from the foot to the head of the rail.

Full scale submarine structure. Two sections of a submarine structure where examined. The first section was a straight section of a fillet welded T section to represent the fillet welding of a T section, which forms an integral part of the internal frame of a submarine. The second section was a submarine structure that had a diameter of 6600 mm, length 2360 mm, and a thickness of 31 mm. The overall structure is shown in Fig. 4. The shell was strengthened against radial deformation using T-shaped rings, welded internally to the shell, as shown in detail A of Fig. 4(*a*). The submarine structure was fabricated from 80 HLES steel and welded using submerged manual arc welding of length 1000 mm, 255 mm high, 140 mm wide, and 35 mm thick.

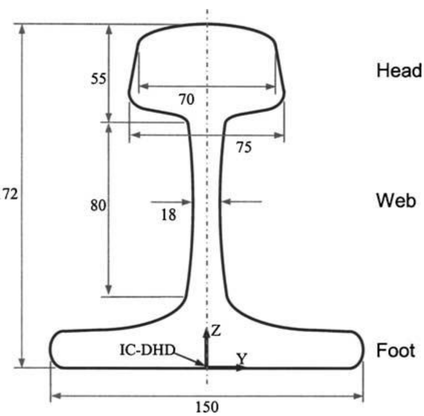

FIG. 3—*Schematic diagram of a section through the rail sample. The DHD measurement was along the center of the rail section. All dimensions in millimetres.*

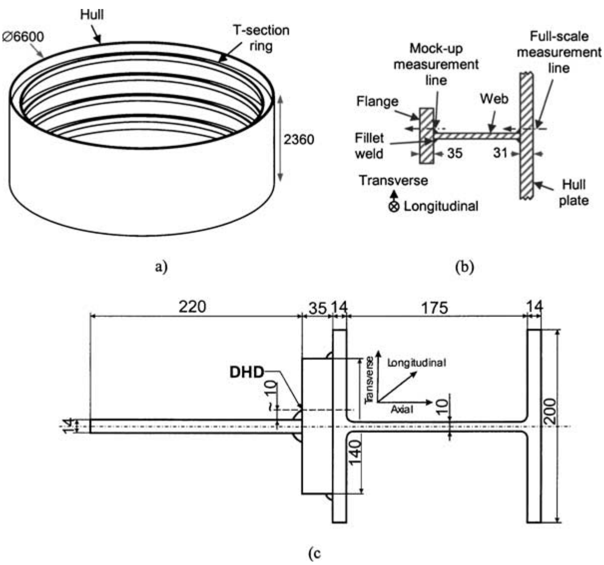

FIG. 4—*Submarine section. (a) A full sized section of the submarine with the shell plate reinforced by T-section rings. (b) A cross section through a T-section reinforcement ring. A DHD measurement was performed at the junction of the T-section fillet welded and the shell plate. (c) T section attached to an I beam. A DHD measurement was performed at the toe of the fillet weld. All dimensions in millimetres.*

The straight section of a fillet welded T section was used to simulate the welding conditions of a real submarine structure. For this, the T-shaped specimen was attached to an I beam, 1000 mm long, 203 mm high, 200 mm wide, and 14 mm thick. The mock-up specimen, shown in Fig. 4(*b*), was fabricated from 80 HLES steel and welded using submerged manual arc welding. Measurement of the residual stress distribution was performed in the as-welded condition for both the submarine structure and the T section.

Friction stir welded cylinder: This component consisted of a friction butt-welded titanium alloy hollow cylinder with dimensions of 140 mm long, 60 mm outside diameter, and an average wall thickness of 19.5 mm, as shown in Fig. 5. The titanium alloy was Ti-10V-2Fe-3Al, which is used widely in the aerospace industry for the manufacture of landing gear and airframes.

The friction weld was a 4 mm wide, full depth (20 mm), fully circumferential weld at the mid-length of the cylinder. The welding process was carried out with one half of the pipe fixed and the other half spun at high speed before being rammed together creating friction, excessive heat buildup, and the subsequent

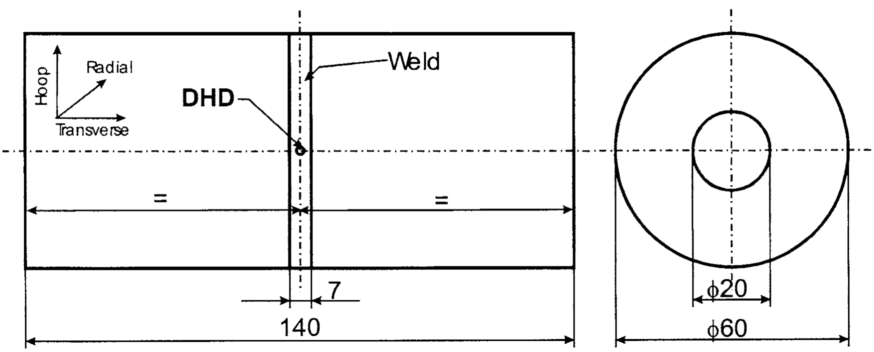

FIG. 5—*Schematic diagram showing the friction stir welded titanium tube. All dimensions in millimetres.*

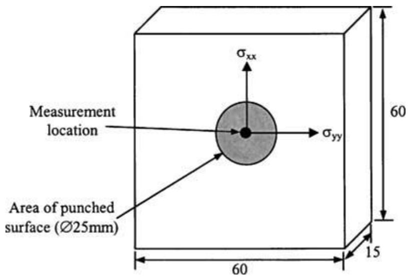

FIG. 6—*Schematic diagram showing the punched plate component. All dimensions in millimetres.*

welding of the two halves. The excess material created during friction welding was removed by machining after welding. The DHD technique was applied in the center of the friction weld through the wall thickness of the cylinder.

Punched plate: An aluminum alloy AL2650 rectangular sample, 60 mm by 60 mm by 15 mm thickness (Fig. 6), was subjected to local compression (punching). The compression was applied to both sides of the thickness of the plate using 25 mm diameter hardened steel punching tools. The DHD technique was used to obtain the distribution through the center of the compressive zone created by local compression.

Experimental Procedures

For residual stress measurement the DHD technique was adapted to the specific geometry and requirements concerning the spatial resolution of each component. In this section, the standard procedure, containing elements common to all measurements performed, is described. This is followed by a description of the specific elements required for measurements in the forged roll, rail section, and submarine structure. In the case of the friction welded cylinder and the punched plate the standard procedure was applied. All components, with the exception of the full-scale submarine structure, were measured in laboratory conditions. The submarine structure was measured in situ in a fabrication workshop.

Standard Deep-Hole Drilling Procedure

The standard DHD procedure consisted of gundrilling a 3.175 mm diameter reference hole through the component at the measurement locations shown in the figures. The diameter of the hole was subsequently measured using an air probe system that has a resolution of about 0.5 μm. Measurements were carried out at 18 different angles around the axis of the hole and at increments of 0.2 mm along the axis of the hole. The minimum number of measurement angles is three but experience has shown that substantial improvements in stress measurement are obtained using more angles. A 10 mm core, coaxial to the reference hole, was trepanned free of the plate using electrodischarge machining. Finally, after trepanning, the reference hole diameter was remeasured using the air probe system. The change in hole diameter before and after trepanning was used to determine radial displacement and, subsequently used to reconstruct the in-plane residual stresses by using a two dimensional data analysis, based on Eqs. 1–6. It was assumed that $\sigma_{zz} = \varepsilon_{zz} = 0$, in other words, no account of the axial deflection was considered. The elastic modulus used for each residual stress calculation is shown in Table 1. The errors in measured residual stress were estimated from earlier calibration studies (George et al. [11]) and are also shown in Table 1 for each component.

Forged "mini" roll and rail section: The main characteristic for these specimens regarding the application of the DHD technique was their very large thicknesses, which ranged from 172 to 435 mm. The primary challenge consisted of evaluating the ability of the drilling and EDM trepanning operations to drill and trepan a straight reference hole and a coaxial core through the section of the rail and across the diameter of the roll. For residual stress measurement, the standard procedure described above was applied. The element specific to this component was the use of a specially designed guide for the EDM electrode, which reduced the misalignment and resulted in an excellent coaxiality.

Submarine structure: There were two challenges in performing measurements on the submarine structure. One was associated with the in situ measurement of the full-scale submarine structure. The second

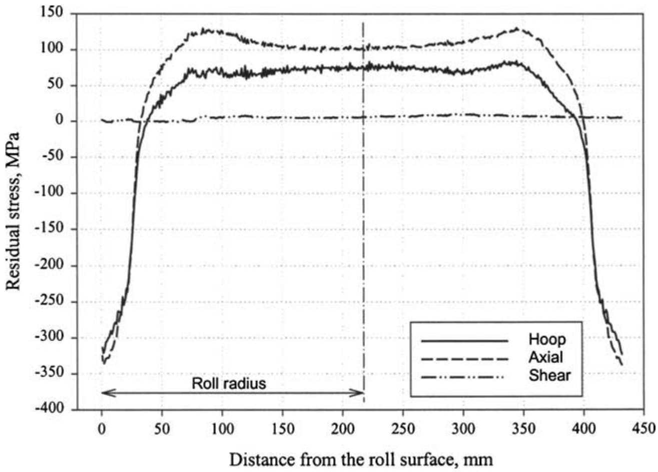

FIG. 7—*Residual stress distribution measured in the forged roll.*

challenge was created by restricted access to the measurement location on the mock-up T section, Fig. 4(*b*). Due to the large dimensions of the submarine structure, an in situ measurement was required and thus the challenge consisted of developing portable system. The standard procedure described above was used to perform residual stress measurements. The axis of the reference hole was through the thickness of the hull at the point of intersection with the weld root. This location was chosen in order to measure the residual stresses generated in the heat-affected zone (HAZ) between the weld and the hull material. The measurement was carried out with the entrance of the reference hole located on the outer surface of the hull at an arbitrary position around its circumference. The portable machine was positioned horizontally on the outside of the hull section, at a height of approximately 2.5 m above the ground. The DHD technique was thus carried out in a horizontal position, i.e., the axis of the reference hole was horizontal.

In the laboratory, measurement at the toe of the fillet weld gave restricted access for the mock-up T section. A specially designed guide for the gun drill and EDM electrode was used to prevent any sizeable deviation from the measurement location, i.e., the toe of the weld.

Friction welded tube: The challenge imposed by the friction stir welded cylinder was due to the material type and high spatial resolution required. The standard DHD measurement technique was used. The measurement location was on the centerline of the weld at an arbitrary position around the circumference. The axis notation used for this measurement location is shown in Fig. 5.

Punched plate: The challenge for measurements on the punched plate was to obtain the residual stress distributions close to the surface and also to measure a high gradient residual stress field along a path coincident with measurements using the x-ray synchrotron (XRS) technique. For DHD residual stress measurements the standard procedure described above was applied except that a 1.5 mm diameter reference hole was created and the trepanning diameter was 5 mm. Near surface residual stress measurements were also obtained using an incremental center hole (ICHD) method, which is described in detail by Stefanescu et al. [14].

Results and Discussion

Forged "mini" roll: The residual stresses measured in the forged roll are presented in Fig. 7. Here, hoop stress refers to the stresses in the circumferential direction of the roll, and axial stress refers to the stresses along the main axis of the roll.

The hoop and axial residual stresses were compressive in the outer layers and tensile in the bulk. The in-plane shear stresses across the diameter of the roll were approximately zero, indicating that the hoop and longitudinal stresses were the principal stresses. The hoop and axial residual stresses were approximately equibiaxial and compressive for the first 30 mm depth. Once tensile, the hoop and axial residual

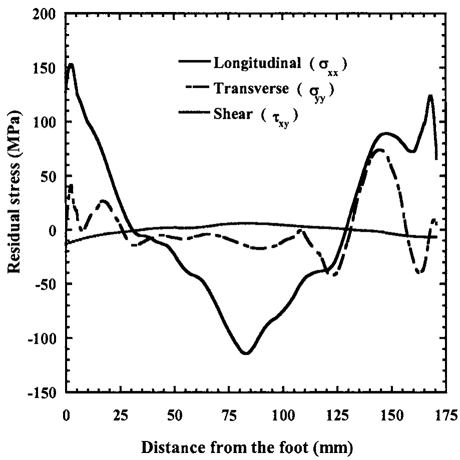

FIG. 8—*Residual stress distribution measured in the rail sample using DHD.*

stresses separated, with a maximum tensile axial residual stress of 135 MPa at a distance of approximately 85 mm from the surface of the roll. In contrast to the measured distributions in some of the other components, there were no other measurements available for comparison.

Rail Section: The in-plane residual stresses calculated from the DHD strains are presented in Fig. 8. The longitudinal stresses are those along the length of the rail, and the transverse stresses are those perpendicular to the rail length. At the foot (Z=0) and at the head (Z=172 mm) of the rail the longitudinal residual stresses were both approximately 150 MPa. These tensile longitudinal stresses were balanced by compressive residual stresses in the center of the web, which reached a maximum magnitude of approximately 100 MPa. The magnitude of the transverse residual stresses was lower than that of the longitudinal stresses. The largest transverse residual stress (75 MPa) occurred at the junction between the head and web (Z=140 mm) of the rail. The shear stress was approximately zero through the complete rail thickness. This demonstrated that the longitudinal and transverse residual stresses were the principal stresses through the center of the rail.

Residual stresses in rails have also been measured previously using other experimental techniques (Groom [15], Webster et al. [16], Osterle et al. [17], and Deputat. [18]). Finite element (FE) analyses have also predicted residual stresses in rails (Finstermann et al. [19] and Schleinzer and Fischer [20]). The DHD measured longitudinal residual stresses are shown in Figure 9 together with neutron diffraction (ND) results (Webster et al. [16]) for comparison. A good agreement can be observed between the two sets of results. In order to reduce neutron absorption to acceptable levels the neutron diffraction measurements were performed on a rectangular plate of dimensions 350 mm by 173 mm plate by 10 mm thick, which was extracted along a plane, symmetrically about the center line of the rail. Extraction of the plate substantially relaxed the transverse stresses but it was assumed that the plate retained a large proportion of the longitudinal stress. The relaxation effect generated by cutting is a likely reason for the differences between the DHD and ND results seen in the foot and head of the rail. In the web, where material removal for ND measurements was much less, there is excellent agreement between the results obtained from the two techniques. Because the DHD technique could be applied to an uncut rail, it is a preferable technique for this type of component, as compared to techniques, which involve slicing the rail.

Full-scale submarine structure: Two residual stress distributions were obtained, one from the full-scale structure, Fig. 4(*a*), and the other from the fillet welded T section, Fig. 4(*b*). The residual stresses through the submarine hull are shown in Fig. 10. The residual stresses are shown for directions transverse and longitudinal to the fillet weld axis. Also shown are the associated in-plane shear residual stresses. The residual stresses are shown as functions of depth through the hull measured from the toe of the fillet weld on the inside of the hull.

The longitudinal (or hull hoop) and transverse (or hull axial) residual stress distributions were found to be similar in distribution, both exhibiting an oscillatory distribution centered at 0 MPa. The longitudinal

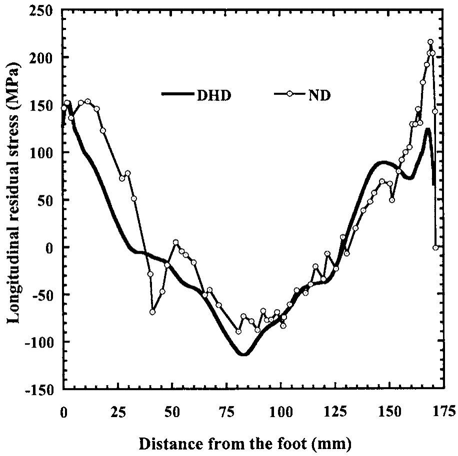

FIG. 9—*Comparison between the DHD and neutron diffraction results for the rail sample.*

residual stress was found to be the larger of the two throughout the majority of the thickness. The maximum longitudinal residual stress was in the longitudinal direction with a peak value of 525 MPa close to the welded surface. It can be seen that the magnitude of the in-plane shear stresses was small; hence the principal stresses were approximately equal to the longitudinal and transverse residual stresses.

A similar set of residual stresses was observed in the mock-up T section, except the residual stresses away from the fillet weld were significantly different from the full-scale structure. Figure 11 illustrates the longitudinal residual stresses for both the submarine structure and the mock-up T section. Close to the toe of the fillet weld the residual stresses were of similar magnitude. For depths larger than about 12 mm the longitudinal stress was zero in the mock-up T section.

The difference between the residual stresses (longitudinal and transverse) in the mockup and the submarine structure is shown in Fig. 12. These new residual stress distributions are 180° rotationally symmetric about mid-depth. The symmetric, oscillatory distribution is consistent with the residual stresses generated by plastic bending of a plate (by rolling) to form the curved submarine structure. Consequently, the residual stress profiles presented in Fig. 10 are a combination of welding residual stresses and residual stresses generated by bending moments applied during rolling of the plate.

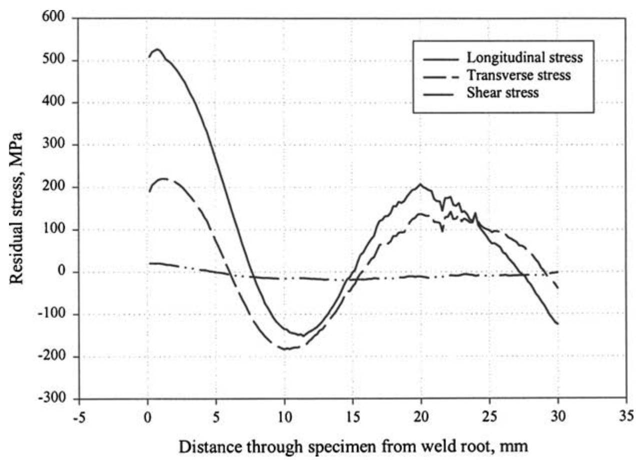

FIG. 10—*Residual stresses measured in the submarine hull, obtained with a portable DHD machine.*

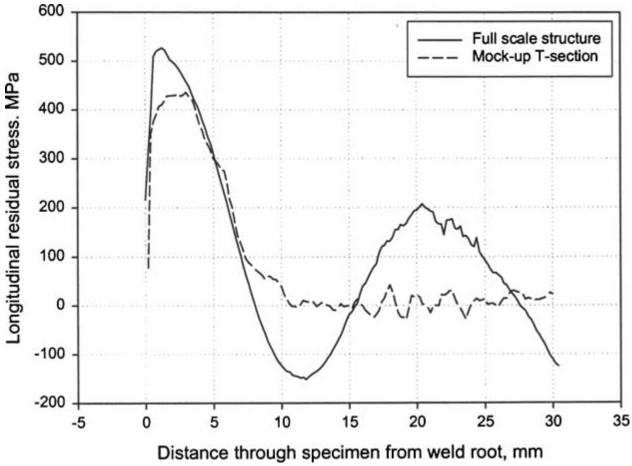

FIG. 11—*Comparison of the residual stresses measured in the full scale structure and the mock-up T section.*

Friction stir welded cylinder: The measured residual stress distribution is shown in Fig. 13. The transverse, longitudinal, and associated in-plane shear residual stresses are shown. The residual stresses are shown as functions of depth through the pipe thickness measured from the outer surface. The transverse and longitudinal residual stresses are similar in shape, both being compressive for the first 6.5 mm and then becoming tensile. A 10 mm core containing a 3.18 mm diameter reference hole was extracted from the titanium cylinder. The diameter of the extracted core was such that it contained weld, HAZ, and parent material. Therefore the residual stresses released and measured were those experienced by the weld, HAZ, and in part the parent material.

Punched plate: In-plane residual stresses measured through the thickness of the punched plate are shown in Fig. 14. Due to the symmetry of punching process, the magnitude and directions of the two principal in-plane stresses were similar and only one stress component is shown in Fig. 14. Also shown in Fig. 14 are the results obtained from XRS and ICHD measurements. The XRS measurements were undertaken prior to the DHD measurement at the same location. There is excellent agreement between the

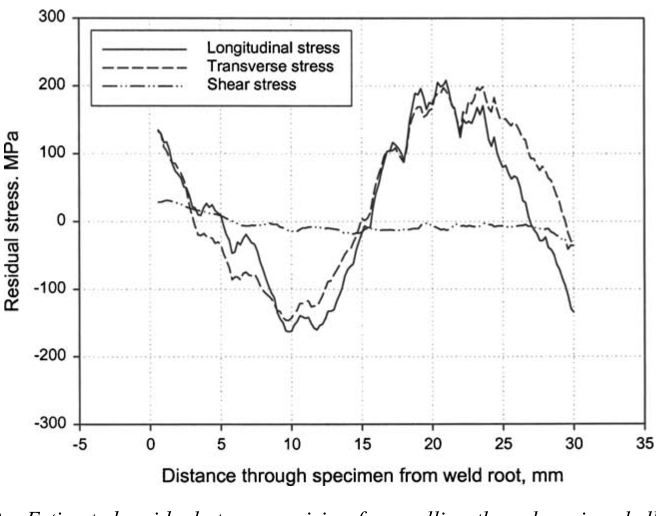

FIG. 12—*Estimated residual stresses arising from rolling the submarine shell plates.*

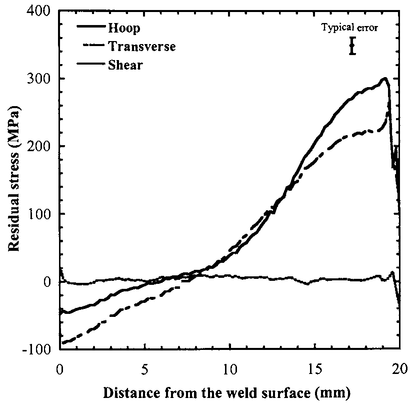

FIG. 13—*Residual stresses measured in a titanium alloy friction weld.*

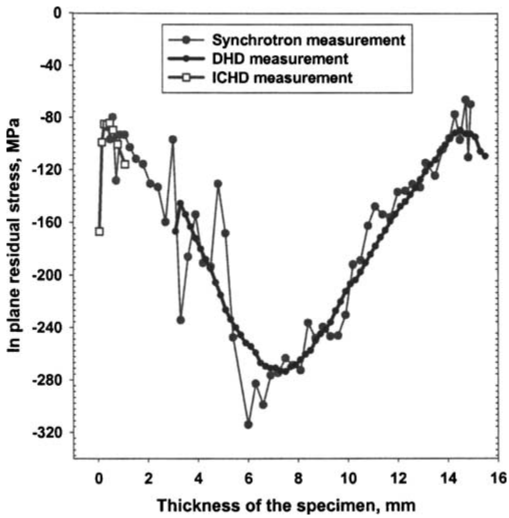

FIG. 14—*Residual stresses measured in a punched plate.*

measurements from the different techniques. The XRS measurements reveal variations in residual stress that oscillate about the DHD measurements. This may be evidence of intergranular stresses that can be measured using the XRS method that cannot be measured using the DHD method.

Conclusions

It has been demonstrated that the deep-hole drilling technique can be applied to a wide range of engineering components and different metallic alloys. In all the examples provided, the DHD method has obtained the through-thickness distribution of the in-plane residual stresses. In examples where alternative measurement methods have been applied, the agreement with DHD measurements has been excellent.

Acknowledgments

The measurements on the submarine structure and the mock-up T section were carried out as part of an EU-FP5/ELIXIR project and the financial support from the EU is gratefully acknowledged. Many thanks are due to Sheffield Forgemasters for providing the forged roll, to Dr. A. Wisbey of Qinetiq for providing the friction stir welded cylinder and Dr. P. Browne of Balfour Beatty Rail for supplying the rail section. The material for the punched plate was supplied by Airbus UK.

References

[1] Zhdanov, I. M. and Gonchar, A. K., "Determining The Residual Welding Stresses At A Depth In Metals," *Automatic Welding*, 31(9), 22–24 (1978).
[2] Beaney, E. M., "Measurement Of Sub-Surface Stresses," Cegb Report No. Rd/B/N4325, 1978.
[3] Jesensky, M. and Vargova, J., "Calculation And Measurement Of Stresses In Thick-Walled Welded Pressure Vessels," *Svaracske Spravy*, 4, 79–87 (1981).
[4] Proctor, E. and Beaney, E. M., "Advances In Surface Treatments: Technology-Application-Effects," *International Guidebook On Residual Stresses*, Vol. 14, Oxford, Pergamon, 1987, pp. 165–198.
[5] Smith, D. J. and Bonner, N. W., "Measurement Of Residual Stresses Using The Deep-Hole Method," *PVP (Am. Soc. Mech. Eng.)*, 327, 53–65 (1996).
[6] George, D., Bouchard, P. J. and Smith, D. J., "Evaluation Of Through Wall Residual Stresses In Stainless Steel Weld Repairs," *Mater. Sci. Forum*, 347–349, 646–651 (2000).
[7] George, D. and Smith D. J., "The Application Of The Deep-Hole Technique For Measuring Residual Stresses in Autofrettaged Tubes," *ASME Pvp High Pressure Technology*, 406, 25–31 (2000).
[8] George, D. and Smith, D. J., "Residual Stress Measurement in Thick Section Components," *ASME Pvp Assessment Methodologies For Preventing Failure: Deterministic and Probabilistic Aspects And Weld Residual Stress*, Vol. 410-1, pp. 275–282 (2000).
[9] Leggatt, R. H., Smith, D. J., Smith, S. D., and Faure, F., "Development And Experimental Validation Of The Deep-Hole Method For Residual Stress Measurements," *J. Strain Anal.*, 31, pp. 177–186 (1996).
[10] Bouchard, P. J., Holt, P. and Smith, D. J., "Prediction and Measurement Of Residual Stresses in A Thick Section Stainless Steel Weld," *Proc. ASME-Pvp Conf.*, Vol. 347, pp. 77–82 (1997).
[11] George, D., Kingston, E. and Smith, D. J., "Measurement Of Through-Thickness Stresses Using Small Holes," *J. Strain Anal. Eng. Des.*, 37(2), 125–139 (2002).
[12] Dewald, A. T. and Hill, M., R. "Improved Data Reduction For The Deep-Hole Method Of Residual Stress Measurement," *J. Strain Anal. Eng. Des.*, 38(1), 65–78 (2003).
[13] Garcia Granada, A. A, George, D., and Smith, D. J., "Assessment Of Distortions In The Deep-Hole Drilling Technique For Measuring Residual Stresses." in *Proceedings Of The 11th International Conference On Experimental Mechanics*, Oxford, Uk, 1998, pp. 1301–1306.
[14] Stefanescu, D., Truman, C. E. and Smith, D. J., "An Integrated Approach For Measuring Near And Sub-Surface Residual Stress In Engineering Components," *J. Strain Anal. Eng. Des.*, in press.
[15] Groom, J. J., "Determination Of Residual Stresses In Rails," *Final Report*, Dot/Fra/Ord-83/05, 1983.
[16] Webster, P. J., Wang, X., Mills, G., and Webster, G. A., "Residual-stress changes in Railway Rails," *Physica B*, 180, 1029–1031 (1992).
[17] Osterle, W., Rooch, H., Pyzalla, A. and Wang, L., *Mater. Sci. Eng.*, A303, 150–157 (2001).
[18] Deputat, J., Szelazek J. and Adamski, M, *Rail Quality and Maintenance For Modern Railway Operation*, 1993, p. 109.
[19] Finstermann, G., Fischer, F. D., Shan, G. and Schleinzer, G., "Residual stresses in rails due to roll straightening," *Metal Working, Steel Res.*, 69(7), pp. 272–278 (1998).
[20] Schleinzer, G. and Fischer, F. D., *Int. J. Mech. Sci.*, 43, 2281–2295 (2001).

www.astm.org

ISBN: 0-8031-4472-5
ISBN: 978-0-8031-4472-9
Stock#: STP1497